Experimental study of collapse mechanisms in gravelly soils

LUAI ELHUSAIN

Imperial College London, Department of Civil and Environmental Engineering

A thesis submitted to Imperial College London in partial fulfilment of the requirements for Doctor of Philosophy and the Diploma of Imperial College London

April 2022

Abstract

Unusual collapsible gravelly soils from Khartoum, Sudan, have led to severe structural damage, usually caused by water infiltration into the underlying ground. As taking undisturbed block samples of the natural soil was not possible because of its friable gravelly nature, analogue specimens were prepared from lightweight aggregate (Lytag) bonded with kaolin.

Results from previous studies did not predict degrees of 'collapse potential' (CP) levels that correspond to the severe damage observed. A theoretical procedure is developed, based on differences between in-situ soil density and the maximum compacted density, which resulted in a more realistic magnitudes of CP (ratio of collapse settlement to layer thickness).

The primary research focus involved an experimental programme, developed in three stages using analogue specimens. First, the effectiveness of conventional 1-D collapse tests was assessed. Second, larger diameter analogue specimens were tested under different boundary conditions with (a)full and (b)partial lateral confinement (similar to footing tests). The latter tests produced far more realistic collapse (10x the 1-D tests, i.e., from moderate to severe CP). Consequently, the third approach was to test under triaxial conditions, with careful control of lateral and deviatoric stresses (close to those in situ), and allowing axial, volume and radial collapse strains to be determined.

Test boundary conditions strongly govern the magnitude of CP and collapse mechanism. Two different collapse mechanisms were identified. At high deviatoric stresses and low confining stresses, when the specimen was inundated, there was radial dilation, while radial contraction occurred under low deviatoric stresses and high confining stresses. The severity of CP increases with inundation collapse stress.

A relationship between collapse strain and resulting increased collapse density with inundation collapse stress is developed: at constant cell pressures, this relation has a unique curve which can be used to classify the collapse mechanisms; a soil collapse classification chart is proposed.

Declaration

I declare that the work provided in this thesis was undertaken in the Geotechnics Section of the Department of Civil and Environmental Engineering premises at Imperial College London. This thesis is genuine which was resulted from my own commitments to participate in solving a real ground problem in my home country 'Sudan'. Others' work, whether its published or unpublished, is acknowledged in the reference section.

I also declare that the work in thesis is not similar to any work that I have submitted for any degree, diploma or other qualification at this university or any other university.

The copyright of this thesis rests with the author and is made available under a Creative Commons Attribution Non-Commercial No Derivatives licence. Researchers are free to copy, distribute or transmit the thesis on the condition that they attribute it, that they do not use it for commercial purposes and that they do not alter, transform or build upon it. For any reuse or redistribution, researchers must make clear to others the licence terms of this work.

Luai Elhusain

London - April 2022.

Acknowledgements

This research was financially supported by the Professor Shawki Saad Fellowship. His generous donation for sponsoring my PhD research as a graduate of the Civil Engineering Department at the University of Khartoum is gratefully acknowledged.

The research has been supervised by Professor J.R. Standing whose guidance and empower are appreciatively acknowledged. I am thankful for his time, patience, and motivation throughout the years of my PhD research journey. He has not been only my academic adviser but also his friendship and kindness have been my pressure removal.

I am also grateful for the unlimited technical support that was provided by the laboratory staff and for benefiting from their broad experience. Namely I have to mention: S. Ackerley, G. Keefe, A. Stefanos and P. V. Hirani. Thanks for organising helpful regular laboratory meetings with the lab staff and other colleague. Special thanks for the laboratory academic manager and the meetings' organiser (Dr. J. A. Carraro) and the Section head Professor L. Zdravkovic. Also, from the Material Section – ICL, I have to acknowledge the generous support of Dr. Marcus Yio for his help on characterising the Lytag and special thanks for my colleague, Toney Maher for helping with the producing the SEM photographs.

I have also to acknowledge the friendly, academic, and supportive environment in the Geotechnic Section. My gratitude for Professor J.B. Burland, Professor R. J. Jardine, Professor K. O'Sullivan, Dr. J. A. Carraro, and Dr. D. Taborda for their educational input.

My deep gratitude is expressed to my big family members who keep encouraging and wishing for my success from a distance during this period: my father my role model, my mother, my brothers and my sisters.

Finally, thanks to my wife my life and our daughters the apples of my eye for being supportive during this academic journey in the UK.

Contents

Abstract i
Declaration ii
Acknowledgements iii
Contents iv
List of Tables viii
List of Figures ix
List of abbreviations and symbols xiv
Chapter 1 : Introduction 1
1.1 General background 1
1.2 Research motivation 1
1.3 Research background 2
1.4 Research aims, methodology and findings 3
1.5 Thesis structure 4
Chapter 2 : Literature review 7
2.1 Collapse in different soil types 7
2.1.1 Introduction to collapse in soils 7
2.1.2 Formation and distribution of collapsible soils 8
2.1.3 General features of collapsible soils 10
2.1.4 Particle bonds in collapsible soils 11
2.1.5 Definitions and terminologies 13
2.1.6 Collapse measures and classification 16
2.1.7 Identification of collapse potential from soil properties 25
2.1.8 Review of some collapse tests from previous studies 27
2.2 Review of collapse in gravelly soils in the study area. 31
2.2.1 Introduction 31
2.2.2 Collapsible soils in Sudan 32
2.2.3 Collapse and heave in the capital Khartoum 37
2.2.4 The climate in Khartoum 38
2.2.5 Omdurman geological formation 38
2.2.6 Collapse occurrences in the study area 39
2.2.7 Soil collapse history in the study area 42
Chapter 3 : The collapse potential of the Omdurman gravelly soil 51
3.1 Introduction 51
3.2 Field observations 51

3.2.1 The selection of location of the study area and site visits 51
3.2.2 Field observations related to collapse 51
3.3 Sampling process 64
3.4 Soil characterisation 67
3.4.1 Particle size distribution 67
3.4.2 Gravel shape and density 68
3.4.3 Soil mineral characterisation 69
3.5 Soil classification 72
3.6 Collapsibility of soils at the study area 73
3.6.1 Collapse from an in-situ plate load test 73
3.6.2 Estimating collapse from soil properties 74
3.7 Chapter summary 81
3.7.1 Soil collapse in the study area 81
3.7.2 Difficulties in measuring soil collapse in the study area 81
Chapter 4 : Analogue collapsible soil specimens 82
4.1 Introduction 82
4.2 Issues with soils in the study area 82
4.3 Using more controllable materials 83
4.4 Kaolin properties 84
4.5 Lytag characteristics 85
4.5.1 Lytag particle size and shape 86
4.5.2 Surface roughness and micro surface pores of Lytag 87
4.5.3 Lytag particle density 89
4.5.4 Lytag water absorption 90
4.5.5 Minimum density of Lytag 93
4.6 Analogue collapsible gravelly specimens 96
4.6.1 Introduction 96
4.6.2 Preparing analogue specimens using natural gravel from the study area 97
4.6.3 Preparing analogue specimens using Lytag 101
Chapter 5 : Collapse in compression tests with lateral confinement 106
5.1 Introduction 106
5.2 Test considerations 107
5.3 Analogue collapsible specimens 109
5.3.1 Protocol for preparing analogue collapsible specimens 109
5.3.2 Evaluation of changes during drying of analogue specimens 110
5.4 1-D Collapse test apparatus and procedure 112

5.4.1 Apparatus description 112
5.4.2 Test set-up 113
5.4.3 Test procedure 114
5.5 Analogue specimen test results and discussion 115
5.5.1 Collapse from natural gravel analogue specimens 115
5.5.2 Collapse of the Lytag analogue specimens 116
5.5.3 Collapse mechanism 118
5.5.4 Effect of kaolin percentage on collapse potential 119
5.5.5 Collapse of partially confined specimens 120
5.5.6 General failure under partial confinement 122
5.6 Chapter 5 conclusions 122
Chapter 6 : Procedures for the 3-D triaxial collapse testing 124
6.1 Introduction 124
6.2 Studied parameters 125
6.3 Characteristics of the analogue specimens for triaxial testing 125
6.4 Description of triaxial apparatus 127
6.5 Specimen set-up for triaxial testing 128
6.6 Challenges related to testing gravelly specimens 130
6.6.1 Membrane rupture 130
6.6.2 Measurement of the volume of membrane penetration 135
6.6.3 Development of local strain measuring system 138
6.7 Test stages and procedures 140
6.7.1 Dry shearing test description 140
6.7.2 Collapse test description 141
6.8 Recording and processing the triaxial testing data 146
6.8.1 Data collected from the GDS triaxial system 146
6.8.2 Processing of the test data 147
6.9 Stress paths 153
6.9.1 Range of the applied inundation collapse stress 153
6.9.2 Dry failure envelope 153
6.10 Chapter 6 Summary 154
Chapter 7 : Analysis and discussion of the 3-D triaxial tests results 154
7.1 Triaxial tests results 154
7.2 Dry shearing response 157
7.2.1 Stiffness of the analogue specimens 161
7.3 Wet failure envelope 162

7.4 Stress paths for the tested specimens 164
7.4.1 Dry failure envelope in (t' vs s') plot space 164
7.4.2 Stress paths of specimens tested for collapse 164
7.5 Stress-strain relations from triaxial collapse tests 165
7.5.1 Effect of cell pressure on collapse strains 165
7.5.2 Effect of inundation collapse stress on collapse strains 169
7.5.3 Strain captured using LVDTs 174
7.5.4 Radial strain assessment 177
7.6 Axial strains before and after collapse 181
7.6.1 Density before and after collapse 181
7.7 Collapse mechanisms 183
7.8 Effect of specimen dry density on collapse potential 184
7.8.1 Application of density charts 188
7.8.2 Defining the collapse mechanism using density charts 189
7.9 Summary of Chapter 7 191
Chapter 8 : Main conclusions and recommendations for future research. 192
8.1 Collapsibility of the soils at the study area 192
8.2 Theoretical evaluation of collapse 193
8.3 Analogue specimens 193
8.4 1-D and partially confined 3-D footing collapse tests 194
8.5 Triaxial collapse test 195
8.6 Recommendations for future research 198
List of references 200
Appendix A: The GDS permeameter – triaxial apparatus 208
A.1 the GDS permeameter description, operation, and calibrations 208
A.1.1 Description 208
A.1.2 Operation for conducting the considered tests 208
A.1.3 Calibrations 212
Appendix B: 216

List of Tables

TABLE 2.1: CHARACTERISTICS AND COLLAPSE POTENTIAL OF SOILS FROM ALBUQUERQUE, NEW MEXICO, FOR LOESS, ALLUVIAL FAN AND ALLUVIAL DEPOSITS AFTER LOMMLER AND BANDINI (2015) 11
TABLE 2.2: MINIMUM OEDOMETER MOULD DIMENSIONS FROM DIFFERENT STANDARDS (AFTER NG ET AL., 2006) 18
TABLE 2.3: CATEGORISATION OF DEGREE OF COLLAPSE 24
TABLE 2.4: CRITICAL DEGREE OF SATURATION FOR DIFFERENT PARTICLE SIZES - JENNINGS AND KNIGHT (1975) 28
TABLE 2.5: SOIL PROPERTIES OF THE COLLAPSIBLE SOILS AT THE AREA OF STUDY AFTER (HAMID, 2012) 45
TABLE 2.6: SOIL CHARACTERISTICS WHERE THE IN-SITU PLATE LOAD TEST WAS PERFORMED (AFTER OSMAN, 2004) 48
TABLE 3.1: SEMI-QUANTITATIVE XRD ANALYSIS FOR GRAVEL POWDER 72
TABLE 3.2: SEMI-QUANTITATIVE XRD ANALYSIS FOR THE CLAY FRACTION 72
TABLE 4.1: KAOLIN (SPESWHITE) CHARACTERISTICS AFTER (MAHMOUD, 1989) 85
TABLE 5.1: CHARACTERISTICS OF THE CONTAINERS 107
TABLE 5.2: LYTAG GROUPS USED IN THE SPECIMENS 109
TABLE 6.1: EXAMPLE FOR EXPLAINING THE TRIAXIAL SPECIMENS' DENOMINATION 126
TABLE 6.2: CHARACTERISTICS OF THE ANALOGUE SPECIMENS FOR TRIAXIAL TESTING 126
TABLE 7.1: SUMMARY OF THE TRIAXIAL TESTING PROGRAMME 156
TABLE 7.2: STRESS PATH PARAMETERS 165
TABLE 7.3: STRAIN RESULTS FROM TRIAXIAL COLLAPSE TESTS 173

List of Figures

FIGURE 1.1: SOME OF THE AFFECTED BUILDINGS IN THE STUDY AREA – SITE VISITS IN DECEMBER 2018 AND DECEMBER 2019 6
FIGURE 2.1: A LOADED METASTABLE SOIL STRUCTURE BEFORE AND AFTER INUNDATION – (JENNINGS AND KNIGHT, 1957) 8
FIGURE 2.2: SCHEMATIC DIAGRAM ILLUSTRATES THE RELATION BETWEEN DEGREE OF SATURATION AND SOIL SUCTION THAT CAN BE ACCOUNTED FOR – AFTER SMITH (2003) 12
FIGURE 2.3: DIFFERENT POSSIBILITIES OF WEAKLY BONDED SOIL FABRICS IN COLLAPSIBLE SOILS - BARDEN ET AL. (1973), CITED BY CLEMENCE AND FINBARR (1981) AND MASWOSWE (1985) 13
FIGURE 2.4: COLLAPSE SETTLEMENT (JENNINGS AND KNIGHT, 1975) 14
FIGURE 2.5: (A) SCHEMATIC DIAGRAM FOR UNSATURATED SOIL FABRIC-CAPILLARY BONDING (B) SOIL–WATER CHARACTERISTIC CURVES COMPUTED FROM GRAIN-SIZE DISTRIBUTION CURVES FOR VARIETY OF SOIL TYPES (M.D. FREDLUND, 2000) – CITED BY FREDLUND ET AL. (2012). 15
FIGURE 2.6: TYPICAL EXAMPLE OF A DOUBLE OEDOMETER TEST CONDUCTED ON SILTY A SAND SOIL TO MEASURE COLLAPSE – AFTER JENNINGS AND KNIGHT (1956) 17
FIGURE 2.7: THE SETUP OF THE LARGE-SCALE OEDOMETER - NG ET AL. (2006) 20
FIGURE 2.8: COMPARISON BETWEEN TRIAXIAL AND OEDOMETER COMPRESSION CURVES ON LCT SPECIMENS – MASWOSWE ET AL. (1992) 21
FIGURE 2.9: COMPARISON BETWEEN MODEL SIMULATIONS BY MIHALACHE AND BUSCARNERA (2015) AND DATA FROM MASWOSWE (1985) 22
FIGURE 2.10: DIAGRAM SHOWING IN-SITU COLLAPSE TEST DEVELOPED BY MAHMOUD (1991) - CITED BY HOUSTON ET AL. (1995) 23
FIGURE 2.11: COLLAPSE MEASUREMENT USING OEDOMETER 24
FIGURE 2.12: EFFECT OF DRY BULK UNIT WEIGHT, WATER CONTENT ON THE COLLAPSIBILITY OF THE SOIL FABRIC, AFTER HOLTZ AND HILF (1961) 26
FIGURE 2.13: RELATIONSHIP BETWEEN DRY UNIT WEIGHT AND LIQUID LIMIT AND COLLAPSE - HOLTZ AND HILF (1961) – CITED BY HAMID (2012) 27
FIGURE 2.14: OEDOMETER CURVES FOR SILTY SAND TESTED AT VARIOUS INITIAL DEGREES OF SATURATION – AFTER JENNINGS AND BURLAND (1962) 28
FIGURE 2.15: LABORATORY STUDY OF COLLAPSE BEHAVIOUR OF REMOULDED LOESS UNDER CONTROLLED WETTING AND FLOODING (AFTER SINGHAL ET AL., 2016) 29
FIGURE 2.16: EFFECT OF PLASTICITY OF FINE PARTICLES AND SIZES OF COURSE CONTENT ON COLLAPSE POTENTIAL (ROLLINS ET AL., 1994) 31
FIGURE 2.17: SUDAN MAP (LOCATION AND ITS CLIMATE) 32
FIGURE 2.18: SUDAN GEOLOGICAL MAP – AFTER WHITEMAN (1971) - CITED BY ELSHARIEF ET AL. (1999). 33
FIGURE 2.19: PERPENDICULAR AND PARALLEL GROUND COLLAPSES AROUND WATER CHANNELS - NILE RIVER STATE 34
FIGURE 2.20: A MASSIVE GROUND CRACK IN A LOESS SOIL IN SOUTHWEST SUDAN, BABANOUSA CITY JUNE 2018, (ALRAKOBA NEWS, 2018) 35

FIGURE 2.21: COLLAPSE DUE TO A WATER LEAK IN THE CITY OF ABU HAMAD - NORTH SUDAN (PHOTOGRAPHS COUNTESY OF DR KHALID ABDELFATTAH)..... 36
FIGURE 2.22: LOCATIONS OF THE SUDANESE CITIES WHERE COLLAPSIBLE SOILS WERE ENCOUNTERED..... 37
FIGURE 2.23: LOCATIONS OF THREE WELLS USED TO DESCRIBE THE OMDURMAN FORMATION (GOOGLE EARTH) – AFTER ALZUBAIR (2020)..... 39
FIGURE 2.24: OMDURMAN CITY SURROUNDED BY MOUNTAINS AND THE RIVER – GOOGLE EARTH..... 41
FIGURE 2.25: STRUCTURAL DAMAGE IN THE STUDY AREA (OSMAN, 2004) 41
FIGURE 2.26: STRUCTURAL DAMAGE IN THE STUDY AREA (HAMID, 2012) 42
FIGURE 2.27: LOCATION OF THE TEST PITS 1 AND 2 (AFTER OSMAN AND AHMED, 2015) 43
FIGURE 2.28: PARTICLE SIZE DISTRIBUTION CURVES FROM TRIAL PITS 1 AND 2 AFTER (HAMID, 2012) 44
FIGURE 2.29: PARTICLES CONTENT AND PLASTICITY INDICES, NATURAL WATER CONTENT FOR TPS 1 AND 2 46
FIGURE 2.30: PLATE-LOAD TEST SET-UP (OSMAN, 2004)..... 47
FIGURE 2.31: AVERAGE SETTLEMENT VERSUS TIME - PLATE LOAD TEST (AFTER OSMAN, 2004) 48
FIGURE 2.32: THREE-STATIC CONE PENETRATION TESTS AROUND THE AREA OF THE PLATE TEST AFTER OSMAN (2004) AND LUNNE ET AL. (1997) 49
FIGURE 3.1: DIFFERENT PATTERNS OF MOVEMENT AND CRACKING CAUSED BY SUBSIDENCE AND HEAVE – AFTER FREEMAN ET AL. (2002)..... 53
FIGURE 3.2: CRACK PATTERNS IN THE THE BULDINGS AT THE ALTHAWRA (19) STUDY AREA 54
FIGURE 3.3: EFFECT OF GRAVEL CONTENT ON HYDRAULIC CONDUCTIVITY OF A SILTY CLAY SOIL..... 55
FIGURE 3.4: FÜLLER GRADING CURVES FOR THE NATURAL GRAVEL..... 55
FIGURE 3.5: THE URBANISATION EXPANSION INTERRUPTS NATURAL WATER DRAINS – ALTHAWRA (42)..... 56
FIGURE 3.6: EXAMPLE FOR IMPROPER WATER USAGE LEADING TO A TWO-STOREY BUILDING COLLAPSE 57
FIGURE 3.7: SCHEMATIC DIAGRAM FOR THE FOUNDATION TYPES IN THE STUDY AREA..... 58
FIGURE 3.8: STRIP FOUNDATION TYPE IN THE STUDY AREA 59
FIGURE 3.9: USING STONES AND SANDS IN THE CONSTRUCTION OF STRIP FOUNDATIONS – AN OLD STRIP FOUNDATION IN THE STUDY AREA..... 59
FIGURE 3.10: ISOLATED PAD FOOTINGS SYSTEM IN THE STUDY AREA..... 60
FIGURE 3.11: SOIL PROFILES IN TWO DIFFERENT PARTS: (A) NORTH THE STEADY AREA (B) SOUTH THE STUDY AREA..... 61
FIGURE 3.12: A TYPICAL COLLAPSIBLE SOIL PROFILE IN THE STUDY AREA 63
FIGURE 3.13: A TYPICAL SOIL COLLAPSE OBSERVED IN THE FIELD IN THE STUDY AREA 63
FIGURE 3.14: SCHEMATIC DIAGRAM TO EXPLAIN COLLAPSE IN THE GRAVELLY SOIL..... 64
FIGURE 3.15: LOCATION OF THE SAMPLES COLLECTED (TP0) 65
FIGURE 3.16: DISTURBED SAMPLES INCLUDING SOME CEMENTED SOIL AGGREGATION 65
FIGURE 3.17: COLLECTING OF AN UNDISTURBED SOIL BLOCK 66
FIGURE 3.18: SOIL AGGREGATION AFTER SOLIDIFICATION 67
FIGURE 3.19: PARTICLE SIZE DISTRIBUTION FOR THE COLLECTED SAMPLES..... 68
FIGURE 3.20: PARTICLE SIZE DISTRIBUTION CURVES FOR THREE DIFFERENT LOCATIONS IN THE STUDY AREA 68
FIGURE 3.21: DESCRIPTION OF THE GRAVEL SHAPE..... 69
FIGURE 3.22: CLAY FRACTION X-RAY DIFFRACTOMETER SCANNING USING NI-FILTERED CUKA RADIATION..... 70

FIGURE 3.23: GRAVEL POWDER X-RAY DIFFRACTOMETER SCANNING USING NI-FILTERED CUKA RADIATION 71
FIGURE 3.24: PLATE LOAD TEST RESULTS, AFTER OSMAN (2004) 74
FIGURE 3.25: NATURAL DRY DENSITY AND MOISTURE STATE, AFTER HOLTZ AND HILF (1961) 75
FIGURE 3.26: SOIL CONTENT AND DRY UNIT WEIGHTS FROM T.P. (1) - AFTER HAMID (2012) 77
FIGURE 3.27: VARIATION OF DRY DENSITY AND VOID RATIO AND WATER CONTENT WITH DEPTH - AFTER HAMID (2012) 79
FIGURE 3.28: MAXIMUM EXPECTED (A) COLLAPSE POTENTIAL AND (B) SETTLEMENT DUE TO COMPACTION 80
FIGURE 4.1: VARIABILITY OF THE GRAVELLY COLLAPSIBLE FABRIC 83
FIGURE 4.2: COMPARISON OF PARTICLE SIZE DISTRIBUTIONS FOR NATURAL GRAVEL AND LYTAG 84
FIGURE 4.3: (A) CLEAN NATURAL GRAVEL AND (B) AN ANALOGUE SAMPLE PREPARED FROM IT 86
FIGURE 4.4: (A) CLEAN LYTAG AND (B) ANALOGUE LYTAG SPECIMEN 86
FIGURE 4.5: SCANNING ELECTRON MICROSCOPE (SEM) ON LYTAG PARTICLE (A) SCANNED SURFACE IMAGE (B) GRAVEL PARTICLE 88
FIGURE 4.6: SCANNING ELECTRON MICROSCOPE (SEM) ON NATURAL GRAVEL (A) SCANNED SURFACE IMAGE (B) GRAVEL PARTICLE 88
FIGURE 4.7: LYTAG PARTICLE DENSITY DETERMINATION USING: (A) 50-ML PYCNOMETERS (B) 250-ML GAS JARS 88
FIGURE 4.8: CHANGE IN LYTAG PARTICLE DENSITY FOR DIFFERENT LYTAG SIZES 89
FIGURE 4.9: THE PERFORATED NET USED IN LYTAG WATER ABSORPTION TEST 91
FIGURE 4.10: LYTAG WATER ABSORPTION AGAINST APPLIED WATER PRESSURE 92
FIGURE 4.11: STEREO-MICROSCOPIC SCAN ON CROSS-SECTIONS OF COARSE LYTAG PARTICLES 92
FIGURE 4.12: STEREO-MICROSCOPIC SCAN ON CROSS-SECTIONS OF FINE LYTAG PARTICLES 93
FIGURE 4.13: ASSESSING THE MINIMUM DENSITY OF LYTAG USING NON-STANDARD PROCEDURES 94
FIGURE 4.14: LYTAG MINIMUM DENSITY USING STANDARD PROCEDURES (BS 1377 AND ASTM D4254 - 16) 95
FIGURE 4.15: LYTAG MINIMUM DENSITY FROM BOTH STANDARD AND NON-STANDARD PROCEDURES 96
FIGURE 4.16: VARIATION OF (A) WATER CONTENT AND (B) BULK DENSITY WITH TIME - NATURAL DRYING AT ROOM TEMPERATURE (20°C) OF A SPECIMEN CONTAINS WHOLE PARTICLE RANGE OF THE NATURAL GRAVELLY SOIL 97
FIGURE 4.17: ANALOGUE SPECIMEN PREPARED WITH 20% KAOLINITE BY DRY MASS AT A WATER CONTENT OF 14.8% 100
FIGURE 4.18: ANALOGUE COLLAPSIBLE SPECIMENS FOR 1-D COLLAPSE TEST 102
FIGURE 4.19: ANALOGUE COLLAPSIBLE SAMPLES FOR TRIAXIAL COLLAPSE TEST 103
FIGURE 4.20: EFFECT OF NUMBER OF TAMPING BLOW AND KAOLIN PERCENTAGE ON SAMPLE DENSITY 104
FIGURE 4.21: SPECIMEN COLLAPSE DUE TO THE EXTRUSION PROCESS: K=8.5% AND T=0 105
FIGURE 5.1: STRESS DISTRIBUTION UNDER STRIP CIRCULAR FOOTINGS (SOM AND DAS, 2006) 108
FIGURE 5.2: ANALOGUE SPECIMEN PROPERTIES DURING DRYING AT 60°C: (A) AND (B) WATER CONTENT W VERSUS TIME; (C) AND (D) DRY DENSITY P_{DRY} VERSUS TIME AND (E) AND (F) W VERSUS P_{DRY} FOR SPECIMENS *S*1 TO *S*4 (FINE LYTAG) *S*5 TO *S*8 (COARSE LYTAG) 111
FIGURE 5.3: 1-D COLLAPSE TEST SETUP 113
FIGURE 5.4: VARIATION OF (A) VOID RATIO AND (B) VERTICAL STRAIN WITH STRESS LEVEL AND GRAVEL SIZES 116
FIGURE 5.5: COLLAPSE POTENTIAL UNDER FULL LATERAL CONFINEMENT 116

FIGURE 5.6: SPECIMEN DENSITY (A) AND WATER CONTENT (B) BEFORE TESTING 117
FIGURE 5.7: THE EFFECT OF SPECIMEN DENSITY (A) AND WATER CONTENT (B) ON COLLAPSE POTENTIAL 118
FIGURE 5.8: VERTICAL STRAINS THAT DEVELOPED DURING LOADING AND INUNDATION FOR THE FULLY LATERAL CONFINED SPECIMENS 119
FIGURE 5.9: EFFECT OF LYTAG SIZE AND BINDER PERCENTAGE ON COLLAPSE POTENTIAL (OFOSU, 2019) 120
FIGURE 5.10: VERTICAL STRAINS THAT DEVELOPED DURING LOADING AND INUNDATION FOR THE PARTIALLY LATERALLY CONFINED SPECIMENS OF (A) FINE AND (B) COARSE LYTAG AND (C) COMBINED RESULTS 121
FIGURE 6.1: THE GDS SYSTEM USED FOR THE TRIAXIAL TESTING PROGRAMME 128
FIGURE 6.2: SPECIMEN SET-UP FOR TRIAXIAL TESTING 129
FIGURE 6.3: IMPROVING THE MEMBRANE RUPTURE RESISTANCE BY TRIPLING THE NUMBER OF MEMBRANES 131
FIGURE 6.4: (A) MEMBRANE PENETRATION IN A TRIAXIAL SPECIMEN (B) DETERMINATION OF MEMBRANE FLEXIBILITY FROM THE RESULTS OF ISOTROPIC COMPRESSION TESTS (AFTER LADE AND HERNANDEZ, 1977) & VOLUMETRIC STRAIN DUE TO MEMBRANE PENETRATION FOR TESTS (C) WITHOUT AND (D) WITH LATEX COATED MEMBRANES (AFTER TORRES, 1983) – CITED BY (EVANS AND SEED, 1987) 132
FIGURE 6.5: REDUCING MEMBRANE RUPTURE BY USING FIBRE CLOTH STRIPS 134
FIGURE 6.6: MEMBRANE RUPTURE AT THE MIDDLE OF THE SPECIMEN 135
FIGURE 6.7: MEMBRANE PENETRATION AND CHAMBER EXPANSION MEASUREMENTS 136
FIGURE 6.8: DESCRIPTION OF THE LOCAL LVDTS AND THEIR ASSEMBLY 139
FIGURE 6.9: IMPROVEMENT OF THE LVDTS STABILITY BY USING 30 MM DIAMETER ACETATE DISCS 140
FIGURE 6.10: SCHEMATIC DIAGRAM DESCRIBING (A) THE TRIAXIAL COLLAPSE TEST STAGES; (B) THE STRESS PATH FOLLOWED; AND (C) A SCHEMATIC STRESS-STRAIN PLOT. 142
FIGURE 6.11: TYPICAL EXAMPLES OF STRAIN EQUILIBRIUM BEFORE AND AFTER INUNDATION 144
FIGURE 6.12: SCHEMATIC DIAGRAM ILLUSTRATING THE GDS TRIAXIAL SYSTEM COLLAPSE TEST STAGES (LABELLED IN RED) 145
FIGURE 6.13: AN EXAMPLE ILLUSTRATING THE CAPTURING PROCESS OF THE SPECIMEN VOLUME DEFORMATION (INCLUDING THE BEDDING STRAINS), DEVIATOR STRESS AND AXIAL STRAIN FOR ONE OF THE SHEARING TESTS 148
FIGURE 6.14: SCHEMATIC DIAGRAM EXPLAINING DIFFERENT SPECIMENS' DEFORMATION SCENARIOS 149
FIGURE 6.15: SCHEMATIC DIAGRAM ILLUSTRATING THE ADOPTED SPECIMEN DEFORMATION FOR CALCULATING RADIAL STRAIN 150
FIGURE 7.1: THE DRY SHEARING RESPONSE OF ANALOGUE TRIAXIAL COLLAPSIBLE SPECIMENS 157
FIGURE 7.2: STRESS-STRAIN RESPONSE OF (A) LYTAG (GRAVEL SCALE) (B) OTTAWA SAND, AFTER CARRARO ET AL. (2009), AND THEIR CORRESPONDING VOLUMETRIC STRAIN (C) AND (D) RESPECTIVELY 160
FIGURE 7.3: TANGENT AND SECANT STIFFNESSES AND THEIR NORMALIZED VALUES FROM THE DRY SHEARING TESTS 162
FIGURE 7.4: COMPARISON BETWEEN DRY AND WET SHEARING FAILURE ENVELOPES 163
FIGURE 7.5: STRESS PATHS FOR THE TESTED SPECIMENS 166
FIGURE 7.6: EFFECT OF CELL PRESSURE ON COLLAPSE DEFORMATION AT $qc = 0.5qmax$: (A) $q - EA$ (B) $\varepsilon v - EA$ (C) BOUNDING RELATIONSHIPS FOR TYPICAL CLAYEY SILT SOIL (FREDLUND, 2006) - CITED BY FREDLUND ET AL. (2014) 167

FIGURE 7.7: STRESS-STRAIN RESPONSE DUE TO COLLAPSE STRESSES OF $0.10, 0.25, 0.5\ and\ 0.75q$MAX AND AT $CP = 25, 50, 100, 150, and\ 200$KPA (FINAL TWO PLOTS SET COMPARES THE TWO EXTREME CP LEVELS OF 25KPA AND 200KPA) 170
FIGURE 7.8: STRESS-STRAIN RESPONSE FOR ALL TESTED SPECIMENS FOR AXIAL STRAIN RANGE BETWEEN 0% TO 5% (ZOOMED-IN IMAGE FROM FIGURE 7.7) 171
FIGURE 7.9: EFFECT OF CELL PRESSURE ON THE STRESS-STRAIN RESPONSE (ZOOMED IN IMAGES COVERING $\varepsilon a <$ 5%) 172
FIGURE 7.10: LOCATIONS OF THE AXIAL STRAIN MEASURING UNITS AND THEIR CAPTURED AXIAL STRAIN DATA 175
FIGURE 7.11: SECONDARY BEDDING STRAIN AREA IN $q - \varepsilon A$ PLOT 177
FIGURE 7.12: COMPARISON OF RADIAL STRAIN CALCULATED FROM THE LINEAR EXPRESSION OF THE MEASURED AXIAL STRAIN 178
FIGURE 7.13: RADIAL STRAIN ASSESSMENT USING THE LONG (SHOWN IN GREY) AND SHORT (SHOWN IN RED) RADIAL STRAIN EQUATIONS 179
FIGURE 7.14: EFFECT OF COLLAPSE STRESS (qc) ON AXIAL STRAIN (εA), VOLUME STRAIN (εV), AND RADIAL STRAIN (εR) 180
FIGURE 7.15: CHANGE IN AXIAL STRAIN AND DENSITY DUE TO APPLICATION OF QC AND INUNDATION 182
FIGURE 7.16: MATHEMATICAL EXPONENTIAL EXPRESSIONS FOR DESCRIBING THE AF FACTOR 182
FIGURE 7.17: MATHEMATICAL LINEAR EXPRESSIONS FOR DESCRIBING THE DF FACTOR 183
FIGURE 7.18: COLLAPSE MECHANISMS IN THE TESTED SPECIMENS 185
FIGURE 7.19: CHANGE IN AXIAL STRESS DUE TO COLLAPSE VERSUS COLLAPSE STRESS 187
FIGURE 7.20: DENSITY CHANGES AGAINST COLLAPSE STRESS 187
FIGURE 7.21: RELATION BETWEEN DENSITY-AXIAL STRAIN RATIO TO COLLAPSE STRESS EXPERIMENTAL DATA AND MATHEMATICAL FITS USING (A) POWER TREND, (B) POLYNOMIAL, (C) LOGARITHMIC, AND (D) LINEAR FUNCTIONS 188
FIGURE 7.22: EXAMPLES FOR THE ACTUAL GRAVELLY SOIL FABRIC IN THE STUDY AREA 189
FIGURE 7.23: EFFECT OF CELL PRESSURE (CP) ON THE CHANGE OF DENSITY TO THE AXIAL COLLAPSE STRAIN AGAINST INNUDATION COLLAPSE STRESS (qc)AND THE COLLAPSE MECHANISM 190

List of abbreviations and symbols

ASTM	American Society for Testing and Materials
AEV	Air-entry value
BS	British Standards
CPVG	Cell pressure volume gauge
CPT	Static cone penetration test
CS	Collapse settlement
DEF	Dry failure envelope
E	East direction
EDT	External displacement transducer
FC	Fine content
FC_{th}	Threshold fine content
LVDT	Linear variable differential transformers
MPV	Membrane volume penetration
PSD	Particle sizes distribution
SEM	Scanning electron microscope
SPT	Standard penetration test
TP	Trial pit
USCS	Unified Soil Classification System
WGS	World Geodetic System
XRD	X-ray diffraction
A_c	Corrected area
A	An empirical constant
A_0	Initial specimen cross-section area
Cc	PSD curvature coefficient
Cu	PSD uniformity coefficient
CP	Collapse potential, Cell pressure
c'	Specimen cohesion
D	Particle size
D_{10}	Particle size corresponding to 10% passing
D_{30}	Particle size corresponding to 30% passing

D_{50}	Particle size corresponding to 50% passing
D_{60}	Particle size corresponding to 60% passing
D_0	Initial specimen diameter
D_c	Corrected specimen diameter
D_{max}	Maximum particle size
D_{max}	Minimum particle size
d	Specimen diameter
E_s	Secant stiffness
F	Load cell reading
e	Void ratio
e_0	Initial voids ratio
e_1	Voids ratio at water inundation
e_2	Voids ratio after equilibrium due to water inundation
f_s	Sleeve friction
G_s	Specific gravity of soil particles
H_0	Initial specimen height or layer thickness
K_0	Coefficient of earth pressure at rest
k	kaolin percentage, Stress ratio ($0 < k < 1.0$)
LL	Liquid limit
N	North direction
N_{60}	Number of blows in the standard penetration test
NWC	Natural water content
OWC	Optimum water content
P_a	Applied pressure, footing stress
PI	Plasticity index
PL	Plastic limit
Q	Structural load
q	Deviator stress, $\frac{F}{A_c}$, $(\sigma_a - \sigma_r)$
q_c	Cone resistance
q_c	Inundation collapse stress
q_{max}	Maximum deviator stress
q_f	Failure deviator stress

r	radii of the menisci
S	Specimen
S_{c}	Slope of the collapse, $(\Delta\rho_{\mathrm{c}}/\Delta\varepsilon_{\mathrm{ac}})$
S_{r}	Degree of saturation
s'	Stress path parameter, ½ $(\sigma_1' + \sigma_3')$
T	Number of tamping blows
T_{s}	Surface tension, water tension
t	Temperature (C°), time
t'	Stress path parameter, ½ $(\sigma_1' - \sigma_3')$
t'_{max}	Maximum shear stress
u_{a}	Pore-air pressure
u_{w}	Pore-water pressure
V_0	Initial specimen volume
w	Gravimetric water content
γ_{dry}	Dry unit weight
γ_{dmax}	Maximum dry unit weight
γ_{idry}	In-situ dry unit weight
γ_{w}	Unit weight of water (9.81 kN/m^3)
Δe	Change in void ratio
ΔH	Change in specimen height or layer thickness
$\Delta\rho_{\mathrm{c}}$	Change in density due to collapse
ΔV	Change in specimen volume
$\Delta\varepsilon_{\mathrm{ac}}$	Change in axial strain due to collapse
$\Delta\varepsilon_{\mathrm{sb}}$	Secondary bedding strain
σ	Total stress
σ_{n}	Normal stress
σ_{r}	Radial stress
$\sigma_{\mathrm{v}}^{\mathrm{net}}$	net vertical stress = $\sigma_v - u_a$
σ_{v}	Vertical stress in 1-D test
$\sigma_{\mathrm{collapse}}$	Collapse stress in 1-D test
σ_{f}	Flooding stress
ρ_{dry}	Dry mass density

ρ_{dmax}	Maximum dry mass density
ρ_0	Initial specimen mass density
δ_{ij}	Kronecker delta
ε_a	Axial strain
ε_r	Radial strain
ε_v	Volume strain
ε_c	Collapse strain
ε_{ac}	Axial collapse strain
ε_{rc}	Radial collapse strain
ε_{vc}	Volume collapse strain
φ'	Angle of internal friction
τ_f	Failure shear stress
τ_n	Normal shear stress

Chapter 1 : Introduction

1.1 General background

This study focusses on a ground stability problem involving a collapsible gravelly soil found in Omdurman city, Khartoum, Sudan. Urban expansion in this area has led to extensive building, mostly of domestic dwellings. These structures subsequently suffered severe damage from subsidence caused by this collapsible soil. Previous research studies by Osman (2004), Hamid (2012), and Osman and Ahmed (2015) have investigated this soil collapse problem. They identified the collapse characteristics of this soil but assessing the collapse behaviour remained an obstacle. Unlike other common collapsible soils, this soil contains more than 50% gravel bonded together with clay and silt fines and sand forming a high permeable soil layer. This layer, of varying thickness (depending on the location), is usually encountered at shallow depths and is underlain by the very dense and thick Nubian Sandstone formation. It is strong and stable when it is dry but when it is inundated, it has potential to deform and settle, especially when existing stresses are increased by new structural loads.

Many structures built on this collapsible gravelly soil have been severely damaged from water-induced settlement/collapse. The structural damage varies in severity from cosmetic to serious structural instability issues as shown in Figure 1.1 (from the Author's site visits in December 2018 and December 2019). The wetting originates from water flow from different sources such as irrigation systems for planting/gardening, wastewater leaks and water runoff from rainfall because of improper surface drainage systems.

1.2 Research motivation

The affected areas were previously desert, but recently they have been progressively developed with urban expansion. Because of the massive population growth in this area, the Sudanese authorities plan to construct a new vital infrastructure project 'New Khartoum Airport' in the south of Omdurman. It is therefore essential that the issues from the collapsible gravelly soil are understood and can be dealt with. This new project will increase the scope for investigating this ground stability problem and the findings from this current study will form the basis of future ground investigation programmes and the solutions implemented to deal with this problematic collapsible gravelly soil.

Soil collapse phenomena commonly occur in silty/sandy soils but have not been recognized for gravelly soils. Detailed measurements of collapse and the mechanisms occurring have not been established yet. Therefore, this research has developed a detailed experimental framework to assess collapse in gravelly soils which is expected to be the start for developing a solution for this frequent problem of ground collapse that has caused severe building damage in the Omdurman area.

1.3 Research background

Records indicate that Osman (2004) conducted the first research in the study area, to investigate the reasons for the structural damage that had started to develop in relatively recently constructed buildings. He analysed and assessed stresses imposed by a typical two-storey load-bearing cracked residential building and performed an in-situ plate load and three cone penetration tests. The conclusion from his research was that the cracks in this building were due to soil collapse within a gravelly layer found beneath the building's foundations. Hamid (2012) undertook further research to investigate the physical and collapse characteristics of this gravelly soil. This research confirmed Osman's (2004) proposition that soil collapse within this gravelly layer was associated with the structural damage in the study area. Hamid (2012) provided comprehensive data related to the properties of this soil, including particle size distributions, soil water contents, Atterberg limits, and values of in-situ density. Osman and Ahmed (2015) published an article on this continuing problem and confirmed the collapsibility of this gravelly soil.

In 2018 and 2019, the Author visited the study area to evaluate the continuation of this collapse problem by assessing progressive structural damage, to report soil collapse-related observations and to collect soil samples. He also talked to a group of local people whose houses had been affected. His conclusions from these field visits are as follows: (i) the number of cracked houses is increasing, especially the recently built houses; (ii) the development of cracks is seasonal and mainly due to rain; (iii) the affected houses are often in lines, suggesting that the topography of the ground might have contributed to this soil collapse problem; (iv) the profile of this gravelly layer is very similar to the soil profile described by Hamid (2012); (v) the predominant building type affected is single-storey and constructed on strip or pad foundations; (vi) the very serious cracking problem greatly irritated the local people who had suffered much discomfort and anxiety and wasted their money on the continuous repair and renovation of their homes.

The Author also observed that this soil fabric was very stiff when in a dry state but when exposed to water disintegrated with its fines washed out and the gravels left clean. The gravel content creates a free draining soil fabric which means the soil is very susceptible to any water influx with it easily flowing between particles, and even if only a small amount of water entered, this could lead to an immediate collapse.

In these previous studies and the Author's observations, taking undistributed samples to assess experimentally the collapse behaviour of this type of soil is fraught with difficulties. The primary reason is the high percentage of gravel and its fines content not being sufficient to create a stable soil structure. Consequently, soil collapse in this soil has not been previously assessed in a controlled element test set-up. Therefore, the necessity of developing a new methodology for assessing soil collapse in such soils has led to this current research. Another key objective is to provide vital support for those who live in this region.

1.4 Research aims, methodology and findings

The aim of this research was to experimentally assess the collapse behaviour of this problematic gravelly soil. The natural fabric of this soil is complex and there are various soil-related factors affecting its collapsibility such as: gravel shape, texture, and grading; silt and sand content and their grading; the micro and macro pores of this fabric; and the nature of bonding between these particles. In view of this, analogue specimens were tested instead of the natural soil. These collapsible analogue specimens were prepared using a lightweight aggregate (commercial name: Lytag), which has regular rounded particles whose shape and size range are similar to the natural gravel, and these were bonded by means of a kaolin slurry. This simplified the collapsible soil fabric, facilitating the interpretation of the collapse mechanisms by reducing the number of factors affecting collapse.

The experimental approach ended up with three main components. Initially tests were performed in the conventional way for assessing collapsible soils, one dimensionally in oedometer apparatus. However, the magnitude of collapse potential determined did not correlate with the structural damage (see figure 1.1). Further tests were performed using larger specimens, initially loaded over their full area and later the same loading platen was used for testing a set of specimens of greater diameter, thus creating boundary conditions similar to a footing test. Under these conditions lateral displacements could take place but could not be controlled. The magnitude of collapse potential increased considerably and was more in line

with those in the field. This finding led to the third approach: testing the analogue specimens in the triaxial apparatus where radial and axial stresses could be applied independently.

Prior to starting the experimental programme, a theoretical procedure for estimating the soil collapse potential for the natural soil was developed, based on the previous field and experimental data generated by Hamid (2012). In essence the in-situ density was compared with the maximum compacted dry density, the difference representing the potential change in volume. Following the partially confined 'footing' tests, a programme of triaxial tests were performed. The failure envelope of the dry analogue specimens was established first to establish feasible stress states at which to inundate the specimens to cause collapse. A range of stress levels were investigated, roughly corresponding to those encountered in situ. Exploring how collapse potential changed at varying levels of mean and deviatoric stress allowed to collapse mechanisms to be identified. At high deviator stress levels and low confining stresses there was radial dilation while conversely at low deviator stresses and high confining stresses there was radial contraction. These mechanisms had a profound effect on collapse potential with the former leading to much greater collapse. Additionally, it was possible to correlate changes in specimen density due to collapse with collapse stress and the subsequent collapse strain.

1.5 Thesis structure

The current Chapter 1 provides an introduction, including a general description, research motivation and background, research aims and methodology and findings, and thesis structure.

Chapter 2 contains an up-to-date literature review that relates to collapsible soils, including: an introduction; their formation, distribution, and general features; particle bonding in collapsible soils; definitions and terminology; collapse measurements and classification; and a review of the characteristics of the collapsible gravelly soil found at the study area and the conducted collapse tests from previous studies.

Chapter 3 describes the field observations, sampling processes, soil characterisation and classification, collapsibility of soils at the study area based on data from previous research.

Chapter 4 explains the reasons for modelling the in-situ soil with analogue specimens and how the analogue collapsible soil fabric was formed using Lytag as gravel with kaolin as a binder material. Forming the specimens was refined in several ways, for example by changing the

drying procedure. The chapter starts by characterising these artificial materials and then details the procedure for preparing the analogue collapsible gravelly specimens.

Chapter 5 covers how the 1-D and partially confined footing collapse tests were performed including descriptions of the analogue collapsible specimens used, test set-ups and procedures, and the analysis and discussion of the results.

Chapter 6 contains the core of this research which includes details about performing the 3-D triaxial collapse testing programme, the characteristics of the analogue collapsible specimens used for triaxial testing, and the test set-up and test procedures. The challenges encountered due to the nature of the tested specimens and how they were solved are explained. Corrections relating to the volume deformation of the tested specimens and their deformed cross-sectional area and radial strain calculations are discussed.

Chapter 7 discusses the analysis of triaxial test results. A key component of this chapter is that two collapse mechanics are identified, and specimen density correlated with collapse stress and collapse strain. A proposal of how this correlation can be implemented for in-situ soils to assess their collapsibility is presented.

Finally, Chapter 8 summarises the main conclusions derived from this study and gives recommendations for future work.



Figure 1.1: Some of the affected buildings in the study area – site visits in December 2018 and December 2019

Chapter 2 : Literature review

This literature review chapter is divided into two parts to approach the different topics that were covered in this thesis. First, collapse in soils is presented, including collapsible soil types, collapse characterisation, collapse measurements, and review of collapse tests from previous studies. Second, an up-to-date review concerning collapsible soils that have been discovered in Sudan is delivered, including gravelly collapsible soil in the study area and the consequential structural damage that has been observed.

2.1 Collapse in different soil types

2.1.1 Introduction to collapse in soils

Collapse potential in a soil relates to a state found in some soils rather than a specific soil type. Any soil that exhibits collapse due to an increase in its water content, whether it is at its current overburden stress or at higher stress levels, is considered as a collapsible soil. This means that a collapse potential can be present in different soil types such as clay, silt and sand or in a mixture of them. Collapsible soils are generally unsaturated, metastable, with an open fabric and can be natural or man-made soil (Rogers, 1995).

The particle structure in collapsible soils is often weakly bonded and potentially unstable under conditions relating to water content increases, following which it can undergo large volume reduction through restructuring its particles' fabric as depicted in Figure 2.1. This large volume reduction can cause significant damage to various engineering structures such as buildings, roads and earth dams.

Figure 2.1 depicts an idealization of the collapse concept. This hypothetical structural arrangement for sand grains in a loose silty sand was illustrated by Jennings and Knight (1957) to demonstrate that a portion of the fine fraction of the soil can exist as bonds for the larger grains and these bonds are subjected to local compression in the small inter-particle spaces between the adjacent larger grains resulting in the development of strength.

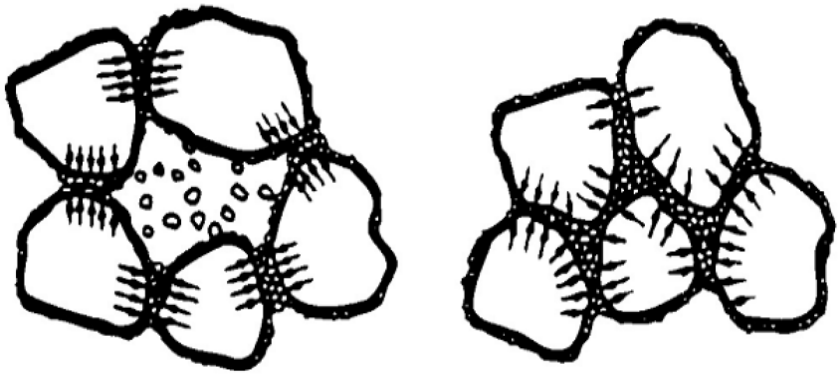


Figure 2.1: A loaded metastable soil structure before and after inundation – (Jennings and Knight, 1957)

The main factor generating collapse in a soil is the history of drying-wetting cycles after a deposition process or oxidisation forming weak soil particle bonds (Derbyshire, 1995). The different type of bonds in collapsible soils are discussed in Section 2.1.4.

2.1.1.1 Collapsible soil as unsaturated soil

If a soil is in an unsaturated state, the fine fracture bonds shown in Figure 2.1 can be replaced by meniscus water at particle contacts. Collapsible soils are always unsaturated because they contain all three phases of solid particles, water and air. However, the response of collapsible soil to loading and wetting is more complicated because of its honeycombed fabric. The mechanical behaviour of unsaturated soils is related to two stress state variables, net stress ($\sigma - u_a$) and matrix suction ($u_a - u_w$) as concluded by Burland (1961). He found that the pore pressure changes do not correlate with applied stresses and resulting volume changes. This confirmed the realisation that Bishop's equation of effective stress for unsaturated soils (Bishop and Blight, 1963), since is not applicable to unsaturated soil, it superimposes stresses which induce different mechanisms of volume change. Burland (1961) also explained that during wetting-induced collapse the shear resistance at particle contact points decreases due to decreases in the inter-particle normal stresses that exist due to the meniscus forces which also reduce with a water influx.

2.1.2 Formation and distribution of collapsible soils

The widespread deposits of collapsible soil are aeolian sands and silts (loess) (Derbyshire, 1995). Other unstable structure soils have been encountered in alluvial flood plains, in fans and mud flows, in colluvial deposits, residual soils, volcanic tuffs and man-made fill. (Section 2.1.2.2 provides examples of the relevant formations described in the literature).

2.1.2.1 Formation of collapsible soils

The engineering properties of any soil are partly related to its history such as the nature of the parent rock, its deposition, environmental and chemical reactions and its loading history. The properties of collapsible soils are highly affected by the environmental conditions during their deposition, e.g., the mechanical effects of intensive heat, wind, water (e.g., rainfall streams and rivers) and chemical reactions, e.g., those that can take place when electronically unstable mineral oxides of soils are formed, such as ferrous and calcium oxides, that seek equilibration by combining with oxygen: i.e., oxidisation. The following points describe different collapsible soils formation processes due to some of these environmental factors and the susceptibility of this formation to collapse under loading and wetting.

(1) Wind, in many cases, produces wind-blown dunes (known as aeolian deposits or loess) which are deposited by wind in a low-density fabric and thus constitute a collapsible soil under wetting and/or loading conditions. These deposits are common in desert areas, in a loose granular state with a metastable structure which can be sustained by small amounts of meniscus water that condenses from the atmosphere when the temperature drops or can be cemented by mineral oxidization processes.
(2) Water run-off from a high elevation catchment area usually initiates turbulent flows of a mixture of water and scoured soil particles. When this mixture is deposited, water and air bubbles are trapped inside the soil deposits. With heat and time, cemented cavities between soil particles form due to water evaporation leading to highly porous collapsible deposits, known as colluvial deposits.
(3) Rivers with high flow rates scour soils from their beds and banks to be deposited in shallow areas during their journey downstream, these are known as alluvial deposits. These deposits are common in arid and semi-arid climates, where they are usually unsaturated and susceptible to collapse, after which they form more stable soils when subjected to further loading and/or wetting.
(4) The disintegration and mechanical alteration due to heat and chemical reactions at the surface of some parent rocks leads to the leaching out of iron, or calcium carbonate with water. This process produces new residual particles which may vary in size from large fragments to gravel, sand, silt, colloids, and may also contain, organic matter. In some cases, these residual fabrics are susceptible to collapse under loading and wetting.
(5) Fills compacted at a water content below the optimum water content may also be susceptible to collapse under loading and wetting.

(6) Finally, wind-borne volcanic ash deposits are often loose and susceptible to collapse.

2.1.2.2 Types and distribution of collapsible soils

Derbyshire (1995) reports that soil collapse has become a major threat in the construction industry in large parts of eastern Canada, the United States, eastern Europe, China and southern Africa. The collapse sediments related to this threat involve young marine clays and lake sediments, wind-blown deposits (loess and some sand), volcanic ash, and some residual soils. Because of increasing human activities in land reclamation, areas covered by collapsible soils are being encountered and new consequential hazards are increasing.

A comprehensive review about collapsible soil types and their distribution is given by Maswoswe (1985) who categorised these deposits into five groups.

(1) First aeolian silts (loess) cover midwestern and western United States, and parts of Asia and southern Africa, while aeolian sands occur in extensive areas of South Africa, Zimbabwe, Botswana and Namibia (Knight 1960 – cited by Maswoswe (1985)).
(2) The second group is water-laid deposits which consist primarily of loose water deposited sediments which form alluvial fans. In the south-western United States, Rollins et al. (1994) describe six case histories associated with collapse in gravel soils in Nevada, Utah and Arizona. Also, in the San Joaquin Valley of California ground settlements related to ground water changes have been observed (Levy et al., 2020). The soil considered in this research is part of this group.
(3) The third group is residual soils which form due to the weathering of the parent rocks in situ through disintegration and mechanical alteration. Residual decomposed granite soils, as an example, in South Africa and Zambia, were found to have a total collapse leading to an increase of about 7% to 10% in density (Brink and Kantey, 1961).
(4) The fourth group is man-made fills. Clay soils can be difficult to compact and consequently they can collapse under load when soaked, especially if compacted dry of proctor optimum water content (Barden et al., 1973).
(5) Finally, other soil types that exhibit collapse upon soaking include those derived from volcanic tuff, gypsiferous soils, loose sands cemented by soluble salts and dispersive clays (Clemence and Finbarr, 1981).

2.1.3 General features of collapsible soils

Collapsible soils are characterized by very distinct geotechnical properties that include high void ratio, low initial bulk density and water content, high strength and stiffness when it is in

a dry or partially dry state. The severity of collapse, in absolute terms, depends on the amount of wetting, depth and thickness of the collapsible deposit and the weight of the overburden soil and any existing overlying structures.

Examples of some of these collapsing features relating to soils from the Albuquerque area in New Mexico involving loess, alluvial fans and alluvial deposits were reported by Lommler and Bandaini (2015). Five soil characteristics are assessed to describe the collapsibility of these soils as shown in Table 2.1. (1) In-situ dry unit weight, as a primary factor affecting soil collapse was used to divide these soils into four groups: highly collapsible when $\gamma_{\text{idry}} < 12.6\ \text{kN/m}^3$; likely collapsible when $12.6 < \gamma_{\text{idry}} < 14.2\ \text{kN/m}^3$; possibly collapsible when $14.2 \leq \gamma_{\text{idry}} \leq 16.2\ \text{kN/m}^3$; and not likely collapsible when $\gamma_{\text{idry}} > 16.2\ \text{kN/m}^3$. (2) If the number of blows of the standard penetration test (SPT) $N_{60} \leq 10$ it is likely to be collapsible. (3) If In-situ moisture content is less than 6% it is likely to be collapsible. (4) If the degree of saturation (S_r) is between 3 to 20% it likely to be collapsible. (5) If the plasticity index is less than 10% then collapse is possible.

Table 2.1: Characteristics and Collapse Potential of soils from Albuquerque, New Mexico, for loess, alluvial fan and alluvial deposits after Lommler and Bandini (2015)

Characteristic or Property	**Range of Property**	**Collapse Potential**
In-situ dry unit weight (γ_{idry})	< 12.6 kN/m^3	Highly collapsible
	12.6 to 14.2 kN/m^3	Likely collapsible
	14.2 to 16.2 kN/m^3	Possibly collapsible
	> 16.2 kN/m^3	Not likely collapsible
SPT blow count, N_{60}	$N_{60} \leq 10$	Likely collapsible
Natural water content (w)	1 to 6%	Likely collapsible
Degree of saturation (S_r)	3 to 20%	Likely collapsible
	35%	Collapse starts
	> 85%	Collapse completed
Plasticity index (PI)	< 10%	Possibly collapsible

2.1.4 Particle bonds in collapsible soils

The bond between particles within any collapsible open structure fabric can form either from simple capillary suctions, clay buttresses coating groups of sand/silt particles or chemical cementing. In some collapsible soils, one type of bond may dominate but in other collapsible soils there can be a complex interaction.

In general, capillary tension represents the primary reason for the apparent strength in collapsible soils before inundation. In Figure 2.2, a schematic diagram is presented to illustrate the effect of degree of saturation on soil suction. At very low degrees of saturation, soil suction reaches high values which produces a bond between soil particles and, vice versa, this bond decreases with water content increase. The suction range for different soil sizes is discussed in Section 2.1.5.3.

In collapsible soil, although the amount of soil fines is relatively small, it creates a suction bond between the major particles such as when clay fines bond sand particles together as illustrated in Figure 2.3. Quantifying the suction produced by these fines is fraught with difficulty but the effect of fines content on collapse potential can be assessed in collapsible soils. Also, the nature of the clay minerals has a significant contribution on the effect of fines in collapse potential as discussed in Section 2.1.8.4. In conclusion, fine particles in collapsible soils play a major role in the degree of weakness of these bond (Ho et al., 1988), which are strongly affected by water (Lommler and Bandini, 2015).

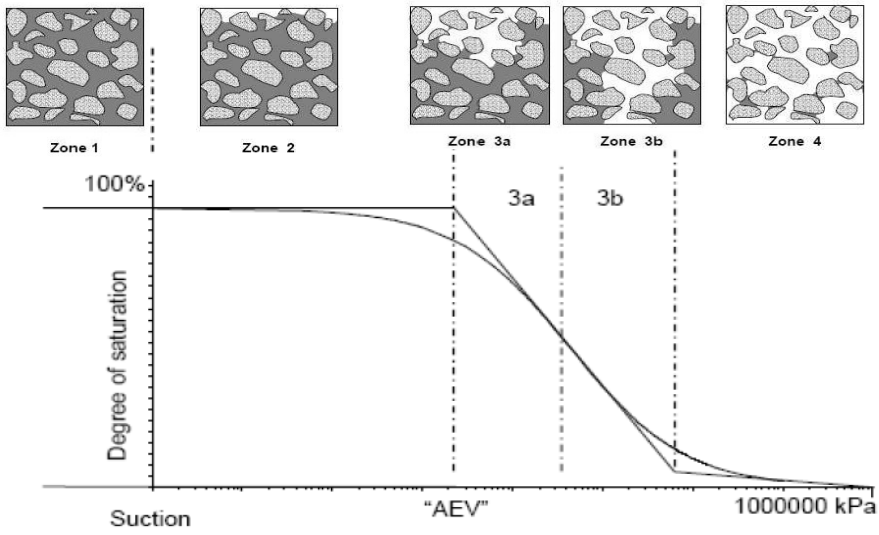


Figure 2.2: Schematic diagram illustrates the relation between degree of saturation and soil suction that can be accounted for – after Smith (2003)

During inundation, the various bonds of collapsible soils are softened regardless of their nature (Maswoswe, 1985). Sketches of six possible type of bonds (Clemence and Finbarr, 1981) are shown in Figure 2.3. These different types of weak bonds are usually formed depending on the nature of deposition of these soils and the amount and type of their fines, leading to the formation of meta-stable soil structures.

Maswoswe (1985) reported that the weak bond between the particles of aeolian collapsible sands occur in South Africa, Zimbabwe, Botswana and Namibia is considerably similar in the

composition and structure, according to Knight (1960), resulted from weathering of feldspar grains laid down by wind to form an initial loose open structure of quartz particles. Due to a change in climatic conditions from arid to more humid, in-situ chemical weathering occurred, affecting the more easily weathered minerals to produce mainly kaolinite (with traces of illite) and ferrous and ferric oxides. Knight (1960) confirmed this through optical observation, X-ray diffraction and differential thermal analysis.

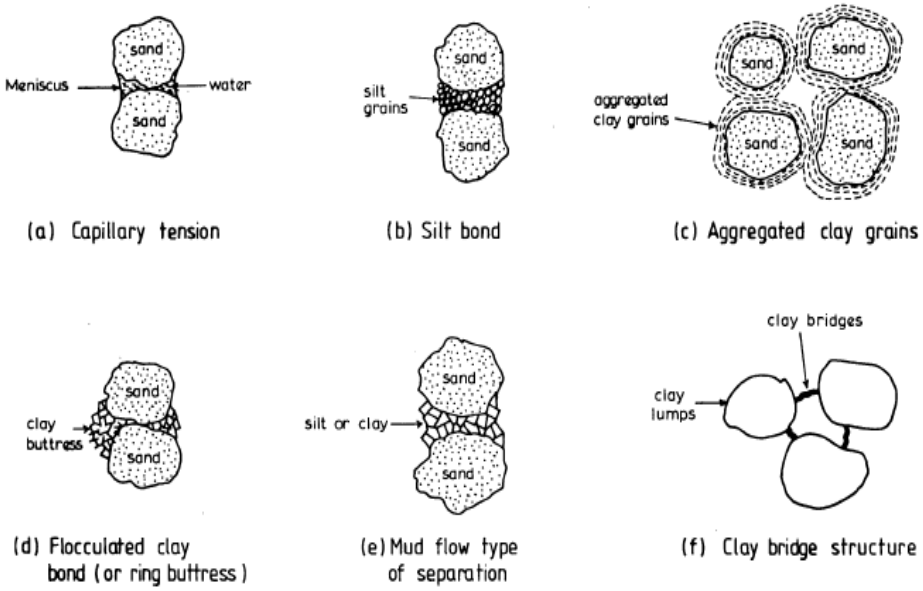


Figure 2.3: Different possibilities of weakly bonded soil fabrics in collapsible soils - Barden et al. (1973), cited by Clemence and Finbarr (1981) and Maswoswe (1985)

2.1.5 Definitions and terminologies

2.1.5.1 Collapsible soil

Collapsible soil has been defined in many ways but most of them are consistent that collapse occurs when soil is loaded and/or wetted. A commonly used definition was suggested by Rogers, (Rogers, 1995) which is as follows: ‘A collapsible soil is one in which the constituent parts have an open packing, and which forms a metastable state that can collapse to form a closer packed, more stable structure of significantly reduced volume. In most collapsible soils the structural units will be primary mineral particles, rather than clay minerals. The collapse process that occurs in these soils gives them a geotechnical significance’.

A more specific definition given by Ho et al. (1988) is: ‘collapse is the decrease in the total volume of soil caused due to an increase in water content under constant stress conditions. In the literature, collapse has been described using other terms such as hydro-consolidation, hydro-compaction, and hydro-collapse and near surface subsidence (Ho et al., 1988). The

process of adding water to induce collapse has also been described using various terms, such as wetting, saturation, flooding or inundation. In this study 'inundation' term is used to describe the process of adding water to induce collapse.

2.1.5.2 Collapse potential and collapse settlement

The percentage of the vertical strain due to wetting at a given applied stress is known as the collapse potential (*CP*) as defined by Equation 2.1. Collapse settlement is defined by Jennings and Knight (1975) as follows: 'Collapse settlement is the term applied to an additional settlement of a foundation due to wetting-up of a partly saturated subsoil, normally without any increase of applied pressure. This settlement could cause considerable structural damage. Figure 2.4 summarizes this definition using a schematic. Both the foundation and water leak source should be above the water table.

$$CP = \frac{\Delta H}{H_1} \tag{2.1}$$

Where ΔH and H_1, as illustrated in Figure 2.4, are the vertical settlement due to wetting and vertical soil thickness between the foundation and water table level before wetting respectively at constant applied pressure.

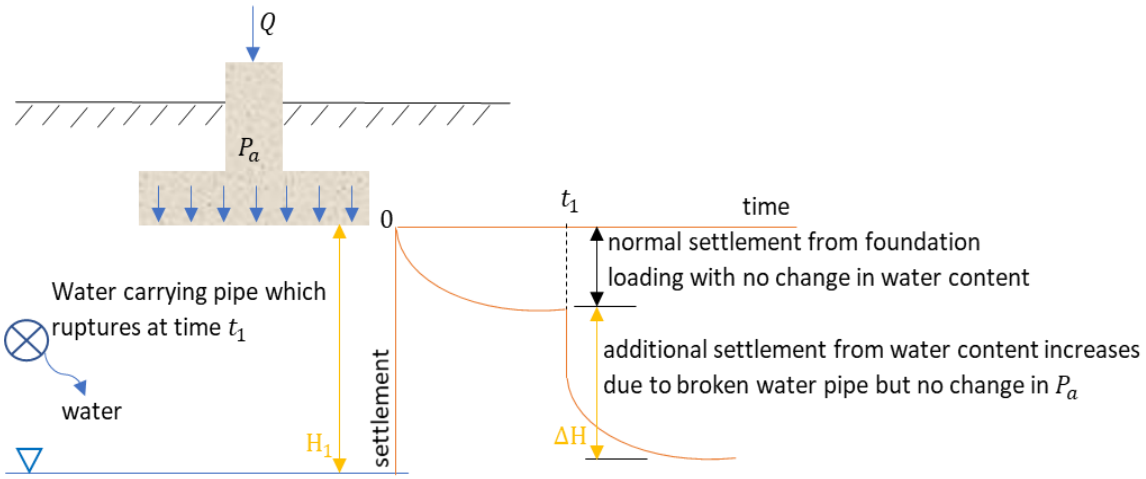


Figure 2.4: Collapse settlement (Jennings and Knight, 1975)

2.1.5.3 Collapse mechanisms

In a partly saturated soil collapse occurs when the inter-particle bonds, between aggregations of particles surrounded by a clayey or fine silt coat, break down due to an increase of water content and decrease in the matrix suction ($u_a - u_w$) as shown in Figure 2.5b (Fredlund et al., 2012).

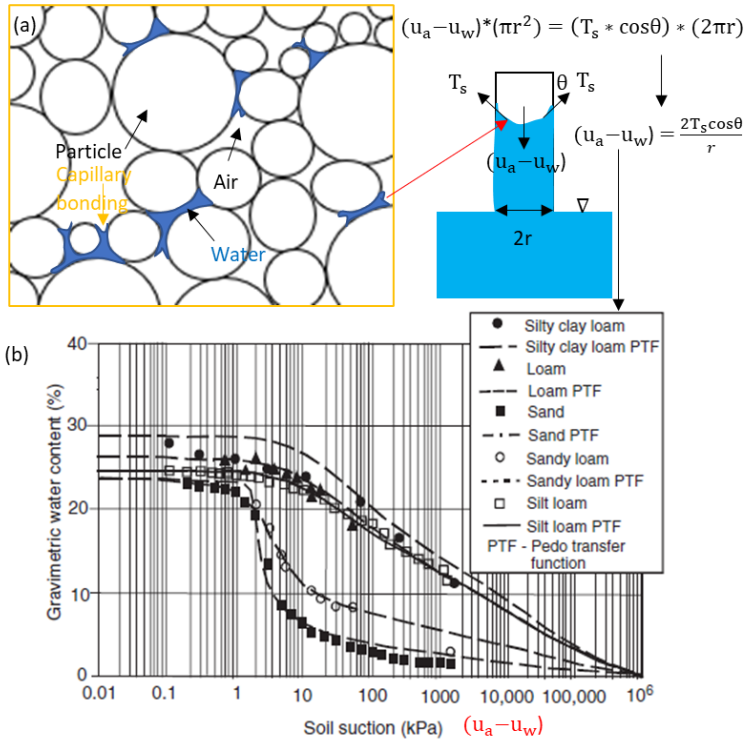


Figure 2.5: (a) Schematic diagram for unsaturated soil fabric-capillary bonding (b) Soil–water characteristic curves computed from grain-size distribution curves for variety of soil types (M.D. Fredlund, 2000) – cited by Fredlund et al. (2012).

The increase in moisture content reduces the effect of water tension, T_s, by increasing the radii of the menisci, r, at the inter-particle contacts (Ho et al., 1988) as given by the Young-Laplace equation, Equation 2.2 (Fredlund et al., 2012), and illustrated in Figure 2.5a. During inundation/wetting, the contact angle (θ) increases from around 0° at small r (maximum suction) towards 90° value at saturation. In this case ($\theta < 90^\circ$) the 'reference fluid is referred to as the wetting fluid for a given solid surface but if $\theta > 90^\circ$ the reference liquid is referred to as the nonwetting phase' (Mitchell and Soga, 2005). Soil particles deposited in a dispersive structure such that they are aligned in a parallel orientation do not change position drastically and settlement occurs rather than a clear collapse. On the contrary, if the soil particles are deposited in a flocculated manner, the soils have a face-to-edge structure, and are susceptibility to restructuring, and hence collapse can be triggered.

$$u_a - u_w = \frac{2T_s}{r} \tag{2.2}$$

In aeolian collapsible silt, the actual collapse mechanism is unclear and debatable. Some authors consider that clay hulls or film around the silty grains act as a lubricant on wetting, allowing the silty particles to slide over each other. While others argue that collapse is due to

leaching, by water, of weak calcium carbonate bonds which in a dry state keep the particles stable (Maswoswe, 1985).

2.1.6 Collapse measures and classification

Collapse potential can be measured in the laboratory or in the field as described in Section 2.1.6.2. In the laboratory the most common tests involve using the oedometer or triaxial apparatus. Laboratory tests have the advantage of good control of different factors that govern the collapse process such as degree of saturation, density and overburden stress.

2.1.6.1 Collapse tests in the laboratory

There are two common laboratory techniques for measuring collapse in a soil using oedometer device: single oedometer test and double oedometer test. These tests were proposed by Jennings and Knight (1956) as depicted in Figures 2.4 and 2.6 respectively.

Test 1: Single oedometer test

This is the most common technique also known as soaked-after-loading test as described by Ho et al. (1988), in which collapsible specimen at its natural moisture content is loaded incrementally in an oedometer to a given stress level and allowed to reach equilibrium. The specimen is then inundated with water, resulting in further volume reduction. The collapse potential is calculated from the volume change due to wetting which is directly to related ΔH as the test is 1-D (see Equation 2.1).

The above description was basically originated by Jennings and Knight (1956) to develop a similar behaviour of a foundation resting on a collapsible soil by applying the field pressure to an oedometer specimen at its natural water content followed by inundation. An analogy of the settlement developed due to the inundation is illustrated in Figure 2.4.

Test 2: Double-oedometer test

The double-oedometer test basically involves two separate tests which are usually conducted on two identical soil specimens. One specimen is loaded under saturated conditions after saturation at low stress levels, and the test run using conventional oedometer procedures, while the other specimen is loaded at its natural in-situ state. Then the compression curves for both specimens are plotted, the difference between these curves represents the swell or collapse potential at any given stress level. Therefore, the maximum collapse potential linked with any current overburden stress can be determined (see Figure 2.6).

The double-oedometer test in this manner allows collapse and swelling to be predicted over a wide range of stress levels from just two tests. The test has been shown to over-predict swelling and collapse potential, this over-prediction is due to particles being much freer to move when inundated at low stresses than that at higher ones. Therefore, the results tend to be conservative. However, this test can still be used to evaluate parameters of swelling and collapse, (Jennings and Knight, 1975).

Figure 2.6 shows a typical example for double oedometer test which was conducted on a silty sand soil to measure collapse (Jennings and Knight, 1956). The upper curve represents the oedometer test at the natural moisture content (w=15.8%) while the lower curve represents the oedometer on a specimen at full saturation (w=21%). The vertical distance between these two curves at any stress level represents collapse for all the applied stress range between 0 to 4.2 ton/sq. ft (450kPa). Collapse reached a maximum at 2 ton/sq. ft (215 kPa) at which the change in voids ratio, Δe, was 0.18. Beyond this point the two curves were semi-parallel.

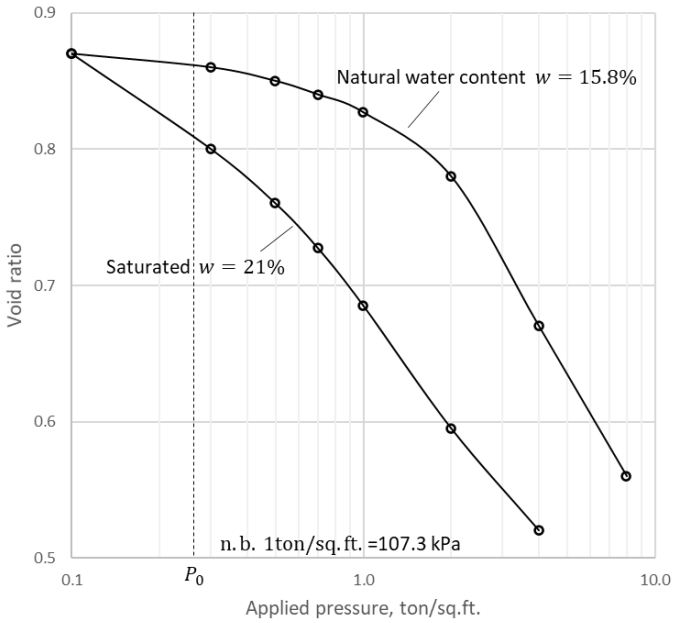


Figure 2.6: Typical example of a double oedometer test conducted on silty a sand soil to measure collapse – after Jennings and Knight (1956)

Oedometer characteristics

The oedometer is an important apparatus used in geotechnics to determine compressibility and swelling indices for clay, silt and some sandy soils. In the case of collapsible soils, reductions in volume change predominate so a suitable oedometer with appropriate size is used to determine soil collapse in one-dimensional stress-strain relations.

In the standard conventional oedometer (Casagrande-type, Casagrande (1936), cited by Ng et al., 2006), a range of stresses up to about 3 MPa can be applied (n. b. depends on diameter of containing ring), which is higher than stresses exerted by most engineering structures. However, the Casagrande-type oedometer can only be used to measure the consolidation characteristics of fine-grained soils and sands. Therefore, modifications to the oedometer's capacity are necessary to test gravel-size granular collapsible soils under higher stresses. Consequently, Ng et al. (2006) designed a large-scale oedometer of 425 mm internal diameter with flexible height for testing granular soils of maximum diameter up to 20 mm. This large-scale oedometer was designed, fabricated, and assembled at the University of Hong Kong, where many research projects involve high applied stress levels. To evaluate the applicability of this apparatus, poorly graded sand (SP) was tested, and its results were comparable to the Casagrande-type oedometer's results. One of the limitations of this new apparatus is still impracticable to be used for testing undisturbed specimens but it is very appropriate for studying collapse in gravelly soils because of its large dimensions.

Table 2.2: Minimum oedometer mould dimensions from different standards (after Ng et al., 2006)

Standard	**ASTM D2435**	**BS 1377 Part 5**	**ASTM D4186**	**BS 1377 Part 6**
Oedometer Type	Casagrande	Casagrande	Hydraulic	Hydraulic
Minimum diameter	50 mm	-	50 mm	-
Minimum Height	Greater of 12 mm and 10 × max. particle diameter of the specimen	Greater of 18 mm and 5 × mean dia. of the largest particle of the specimen	Greater of 20 mm and 10 × max. particle diameter of the specimen	6 × dia. of the largest particle of the specimen
Diameter-to-height ratio	2.5 minimum	2.5 minimum	2.5 minimum	2.5 to 4
Reference	ASTM (2003a)	BSI (1990a)	ASTM (2003b)	BSI (1990b)

The height and diameter of the oedometer affect both specimen disturbance and side friction. So minimum values for these dimensions are mentioned in different standards such as ASTM 2003a, 2003b and BSI 1990a, 1990b, (Table 2.2, Ng et al., 2006). By using a large-scale

oedometer apparatus, the frictional resistance between the soil specimen and vertical wall of the confining ring is minimised (Ng et al., 2006) and larger specimens represent more realistically the in-situ soil. The same apparatus was, also, used to reconstitute triaxial specimens.

To control the specimen height in this apparatus, the upper piston is designed to be adjustable and two oedometer cells of 220mm and 370mm height were devised. Also, to guarantee one-dimensional deformation, the confining ring has been designed to be rigid and with a smooth inner surface to minimize friction. To allow water to drain freely during consolidation of the soil specimen, two perforated composite rigid plates were fabricated and used at the top and base of the specimen. To deliver sustained and accurate vertical loads of up to 2 MN to the specimen (12.5 MPa), a hydraulic loading actuator was fixed to a loading frame through a hinge connection to ensure that the loads are applied vertically and centrally to the specimen as shown in Figure 2.7.

Test 3: Triaxial compression test for measuring collapse

Maswoswe et al. (1992) compared collapse test results from compacted clayey sand specimens of the Lower Cromer Till (LCT) which were tested in both an oedometer apparatus and a hydraulic triaxial stress path cell (the cell type reported by Bishop and Wesley (1975)), in which the specimens were soaked at constant total vertical stress and zero lateral strain (K_0 condition).

Figure 2.8 shows the stress-strain tests plotted as void ratio versus vertical stress in log scale for both the triaxial and oedometer tests. The triaxial specimens SK1, SK2, SK5 and SK9 were tested for different scenarios: SK1 and SK2 were soaked at different vertical stress levels and rates (SK1 was soaked in stages while SK2 was soaked at once); SK5 and SK9 were compressed similarly unsoaked up to an applied stress of about 1275 kPa but SK9 was compressed at 10 times the SK5 rate (100kPa/hr). Oedometer specimen 16A was soaked and compressed while 16B was soaked at 430 kPa and 16C and 16D were compressed without soaking.

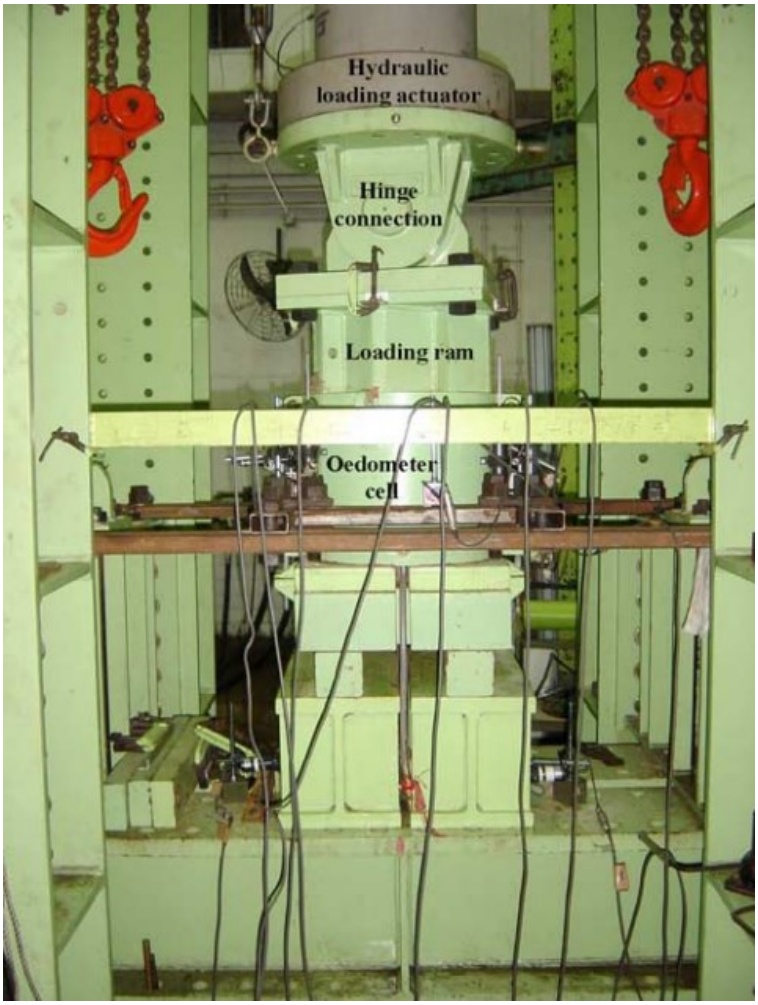


Figure 2.7: The setup of the large-scale oedometer - Ng et al. (2006)

These two test set-ups indicated similar specimen responses for unsoaked triaxial specimens (SK5) and (SK9) with the unsoaked oedometer specimen (16C). However, after collapse at a given soaking stress, the void ratio of triaxial specimens SK1 and SK2 were slightly higher than in the oedometer specimen (16A).

The authors concluded that the actual field collapse would be over-estimated. They argued that this over-estimation is probably due to one or a combination of the following reasons: (1) in the field, the lateral confinement of the soil is less than in the laboratory oedometer test (n.b. converse to this conclusion, in this present study it was found that, for the gravelly specimens tested, collapse increases with decrease of lateral confinement); (2) the inundation in the field is slower than in the oedometer; (3) soil fabric in the tested specimen is different to that of the soils compacted in the field.

Another comment to add here is the compression rate increase (10 times) in SK9 did not affect its compression curves.

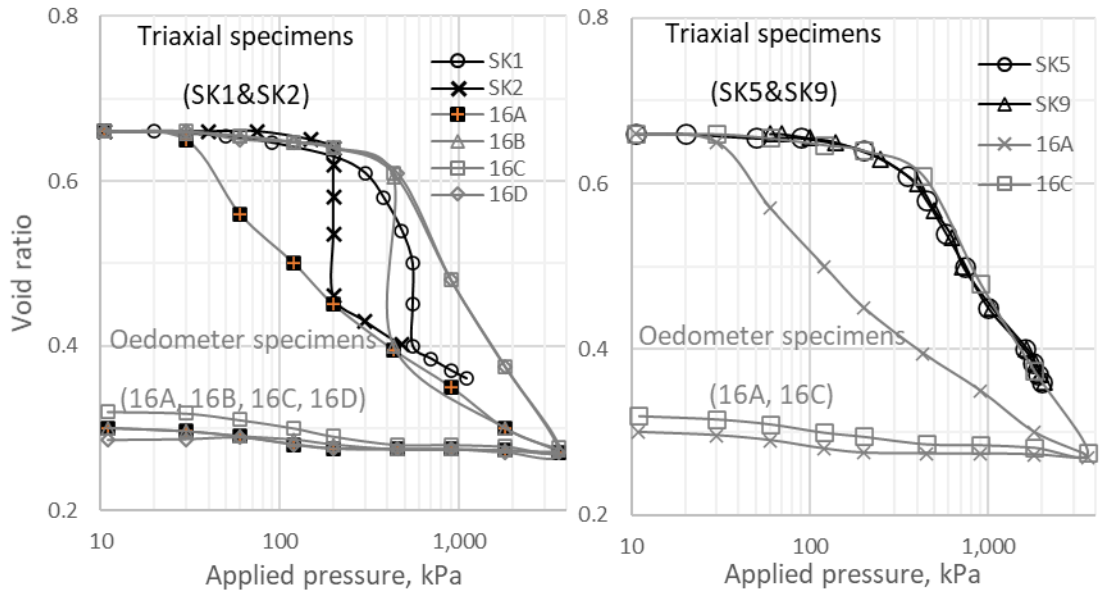


Figure 2.8: Comparison between triaxial and oedometer compression curves on LCT specimens – Maswoswe et al. (1992)

Later Mihalache and Buscarnera (2015) modelled and reinterpreted Maswoswe's results based on principles of material stability to understand whether collapse is a result of an unstable soil response. To achieve this, they assumed that the accumulation of strains during inundation is a plastic response which can be described through a basic constitutive law for unsaturated soils. The results from this model were acceptable as shown in Figure 2.9. These oedometer specimens were labelled as following: LCT_1 for 16A LCT_3 for 16B and LCT_2 for 16C. They suggested that for typical fine-grained soils, collapse is a stable form of compaction controlled by changes in their degree of saturation rather than being actual collapses. This suggestion contradicts the fundamental definition of collapse which starts by application of loading on a soil followed by inundation.

The basic constitutive law used in this model is the elastoplastic law for unsaturated soils proposed by Buscarnera and Nova (2009), as described in Equation 2.3, which relates the effective stress, σ'_{ij}, with total stress, σ_{ij}, and degree of saturation, S_r, and water pressure, u_w, and air pressure, u_a, and δ_{ij} is the Kronecker delta, and i and j represents the directions of the principle stresses.

$$\sigma'_{ij} = \sigma_{ij} - S_r\, u_w\, \delta_{ij} - (1 - S_r) u_a\, \delta_{ij} \qquad (2.3)$$

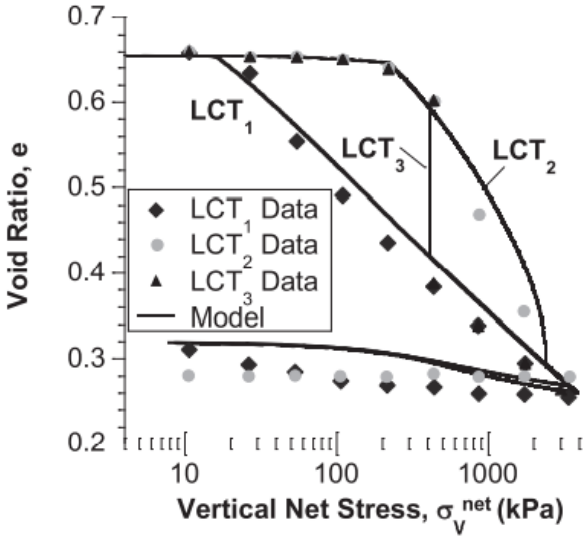


Figure 2.9: Comparison between model simulations by Mihalache and Buscarnera (2015) and data from Maswoswe (1985)

2.1.6.2 In-situ collapse tests

Collapse in fine-grained soils can be assessed from oedometer testing or basic soil properties as described in Sections 2.1.6.1 and 2.1.7 respectively. However, the collapse of coarse-grained soils cannot be assessed using these approaches. This is the case for gravels and sands with small percentages of fines which makes sampling not feasible. An alternative way is to use in-situ tests such as plate-load bearing tests and pre-bored pressuremeter tests. These give good measures of collapse when conducted first under dry natural conditions and then followed by flooding (Rollins et al., 1994). Rollins et al. (1994) also commented that, from an experience viewpoint, flooding of coarse-grained soils in a geologically susceptible environment can lead to collapse regardless of their high densities and very high SPT blow counts. This supports the importance of in-situ tests such as plate loading and pressuremeter to be conducted after the SPT when performing a soil investigation in unsaturated soils.

Houston et al. (1995) report that in-situ methods for testing collapsible soils, including shallow plate load test and down-hole plate load test, greatly reduce specimen disturbance and give a quantitative measure of collapse potential. They concluded that, developing stress-strain relationships from an in-situ test is quicker than developing curves from laboratory collapse test data. In-situ collapse tests are able to immediately detect collapsible soils in the field, which allows modifications to the field-testing plan to be made in early stages of the investigation. The in-situ down-hole collapse test described by Mahmoud (1991), cited by Houston et al. (1995) is simple and capable of controlling both loading, and inundation. The main components

and test set-up for this in-situ test are depicted in Figure 2.10. The loading plate diameter (D) is half the borehole diameter (B) and in the test reported D was 7.6 cm and B was 15.2 cm.

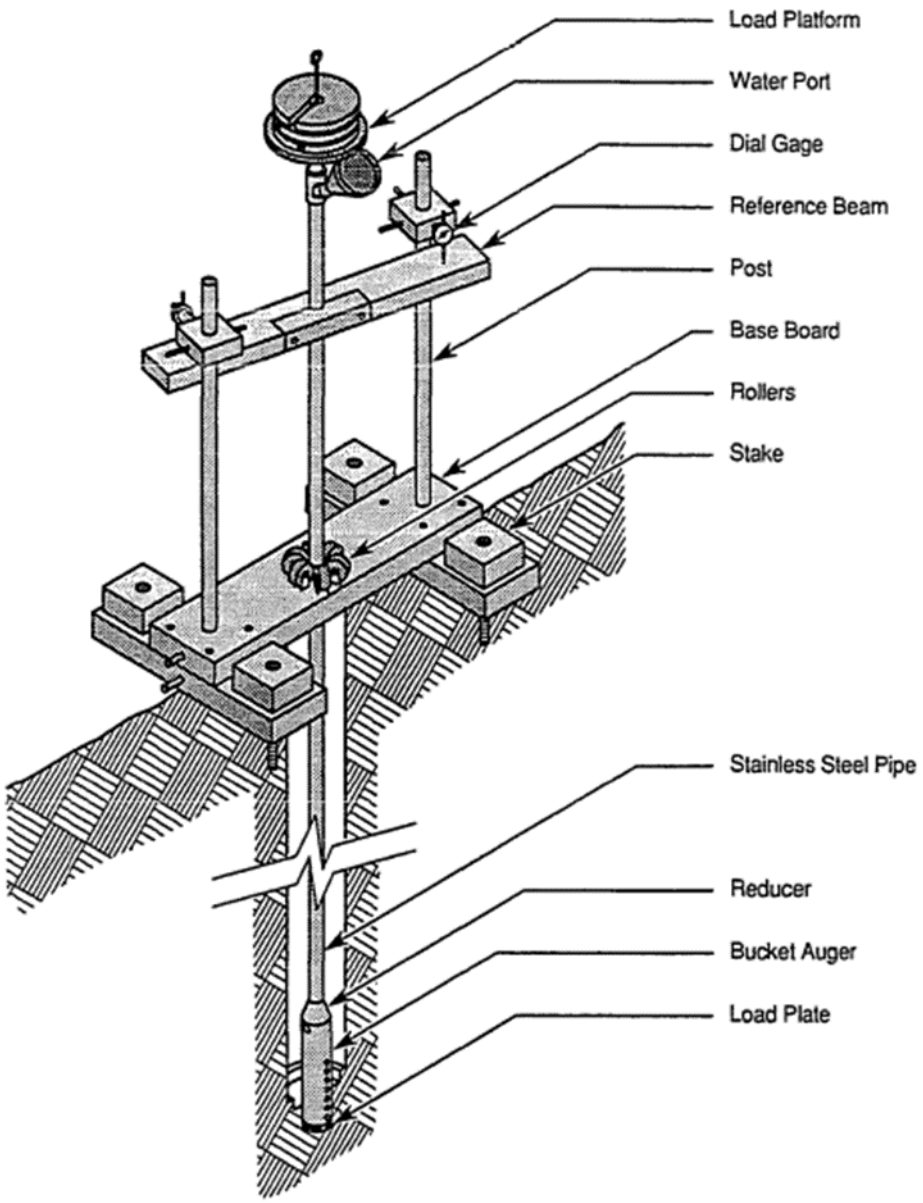


Figure 2.10: Diagram showing in-situ collapse test developed by Mahmoud (1991) - cited by Houston et al. (1995)

2.1.6.3 Collapse potential calculation

Generally, collapse potential can be estimated as the degree of bulk volume change that a collapsible soil can exhibit due to load application followed by water infiltration. For one-dimensional conditions, as in the oedometer test or testing specimens under zero lateral strain conditions, collapse potential is expressed by the change in height after wetting, under a given

applied load, divided by the specimen or layer thickness as given by Equation 2.4 (ASTM, D5333-1996) (as the specimen width remains constant).

$$CP = (\Delta H/H_1) = \Delta e/(1 + e_1) \quad (2.4)$$

where: Δh and Δe are the decrease in height and void ratio due to wetting, and e_1 and H_1 are the specimen void ratio and height before wetting under an applied stress. Δe should be calculated once equilibrium has been reached. Determination of Δe depends on whether it is measured from a single oedometer test (Figure 2.11a) or double-oedometer test (Figure 2.11b).

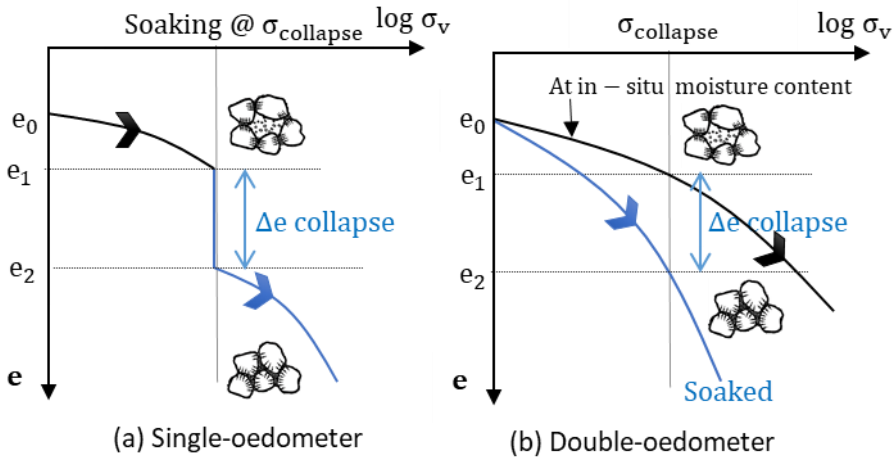


Figure 2.11: Collapse measurement using oedometer

2.1.6.4 Collapse classification

After calculating the collapse potential of a soil, the degree of collapse can be classified as given in Table 2.3 which shows two classification systems for the degree of collapse according to Jennings and Knight (1975) and ASTM (1996) D 5333. Each system is divided into five comparable categories of degree of collapse. Jennings and Knight (1975) have a wider range for the collapse potential than the ASTM. The ASTM specification provides more detail within the low collapse potential range by adding the 'slight' category while Jennings and Knight (1975) have a higher category of 'very severe trouble' for collapse potential more than 20%.

Table 2.3: Categorisation of degree of collapse

ASTM D5333 (1992) (Revised 1996)		**Jennings and Knight (1975)**	
Degree of collapse	Collapse potential, (%)	Degree of collapse	Collapse potential, (%)
None	0	No problem	0 to 1
Slight	0.1 to 2.0	Moderate trouble	1 to 5
Moderate	2.1 to 6.0	Trouble	5 to 10
Moderately severe	6.1 to 10.0	Severe trouble	10 to 20
Severe	>10	Very severe trouble	> 20

2.1.7 Identification of collapse potential from soil properties

Several indirect empirical collapse measures for the evaluation of soil collapsibility from basic soil states and properties such as void ratio, liquid limit and density have been proposed in the literature. One of these measures is considered here for evaluating collapse potential in gravelly soils. The suitability of using empirical methods for evaluating collapse of gravelly soils was assessed by Hamid (2012) and is discussed in Section 2.2.7.3.

Only one example of these empirical methods is discussed in this section because it includes the effect of the density and water content which are the major variables that govern collapse. Holtz and Hilf (1961) cited that the original formulation of collapse based on liquid limit and the in-place dry density of a soil was originated by Denisov (1946). In low density soils such as much finer grained loess soils, the water content at saturation is greater than the liquid limit (near-zero strength) soil structure is subject to collapse. At such soils the water content saturation or liquid limit and density will be above the curve in Figure 2.12, indicating susceptibility to collapse (Holtz and Hilf, 1961).

The solid curves in Figure 2.12 were produced assuming that collapse takes place at saturation (S_r=1.0) using Equation 2.5d which is derived from Equations 2.5a to 2.5c. The dotted curves are added to this plot to provide an example of the soil state when Sr = 0.5. As the water content and degree of saturation reduce; there is an associated development of capillary bonds (from increasing matrix suction) which lead to a greater collapse possibility.

$$\gamma_{dry} = \frac{\gamma_w G_S}{(1+e)} \tag{2.5a}$$

$$e = \frac{w.G_S}{S_r} \tag{2.5b}$$

$$w = \left[\frac{\gamma_w}{\gamma_{dry}} - \frac{1}{G_S}\right].S_r \tag{2.5c}$$

$$\frac{1}{\gamma_{dry}} = \left[\frac{1}{\gamma_w * G_S} + \frac{w}{S_r * \gamma_w}\right] \tag{2.5d}$$

Where: γ_{dry} is the dry unit weight of the soil, γ_{w} is the unit weight of water, G_{S} is the particle specific gravity, e is the void ratio, w is the soil water content, and S_{r} is the degree of saturation.

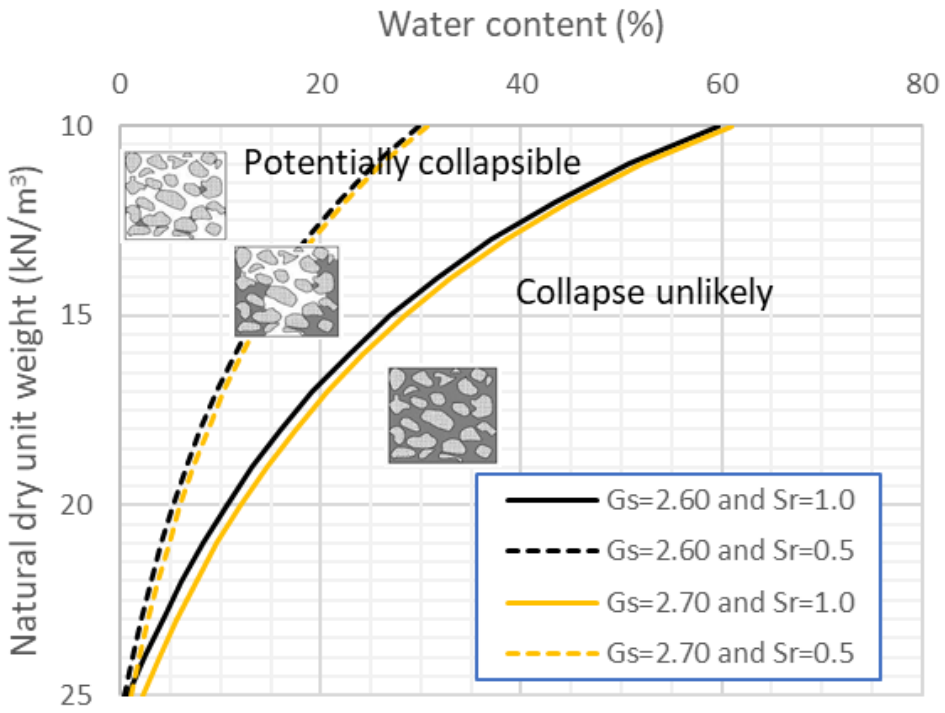


Figure 2.12: Effect of dry bulk unit weight, water content on the collapsibility of the soil fabric, after Holtz and Hilf (1961)

Hamid (2012) used the Holtz and Hilf (1961) plot for predicting collapse of the soils in the study area. The shaded area in Figure 2.13 represents the zone liquid limit and dry unit weight of a soil to be susceptible to collapse without any consideration for the stress level.

Figures 2.12 and 2.13 are both plotted from Equation 2.5d, but the liquid limit is used instead of water content. For this case, there is another assumption which is, at full collapse, the water content between fine particles reaches the liquid limit and maximizes the effect of water in the bond between the coarse particles. To project this to collapsible soils having coarse particles at the gravel scale, the liquid limit of the fine particles needs to be considered separately.

In gravelly collapsible soils, although fine particles are associated with creating most of the capillary bonds because of their small particle sizes, using their liquid limit in Figure 2.13 might under-estimate the possibility of collapse in these soils as shown later in Figure 3.25. In this figure the liquid limit and dry density values for these collapsible gravelly soils are below the curve, indicating that these soils unlikely to collapse. This is mainly because there might be micro and macro voids in these soils with respective values of micro and macro water content and dry bulk unit weight.

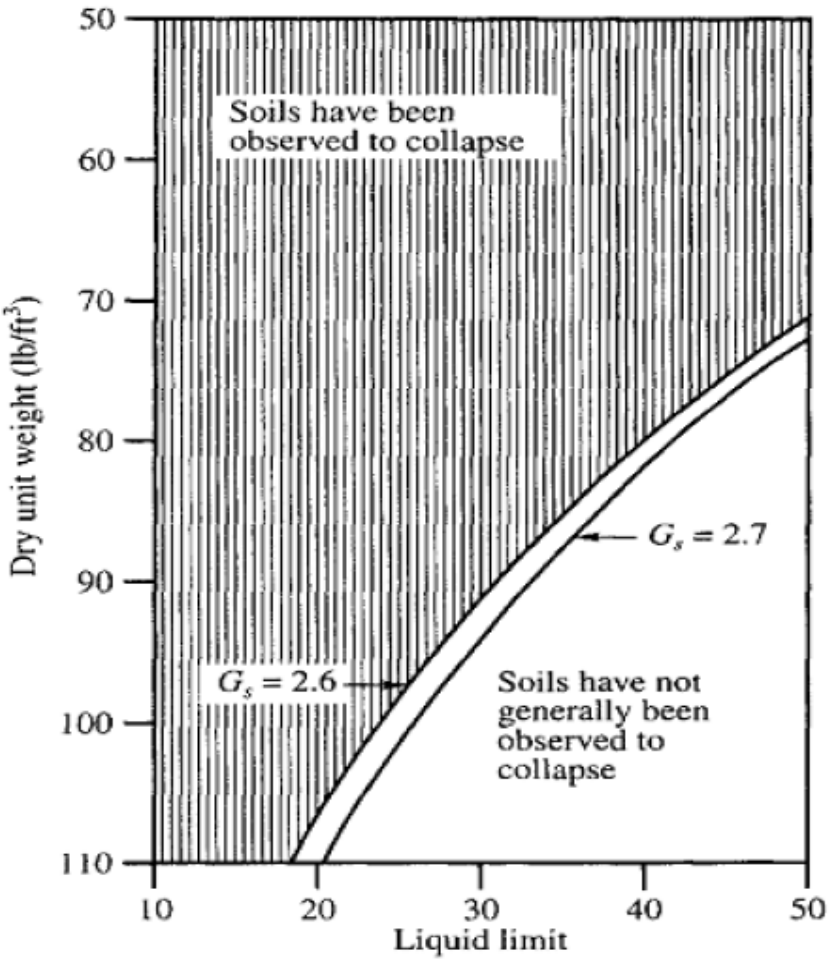


Figure 2.13: Relationship between dry unit weight and liquid limit and collapse - Holtz and Hilf (1961) – cited by Hamid (2012)

2.1.8 Review of some collapse tests from previous studies

2.1.8.1 Collapse in silty sand soil

Jennings and Burland (1962) reported on a series of oedometer tests performed on specimens of silty sand (50% fine to medium sand with a clay fraction of 7%) that were allowed to dry to different degrees of saturation (See Figure 2.14). For each collapsible soil there is a critical degree of saturation at which the soil can reach its maximum collapse under a specific applied stress. For this silty sand, the critical degree of saturation is expected to be slightly higher than 40.7% (this is the S_r value that experiences the greatest collapse of the S_r values tested) which correlates roughly with the classification given by Jennings and Knight (1975) for the critical degree of saturation as shown in Table 2.4. At $S_r = 40.7\%$, the collapse potential was about 13% at an applied stress of 16 tons/ft^2 (1532 kPa).

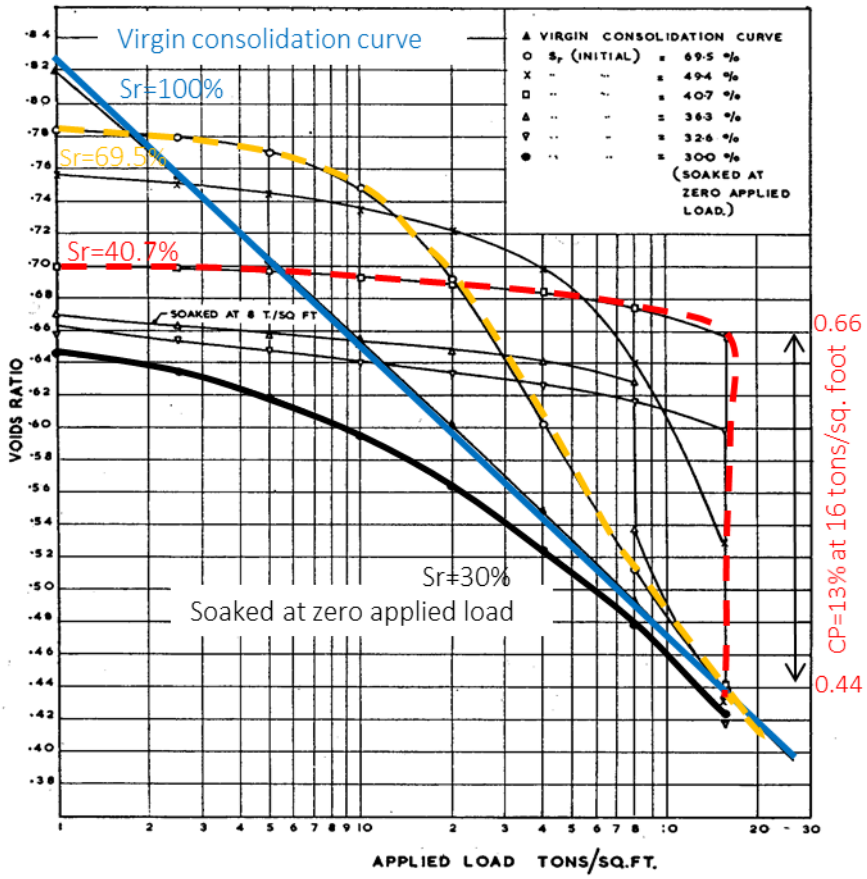


Figure 2.14: Oedometer curves for silty sand tested at various initial degrees of saturation – after Jennings and Burland (1962)

Table 2.4: Critical degree of saturation for different particle sizes - Jennings and Knight (1975)

Particle size range	**Critical degree of saturation**
Fine gravel, 1 - 6 mm	6 – 10 %
Fine silty sands, 150 - 2 µm	50 – 60 %
Clayey silts, 150 – 0.2 µm	90 – 95 %

2.1.8.2 Collapse in clayey sand soil

Maswoswe (1985) studied the stress path followed during soaking in remoulded specimens of Lower Cromer Till (LCT) which is a glacial deposit of gap-graded clayey sand with a low plasticity clay (fine sand 50% and its clay fraction 17%). His work focused on studying the stress and volume changes during soaking under zero lateral strain conditions. He conducted oedometer, isotropic compression, and triaxial shear tests as explained in Section 2.1.6.1 (See Figure 2.8).

2.1.8.3 Collapse in remoulded loess soil

Collapse is common in aeolian deposits, therefore, several factors effecting collapse were investigated for a remoulded loess by Singhal et al. (2016). This loess contained low plasticity silt (91%), clay (5%) and sand (4%) and had natural water content of 9%.

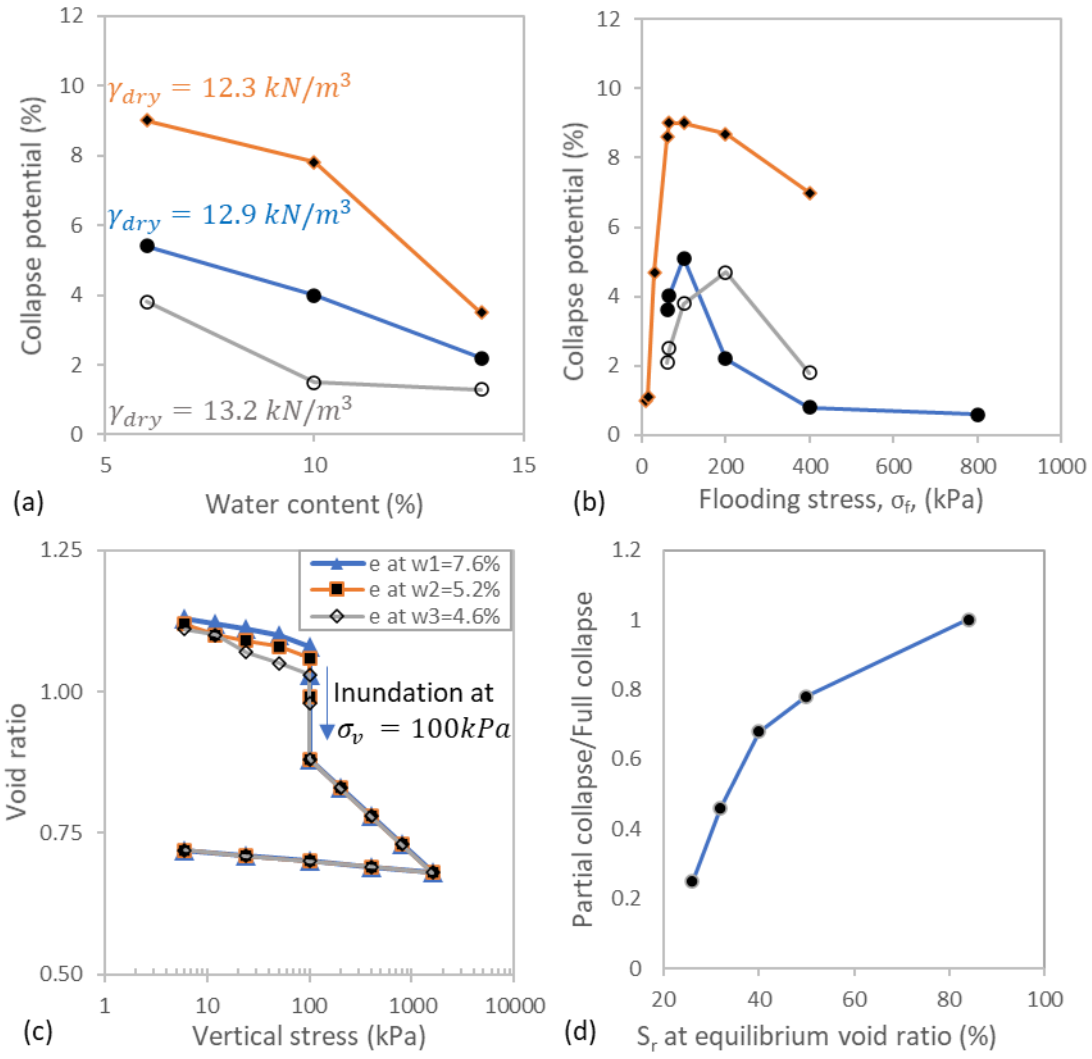


Figure 2.15: Laboratory study of collapse behaviour of remoulded loess under controlled wetting and flooding (after Singhal et al., 2016)

In Figure 2.15 it can be seen that collapse potential depends on various factors such as (a) initial dry unit weight, (b) applied stress level, (c) initial water content, and (d) degree of incremental flooding. The initial dry density (or dry unit weight) governs the collapse potential, a lower initial density leading to higher collapse (Figure 2.15a). Collapse potential increases with increasing flooding stress level up to a certain value and then decreases (Figure 2.15b). Collapse reduced with decreasing water content for all initial dry densities (an example at a given initial dry density is shown in Figure 2.15c). The degree of collapse increased cumulatively with flooding when water was added incrementally with the initial flooding

stages producing greater collapse than the final stages. In Figure 2.15d the amount of water added is expressed in terms of degree of saturation, and the degree of collapse (i.e., partial collapse) as a percentage of the final full collapse. Increases in both degree of saturation and flooding stress level lead to the development of a more stable soil fabric. It was also found that rebound on unloading is independent of flooding stress (one example of rebound is shown in Figure 2.15c).

2.1.8.4 Collapse in a remoulded uniform sand bonded with clay

The effects of fines content and their plasticity on collapse potential in clayey sands were investigated by Rollins et al. (1994). They tested artificially bonded specimens of mixtures of various clays and uniform sands. Their results are shown in Figure 2.16. It can be concluded that, in these uniform sands, collapse potential increases with the increase of clay content for both bentonite and kaolin for coarse sand, but there was a dramatic increase in collapse potential for very small increases in bentonite. However, because of the heave characteristics of bentonite, it is expected that at higher bentonite percentages the collapse potential will not be so dramatic. Regarding the sand size, larger sand particles for a given percentage of kaolin result in higher strains (i.e., collapse potential) than the smaller sizes.

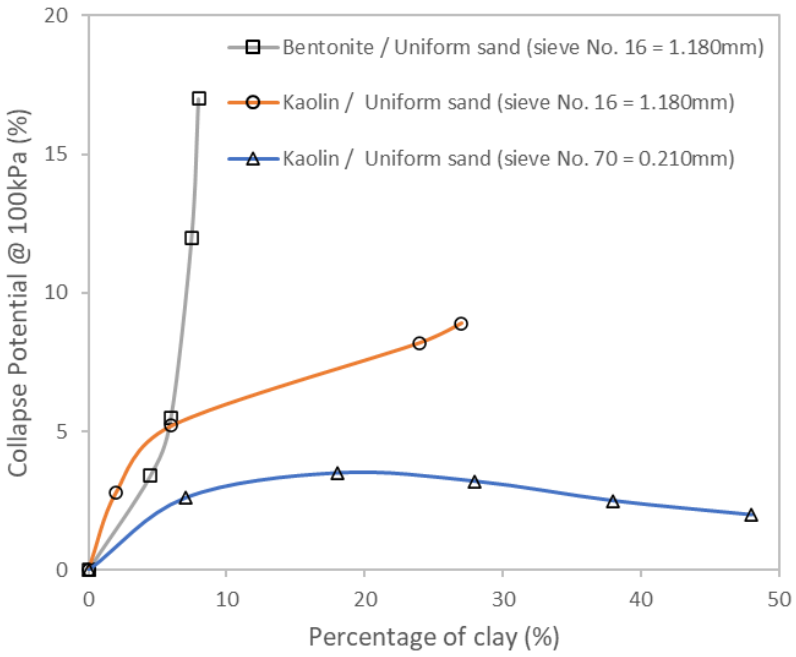
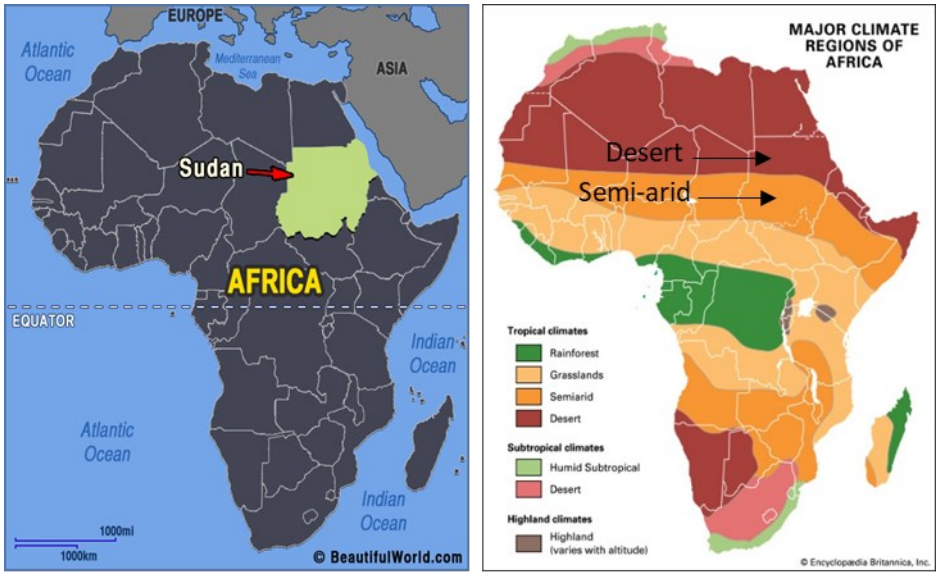


Figure 2.16: Effect of plasticity of fine particles and sizes of course content on collapse potential (Rollins et al., 1994)

2.2 Review of collapse in gravelly soils in the study area.

2.2.1 Introduction

Sudan is one of the largest countries in Africa, covering 2.5 million square kilometres (before separation). It is one of the North African countries just south of Egypt. It is a country with extremes of weather and geology. The rainfall is seasonal with an intensity ranging between 10 mm in the North and 1500 mm in the far South. There are a wide range of soil types: desert soils in the North; alluvial and lacustrine soils in the central and the East; and aeolian soils in the West (Whiteman 1971). These soils were formed during the early dry phases of the Pleistocene, but the main period of formation was during the Middle Palaeolithic dry phase, more than 25,000 years ago. Another phase of deposition was during the period of the following very wet climate which is thought to be the main reason for the stabilization (the formation of weak capillary bonds because of the fine particles matrix suction) of these aeolian deposits due to washing down fine particles. These formations are mostly part of the eastern Sahara basement, the north-east Africa Nubian sandstone, (Edmonds, 1942) and cover two tropical climates: desert in northern part and semi-arid in the southern part as shown in the right picture in Figure 2.17.



© BeaufulWorld.com

© Encyclopædia Britannica, Inc./Kenny Chmielewski

Figure 2.17: Sudan map (location and its climate)

2.2.2 Collapsible soils in Sudan

Problematic collapsible soils are widespread in Sudan. Many vital infrastructure and developmental projects such as airports, roads and buildings have been founded in these soils (Elsharief et al., 1999). There are two reported collapsible soil types originating from aeolian and colluvial deposits. The first of these are aeolian soils, also locally known as ‘qoz’ soil, comprise weakly bonded fine silty sand deposits located west of the White Nile as shown in the dotted zone in Figure 2.18. These are an extension of the non-stabilized desert sands and sand dunes in the North. There are two stabilisation sources bonding these aeolian soils: the oxidisation of a thin surface crust of iron oxide and the capillary suction of fine silt or clay particles (Whiteman, 1971).



Figure 2.18: Sudan geological map – After Whiteman (1971) - cited by Elsharief et al. (1999).

The second prevalent collapsible soil type derive from colluvial deposits which contain a considerable amount of gravelly soil with a wide range of fines. This deposit is located between two mountain ranges (Merkhiyat mountains in the north-west and Toriya mountain in the south-west) and the White Nile and River Nile in the east. It is part of the Omdurman Formation, and this type of soil is the focus of the research presented in this thesis. The steady increase in collapsible soils encountered in Sudan is related to urban expansion and developments on hitherto unexploited land. In the Nile River state, just north of Khartoum state, the aeolian deposits of sandy silt exhibit collapse. Omer (1973) investigated the collapse characteristics of loess clayey soil (34% clay) deposits found in the city of Berber within the Nile River state, where collapse behaviour is prevalent. Also, in the early 2000s, the expansion of agricultural schemes in the Nile River state, led to the ground either side of the water channels developing perpendicular and parallel cracks due to water leakage as shown in Figure 2.19. The parallel cracks are thought to result from partial wedge failure of the embankments constructed to contain the channels.

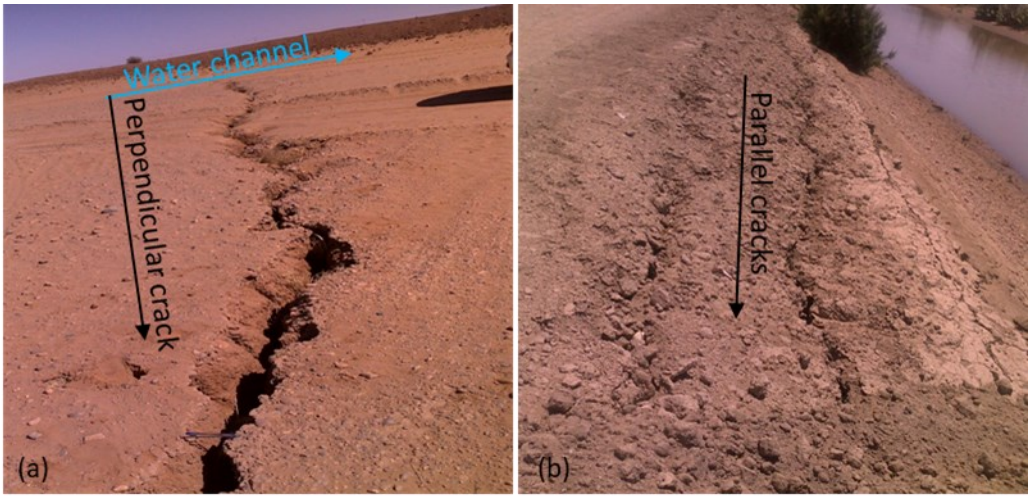


Figure 2.19: Perpendicular and parallel ground collapses around water channels - Nile River state

Recently in the southwest of Sudan, a massive collapse in loess soil in the suburb of the city of Babanousa took place in June 2018 (Alrakoba news, 2018). The collapse zone, as depicted in Figure 2.20, was estimated to be of about 5 km length and up to 5 m depth and there is not any potential reason was mentioned to be the reason of this massive crack.

In August 2021, Dr Khalid Abdelfattah, the Principal of Merowe University of Technology - Abulatif Alhamad, sent the Author a set of photographs documenting for the first time a massive ground crack in Abu Hamad city in northern Sudan. This feature developed mainly from a leak from a nearby water channel resulting in this massive crack toward the River Nile and a spring appeared close to the river at the end of the crack. These photographs are annotated and shown in Figure 2.21.

Figure 2.22 indicates the locations and names of some of the Sudanese cities where collapsible soils were encountered including the collapsible gravelly soils found in Omdurman which is described in the following sections.



Figure 2.20: A massive ground crack in a loess soil in southwest Sudan, Babanousa city June 2018, (Alrakoba news, 2018)

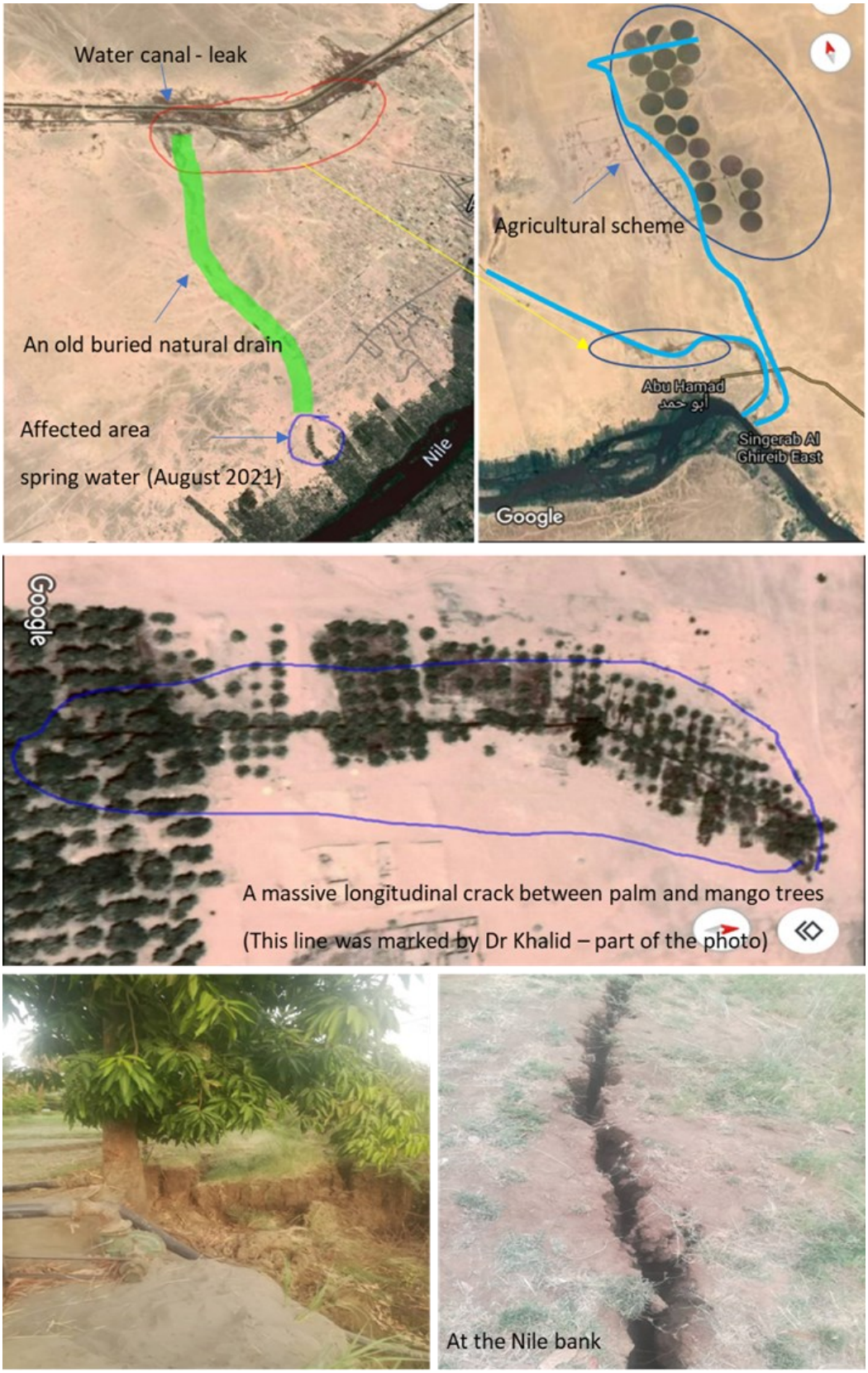


Figure 2.21: Collapse due to a water leak in the city of Abu Hamad - North Sudan (photographs countesy of Dr Khalid Abdelfattah)



Figure 2.22: Locations of the Sudanese cities where collapsible soils were encountered

2.2.3 Collapse and heave in the capital Khartoum

In the near vicinity of Khartoum state, where the confluence of the Blue and White Niles is located, both highly expansive and highly collapsible soils are found, which historically have caused trouble in the construction industry. In the eastern part of Khartoum, either side of the Blue Nile, expansive soil is found. Al Haj (2014) characterised the mechanical response of expansive soil specimens that were collected from this area (Al Haj and Standing, 2015; Al Haj and Standing, 2016). In the western part of Khartoum, especially the area west of the White Nile and Nile River which represents the city of Omdurman and its countryside, a totally different coarse-grained soil formation is encountered, as explained in Section 2.2.5. In many areas in Omdurman this formation exhibits collapse behaviour which has been investigated by Osman (2004), Hamid (2012) and Osman & Ahmed (2015).

Generally, these different soil types in Khartoum are related to their source parent grounds. The expansive soil is scoured from the Ethiopian Hills while the Omdurman formation is an extension of the Sahara Desert.

Althawra (19), in the northern part of Omdurman city as shown in Figure 2.23, was selected as a study area for this research to extend the above researchers' work to evaluate the collapse

response of such soil. Data collected from Osman (2004) and Hamid (2012) investigations are presented in Section 2.2.6 and discussed in Chapter 3.

2.2.4 The climate in Khartoum

Al Haj (2014) reported the description of the physical environment in central Sudan which includes the study area. The study area is located in a region with a semi-arid climate in which the temperature can reach up to 42°C in summer (the period from May to August). The average rainfall in the city of Khartoum is 164-mm per year which is calculated based on the rainy season between July and November in 1971.

2.2.5 Omdurman geological formation

To have a clear understanding about this formation, two descriptions are considered here: a general description to a great depth and detailed description covering shallow depths. The deep description is summarised from research conducted by Alzubair (2020) including three wells in different areas in Omdurman (Althawra Alhara (7), Dar El Salam, and Abu Saaed), as shown in Figure 2.23. This deep description is based on personal experience rather than a standard classification. In the summary of these three wells, the Nubian sandstone formations is described to a depth of more than 150m in six layers.

The first 30m is dominated by surface sediments to a depth of 6m, which is then followed by soft light brown clay, yellow to semi-white sandstone, and red claystone, in addition to medium fine sand, red and brown in colour. The second layer from 30m to 60m contains continuous clay, mudstone and sand, all of them red and yellow. The third layer from 60m to 90m contains clay, and with rough sandstone of red and brown colour. The fourth layer from 90m to 120m is sandy clay with coarse sandstone. The fifth layer from 120m to 150m grades from fine, rough to very rough sandstone, brown to white, with a spherical rather than angular particles. The sixth layer 150m and below also contains yellow sand and whitish sand. The groundwater level is located at depths varying between 150 m to 240 m because of the different texture of sandstone and the irregularity of its underground level.

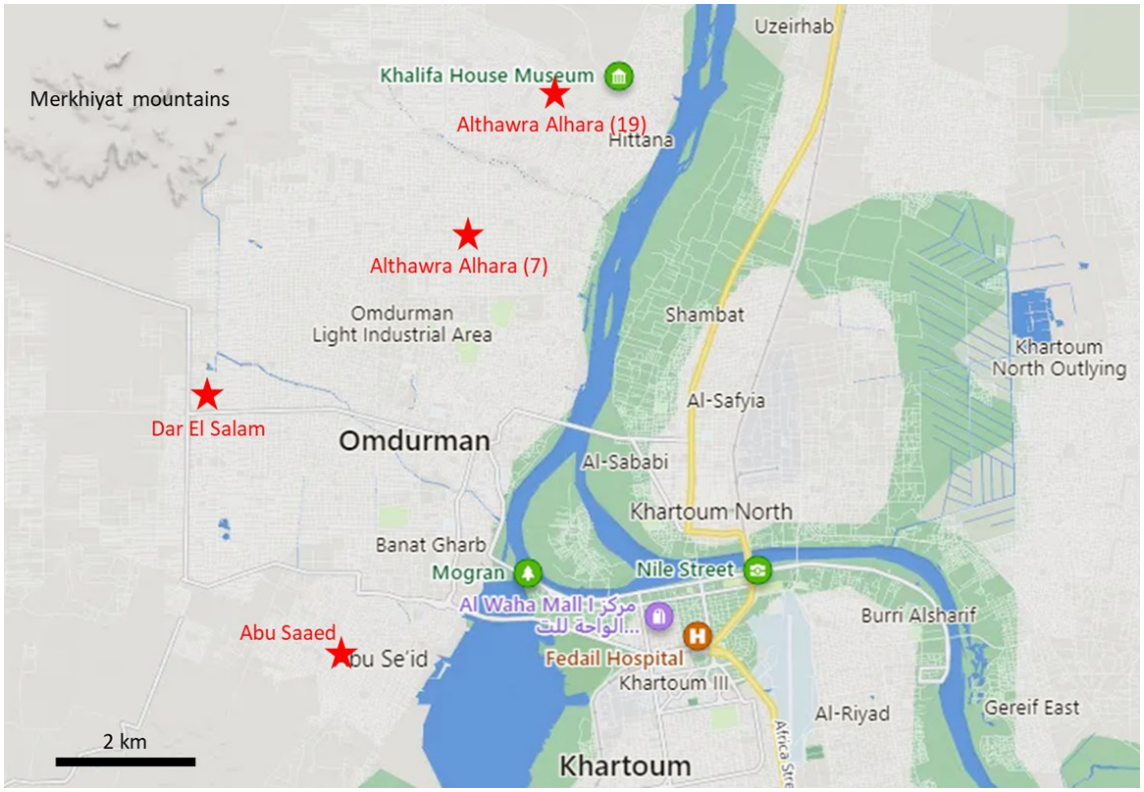


Figure 2.23: Locations of three wells used to describe the Omdurman formation (Google Earth) – after Alzubair (2020)

The detailed descriptions within shallow depths are compiled from three reports from the Building & Road Research Institute (BRRI, 2020; BRRI, 2017a; BRRI, 2017b). The upper part of the Omdurman formation contains a mix of gravel, sand, silt and clay of different percentages and densities. In North Omdurman, particularly in Alhettana which is east of Althawra Alhara (19) in Figure 2.23, the clayey sand and clayey gravel are dominant. Nubian Formation was encountered at depth of 3m (SPT N-value > 50 (BS 5930:2015), see soil profile 1 in Appendix B). South Omdurman, in the Hai Aljamaa part of Abu Saaed, as shown in Figure 2.23, gravel was found mixed with clay and silt and sand. The third report, Althawra Alhara (7), a few gravels and sand are found while clay is dominating. The details of these three profiles are given in Appendix B.

2.2.6 Collapse occurrences in the study area

2.2.6.1 Geological background to this collapsible formation

Omdurman state is part of the capital city of Sudan, Khartoum, which contains three states: Khartoum, Khartoum north and Omdurman. Figure 2.24 shows Omdurman city and the Merkhiyat mountains in the northwest and the Toriya mountain in the southwest. These two mountain ranges are thought to be the main source of the collapsible deposits in Omdurman.

The geological composition of the mountains in these two ranges includes conglomerate, medium to coarse grained pebbly sandstone, siltstone and clay shale. These formations are mostly cemented with siliceous and ferruginous minerals (Moussa, 2019) which are characteristic of the soils found in the study area. Whiteman (1971) noted that the Merkhiyat sandstones contain a clay-silt fraction with a maximum of 34.8% and average of 20.6 % by weight which is thought to have led to the creation of the weakly cemented collapsible soil fabric found in the study area.

The hypothesis for the formation of this collapsible deposit is that heavy rainfall in previous ages, scoured the surficial mountain layers and transported the eroded soils with water. Due to the height of these mountains the water and soil flowed at high energy towards the Nile River, it being the main natural drainage route for the runoff water from within the catchment area of the mountains. During extensive rainfall events, these sediments from the catchment area were gradually deposited as the runoff water lost its energy during its journey to the Nile River.

At high ground levels, sediment rich runoff water could initiate turbulent flows containing a mixture of water and scoured soil particles and air bubbles. This mixture was deposited along the runoff path to the river depending on their weights with the coarser gravel fraction settling out first. With heat and time, the water evaporated and cemented cavities between soil particles were formed, producing highly porous unsaturated collapsible deposits along the runoff path to the river. The repeating of this process led to different layers of collapsible soil. A typical soil profile for this collapsible formation is described and discussed in Section 3.2.

2.2.6.2 Structural damage in the study area

Many areas in Omdurman have undergone severe ground collapse and consequently the gravelly soils responsible are considered to be a collapsible soil (Osman & Ahmed, 2015). The study area in this research is North Omdurman which lies between the Markhiyat Mountains from the West and Nile River on the East. The study area includes one of the most affected areas in Omdurman, referred to as Althawra (19), where most of the buildings were constructed on strip foundations. Some of these buildings suffered severe cracking due to ground collapse from the combination of newly applied surface stresses (from the structures) and water leakages.

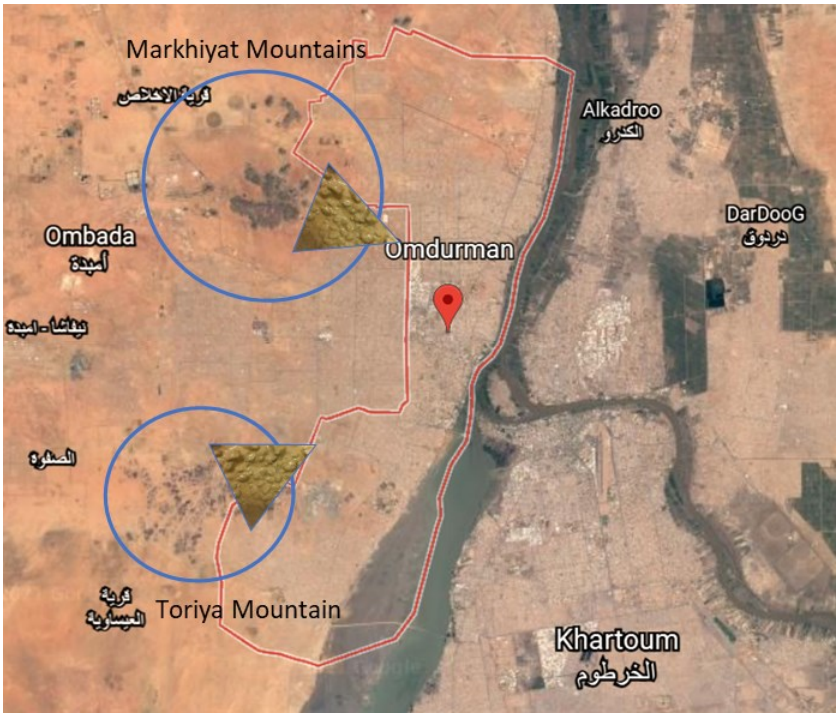


Figure 2.24: Omdurman city surrounded by mountains and the river – Google Earth



Figure 2.25: Structural damage in the study area (Osman, 2004)

Osman (2004) reported various degrees of structural damage in many houses in Althawra (19) - Omdurman city ranging from cosmetic to very severe where there were stability issues, examples of which are shown in Figure 2.25. Hamid (2012) reported similar structural damage in the study area including buildings constructed on isolated footings as shown in Figure 2.26.



Figure 2.26: Structural damage in the study area (Hamid, 2012)

2.2.7 Soil collapse history in the study area

2.2.7.1 Summary of the review from previous studies

Osman (2004) and Hamid (2012) investigated the collapsibility of the soils in the study area. Osman conducted an in-situ plate load test in accordance with BS 1377-9:1990 – part 9. In this test the magnitude of settlement due to loading and then inundation of the soil beneath the plate load set-up was measured. Discussion about this test is given in Section 2.2.7.4.

Hamid (2012) studied the physical properties of the soil and conducted the modified Proctor compaction test, (according to ASTM – D1557-98, 2000 (ASTM, 2000)), to determine values of the maximum dry density and optimum water content. Hamid's data are presented in Figures 2.28 and 2.29 and Table 2.5. These data are utilized in Chapter 3 to estimate soil collapse through a hypothetical procedure.

Osman and Ahmed (2015) reported on an experimental study to identify and classify the collapse potential of soils from five trial pits in different locations in the city of Omdurman as shown in Figure 2.27. Two of these five pits were in Hamid's study area (TPs 1 and 2).

2.2.7.2 Particle size distribution curves relating to the study area

Trial Pits 1 and 2 were overseen by Hamid (2012) and their locations are shown in Figure 2.27. These two pits, excavated to a depth of 3m, were located in the most severely affected part of the study area. The coordinates of TP1 and TP2 are as follows:

(Coordinates, WG1984 ellipsoid zone 36 North).

- TP1; N 0446568, E 1737312
- TP2; N 0447248, E 1736890

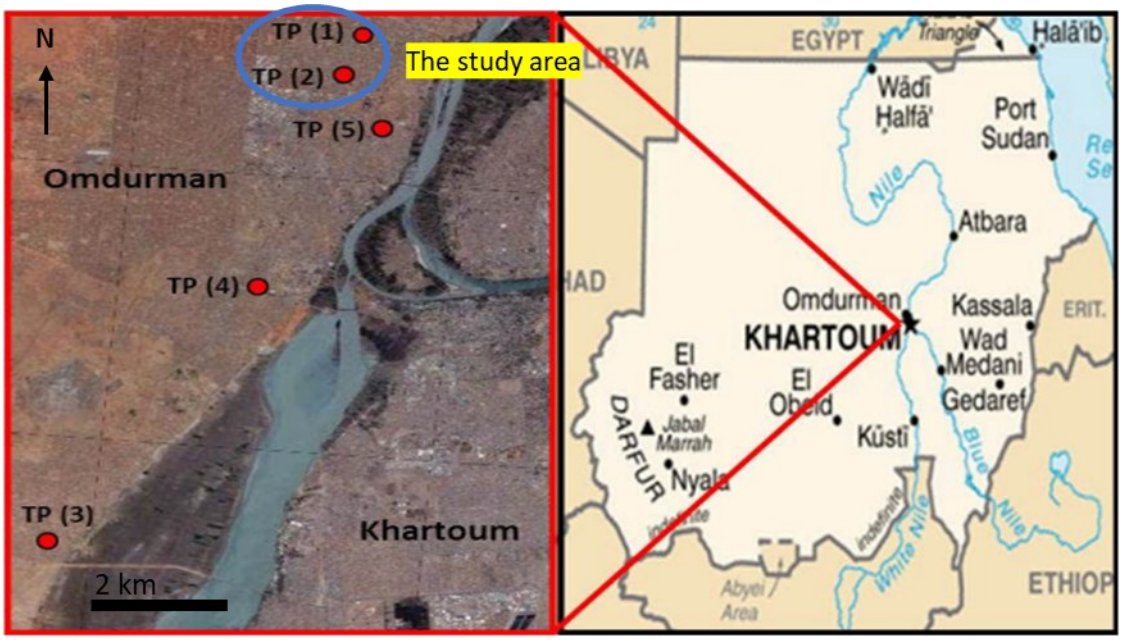


Figure 2.27: Location of the Test Pits 1 and 2 (after Osman and Ahmed, 2015)

The particle size distribution (PSD) curves given in Figure 2.28 were developed by Hamid (2012). There is a similarity between particle distribution curves relating to these two test pits. At all depths in these two TPs the ground was dominated by more than 50% of gravel with fines content ranging between 15% and 30% except for the first 1m in Trial Pit 2 where it was 55%. The photographs and charts in Figure 2.29 show the gravelly nature of the soil and the content of fines.

2.2.7.3 Soil properties in the study area

Table 2.5 lists values of soil physical properties including soil particle density (expressed as specific gravity, G_s), Atterberg limits, natural dry density and maximum dry density and their water contents. Discussion and comparison of these densities is given in Chapter 3.

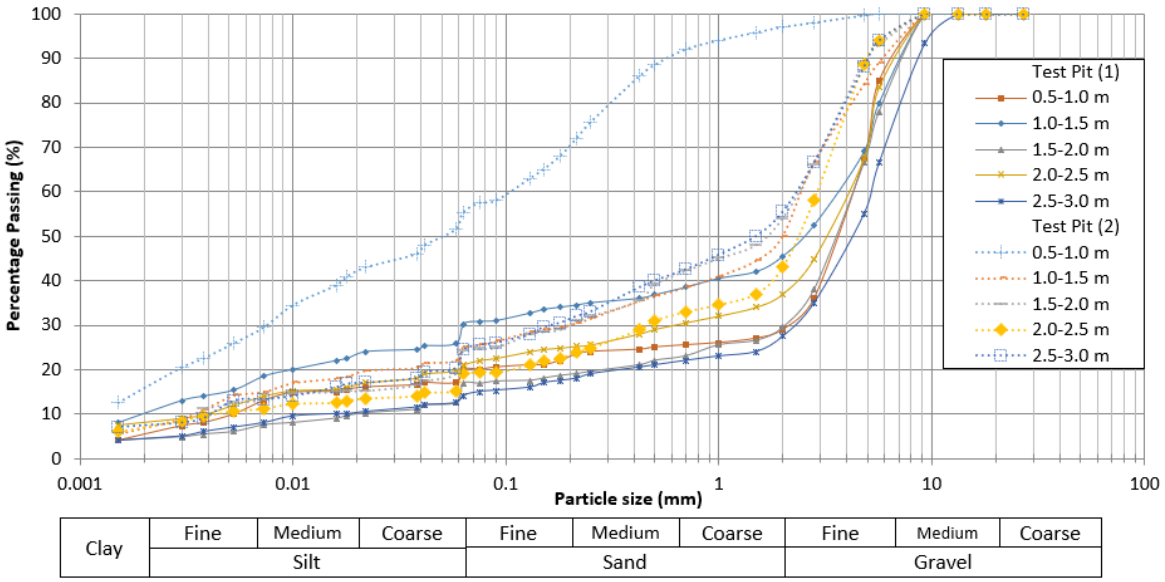


Figure 2.28: Particle size distribution curves from Trial Pits 1 and 2 after (Hamid, 2012)

Table 2.5: Soil properties of the collapsible soils at the area of study after (Hamid, 2012)

Test Pit No.	Soil parameter	Depth (m)					
		0.0-0.5 (Fill)	0.5-1.0	1.0-1.5	1.5-2.0	2.0-2.5	2.5-3.0
Particle Size Distribution							
TP1	Gravel (%)	-	70.6	54.6	70.0	63.0	72.4
	Sand (%)	-	9.4	14.8	13.2	15.6	13.2
	Silt (%)	-	14.2	21.4	12.1	1.4	10.1
	Clay (%)	-	5.8	9.2	4.7	8.0	4.3
TP2	Gravel (%)	-	3.0	50.0	46.0	57.0	44.0
	Sand (%)	-	41.6	24.6	29.8	24.2	31.2
	Silt (%)	-	39.6	19.3	16.2	10.8	16.9
	Clay (%)	-	15.8	6.1	8.0	8.0	7.9
Specific Gravity							
TP1	G_S	-	2.77	2.74	2.78	2.73	2.79
TP2	G_S	-	2.68	2.63	2.68	2.63	2.6
Test Pit No.	**Soil parameter**	**Depth (m)**					
		0.0-0.5 (Fill)	0.5-1.0	1.0-1.5	1.5-2.0	2.0-2.5	2.5-3.0
Atterberg Limits							
TP1	Liquid Limit	-	51.1	40.5	38.4	37.8	40.3
	Plastic Limit	-	31.6	21.3	16.4	18.0	18.7
	Plastic Index	-	19.5	19.2	22.0	19.8	21.6
TP2	Liquid Limit	-	35.7	36.8	35.9	46.0	58.7
	Plastic Limit	-	19.0	18.9	19.8	25.2	32.7
	Plastic Index	-	16.7	17.9	16.1	20.8	26.0
Unified Soil Classification System (USCS)							
TP1	USCS	-	GM	GC	GC	GC	GC
TP2	USCS	-	GL	GC	GC	GC	GC
Natural Dry Density and Water Content							
TP1	ρ_{dry} (t/m^3)	-	1.91	1.84	1.76	1.72	1.83
	NWC (%)	-	5.6	5.4	6.5	8.4	10.1
TP2	ρ_{dry} (t/m^3)	-	1.56	2.04	1.96	1.91	1.65
	NWC (%)	-	11.3	2.7	3.0	4.3	8.4
Maximum Dry Density and Optimum Water Content							
TP1	ρ_{dmax} (t/m^3)	-	2.11	2.24	2.23	2.2	2.24
	OWC (%)	-	8.9	7.7	7.4	7.3	7.0
TP2	ρ_{dmax} (t/m^3)	-	1.81	2.15	2.16	2.16	.84
	OWC (%)	-	14.2	7.4	8.3	8.2	13.6

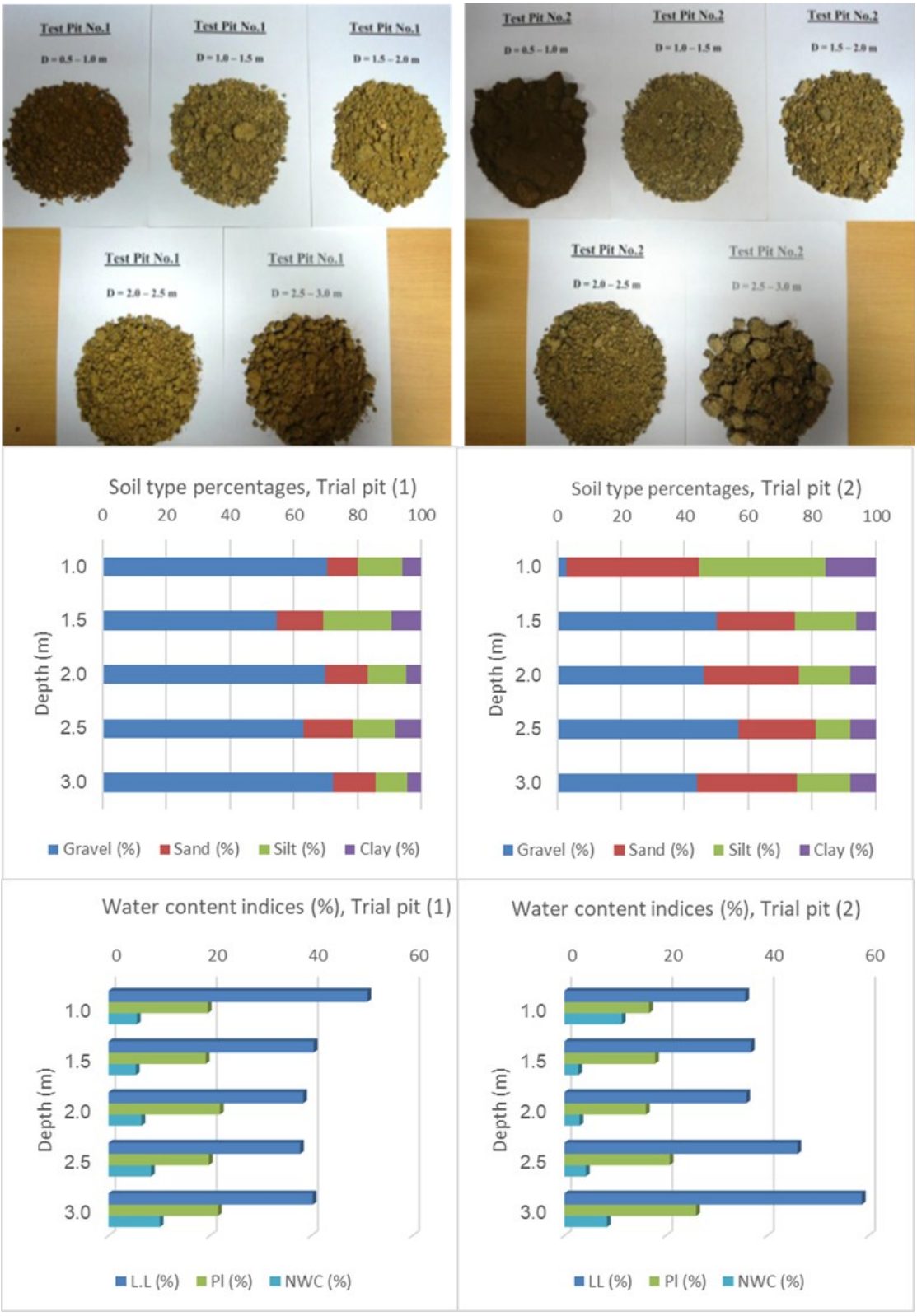


Figure 2.29: Particles content and plasticity indices, natural water content for TPs 1 and 2 (after Hamid, 2012)

2.2.7.4 In-situ plate loading test at the study area

Osman (2004) performed a field plate-load test at Althawra (19) at 0.7 m depth using a square plate of 50x50 cm^2. The soil profile is given in Table 2.6. The maximum target stress for the test was 262 kN/m^2 which represents maximum building footing stress (computed using Structural Analysis Program - SAP90). The plate was set-up in the middle of the pit (2x2 m^2) with four settlement dial gauges which were placed at the plate corners. The set-up of this test is shown in Figure 2.30. The test was conducted in two stages: loading at natural moisture content, followed by flooding of the pit, with settlement measured over a 24-hr period. The total average settlement from this test, under the stress of 262 kN/m^2, was 1.5mm before flooding, and 8.75 after 24 hr as shown in Figure 2.31. With this test set-up, it is possible that the displacement gauges were not sufficiently isolated and so they might have measured relative movement which could under-estimate the amount of settlement.



Figure 2.30: Plate-load test set-up (Osman, 2004)

Table 2.6: Soil characteristics where the in-situ plate load test was performed (after Osman, 2004)

Depth (m)	Soil description	NWC (%)	L.L. (%)	P.L. (%)	P.I. (%)	% Passing #200	Bulk density (t/m³)	USCS
0.0-0.4	Fill	-	-	-	-	-	-	-
0.4-1.2	Clayey gravel with sand	6.8	53	28	25	11.9	1.92	GC
1.2-2.0	Gravelly sand with more fines	5.7	36	18	18	34.9	1.95	SC
2.0-2.4	Clayey sand with gravel	5.0	36	19	17	17.8	1.88	SC

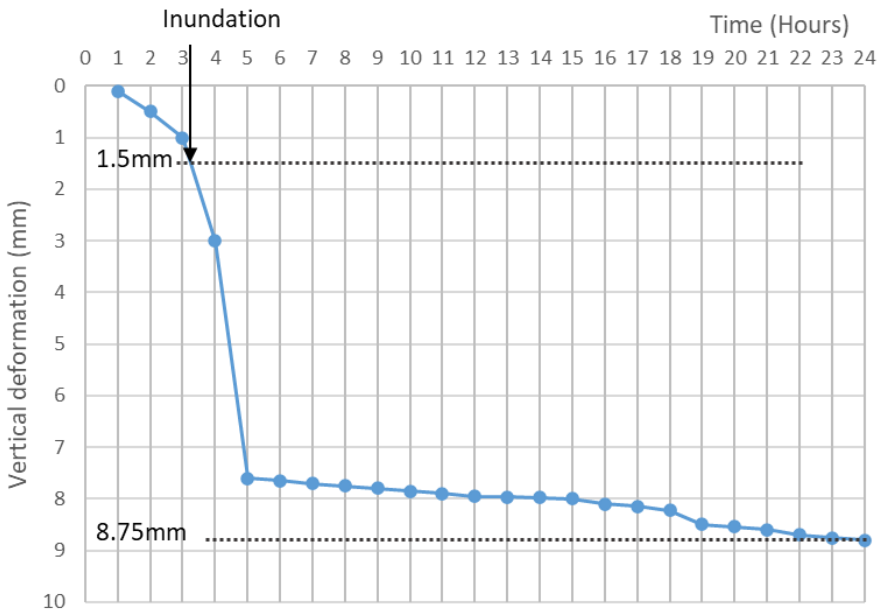


Figure 2.31: Average settlement versus time - plate load test (after Osman, 2004)

2.2.7.5 Static Cone Penetration test (CPT) at the study area

Three mechanical static cone penetration tests (CPT) were conducted in the vicinity of the in-situ plate load test in the natural ground without inundation as shown in Figure 2.32. The CPT results show that generally the cone resistance increases with depth which indicates that these soils below 1.5 m depth are dense (see Figure 2.32) based on the classification given by Lunne et al. (1997). This suggests that using CPT to assess the collapsibility of these soils is misleading. Although, the bulk density is shown to decrease in Table 2.5 at the bottom of this profile, only test q_c1 reached this level but confirms the slightly lower value. Sleeve friction values of $fs2$ and $fs3$ support this reduction in density as well while $fs1$ is a bit random.

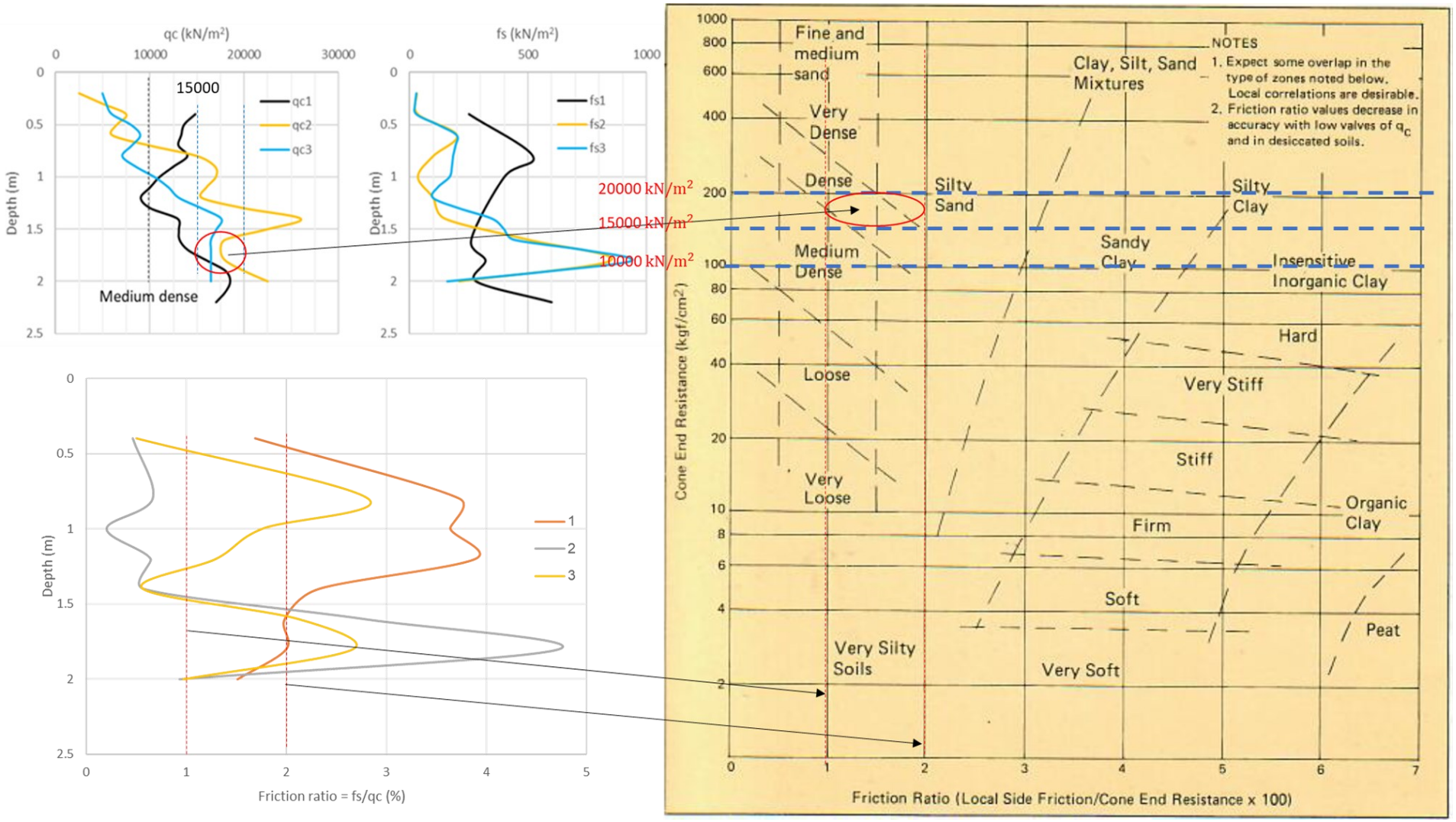


Figure 2.32: Three-static cone penetration tests around the area of the plate test after Osman (2004) and Lunne et al. (1997)

2.2.7.6 Conclusions from previous research about soil collapse in the study area

Hamid (2012) proposed an evaluation of the collapse potential of the gravelly soils at the study area based on their physical properties using an indirect method. However, he found that this approach was not practical when compared with other commonly applied empirical methods. He explained the reason for this under two headings. First, these methods originated from tests on remoulded soil specimens for which the fabric characteristics had been destroyed. Second, these methods were usually established for collapsible aeolian loess soils while the gravelly soil at the study area is a colluvial deposit that contains more that 50% gravel.

Due to the gravelly nature of this soil, there were difficulties in retrieving undisturbed samples to perform laboratory oedometer tests. Equally specially designed and manufactured oedometers would be needed to cater for the gravel-size particles. Hamid (2012) started his evaluation of collapse potential in the study area (where trial pits 1 and 2 were excavated) by reviewing the in-situ plate-load test performed by Osman (2004) in which a collapse settlement of 7.25mm was measured under applied stress of 262 kPa as discussed in Section 2.2.7.4. He then performed a series of in-situ density and modified compaction tests, the results from which are given in Table 2.5.

In the far west of the city of Omdurman, TP3 was dug south edge of Omdurman (in the new airport location) as shown in Figure 2.27. A series of oedometer tests on undisturbed and compacted specimens collected from TP3 were performed by Hamid (2012) as a technique for evaluating and deducing the collapse potential. Hamid (2012) concluded that the Omdurman area is dominated by collapsible soil of slight to moderate degrees severity based on the in-situ plate-load test in the study area and the data from Trial Pit 3. At that time no experimental method had been developed to quantify collapse in this soil.

Osman and Ahmed (2015) concluded that collapsible soils, containing considerable amounts of fine to medium gravel with low silt and clay contents, cover many areas in Omdurman following a review of Hamid's work. Also, they commented that the fabric of these soils frequently has a loose packing and comprises significant amounts of gravel, which makes taking undisturbed samples very difficult.

Chapter 3 : The collapse potential of the Omdurman gravelly soil

3.1 Introduction

In this chapter, the structural damage, foundation types and main factors that have led to collapse in the gravelly soil in the Omdurman study area are discussed. This includes the following: (i) reflecting on some of the current damaged buildings and foundation types and water leak sources that were observed during the Author's field visits, (ii) soil profile and soil classification and discussion of the likelihood of collapse in this area. The collected data are compared with the data from previous studies to provide a broader understanding of the properties of this soil. This comparison includes crack description and soil properties to demonstrate the continuation of the collapse problem in this area. Data from previous research by Osman (2004) and Hamid (2012) presented in Section 2.2.7 are further used in this chapter. A hypothetical procedure for estimating the collapsibility of soil at the study area using Hamid's data (see Figure 2.28 and Table 2.5) was developed as described in Section 3.6.2.2.

3.2 Field observations

3.2.1 The selection of location of the study area and site visits

After studying the research findings of Osman (2004) and Hamid (2012), discussed in Section 2.2.7.6, the Author organized several site visits in 2018 to different locations in Omdurman including the areas they investigated. These visits focussed on several affected houses and also houses under construction making appropriate observations. On these occasions, local residents were interviewed, photographs taken, and disturbed representative samples and a block of intact soil collected (subsequently shipped to the Imperial College soil mechanics laboratories to conduct this research). A year later, in 2019, the Author revisited the affected houses in the study area for further observations.

3.2.2 Field observations related to collapse

3.2.2.1 Crack development

An essential observation to make during the site visits was to assess the current extent of cracking. Cracks continue to develop, and some are appearing in new houses and others re-appearing in repaired and renovated houses. The crack patterns, as seen in Figures 2.25 and 2.26, are diagonal and sub-vertical with wide openings which appear extensively in the vicinity of water leakage as is discussed in Section 3.2.2.3. This mode of cracking is generally

associated with differential soil settlement rather than soil heave in which the hogging modes leads to heave in floors in contact with the ground, leading to difficulty in opening doors and developing slightly different crack patterns (see Figure 3.1). However, it is appreciated that whether the ground is settling or heaving it is the mode of deformation that is important with hogging modes, associated with tensile strains, being more likely to cause damage. Also, it was observed that cracked houses are clustered in various places which suggests that the severity of ground collapse is localised and also might be related to the ground topography. Load-bearing-brick houses were observed to be more affected than the reinforced concrete frame houses resting on isolated footings.

To differentiate between ground movements and their associated crack patterns, Figure 3.1 explains that crack patterns in a sagging mode are wide at the bottom and narrow at top (Figure 3.1a) and vice versa in hogging and differential settlements shown in Figures 3.1b and 3.1c. Door and window openings represent zones of weakness and cracks pass through them in both scenarios of subsidence and heave. Cracking relating to a hogging mode is generally more severe compared with a sagging mode. The reason for this is that in the sagging mode the lower 'fibre' of the building is in contact with the ground and interface friction between them tends to inhibit cracking. This is further enhanced because the weight of the building increases the normal stress on this plane and hence the interface shear stresses. This is the converse of what happens in hogging.

The photographs in Figure 3.2 provide an example of the cracking within one of the affected load-bearing houses in the Althawra (19) Omdurman study area. The first picture (a) shows an external view of a vertical crack. Its width increases from bottom to top, indicating that the far end part of the house (left hand side) had settled, and the wall rotated anticlockwise. This is a very similar scenario to that shown in Figure 3.1c. There is a wastewater treatment tank (i.e., a septic tank), at the nearby corner of the building, just 2m from this crack, which is made from bricks and rendered with cement mortar. This is almost certainly the main source of the water leak. Photograph (b) shows an internal diagonal crack on the other side of the room facing the above-mentioned external crack. This indicates that this room is partially detached from the building because of collapse. Photograph (c) shows a close-up of one of the cracks and how it varies in width. The digital caliper used for measuring crack widths is shown in this picture where the crack width was about 32 mm.

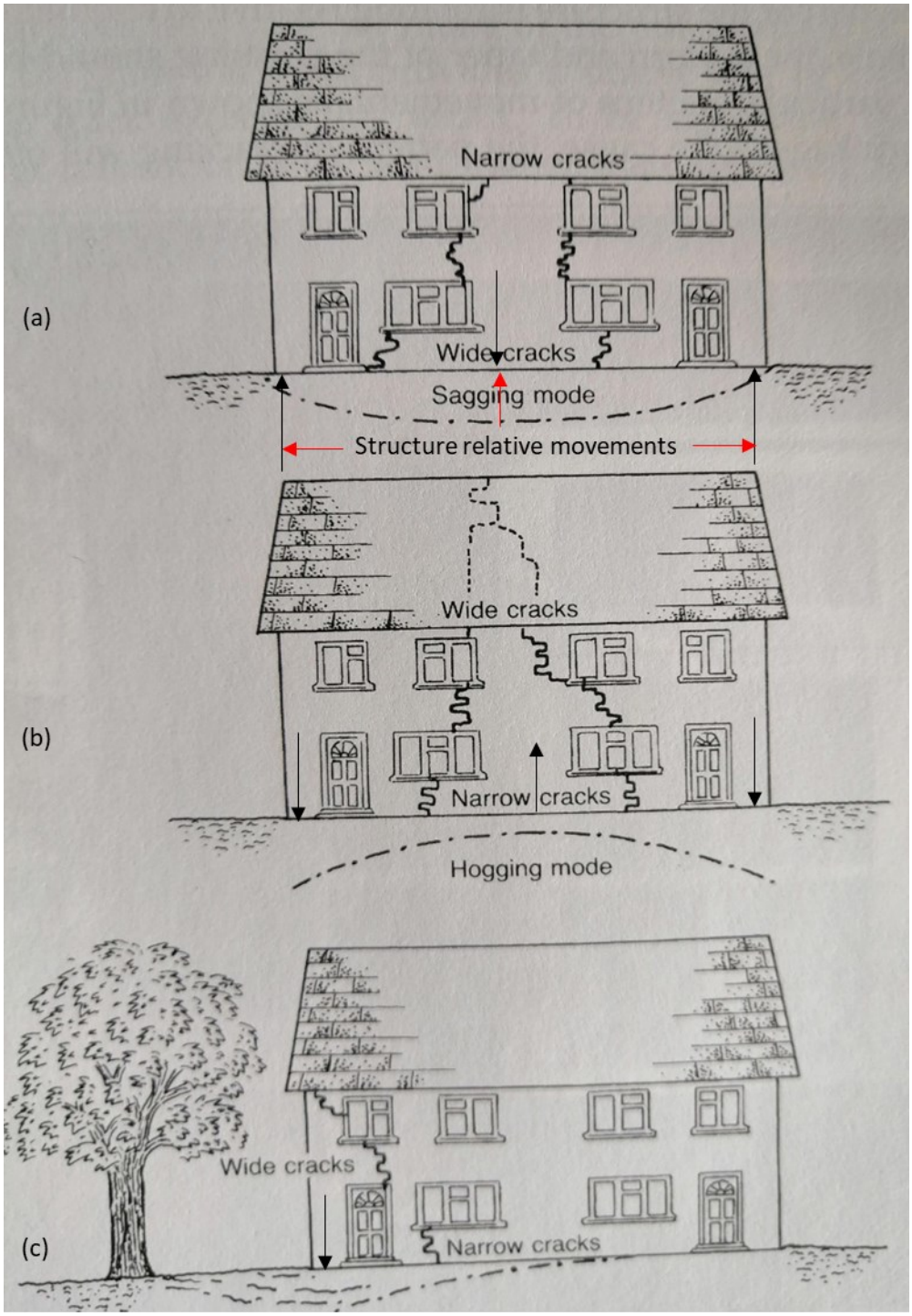


Figure 3.1: Different patterns of movement and cracking caused by subsidence and heave – after Freeman et al. (2002).

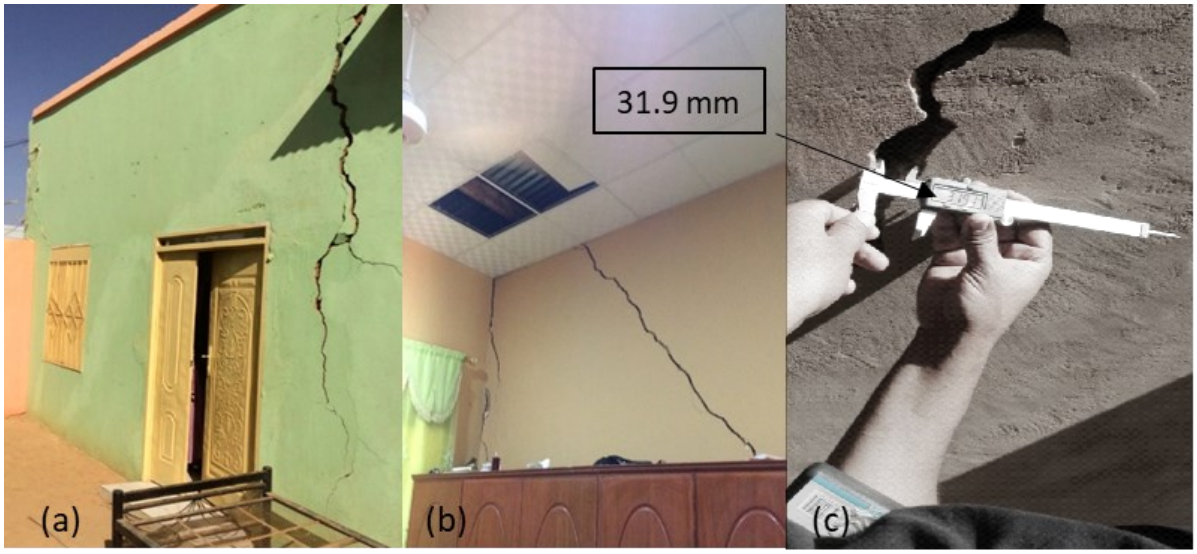


Figure 3.2: Crack patterns in the the buldings at the Althawra (19) study area

In general, the crack patterns in Figure 3.2 are similar to these shown schematically in Figure 3.1b and c which indicates that cracks in the study area are due to ground subsidence because of soil collapse. These cracks are commonly wide at the top and narrow at the bottom, suggesting a hogging mode of deformation. However, in some cases, collapse happened midway along some houses leading to a sagging mode of deformation with cracks narrow at the top and wide at the base.

3.2.2.2 Soil permeability

Soil permeability in this unsaturated open gravelly soil is very high (it can be classified as a free draining medium because of the gravel). The amount of gravel in this soil is up to 70 % as is discussed in Section 3.4.1, thus creating a very permeable fabric. Gravel contents of more than 50% increase fabric permeability markedly as shown in Figure 3.3. In this figure, results from hydraulic conductivity tests on a silty clay (CL) of glacial origin mixed with three gravel groups ranging between 2mm and 18.75mm in 10% increments from 10 to 70% gravel by weight are presented. The tests were performed on specimens compacted at 95% of the maximum dry density and at optimum water content $\pm 2\%$. At gravel contents above 40%, the hydraulic conductivity increased from about 10^{-9} m/s (10^{-7}cm/s) to level off at about 10^{-4} m/s (10^{-2}cm/s) up to about 60% gravel, beyond which there was little change.

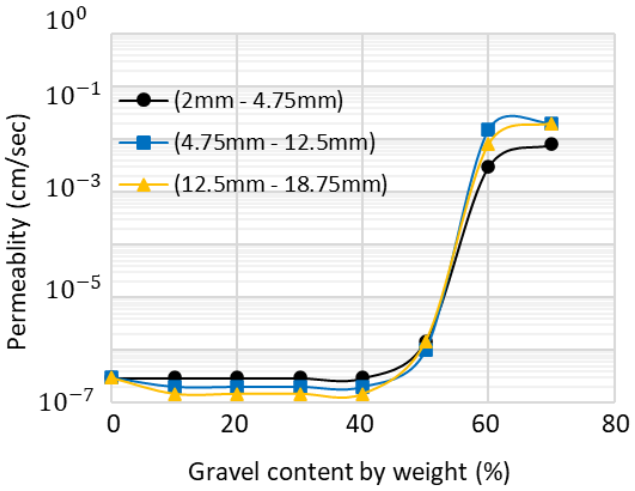


Figure 3.3: Effect of gravel content on hydraulic conductivity of a silty clay soil (Shakoor and Cook, 1990)

To assess the grading of the natural gravel, a Füller grading curve is plotted in Figure 3.4 using Equation 3.1. The $D_{\max}$ value used in this equation is 37.5 mm with different $D_{\min}$ values of 0.0075, 0.075, and 0.75 mm. The resulting curves are not markedly different with the different values of $D_{\min}$. They are concave and to the right of the natural grading curves. This indicates that the natural gravel gradings are over-filled with fines (Vaughan, 2006) instead of under-filled with a lack of fines and high contact stresses as might be expected. This empirical equation underestimates the assessment of this highly permeable fabric which readily allows water to percolate through it under gravity as was observed in the field.

$$D_x = \left[\frac{x}{100} + (1 - \frac{x}{100})(\frac{D_{\min}}{D_{\max}})^{1/2}\right]^2 * D_{\max} \qquad (3.1)$$

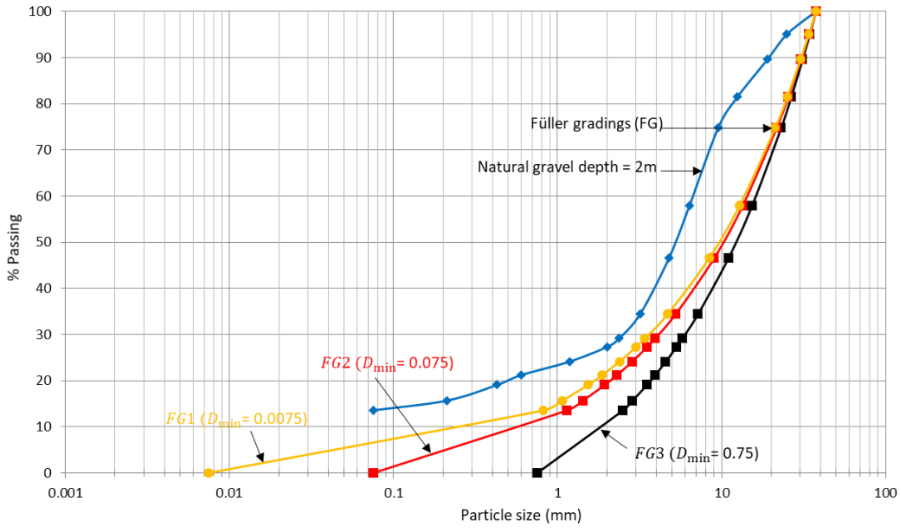


Figure 3.4: Füller grading curves for the natural gravel

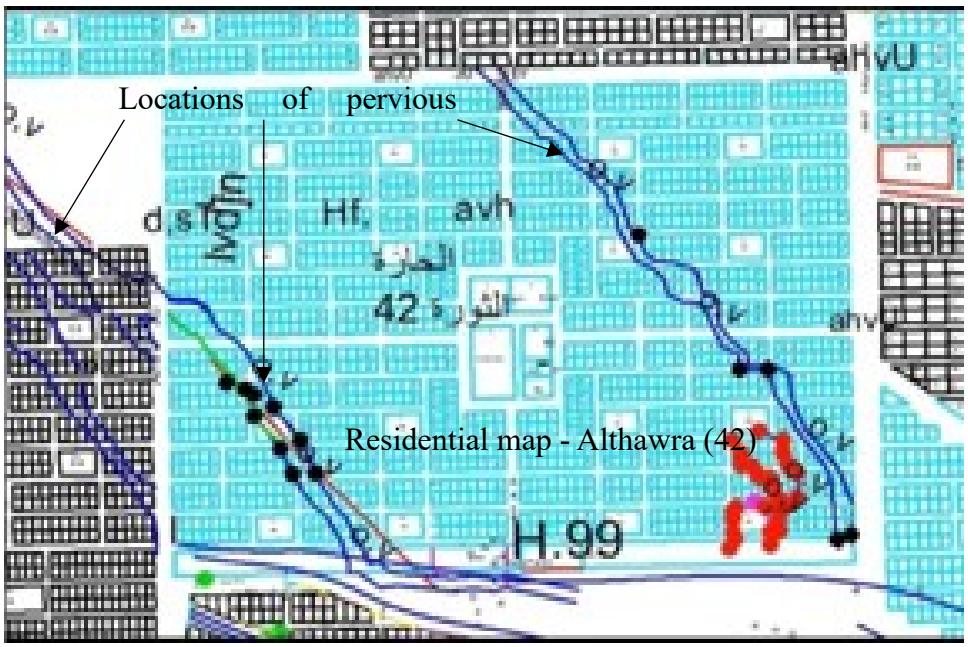


Figure 3.5: The urbanisation expansion interrupts natural water drains – Althawra (42)

3.2.2.3 Water sources

The main sources of water leading to collapse in this area are as follows (1) seasonal rainfall, most of the cracks in houses appear in the rainy season. A particular problem is that rainfall water runoff is, in many cases, redirected from its natural route by the construction of new houses as shown in Figure 3.5 (Seedahmed, (2021). Also, there is no local drainage system for the rainfall water to drain to and so the water ponds around houses and percolates beneath their foundations. (2) In some locations, local people planted gardens around their houses without any sort of water barrier or isolation, leading to uncontrollable and consequently water leakage under the foundations from watering the garden plants. (3) There are two common wastewater disposal systems: deep wells and surface soaking filters. The deep wells take the wastewater to the ground water without leakage issues in many cases, but this leads to serious health implications by allowing wastewater to mix with the ground water. However, surface filters are implemented in most of the houses, through which the wastewater is passed with the effluent draining into very shallow depths. (4) Other water sources such as from improper water usage and disposal in markets and industrial areas. Figure 3.6 shows an example of improper water usage and the consequent damage caused by this. A two-storey building (Figure 3.6a) constructed on reinforced concrete isolated footings was located less than 100 m away from a car-washing unit (Figure 3.6b). It is evident from Figure 3.3a that this building was severely damaged. This photograph was taken in January 2018. By the time a second visit was made in January 2019, the building had party collapsed and it was subsequently totally demolished.



Figure 3.6: Example for improper water usage leading to a two-storey building collapse

3.2.2.4 Types of foundations in the study area

There are two common types of foundations in the study area as illustrated in Figure 3.7. Strip foundations (Figure 3.7a) are usually used to support load-bearing walls of houses and isolated pads (Figure 3.7b) support load-bearing columns in reinforced concrete frame structures. These two types of foundation are constructed in different ways as explained below.

Strip foundations are usually constructed to carry the direct loads from a building's walls with the strip footings taking the shape of the rooms. The construction of strip foundations starts by digging a trench of width between 60 to 80 cm and depth between 80 to 120 cm (Figure 3.8a). Figure 3.8b shows an example of the strip foundation type used in the study area. The base (0.5 to 0.8 m) of the trench is filled with natural/crushed sandstones from nearby mountains as explained in Figure 3.9 (shows part of an old partly demolished strip footing), their sizes are usually up to about 30cm, and they are compacted in layers. Any gaps between these stones in each layer are filled with dry sand and distributed by adding water followed by more sand until all the gaps are filled before starting the next layer. The top of the final layer is levelled with a thin layer of sand-cement mortar.

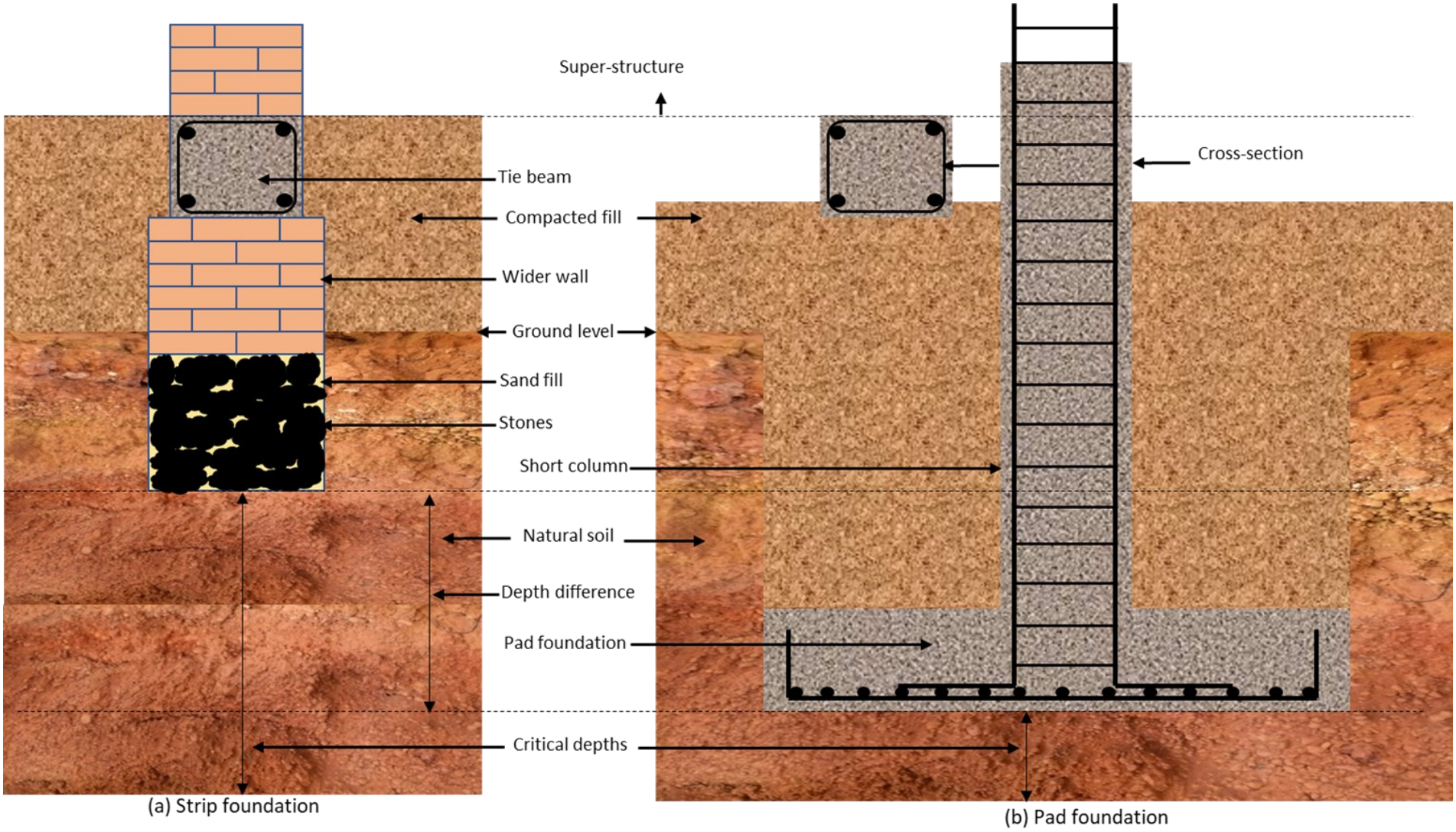


Figure 3.7: Schematic diagram for the foundation types in the study area

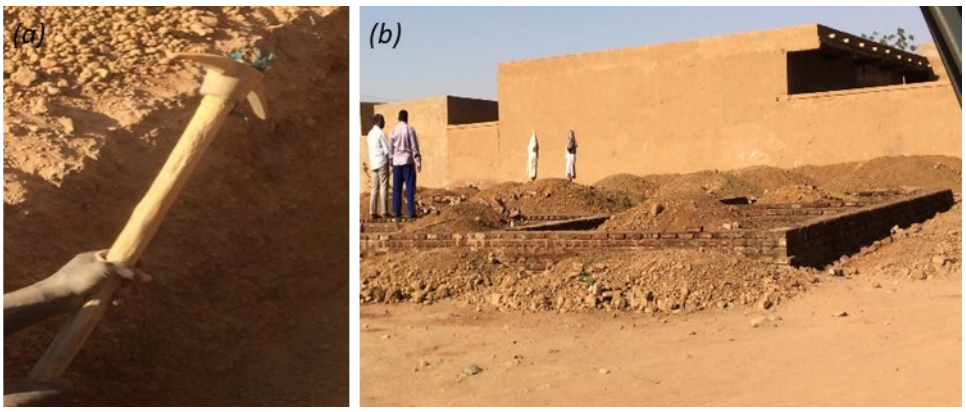


Figure 3.8: Strip foundation type in the study area

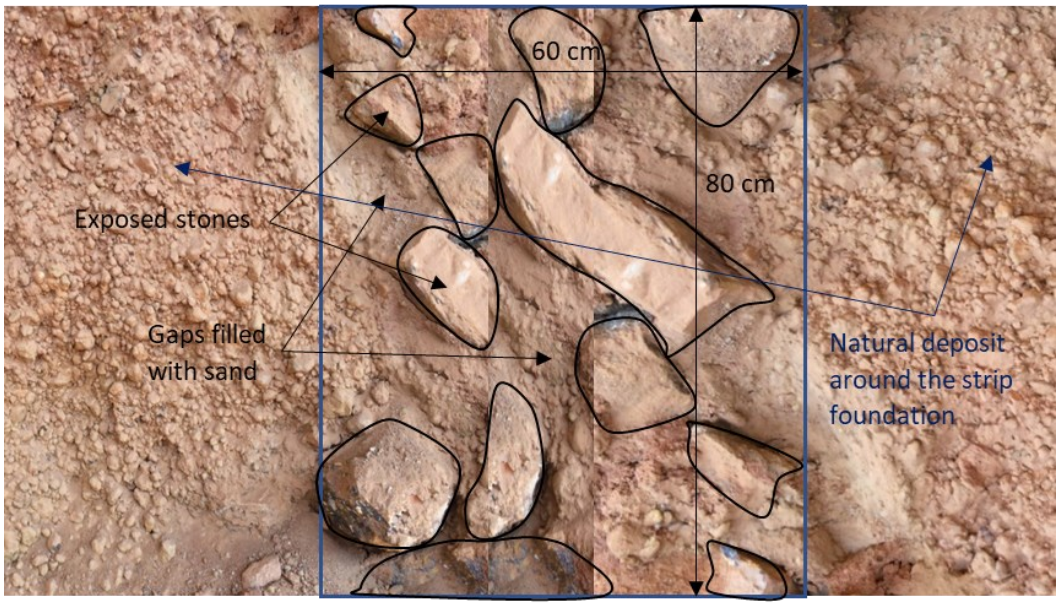


Figure 3.9: Using stones and sands in the construction of strip foundations – an old strip foundation in the study area

Above these stones a wider lower level of bricks creating a wall of about 42 cm width (length of two bricks (40 cm) including the mortar gap between them (2 cm)) is constructed using sand-cement mortar or clayey silt mortar. The height of this wider wall is about 0.5m above the natural ground and provides a reasonable height above the street level along water often drains. The volume above the ground within the building, beside the strip foundation due the 0.5m height, is filled with a compacted fill followed by an unreinforced concrete layer of about 10 cm thickness. Next, construction of the super-structure can start by casting a reinforced grade beam or tie beam centrally over this strip foundation (just below the unreinforced concrete layer), with the same width as the super-structure wall to increase the global stability of

structure. The width of this beam is typically about 32 cm which is equal to the super-structure walls (1.5 length of bricks (30cm) plus the mortar gap (2 cm)). After this beam, construction of the super-structure can start.

The demolished strip foundation in the photograph in Figure 3.9 was subsequently replaced by a new reinforced concrete frame structure as shown in Figure 3.10b. The large gaps between stones seen in Figure 3.9 resulted from particles being removed by the digging process. It can be seen that the natural soil fabric around the strip footing is very open, loose and dry which is probably prone to flooding collapse and allows to the strip footing to deform laterally and vertically.

The second foundation type is isolated reinforced concrete pad footings. This system is usually founded deeper than the strip footing, having an average depth of about 1.5m and square cross-section of 1.5*1.5 m^2 (Figure 3.10a). The average thickness of these reinforced footings is about 40 cm. Above them, short columns are cast to a height of 0.5 m to 1.0 m above the ground surface for the same reason described for the strip foundation. A reinforced concrete beam system tying/connecting the short columns together or a suspended slab system or a combination of the two is constructed following by the super-structure as shown in Figure 3.6b. This type of foundation is more resistant to collapse settlement than the strip foundation system, although some of buildings constructed using isolated footings system have been affected by collapse as shown in Figure 2.26. In such cases it is usually the walls built between the reinforced concrete structural members that suffer damage.

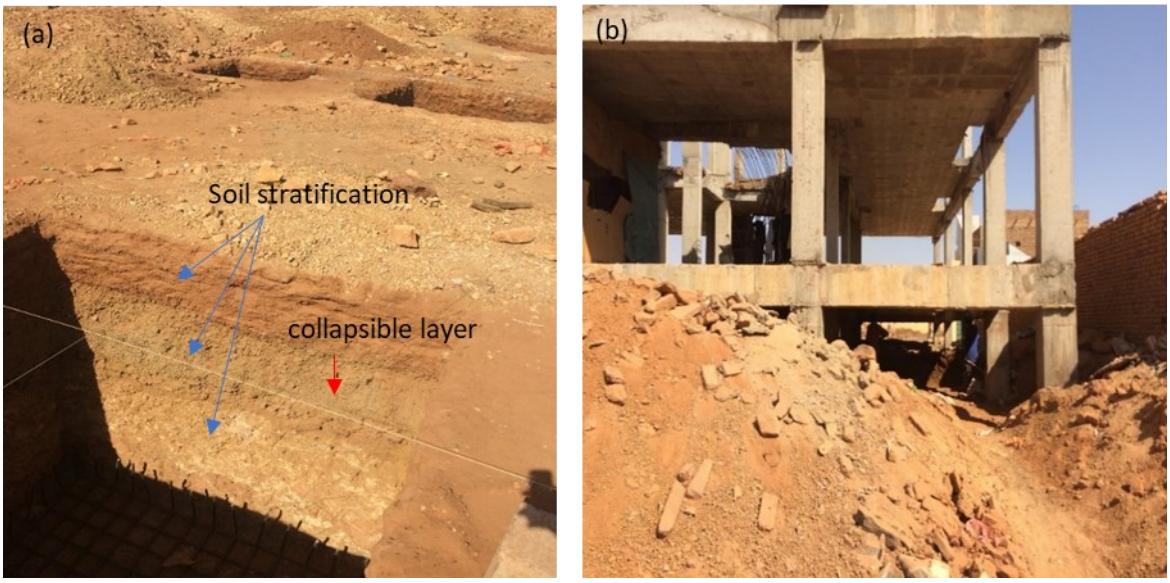


Figure 3.10: Isolated pad footings system in the study area

Figure 3.10a is intended to illustrate of the process of constructing the reinforced isolated pad footings. It also shows the soil profile located outside the study area (the location in Figure 3.10b) in the southwest of the Merkhiyat mountains while the study area east of these mountains, towards the Nile River, is described in Section 2.2.6.1. In contrast with the study area, the collapsible layer is located at a shallower depth (as evident in Figure 3.10a) than at the study area.

3.2.2.5 Soil fabric description in the study area

Physical examinations on site revealed that although the stratification systems in the North and the South of the study area look quite different, they are in fact very related. Towards the South, the fines content increases which is very clear in the first 1m and decreases with depth while the gravel content increases toward the hard formation at about 3m depth as explained in Section 2.2.5.

The photographs in Figure 3.11 provide examples of the differences in appearance between the soil fabrics in the study area from North to South. The soil fabric in the North (Figure 3.11a) is more open and fragile and contains a higher content of gravel than in the South (Figure 3.11b) because in the South the soil contains more fines and less gravel, making the soil fabric less fragile than in the North. However, the layers (stratification) in these two profiles are very similar as both contain higher fines in first 80 cm and more gravel after the first 1m depth as shown in Figures 3.11a and b. However, the soil profile shown in Figure 3.11a is weaker and has an open fabric which is likely to be collapsible and has led to the damage seen in the study area. Therefore, this profile found in the North of the study area is the focus of the following discussion.

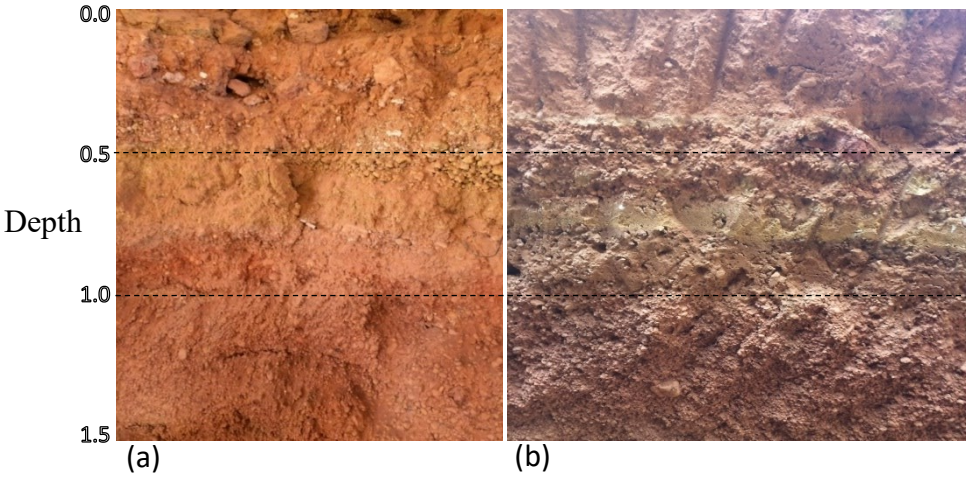


Figure 3.11: Soil profiles in two different parts: (a) North the steady area (b) South the study area

If the spatial variability of the soil strength is considered in this soil as clearly shown in Figure 3.11, the soil bearing capacities under the foundations (strip or pad footings) in the study area would be different depending on the location in the study area. Consequently, the collapse potential under these foundations is different as well and depending on the location. An interesting work on the effect of spatial variability on bearing capacity and the soil deformation around the foundation is given by Wu et al. (2020) while Chwala (2020) proposed a novel method for assessing foundation bearing capacity on spatially variable soil properties. Therefore, a new means of understanding and measuring collapse in 3-D for this type of soil is required.

3.2.2.6 Collapsible soil fabric in the study area

Figure 3.12, an enlarged section of Figure 3.11a, shows a typical soil profile to demonstrate the collapsible nature of soil fabric in the study area. This profile was dug for the foundation construction of a new house (Figure 3.10b) in the study area where many of the houses in the neighbourhood have been severely affected by collapse settlement. In view of this it was decided to build a rigid concrete frame structure as shown in Figure 3.10b. The soil stratification in this profile is very clear and straightforward to explain. The first 1m includes different sublayers: made ground, a gravel band (sandwich) and silty sand with different thicknesses ranging from 0.5 m to 1.0 m which might not all be present, depending on the location within the study area. These are underlain by a thick gravelly soil layer with thicknesses of 1 m to 2 m. This layer is designated as a collapsible layer by Osman and Ahmed (2015) and is the primary focus of the following sections. It is in turn underlain by the hard Nubian Formation (described in Section 2.2.5).

The most probable reason for this gravelly layer being very weak, loose and honeycombed is that the gravels partly resisted the subsequent deposition process of fines including the sands evident in the upper layers as shown in Figure 3.12. Only clay and very fine silt filtered down through this layer by water during the depositional process leading to the gravel particles being coated by clay and silt and a small amount of sand. The Author inundated some parts of this gravelly layer and observed that the fines were easily washed by water and left the gravel clean. This indicates that the bond between gravel particles is weak and sensitive to water. Therefore, this provides in-situ evidence that this fabric has the potential to decrease in volume if inundated with water, especially when new foundation stresses are applied. This can lead to excessive differential settlements in the foundations as shown in Figure 3.13b.

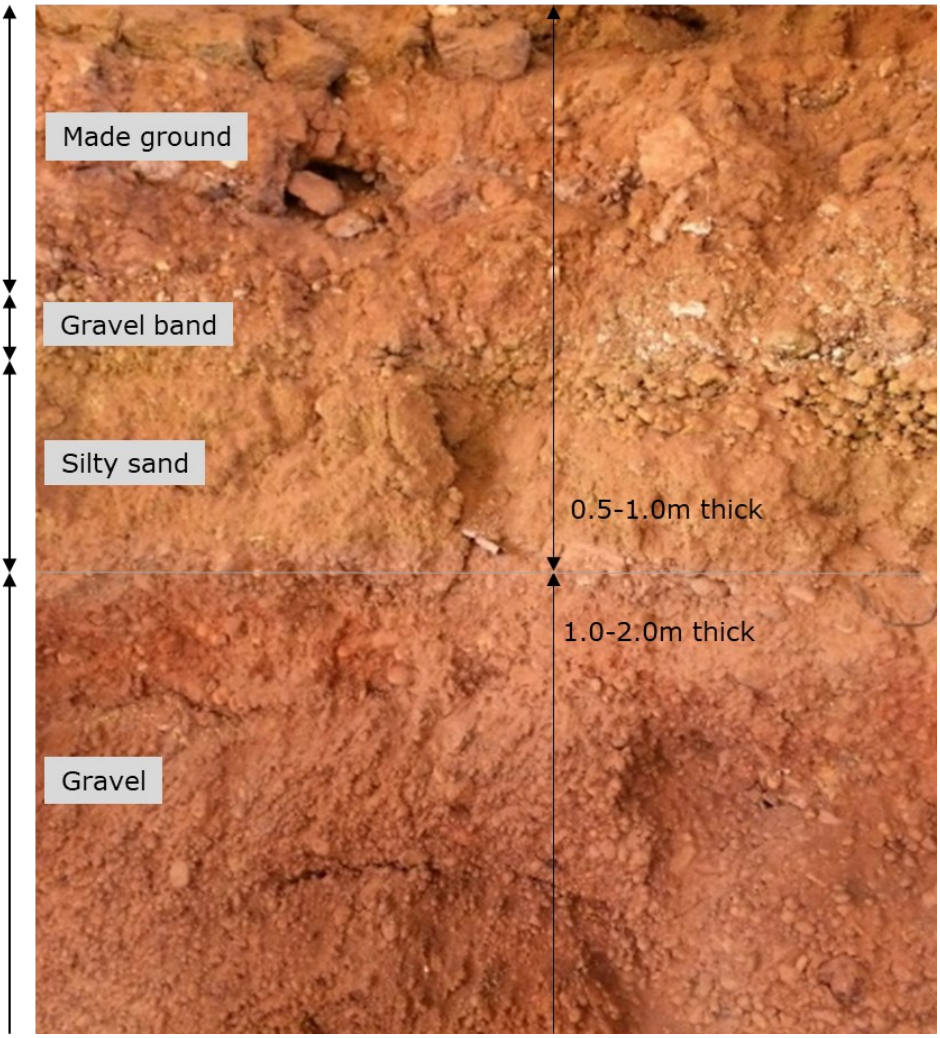


Figure 3.12: A typical collapsible soil profile in the study area

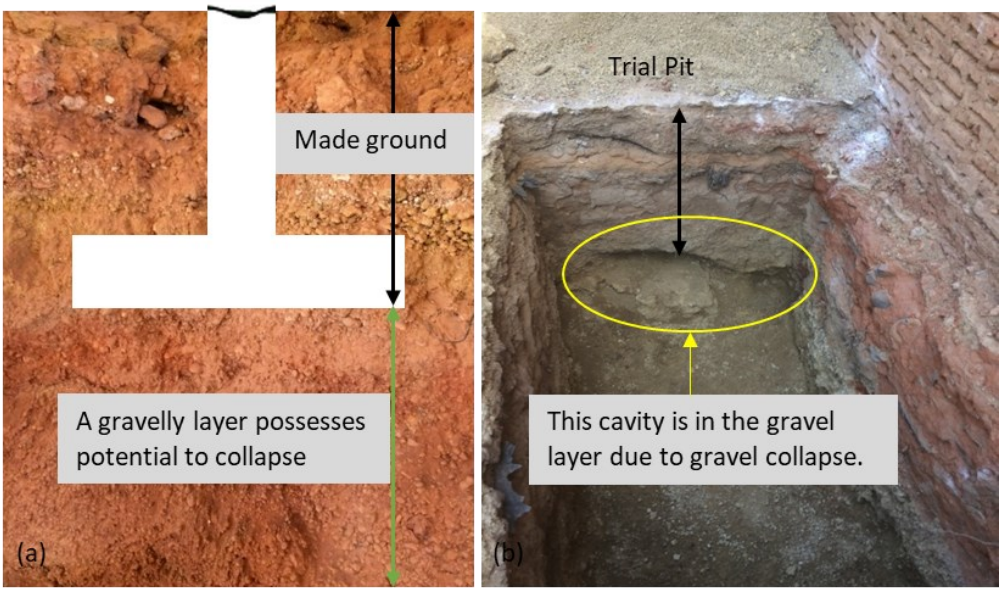


Figure 3.13: A typical soil collapse observed in the field in the study area

In practice, many building foundations were constructed above this weak gravelly layer in dry conditions, as illustrated by the schematic foundation in Figure 3.13a which depicts a hypothetical foundation located on the top of this weak gravelly layer. In these dry conditions the soil appears, misleadingly, to be strong during the digging process, conveying the wrong message to the local contractors. Actually, the soil is only strong in the dry condition, once this layer is wetted under the newly applied building stresses, it starts to settle due to collapse as illustrated in Figure 3.14. This hypothetical situation was exemplified when an investigation pit was excavated beside a strip footing of one of the affected buildings as shown in Figure 3.13b. Two main things can be observed: first, the actual location of this strip footing is just above the gravelly layer; second, the gravelly layer was largely washed away by the water flow.

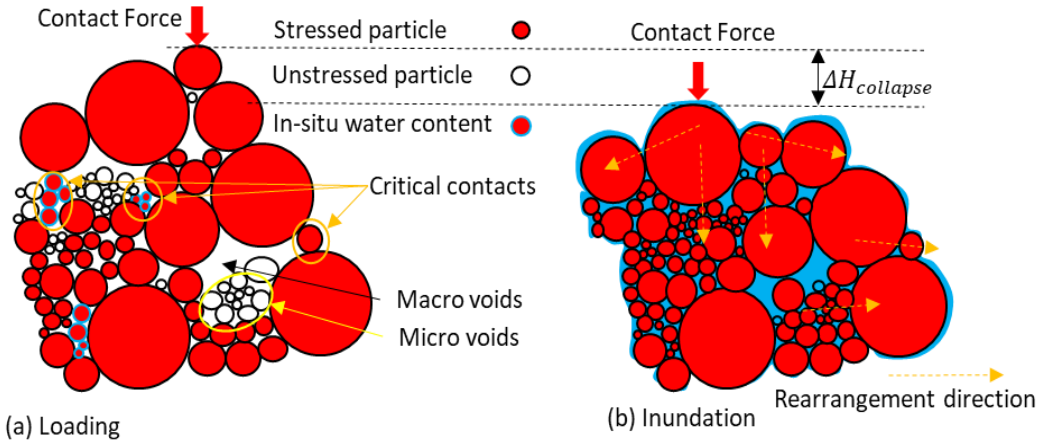


Figure 3.14: Schematic diagram to explain collapse in the gravelly soil

3.2.2.7 Summary of the field observations

In summary, there are real soil collapse issues in the study area as explained in the above discussion, but the magnitude and mechanisms of collapse are not well quantified or understood. Collapse in this gravelly layer is anecdotal and needs to be verified by experimental investigation. However, there is a serious limitation in that the weakness of the fabric makes the process of taking undisturbed samples for an experimental study not practicably feasible. This conclusion was also drawn by Osman (2015). The following section details the attempts made at taking representative samples.

3.3 Sampling process

The coordinates of the location of the collected samples are as follows (Coordinates, WG1984 ellipsoid zone 36 North): N 0446408, E 1737440.

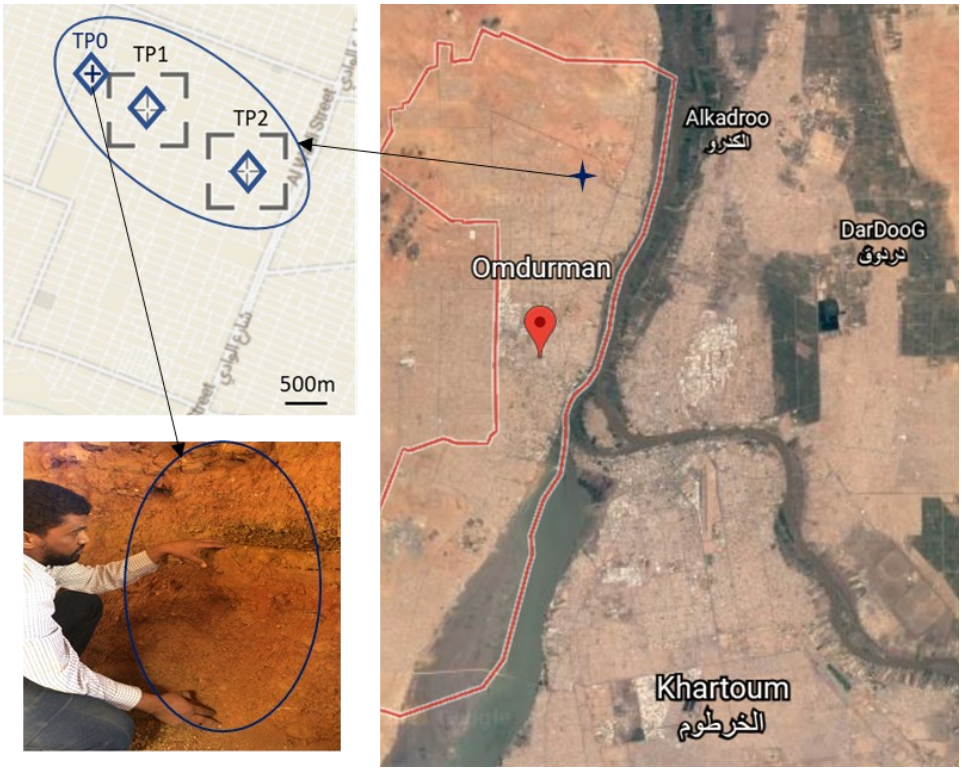


Figure 3.15: Location of the samples collected (TP0)

At this location the gravel content and the resulting fragile fabric would not tolerate any cutting tool action which destroyed most of the fabric during the cutting process. Figure 3.15 shows the location of soil profile where disturbed samples were taken vertically every 1.0 m. The made ground was avoided in this sampling procedure.



Figure 3.16: Disturbed samples including some cemented soil aggregation

Occasional undisturbed cemented soil aggregations were found but only rarely, examples of disturbed samples and the aggregations are shown in Figure 3.16. Unfortunately, these

aggregations are not representative soil samples because they are stiffer and denser than the surrounding soil and more strongly cemented due to their higher percentages of iron oxide. Disturbed samples and some of these soil aggregations were collected from different depths and shipped to the UK.

There was one successful attempt at taking an undisturbed block from the bottom of this pit by waxing it before cutting process as shown in Figure 3.17 but, unfortunately, this sample was found to be solidified when it was opened with most of it being strongly cemented as shown in Figure 3.18.



Figure 3.17: Collecting of an undisturbed soil block

The purpose of this soil block was to study the nature of the bonding between the gravel and other particles and macro voids of this fabric. Unfortunately, after being transported and opened, this fabric was very strong and not representative of the in-situ collapsible fabric. Figure 3.18 shows the biggest part of this soil block after being struck by a hammer. Surprisingly, the hammer blow fractured some of the gravel particles, as shown in black colour in Figure 3.18, while the bond between the particles remained intact and stable. This soil aggregation was soaked in water to see the effect of water on its bonds, but it remained intact and stable. Even the water in the vessel in which it was submerged remained clean indicating that there were no fine particles that became detached, but rather they were firmly bonded together as well. The process of forming this material is still not clear and needs investigation. This fabric was relatively too large to be scanned to investigate the bond nature but XRD

analyses on both the gravel particles and clay fines were conducted to identify the minerals present (described in Section 3.4.3).

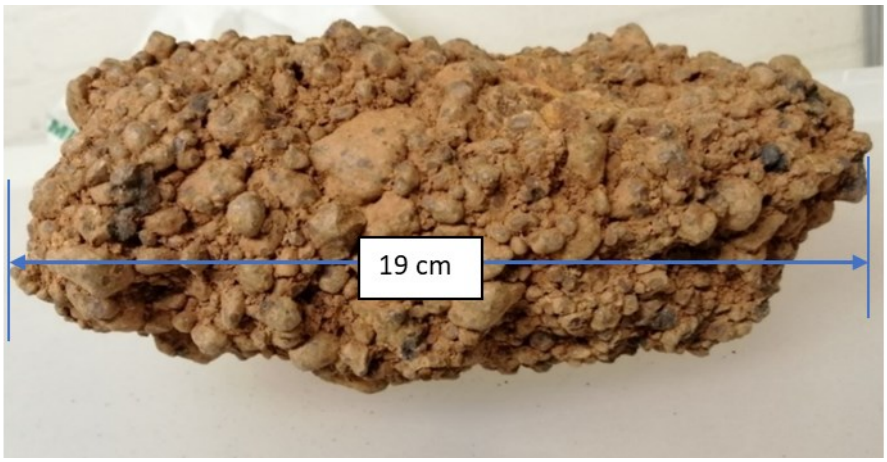


Figure 3.18: Soil aggregation after solidification

3.4 Soil characterisation

In this section, soil characterisation from the collected samples is discussed in conjunction with comparable parts of Hamid's (2012) data which are comprehensive and useful, particularly the density data given in Table 2.5. These are used in the collapse estimation using the newly developed equation discussed in Section 3.6.2.2.

3.4.1 Particle size distribution

Figure 3.19 shows the particle distribution curves for the coarse particles (retained in the sieve with 0.075 mm openings) from the collected samples. The gravel content represents around 70% on average and its uniformity (C_u) and curvature (C_c) coefficients are relatively high, C_u is more than 100 and C_c is more than 11. These coefficients are discussed in Section 3.5. These three PSD curves were plotted in green with Hamid's curves for comparison as shown in Figure 3.20.

Figure 3.20 shows that these three curves are very similar to Hamid's curves that were produced from TP1 and TP2. However, it seems that the gravel content in TP1 and TP2 is less, ranging from 45% to 75%. Gravels sieved in ICL are coarser and closer in size to those from TP1 compared with TP2. The location of the collected samples is near to TP1, and both of these locations are to the west of TP2 as shown Figure 3.15. This coarser distribution correlates with the hypothesis concerning the depositional process discussed in Section 2.2.6.1 in which the

coarser gravels would be deposited first in any runoff from the Merkhiyat mountains to the west.

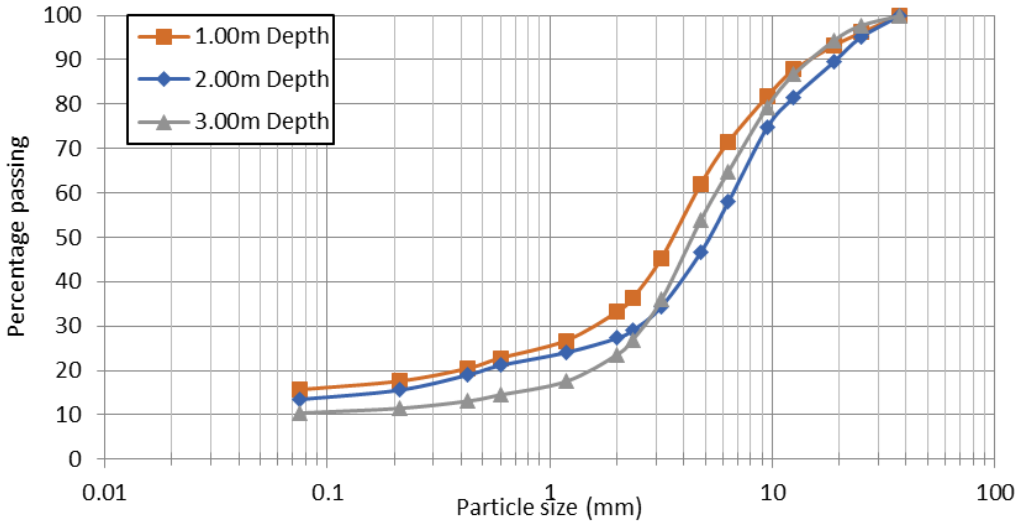


Figure 3.19: Particle size distribution for the collected samples

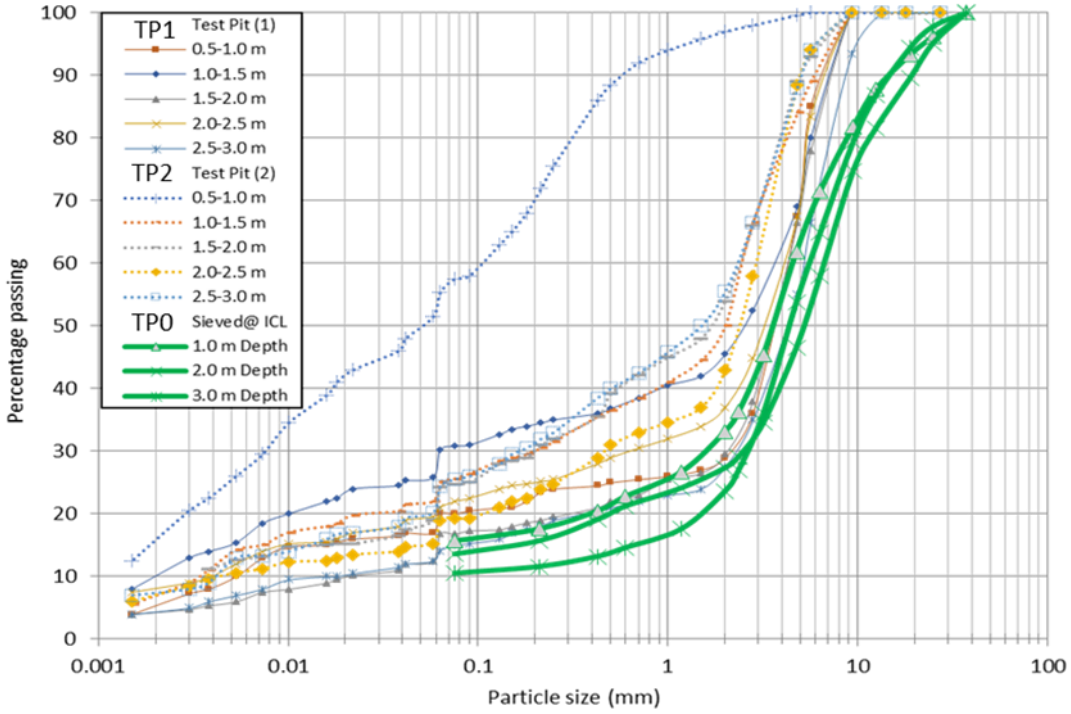
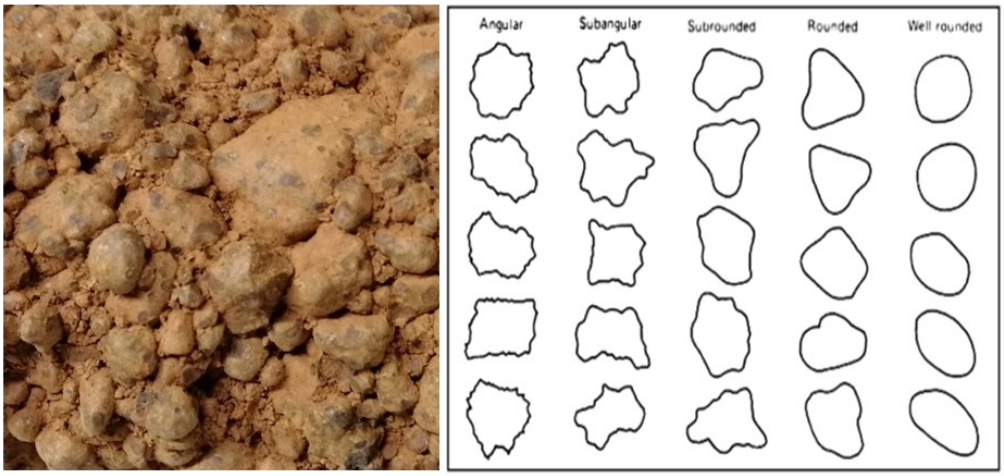


Figure 3.20: Particle Size Distribution curves for three different locations in the study area

3.4.2 Gravel shape and density

It can be seen visually in Figure 3.21a that the gravel shape in the study area varies between rounded to well rounded. This description is based on that given by Mitchell and Soga (2005)

as shown in Figure 3.21b. The specific gravity of this gravel, determined according to BS 1377-2: 1990, ranges from 2.71 to 2.79 which is similar to the values given by Hamid in Table 2.5. The average minimum density for this gravel is 1.61 t/m^3 determined according to BS 1377-4: 1990.



(a) Natural gravel in the study area (b) Mitchell and Soga (2005)

Figure 3.21: Description of the gravel shape

3.4.3 Soil mineral characterisation

Identification of minerals content was important to help understand nature of the bonds and to establish those dominant in the fine particles which needed to be considered in analogue collapsible specimens as discussed in Section 4.3. The X-ray Diffraction Analysis (XRD) described in this section was used to identify the chemical composition of both the gravel and fines components of this soil.

A semi-quantitative XRD analysis was conducted by the company PETROCLAYS on a representative sample from the collected samples. The following sub-section are summarised from a report provided by PETROCLAYS.

3.4.3.1 X-ray diffraction analysis

Test description

For the clay fraction analysis, the fines soil sample was gently disaggregated, placed in distilled water and placed in an ultrasonic bath for 20 minutes to form a clay suspension. The suspension was then centrifuged (1000 revolutions/minute for 4 minutes) to leave only the < 2µm fraction in solution. The clay suspension was then centrifuged to deposit the entire < 2µm fraction,

which was filtered (mixed with a little distilled water to make a thick slurry) onto an unglazed ceramic tile.

The sample was scanned with a Siemens PSD X-ray diffractometer using Ni-filtered CuKa radiation. The clay tile was scanned using a 0.02° step width, with 0.2 mm slits from 2 to 40° 2q. The tile was scanned again after treating with glycol, after heating at 400°C for 4 hours, and after heating at 550°*C*, also for 4 hours. Figure 3.22 shows the results: clay data is in red = air-dried, light blue = glycol solvated, green = heated 400°*C*, dark blue = heated 550°*C*.

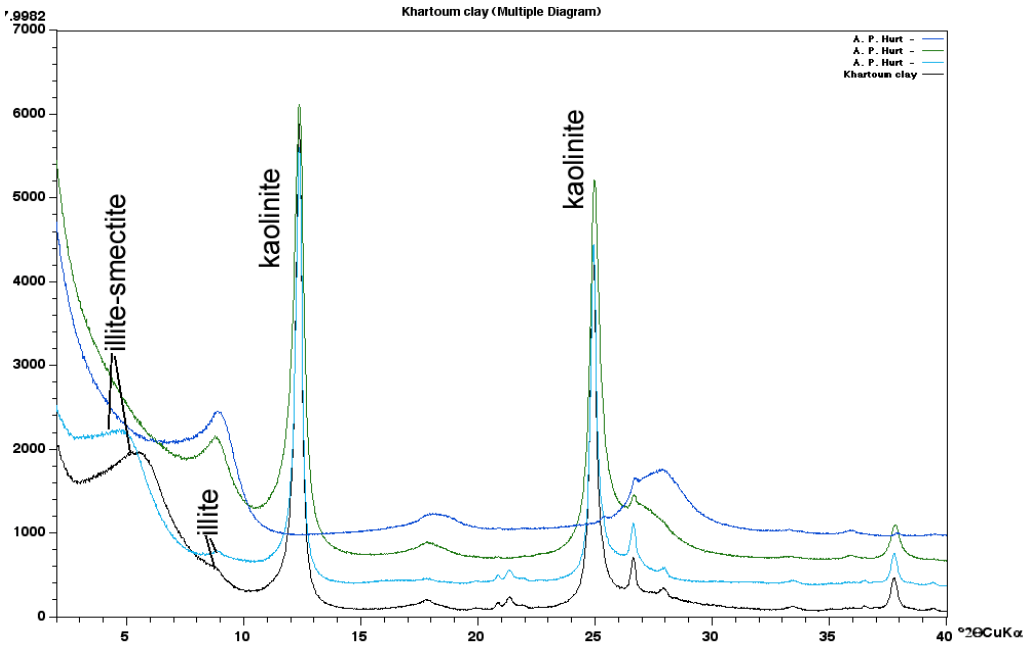


Figure 3.22: Clay fraction X-ray diffractometer scanning using Ni-filtered CuKa radiation

The data have been quantified using Macdiff to deconvolute and measure peak areas. Clays are identified on XRD traces on the basis of the positions of their basal lattice reflections. Reflections used for quantification are ideally free from interference from other mineral reflections, but where this is not possible Macdiff may be used to deconvolute the reflections. Illite is identified from and measured using the reflection at 10*Å* (~9°2 *Θ*), kaolinite with the reflection at 3.57*Å* (~24.8°2*Θ*). The illite-smectite reflections shift to a lower angle after glycol solvation, the amount of shift depends upon the relative proportions of illite (non-expanding) interlayers. The reflection between 15.6*Å* (15.7°2 *Θ*) and 5.1*Å* (17.5°2 *Θ*) are used to estimate the percentage of illite in the illite-smectite. In this sample suite all illite-smectite has 50% smectite layers.

Regarding the gravel content, a portion of sample was ground to a powder in a McCrone micronising mill with the addition of acetone to minimise structural damage to the minerals present. The resulting sample was dried and lightly ground so that the powder could be side-packed into an XRD powder holder and scanned, as shown in Figure 3.23, on at a rate of 5 seconds per 0.02° step width, using 0.3 mm slits from 5 to 70° 2*q*, on a Siemens PSD X-ray diffractometer using Ni-filtered CuKa radiation.

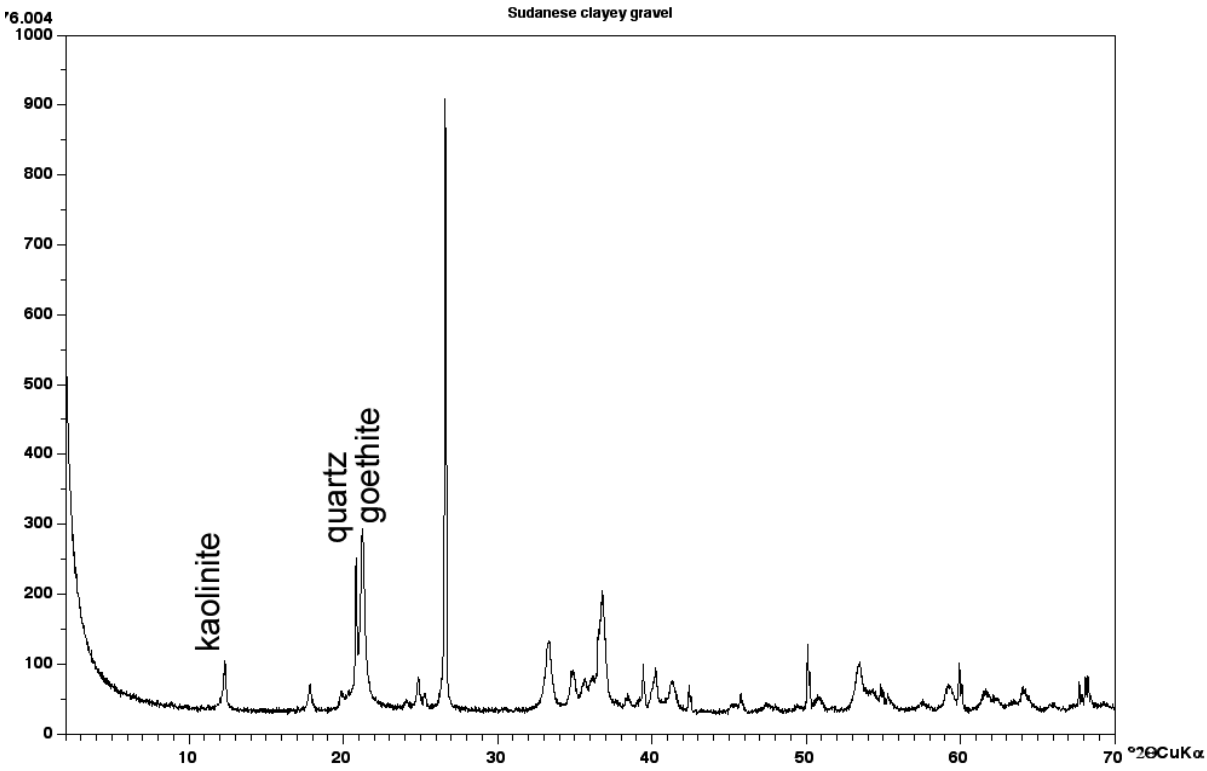


Figure 3.23: Gravel powder X-ray diffractometer scanning using Ni-filtered CuKa radiation

XRD results

The results are shown in Tables 3.1 and 3.2. The relative proportions of each clay mineral are calculated by weighting the area of the chosen mineral reflection by a factor (mineral intensity factor) determined from the measurement of known mixtures of the appropriate minerals and normalizing the results. Table 3.1 shows that the gravel powder contains Kaolinite, Quartz and Goethite and Table 3.2 shows that the clay fraction contains Illite, Smectite and Kaolinite.

The clay fraction has the major contribution on the bonds between the coarse particles. The XRD results indicate that the mineral composition of the clay fraction is complicated as it contains 67% of a combination of Illite-Smectite together in equal amounts. The Kaolinite content is 29% and Illite is least with only 4%.

Table 3.1: Semi-quantitative XRD analysis for gravel powder

Mineral composition	Kaolinite	Quartz	Goethite
Percentage (%)	23	66	11

Table 3.2: Semi-quantitative XRD analysis for the clay fraction

Mineral composition	Illite	Illite-Smectite	Kaolinite	(Illite in Illite-Smectite)
Percentage (%)	4	67	29	(50%)

3.5 Soil classification

The following soil classification is according to the Unified Soil Classification System (USCS), ASTM D2487-06. This classification has mainly been applied on the coarse fraction because it represents the dominant element of the soil particles. To identify the degree of soil gradation, there are two grading coefficients, depending on specific proportions that relate to specific particle sizes (D_{10}, D_{30} and D_{60}), that have to be quantified. First, the uniformity coefficient C_u, Equation (3.2), is defined as the ratio of D_{60} to D_{10}. The coefficient of curvature is C_c is given by Equation (3.3). For a well graded soil, according to the USCS, both C_u and C_c should satisfy the following: $C_u > 6$ and C_c should be $1< C_c <3$ otherwise the soil can be considered to be poorly (or uniformly) graded.

$$C_U = \frac{D_{60}}{D_{10}} \tag{3.2}$$

$$C_C = \frac{D_{30}^2}{D_{60} * D_{10}} \tag{3.3}$$

For the PSD curves of the Omdurman soils given in Figure 3.20, the values of the coefficients of uniformity (C_u) and curvature (C_c) range from 14 - 80 and 3-27 respectively. The higher values of C_u indicate that this soil contains a large range of particle sizes, and this is clear because grain sizes within these soils range from less than 0.075 mm up to 25 mm. Thus, the general description of the coarse fraction of these soils according to USCS is, GP, poorly graded gravel. Regarding the fine fraction of these soils, it is greater than 12% (range from 15 to 25%) so it has to considered in the classification according to the USCS. From the plasticity indices given by Hamid (2012) (see Table 2.5), most of these fine fractions can be classified as clayey fraction according to the USCS. In summary, the classification of the whole fraction of these soils according to the USCS is clayey gravel (GC).

3.6 Collapsibility of soils at the study area

3.6.1 Collapse from an in-situ plate load test

Details of the set-up of the in-situ plate load test conducted by Osman (2004) to measure the collapsibility of the gravelly soil, were given in Section 2.2.7.4. The results are summarised in Figure 3.24. In this test, the soil was inundated at collapse stress of 262 kPa (equivalent to the applied building stress). The plate settlement was measured every hour for 24 hr. The results are presented in Figure 3.24. The average total settlement reported by Osman (2004) was 1.5mm before inundation and 8.75 mm after 24 hr from the inundation as illustrated in Figure 3.24. Thus, collapse settlement after 24hr is 7.25 mm.

Although this test gives an indication of the collapsibility of this soil from flooding, this collapse settlement value was too small to cause the degree of damage shown in Figure 3.2 and that reported by Osman (2004) and Hamid (2012) in Section 2.2.6.2. Therefore, it seems that this plate load test was not a suitable tool for measuring collapse for this soil type.

Apart from the concern about the vertical displacement gauges measuring relative rather than absolute displacements, another potential reason for this small collapse settlement is that the stress developed from the plate did not propagate to sufficient depth to cover the complete profile of the collapsible layer. This is due to its relatively small square area of 50*50 cm^2 which led to a localised settlement under the plate and did not simulate the effect of the strip footing. In fact, greater settlement might have been expected because the plate influences the soil in 3-dimensions while the strip footing operates a 2-dimensional plane-strain mode. Another major limitation of this test is that it does not provide any link between soil properties such as particle size distribution, soil density and the distribution of measured settlement to help understand the reasons for the collapse settlement and the related collapse mechanism. Therefore, it is more beneficial to conduct experimental tests under controllable boundary conditions to overcover these limitations.

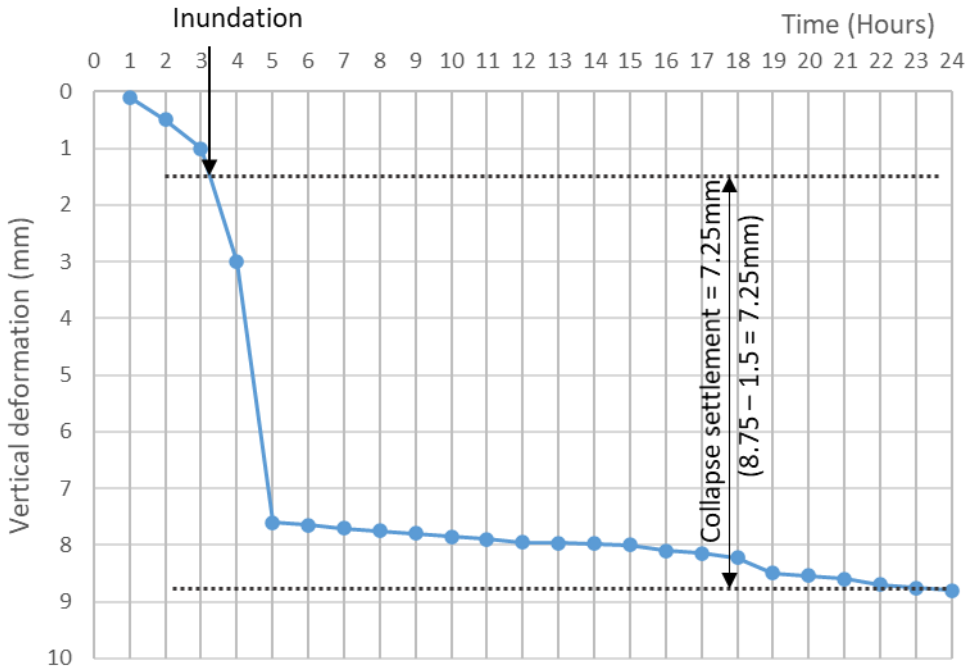


Figure 3.24: Plate load test results, after Osman (2004)

3.6.2 Estimating collapse from soil properties

3.6.2.1 Density and Liquid Limit

The idea of assessing collapse potential by plotting γ_{dry} against either natural water content or liquid limit, as proposed by Holtz and Hilf (1961) was introduced in Section 2.1.7. The liquid limit, natural water content and natural dry unit weight data compiled by Hamid (2012) are presented in this manner in Figure 3.25. The data were summarised in Table 2.5. The natural water content (NWC) of most samples is less than 10% while the liquid limit (LL) values for the clay fraction mostly range from 30% to 50% and natural dry unit weight are less than 20 kN/m^3. Therefore, their projection in Figure 3.25, indicates that all the water content and dry density values of the soil from the two trial pits (TP1 and TP2) are located above this curve and the liquid limit values are located below this curve. The location of the liquid limit values below this curve, according to Holtz and Hilf (1961) as discussed in Section 2.1.7, means that this soil is unlikely to be collapsible. The conclusion from this procedure does not agree with the summary of the field observations in Section 3.2.2.7, which there are real soil collapse issues. The reason for this contradiction is that there is a significant difference between the loess soil that considered by Holtz and Hilf (1961) and this gravelly soil.

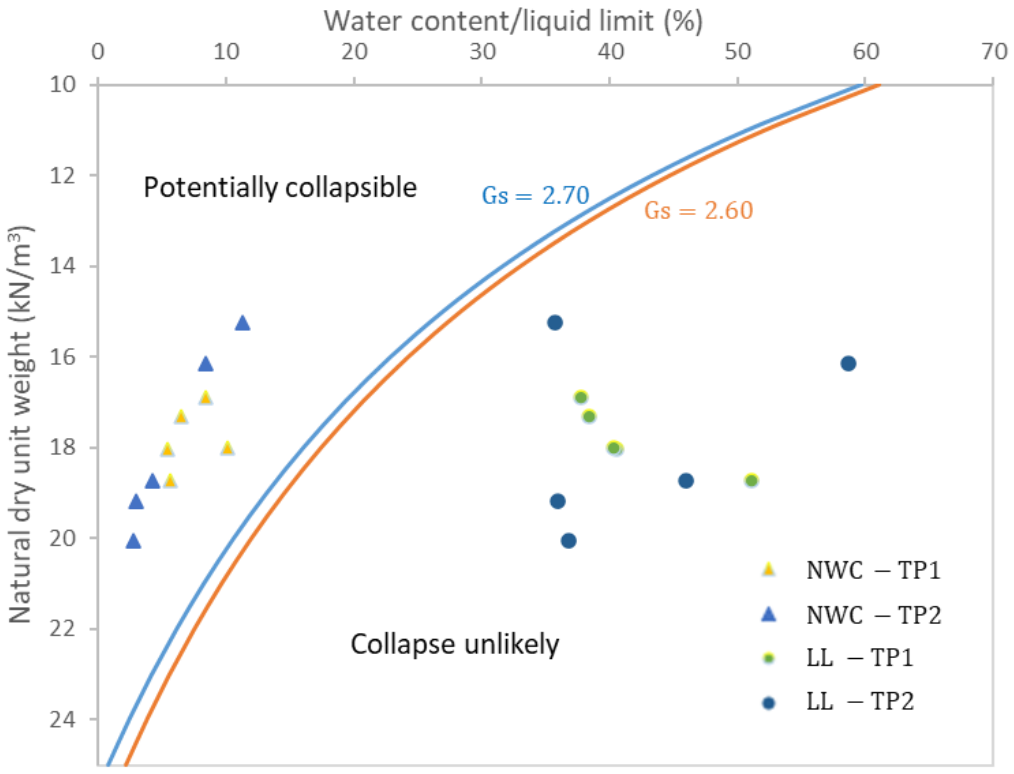


Figure 3.25: Natural dry density and moisture state, after Holtz and Hilf (1961) and Hamid (2012).

Other limitations of this procedure are that it gives only an indication for the collapse possibility, but it does not give any estimation for the magnitude of the collapse potential. Also, it does not necessarily mean that all soils which have water content and density values above this curve are collapsible soils.

3.6.2.2 Hypothetical method

A new hypothetical method for estimating collapsibility of soil based on its in-situ density is proposed in this section to obtain an initial understanding about the potential for collapse in this soil. Either the soil's void ratio or dry unit weight can be used in this method to estimate collapse. The *basic assumption* is that when a soil collapses it compacts from its natural state to its maximum modified compaction state. Consequently, the method approximates the collapse potential value based on the differences between the values of current void ratio or dry unit weight and the values corresponding to maximum compacted density.

The method does not consider the initial compression before inundation due to buildings-stresses. Although there are differences in the loading mechanism and water amount between the compaction test and collapse test, both lead to reduction in the volume of soil due to the decrease in the volume of voids.

This method can be formulated according to the basic assumption. This means that collapse potential can be approximated by the percentage of the change in the dry unit weight between a soil's natural state and the maximum dry density obtained from modified compaction. Consequently, Equation 3.4 is derived which shows the relation between collapse potential and these two dry unit weights, the natural dry unit weight and the maximum dry unit weight. Both unit weights can be determined.

$$\text{Collapse potential, CP (\%)} = \left(1 - \frac{\gamma_{idry}}{\gamma_{dmax}}\right) * 100 \tag{3.4}$$

$$\text{Collapse settlement, } (\Delta H) = \text{CP} * \text{collapse layer thickness } (H_0) \tag{3.5}$$

Equation 3.4 is derived by assuming 1-D compression followed by substituting H_0 and $(H_0 - \Delta H)$ in their corresponding densities ρ_{dry} and ρ_{max} respectively as shown below.

$$\rho_{dry} = \frac{M}{V} = \frac{M}{H_0 A}$$

$$\rightarrow H_0 = \frac{M}{\rho_{dry} A} \rightarrow H_0\, \rho_{dry} = \frac{M}{A} \tag{1}$$

$$\text{and} \quad \rho_{max} = \frac{M}{V} = \frac{M}{(H_0 - \Delta H)A}$$

$$\rightarrow (H_0 - \Delta H) = \frac{M}{\rho_{max} A} \rightarrow (H_0 - \Delta H)\rho_{max} = \frac{M}{A} \tag{2}$$

$$\text{by substituting (1) in (2)} \rightarrow (H_0 - \Delta H)\rho_{max} = H_0\, \rho_{dry}$$

$$\frac{(H_0 - \Delta H)}{H_0} = \frac{\rho_{dry}}{\rho_{max}}$$

$$\rightarrow 1 - \frac{\Delta H}{H_0} = 1 - CP = \frac{\rho_{dry}}{\rho_{max}}$$

$$\rightarrow CP = 1 - \frac{\rho_{dry}}{\rho_{max}} = 1 - \frac{\gamma_{dry}}{\gamma_{max}}$$

To improve the applicability of this equation, a more sensible estimation for the maximum dry density in Equation 3.4 is required, such as developing a new maximum density procedure under static loads. Alternatively, it might be better to adopt the maximum density after collapse from a triaxial test in which similar boundary conditions are applied. As a conclusion, this method is based on a soil's unit weight in two states, current and maximum, which are crucial 'parameters' that control the amount of collapse.

To implement this equation, the unit weight data from compaction tests and in-situ sand replacement tests were used, as given by Hamid (2012) in Table 2.5. As an example, data from

TP1 are plotted in Figures 3.26a and 3.26b to show the soil type percentages and the average difference between the natural and maximum unit weight with depth which is more than 4 kN/m^3. Figure 3.26a indicates that the change in soil content with depth is not significant and the difference in unit weight is mainly due to changes in the volume of voids due to compaction.

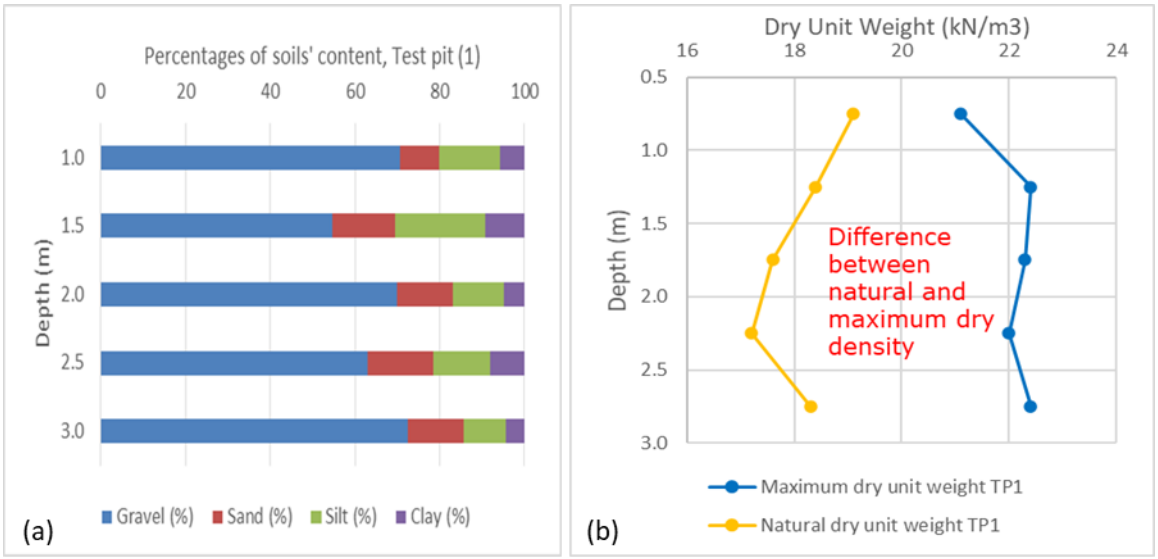


Figure 3.26: Soil content and dry unit weights from T.P. (1) - After Hamid (2012)

Figure 3.27 gives a wider view to compare the change in soil unit weight and void ratio and water content at their in-situ state against their values from compaction test in both TP1 and TP2. There are clear differences in dry density, void ratio and water content in both TPs, although TP1 showed greater differences than TP2. In TP1 the maximum dry unit weight is greater than the natural dry unit weight, by about 5 kN/m^3, while this difference is only about 2 kN/m^3 in TP2. The average difference in void ratio about 0.3 in TP1 and 0.15 in TP2. While the difference between optimum water content and natural water content is clearer in TP2 than TP1. This difference in TP2 is about 4% while in TP1 the optimum water content is even less than natural water content at depths below 2m.

The calculations of voids in this fabric were made at intervals of 0.5 m in these trial pits. The natural dry unit weight and maximum compacted unit weight were used to calculate the maximum/natural and minimum/compacted void ratio respectively using Equation 3.6. The natural void ratio in TP1 in Figure 3.27 increases with depth to a peak of 0.55 at roughly the middle of the gravelly layer then slightly decreases. This visually matches with the typical soil profile given in Figure 3.12.

$$\text{Void ratio, e } = \left(\frac{G_s * \gamma_w}{\gamma_{dry}} - 1\right) \quad (3.6)$$

These differences in soil states between TP1 and TP2 are probably due to relative increase in the sand, silt and clay content in TP2. Consequently, the collapse potential would be expected to be higher in TP1 than in TP2.

The maximum possible collapse that might occur within the 3-m soil profile for TP1 and TP2 and their corresponding settlements, based on calculation using Equation 3.4 and Equation 3.5 respectively, are given in Figure 3.28. These estimated values for collapse give us two insights. The first is that in TP1 the amount of predicted collapse increases with depth to the middle of the gravelly layer and then decreases again which matches with the natural void ratio profiles discussed in the previous paragraph. The predicted collapse in TP2 is almost half that in TP1 but still showed a peak just below 2m depth.

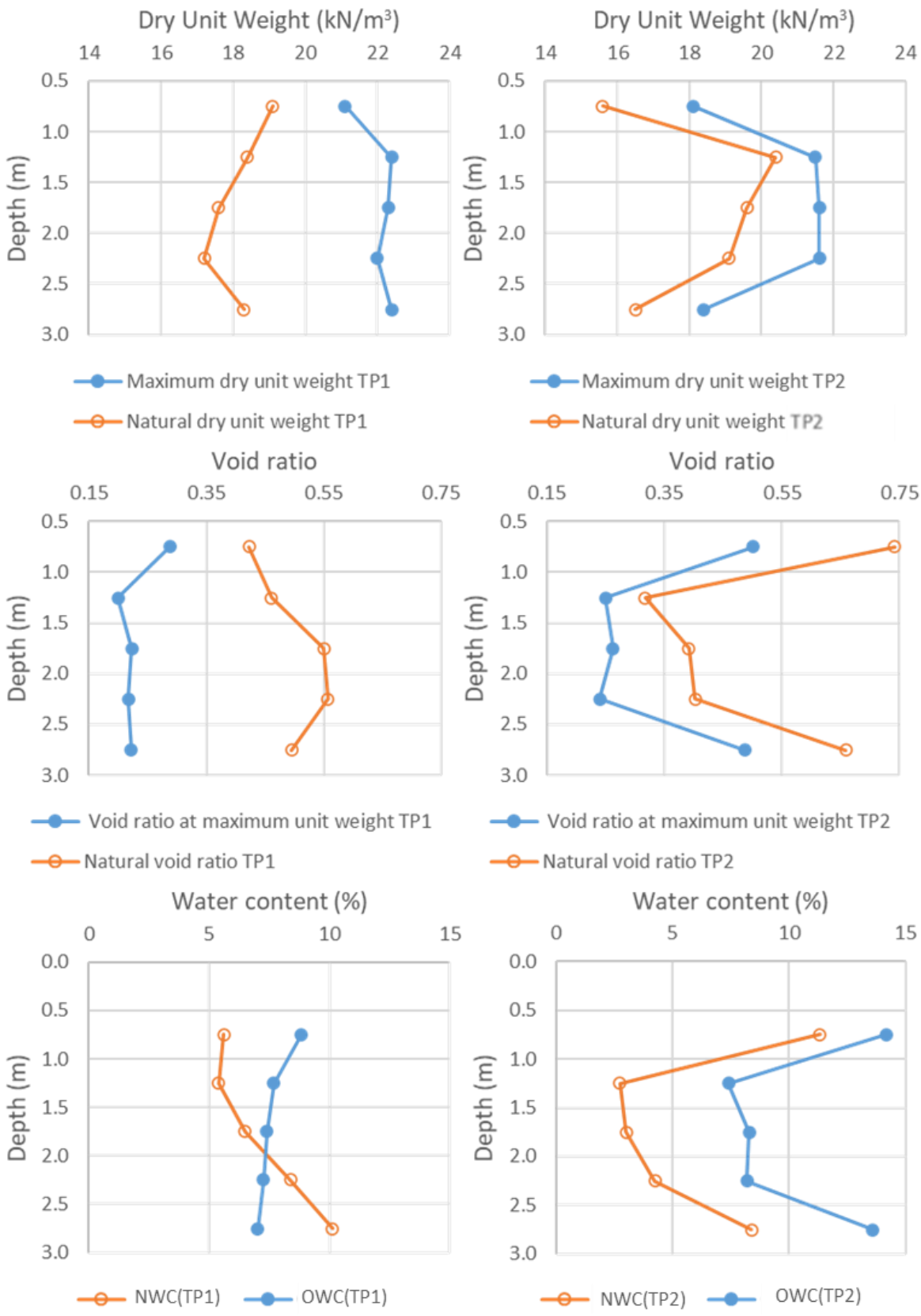


Figure 3.27: Variation of dry density and void ratio and water content with depth - After Hamid (2012)

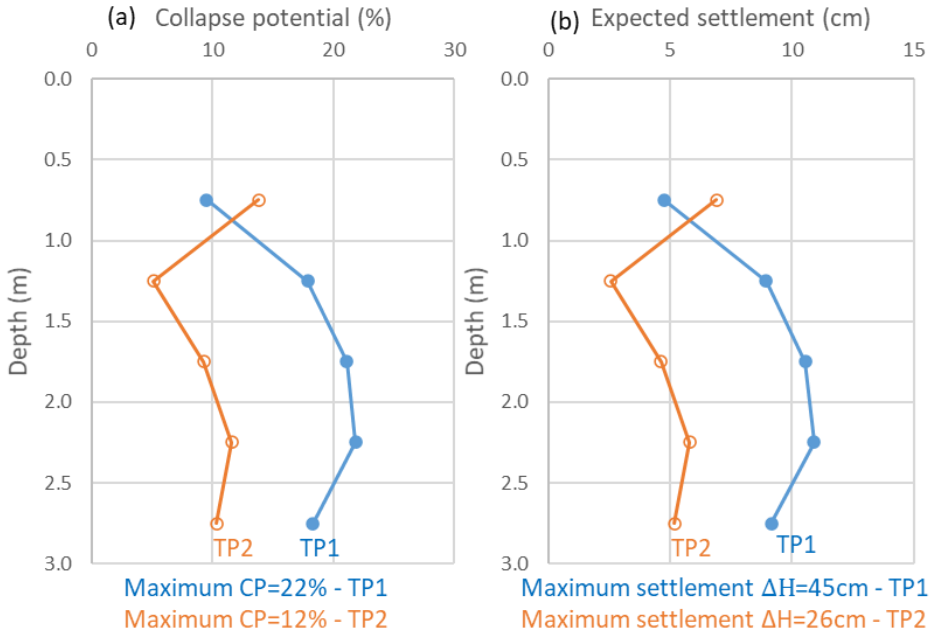


Figure 3.28: Maximum expected (a) collapse potential and (b) settlement due to compaction

The collapse values shown in Figure 3.28a were calculated using Equation 3.4 for five sublayers of 0.5 m thickness each for both TP1 and TP2. In TP1, the collapse potential for these values were 9%, 18%, 21%, 22% and 18% respectively while in TP2 collapse values were about half these values as mentioned above. Also, from this figure, collapse has a semi-parabolic distribution which is a good indication that the gravel layer has a very localised potential to collapse which might make the mitigation process easier to implement and control.

The lower predicted collapse in the upper part of this layer is probably due to the higher percentage of fine particles, which resulted in a denser fabric than the middle part. The reduction in predicted collapse in the lower part of this profile (3m depth) might be due to the effect of the underneath Nubian Sandstone layer which might allow more densification in this part due to the subsequent overburden stresses from the top sub-layers during the depositing process.

From Figure 3.28, the maximum predicted collapse potential values are 22% for TP1 and 12% for TP2. These values would be classified as 'severe' according to ASTM D5333-92 because they are greater than 6%. The total maximum expected settlement (accumulated from the settlement of the five sub-layers of 0.5 m depth using Equation 3.5 as shown in Figure 3.28b) from this prediction method is 45 cm for TP1 and 26 cm for TP2. These predicted collapse potential and collapse settlement values are just an indication for the collapsibility of this soil

profile and over-estimate the in-situ collapse. If the actual applied building stresses are considered in this prediction, it will normalise this maximum prediction. This can be achieved by establishing an experimental framework to study a wide range of stress under suitable testing conditions.

3.7 Chapter summary

3.7.1 Soil collapse in the study area

The field observations described in Section 3.2 and the in-situ plate test described in Section 3.6 indicate that there is certainly a collapse problem in the study area. However, there is still no precise procedure for quantifying or understanding the collapse mechanism in this gravelly soil under typical foundation loads at such shallow depths. Accordingly, developing new laboratory testing methods for studying the collapse behaviour in this soil is the main focus of this research.

3.7.2 Difficulties in measuring soil collapse in the study area

3.7.2.1 Gravelly nature of this collapsible soil

The soil profile in Section 3.2 and sampling process discussed in Section 3.3 describe the difficulties of dealing with this collapsible soil fabric. The first concern is that the soil is dominated by gravel particles, and it is very difficult to take undisturbed soil samples. Therefore, creating a collapsible soil fabric from this soil is a crucial stage of this research and is covered in Chapter 4. The second concern is the gravel size: using a conventional oedometer apparatus to measure collapse in this gravelly soil is not applicable according to the specifications in ASTM D2435-02, because the minimum confining ring height should be greater than 10 times the maximum particle diameter. The maximum gravel size in the Omdurman study area is greater than 10 mm, therefore, to satisfy this requirement, the ring height should be greater than 100 mm.

Chapter 4 : Analogue collapsible soil specimens

4.1 Introduction

Analogue specimens were used to address the issue of the difficulty of taking undisturbed samples of the gravelly soil as discussed in Section 2.2.7.6 and to provide consistency between specimens given the variability of the natural fabric as shown in Figure 4.1 and discussed in the following section.

4.2 Issues with soils in the study area

The interaction between the coarse and fine soil fractions in the gravelly collapsible soil is complex. There are significant differences in volume between the two main fractions and the grading characteristics of the gravels, as discussed in Section 3.5, resulting in large voids within which the distribution of fine particles is somewhat random. As a consequence, there is difficulty in measuring the density and void ratio in different states, and also, investigating the bond between coarse particles, that leads to the collapsible soil structure, is fraught with uncertainty. The random distribution of the fines (clay and silt) and sand within the gravel particle assembly, due to the chaotic depositional process, is evident from Figure 4.1.

There are three scenarios that led to the development of this collapsible fabric from the depositional processes which could not be feasibly dealt with when considering how to produce analogue specimens. First, the depositional events created different horizontally layered sets depending on the storm-water runoff. Consequently, the distribution of the gravel sizes varies with location, as discussed in Section 3.2.2.5. Second, the distribution of fines could result from three possible processes: (i) fines deposited contemporaneously with the coarse content; or (ii) fines partially or totally penetrating into the gravel layer from the subsequent storm-water; (iii) during storm-water runoff, sections of freshly deposited layers might be scoured and deposited again in different locations in such way that they might develop more soil aggregation within the new layer, producing a weak collapsible fabric with more voids.

These scenarios could be considered in future research but are very difficult to quantify. The main focus in this study has been to devise and conduct collapse tests on analogue soil specimens that have a gravel scale/content roughly similar to those encountered in the study area. Therefore, new materials with more consistent physical properties were used as a

replacement for the natural soils. New materials were investigated and adopted to minimize or eliminate the variability of the soil fabric observed in the field, arising from the above-mentioned scenarios. The properties and the advantages of the new materials are discussed in the following sections.



Figure 4.1: Variability of the gravelly collapsible fabric

4.3 Using more controllable materials

It was decided to simplify, as far as possible, the constituents and production of the specimens. It was neither realistic nor practicable to try to replicate the range of particle size distributions and their associated states (as described in Section 4.2) when considering how to produce analogue specimens with a collapsible fabric. First considered simplification in the process of producing analogue specimens was how to expedite the drying procedure of the analogue specimens to reach a similar water content to the in-situ water content. A drying procedure at 60°C in an oven for 7 days managed to achieve this water content instead of 30 days when it was dried at the room temperature as detailed in Section 4.6.2.

Second, to create more controllable and reproduceable collapsible specimens, two artificial materials were used: Lytag (a synthetic lightweight aggregate); and processed china clay Kaolin. Lytag was selected to replace the natural gravel because of the suitability of its characteristics which are comprehensively discussed the following section. Kaolin as low plasticity clay was used as a binder.

To develop an open meta-stable soil structure from these two artificial materials, a wet mixing method was developed. To achieve a collapsible fabric, the density of the analogue specimens should be minimized as far as is practicably possible. Therefore, the minimum density of assemblies of Lytag particles were evaluated to assess the effectiveness of the analogue specimen preparation procedure developed, as described in Section 4.5.

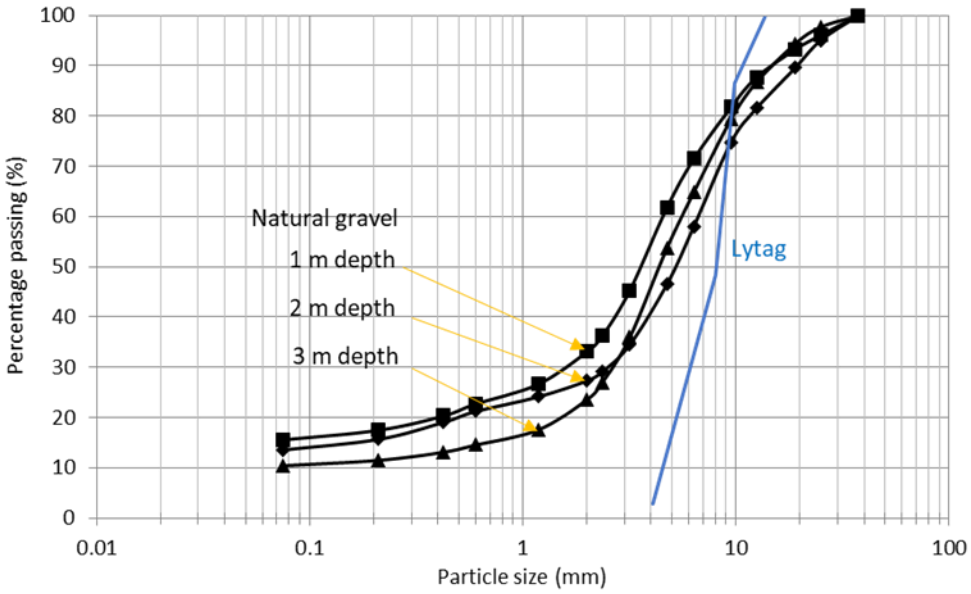


Figure 4.2: Comparison of particle size distributions for natural gravel and Lytag

4.4 Kaolin properties

Kaolin basically consists of single sheets of silica and alumina joined by strong hydrogen bonds having the composition $(OH)_8Si_4Al_4O_{11}$ (Mitchell and Soga, 2005). These strong bonds categorised kaolin as low plasticity clay with specific gravity of solids of about 2.60 and plasticity index of around 30%. The type of kaolin used in this study is China kaolin clay (Speswhite). The chemical composition and physical properties of this type of clay are given in Table 4.1.

Table 4.1: Kaolin (Speswhite) characteristics After (Mahmoud, 1989)

(a) Chemical composition

Symbol of compound	Weight (%)
SiO_2	46.2
Al_2O_3	38.7
K_2O	1.01
Fe_2O_3	0.56
CaO	0.20
MgO	0.20
TiO_2	0.09
Na_2O	0.07
Loss on Ignition	13.14

(b) Physical properties

Property	Value
Liquid Limit (%)	66
Plastic Limit (%)	32
Plasticity Index (%)	34
Clay Fraction (%)	75
Specific Gravity of Solids	2.66

4.5 Lytag characteristics

Lytag is produced by sintering and pelletising pulverised fuel ash (PFA) in a rotary kiln at a temperature of about 1400°C. At this temperature, the moisture in the pellets expands within their outer fused ceramic shell to produce a hard, honeycombed structure of interconnecting voids. The resulting Lytag particles are lightweight, porous and have a high resistance to crushing (with a crushing strength of about 6.5 MPa). This is an important feature when considering using Lytag to investigate collapse mechanisms, as it ensures collapse failure is controlled by the bond between particles rather than the Lytag particles themselves.

The specific gravity of Lytag solids ranges from 1.3 to 2.2 and its oven dry loose bulk density ranges from 700 to 800 kg/m^3 and its packed water content is about 15% as supplied by the manufacturer (water added to minimise the effect of dust). The predominant components of Lytag are oxides of silicon (SiO_2 = 53%), aluminium (Al_2O_3 = 23%) and iron (Fe_2O_3 = 6%) (Specialist Aggregate data sheets, 2006). Specific engineering characteristics of the Lytag are detailed and discussed in the following sub-sections.

4.5.1 Lytag particle size and shape

The Lytag, used in the experiments, was bought in 15-kg bags and washed to remove dust, any irregular particles were removed and then it was dried at 105°C for 24 hr. After that it was sieved and divided into two groups using 9-mm opening sieve. These two groups were designated as fine and coarse Lytag in this research.

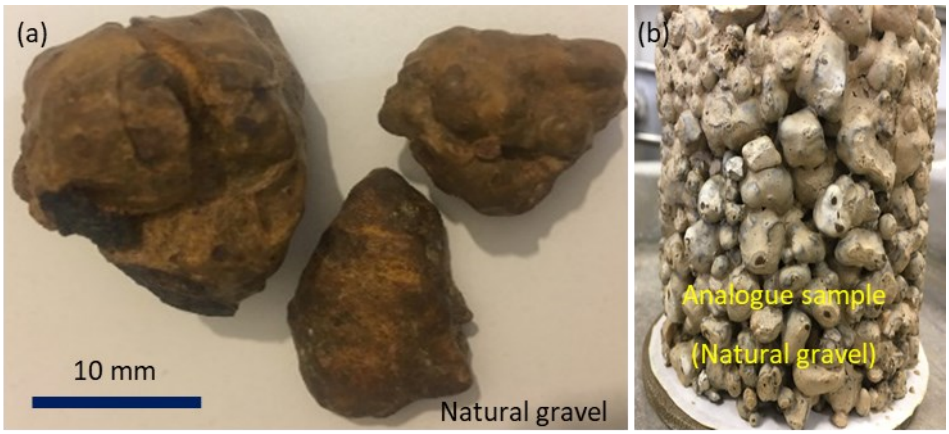


Figure 4.3: (a) Clean natural gravel and (b) an analogue sample prepared from it

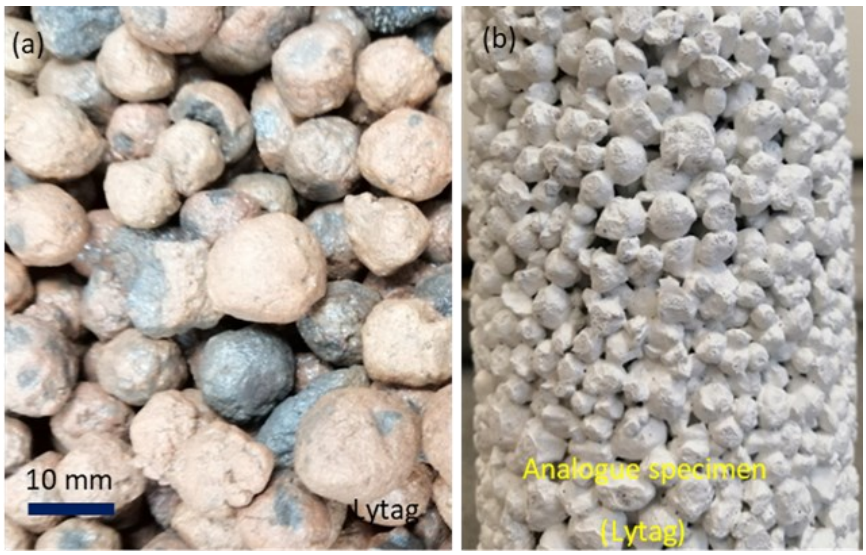


Figure 4.4: (a) Clean Lytag and (b) analogue Lytag specimen

Prior to sieving Lytag has a particle size range between 4-mm to 14-mm as shown in Figure 4.2. The Lytag grading has a higher uniformity (its C_u=1.89 and C_C=0.94) than that of these gravel (for gravel: C_u>14 and C_C>3 as discussed in Section 3.5. However, the Lytag grading is within the natural gravel grading which did not require particle size-scaling. Additionally

limiting the amount of smaller scale particles (fine gravel and sand) would lead to a more open and hence potentially more collapsible structure.

The natural gravel has smooth, although sometimes lumpy, surfaces with nodules as evident from the two images in Figure 4.3. Lytag is more rounded and has relatively rough, porous surface (see Figure 4.4a) compared with the natural gravel. This roundness and low particles density of the Lytag particles reduces the number of contact points in the Lytag analogue specimens, creating a looser packing than when using the natural gravel for which the nodules created an interlocked packing as shown in Figures 4.3b and 4.4b. This was one of the reasons for choosing Lytag to create analogue collapsible gravelly specimens. More details about the density of the packings using these two Lytag particle ranges are discussed in Section 4.5.5.

4.5.2 Surface roughness and micro surface pores of Lytag

To understand the Lytag roughness at the micro scale, Scanning Electron Microscope (SEM) (from the Material Section within the Civil and Environmental Engineering Department at ICL) was used. From the SEM scan shown in Figure 4.5, it appears that the Lytag surface is rough and porous. The shapes of the surface pores are very random and complex as the Lytag is made up of smaller spherical fused particles. An SEM scan was conducted on a natural gravel particle to compare the Lytag as shown in Figure 4.6. Here there is a smoother surface of layers, coating the gravel surface with only minor cracking within them. This indicates that the Lytag is more porous than the natural gravel.

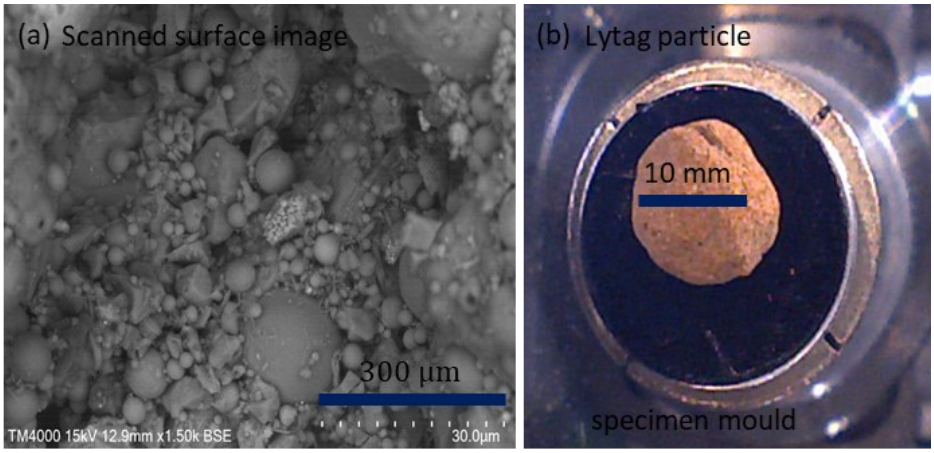


Figure 4.5: Scanning Electron Microscope (SEM) on Lytag particle (a) scanned surface image (b) gravel particle

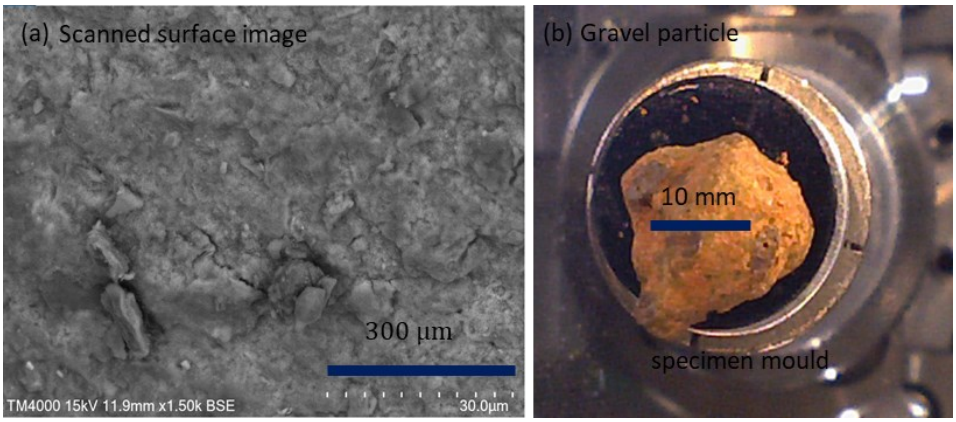


Figure 4.6: Scanning Electron Microscope (SEM) on natural gravel (a) scanned surface image (b) gravel particle

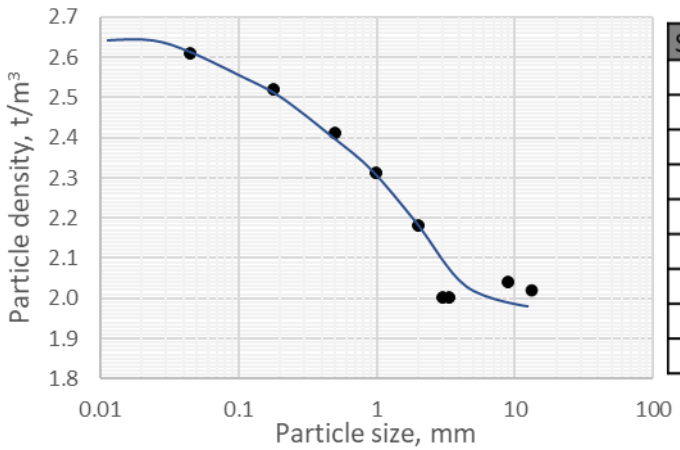


Figure 4.7: Lytag particle density determination using: (a) 50-ml pycnometers (b) 250-ml gas jars

4.5.3 Lytag particle density

As particle density is the specific gravity of the particle multiplied by the density of water ($\rho_s = G_s * \rho_w$) and if it is considered $\rho_w = 1.0\ t/m^3$, then $\rho_s(t/m^3) = G_s$. In this section, ρ_s is used rather than G_s.

In order to evaluate the effect of Lytag particle size and its inherent micro-pores on its particle density, nine samples covering a wide range of particle sizes were prepared from Lytag through grinding and sieving processes. These specimens, were assigned to respective sieve sizes and arranged from fine to coarse, as they passed through sieve openings of 045-micron, 180-micron, 500-micron, 1-mm, 2-mm, 3-mm, 3.35-mm, 9-mm and 13.2-mm. According to BS EN ISO 18847:2016, the first five specimens should be tested using 50-ml pycnometers. The remaining specimens were test using 250-ml gas jars. In both groups a vacuum of 100 kPa was applied to evacuate air from the particles for sufficient time, usually about 6 hr, until no further air bubbles could be seen to be released. As shown in Figure 4.7, the specimens were tested together to guarantee similar test conditions. The tests were run in a room with temperature controlled from 19.5 to 20°C.



Sieve size (mm)	$\rho_s(t/m^3)$
0.045	2.61
0.180	2.52
0.500	2.41
1.000	2.31
2.000	2.18
3.000	2.00
3.350	2.00
9.000	2.04
13.200	2.02

Figure 4.8: Change in Lytag particle density for different Lytag sizes

The particle density test results for the above-mentioned range of particles sizes are summarised in Figure 4.8 which were 2.61, 2.52, 2.41, 2.31, 2.18, 2.00, 2.00, 2.04 and 2.02 respectively. The average particle density for the Lytag sizes considered (4 mm to 14 mm) is G_s=2.03 (the average of the least four values in Figure 4.8. As expected, the apparent particle density decreases with increasing particle size. It is evident from Figure 4.8 that the Lytag particle density, measured using the method given by BS EN ISO 18847:2016, approaches an

asymptotic value with finer particle sizes. This confirms that the volume of micro pores within Lytag particles increases with particle size as the particle density reduces.

This finding (the increase of the particle density of Lytag with decreasing of their size) supports the results and discussion concerning the Lytag packing minimum density in Section 4.5.5 where it is explained that the minimum density of the coarse Lytag particles was smaller than that of the fine Lytag particles. Therefore, it can be concluded that in the loosest particle packing state, for a given mould volume, the fine Lytag has a higher minimum density than the coarse Lytag. Section 4.5.5 covers minimum density of the Lytag and the factors that affect the minimum density packing.

4.5.4 Lytag water absorption

Following the methodology given in BS 812-2:1975 (1990), the water absorption of the two groups of dry Lytag (4 to 9 mm and 9 to 14 mm) was found to be 14% (Ofosu, 2019). This water absorption was calculated as a percentage of the weight of water absorbed (on a damp Lytag surface, where surplus water was removed) to the Lytag particles dry weight. In the given procedure the dry particles are immersed in water under atmospheric pressure. In order to understand the effect of water pressure on the Lytag water absorption, water absorption tests were conducted, first by soaking only and then under pressures of 250, 500 and 750 kPa for 24 hr. A triaxial cell was used to apply these water pressures. The intention was to assess indirectly, by water absorption, the continuity and influence of the micro pores.



Figure 4.9: The perforated net used in Lytag water absorption test

A net bag, as shown in Figure 4.9a, was used to hold the particles and allow water pressure to be applied. The water absorption results from these tests are summarised in Figure 4.10. Up to the applied 250 kPa water pressure, the water absorption remained constant at around 13% for both fine and coarse Lytag, close to the value measured by Ofosu (2019). Beyond that, the water absorption increased with water pressure reaching around 23% at 750 kPa. The fine Lytag measurements indicate a slightly higher water absorption than the coarse Lytag. This can be explained by the higher surface area of the fine Lytag particles. The increase in water absorption with applied pressure indicates that there is partial continuity of the Lytag internal micropores. At low pressures (e.g., atmospheric) the water meniscus forces inhibit water entry through the narrow pore spaces, in the same way as expressed by Young-Laplace equation given by Equation 2.2 in Section 2.1.5.3. As the water pressure increases, the menisci are driven further into the narrow pores within the individual particles. To investigate the continuity of these micropores, a stereo-microscope scan was conducted on selected Lytag particles as shown in Figure 4.11.

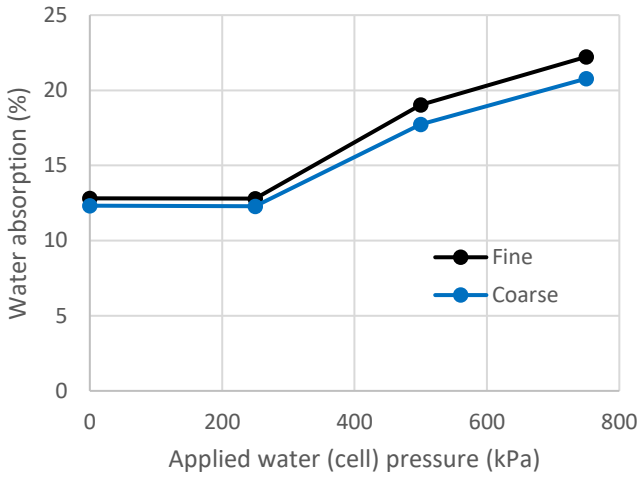


Figure 4.10: Lytag water absorption against applied water pressure

The stereo-microscopic scan images shown in Figures 4.11 and 4.12 indicate small tubes and other irregular shapes of the internal micro-pores. This scan was conducted on slices of the particles, i.e. two-dimensionally, it is difficult to assess the level of continuity between the pore and tube voids that are visible.

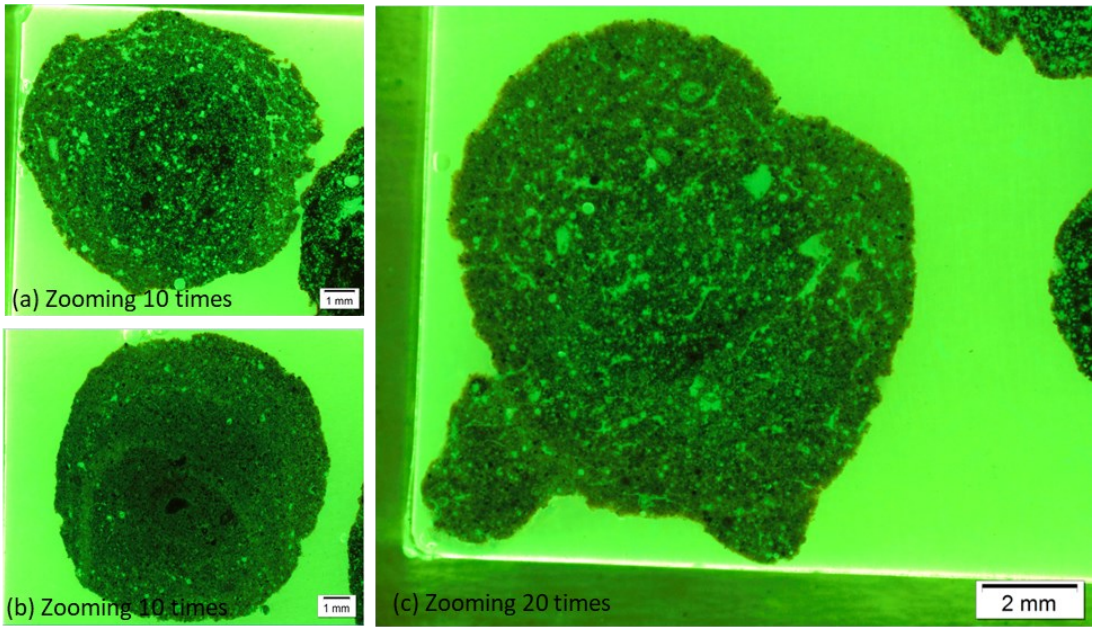


Figure 4.11: Stereo-microscopic scan on cross-sections of coarse Lytag particles

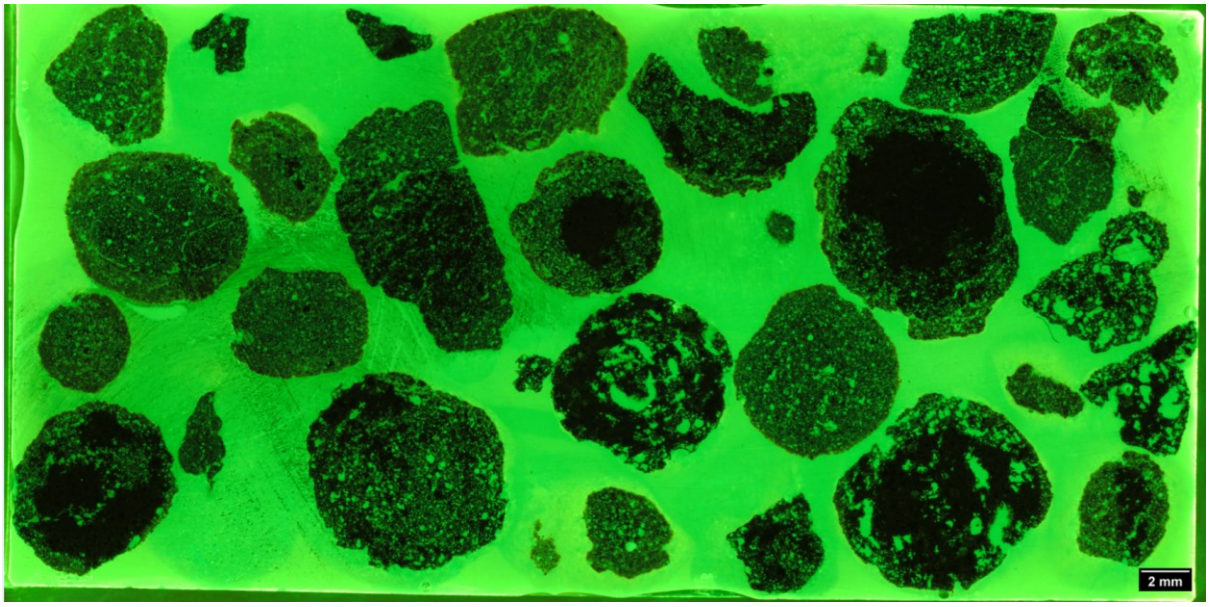


Figure 4.12: Stereo-microscopic scan on cross-sections of fine Lytag particles

4.5.5 Minimum density of Lytag

In order to have an idea of the relative density of the Lytag specimens, it was necessary to establish or estimate the minimum and maximum density of both the two gradings initially considered for the analogue specimens. The minimum density was of particular interest given that the collapse potential was the focus of the research.

The minimum density of the Lytag packing was assessed in different ways to account for the size and nature of this lightweight material and also the diameter of the analogue collapsible

specimens (100mm). A non-standardized procedure was adopted to evaluate the effect of the mould diameter and height on Lytag minimum density. The results are compared with the standardized methods given by BS 1377-4:1990 and ASTM D4254 – 16. Factors affecting the minimum density such as the size of Lytag particles and subjective errors are discussed for both the standardized and non-standardized methods.

4.5.5.1 Non-standard procedure

To study the effect of the diameter and the height of the cylinder on the minimum density, two measuring cylinders of 1-litre and 2-litre capacities were used, their diameters and heights as following: D_1=60mm, D_2=73mm and H_1=450mm, H_2=550mm respectively as non-standard moulds. The procedure was very similar to the inverted cylinder method described in BS1377-4:1990 for measuring minimum density of the sands. However, in the modified method adopted, the specimen mass was increased gradually in intervals of 10% of the cylinder volume to evaluate the effect of specimen mass on minimum density.

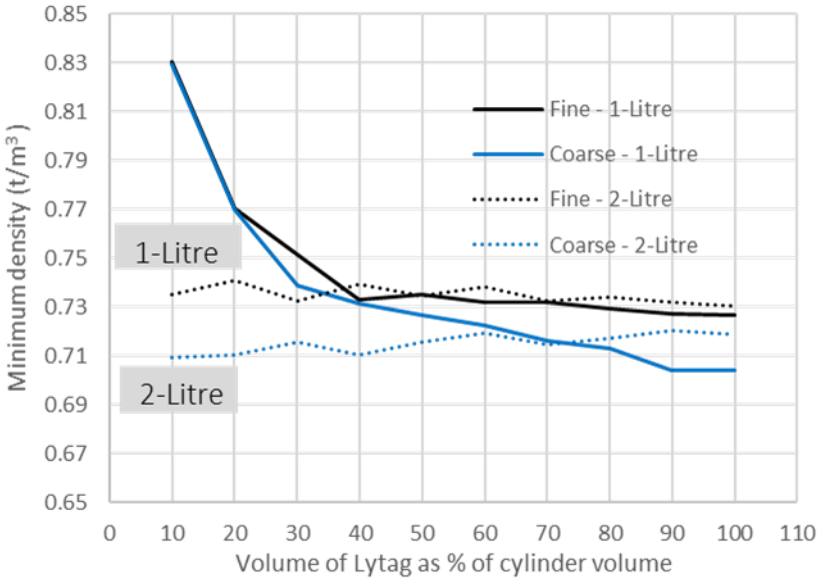


Figure 4.13: Assessing the minimum density of Lytag using non-standard procedures

The results from these two cylinders are plotted in Figure 4.13. With the 1-litre cylinder, at specimen volumes less than 40% of the cylinder volume, both fine and coarse Lytag minimum density values were affected. Above 40% volume, a constant value of minimum density of 0.73 t/m^3 was recorded for the fine Lytag, while for the coarse Lytag it seems that the 1-litre cylinder was too small to determine its minimum density accurately. When using the 2-litre cylinder, a relatively stable reading was recorded for both fine and coarse Lytag of 0.73 t/m^3 and 0.71 t/m^3 respectively regardless of the change of the specimen volume.

4.5.5.2 Standard procedures

The minimum density of Lytag was also measured according to the procedures given in BS1377-4:1990 and ASTM D 4254-16 method B. It can be seen from Figure 4.14 that the ASTM D 4254-16 method provides the lowest minimum density for both fine and coarse Lytag with lower variability between the repeated test results than the BS method. This is mainly because the 0.5 m pouring height in the BS method leads to more densification of the specimen than the ASTM method in which the tube is pulled up leaving the particle resting inside the mould with minimal compaction effect than being poured from 0.5 m height as in the BS.

To minimise the error that arises from estimating the height of the particles inside the tube because of the size of the Lytag particles, after determining the appropriate volume of the Lytag using the tube volume, the particles were weighed and used repeatedly for the rest of the tests. Before each test the Lytag was well mixed in a large container with a volume about three times that of the Lytag to make the mixing process easier. At the end of all 10 tests the Lytag was weighed again to confirm that there was no loss of material during the repeat tests.

In contrast to the results from the ASTM method, the minimum density of the coarse Lytag is greater when using the BS method than the fine Lytag which clearly explains the effect of the pouring height. The larger particles produce a denser fabric with gravity while the smaller particles produce a lighter fabric. Conversely, in the ASTM method, both coarse and fine Lytag have constant volume of particles inside the tube, so the fine Lytag had more weight that the coarse Lytag, and because there is not much effect from the gravity in this test, the minimum density of the fine Lytag was slightly greater than the coarse Lytag.

After describing the various advantages of the ASTM method above, The question is whether this method represents the best one to determine the minimum density of the Lytag? Or does it under-estimate the value of the minimum density of the Lytag? Careful thought needs to be given to the selection of one of these methods to be the most appropriate choice for calculating the Lytag's minimum density. The most consistent method, the ASTM method, does not cater for the fact that in nature soils are deposited in different ways depending on gravitational forces and the momentum/intensity of their environmental carrier such as wind, water or ice. Also, none of them considers the fact that generally soils are deposited in layers which is how the analogue specimens were prepared.

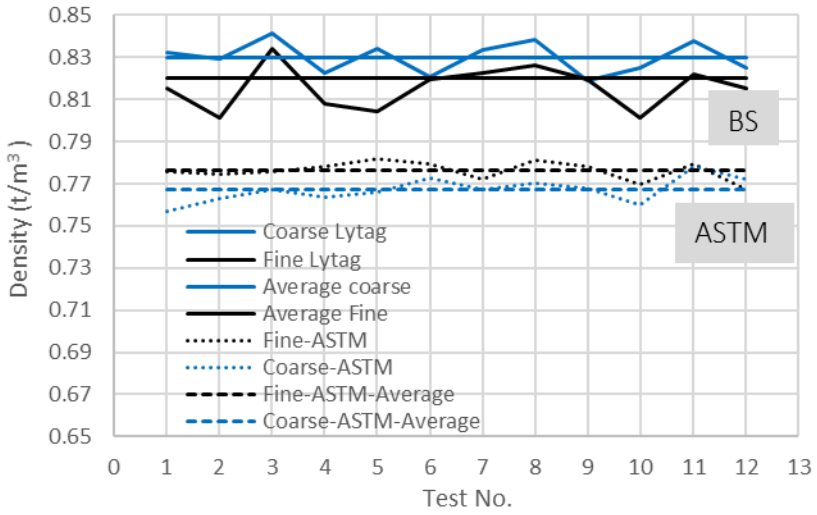


Figure 4.14: Lytag minimum density using standard procedures (BS 1377 and ASTM D4254 - 16)

The non-standard procedure, as shown in Figure 4.15, underestimated the minimum density, which is probably due to the mould diameter effect, helping the Lytag particles to stack over each other. In this study the reference average minimum density of the fine and coarse Lytag was taken to be 0.82 t/m^3 and 0.83 t/m^3 for the coarse Lytag (from the BS method) to be consistent with the analogue procedure as is discussed in the following section.

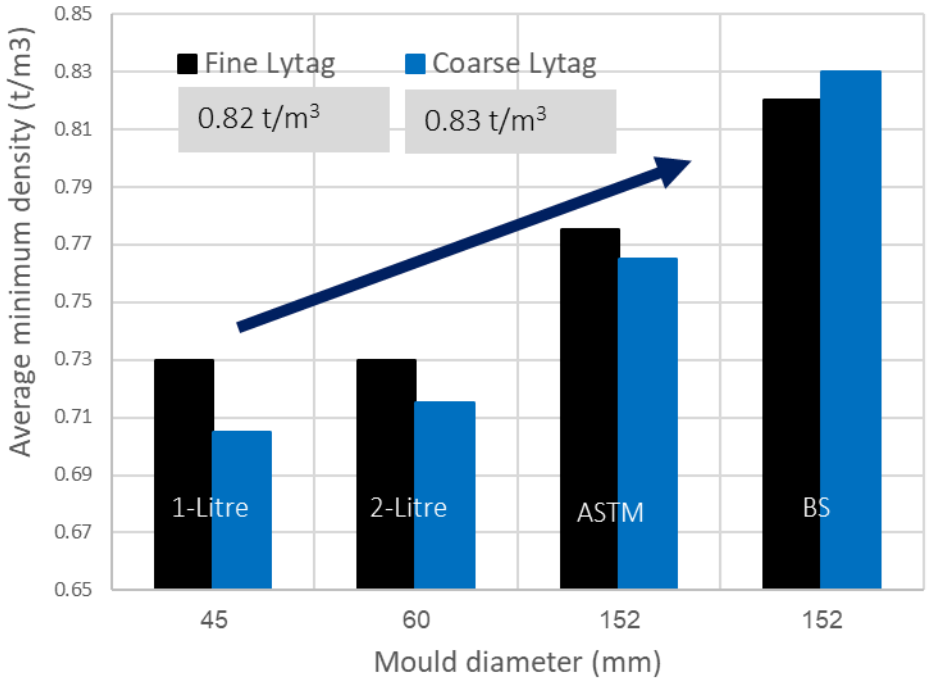


Figure 4.15: Lytag minimum density from both standard and non-standard procedures

4.6 Analogue collapsible gravelly specimens

4.6.1 Introduction

The primary goal of the following specimen preparation procedure is to produce collapsible soil specimens with, in practical terms, a minimum possible density. This specimen preparation method uses a wet mixing procedure to mimic the deposition of colluvial sediments, for which the collapse phenomenon has been observed in north Sudan (Osman and Ahmed, 2015). As mentioned by Selley (2000), this sediment was deposited under flowing water of varying velocity with faster flow rates on the high ground. However, the mixture of the Lytag and kaolin was placed gently in layers from the top of the mould.

The analogue specimen preparation procedure followed in the research, covered next in Sections 4.6.2 and 4.6.3, is based on preparing a slurry of the binder and then mixing the coarse component into it thoroughly to mimic the natural deposition of the gravelly layer found in the study area, as described in Section 2.2.6.1. In the following sections, a description is given of how the analogue collapsible gravelly specimen preparation procedure was developed using trials. These are discussed in sequence to show how the procedure was improved.

4.6.2 Preparing analogue specimens using natural gravel from the study area

The reason for increasing the drying temperature followed from trials trying to replicate the in-situ bonded gravel using the full particle size distribution. In this trial, a soil sample from the area study was mixed together, including its fines content, with water to a homogeneous mixture at water content of 16.4%. The mixture was then poured into the compaction mould to produce an analogue soil specimen. It took 30 days in room temperature (20°C) to reach a water content of 6% as shown in Figure 4.16a. This water content value is acceptable because it is very close to the TP1 in-situ water content values as given in Table 2.5. The corresponding natural bulk density subsequently decreased due to this drying process from 2.00 t/m^3 (ρ_{dry}=1.72 t/m^3) to 1.82 t/m^3 (ρ_{dry}=1.72 t/m^3) as shown in Figure 4.16b.

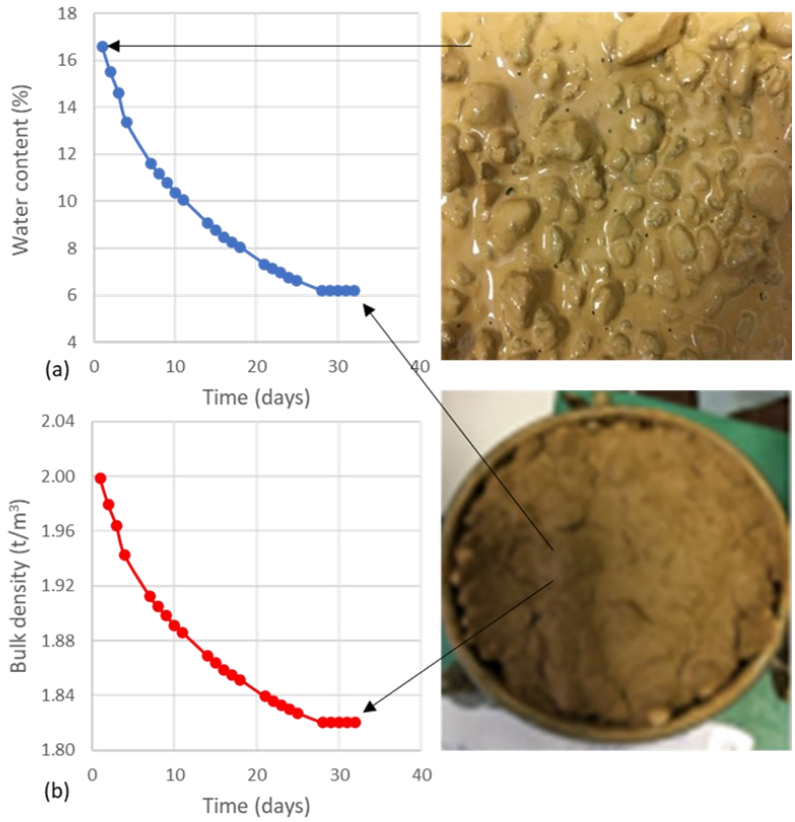


Figure 4.16: Variation of (a) water content and (b) bulk density with time - natural drying at room temperature (20°C) of a specimen contains whole particle range of the natural gravelly soil

This natural drying process, in a room with temperature of 20°C, was time-consuming and it differs from a typical average field temperature of about 42°C (Section 2.2.4). Also, the delay in the drying process was affected by the mould confinement which would have reduced the drying rate. Therefore, it was decided to use a temperature-controlled oven at 60°C to accelerate the drying process of these analogue specimens. By using this procedure, the drying process reduced from month to a week to reach to dry the specimens to the target in-situ water content. Temperatures higher than 60°C such as the standard 105°C, which is used for measuring water content of soils, are avoided for two reasons. First, to replicate the in-situ water content, specimens should not be fully dried. Second, at a temperature 105°C, it was observed that the fine fraction paste develops cracks leading to a different behaviour during the loading and inundation stages.

The first set of three analogue specimens was prepared to study the effect of gravel size on collapse using natural Sudanese gravel bonded with kaolin. For the first specimen, all gravel sizes were used, while for the other two specimens the coarse part was grouped into two groups with fine and coarse gravel fractions. The fine gravel refers to the gravel particles that passed

through a 4.75 mm sieve and were retained on a 3.35 mm sieve, and the coarse gravel relates to those that passed through 6.35 mm sieve and were retained on a 4.75 mm sieve.

The preparation procedure for forming these three analogue specimens involved the following steps: (i) after weighing the oven-dried gravel, the required mass of dry kaolin was calculated representing a given percentage; (ii) water was added to the kaolin so that the target water content would be reached after mixing carefully to produce a kaolin slurry; (iii) the gravel batch was then added to the slurry and mixed thoroughly to create a homogenous wet mixture; (iv) gently pour the gravel-kaolin mixture in three layers using a scoop into a compaction mould of known dimensions (102 mm inner diameter and 112 mm height plus its extension) and mass; (v) after each layer the surface was levelled off using a spatula; (vi) the mass of soil and mould together was then recorded; (vii) for the dry density calculation, the remainder of the mixture was weighed and put in the oven for water content measurement; (viii) finally the specimen was dried in an oven at a controlled temperature of 60°C to reach the required dried state. This 60°C temperature is slightly higher than the field temperature (42°C), as given in Section 2.2.4, to create the same bonding throughout the specimen.

An example of the first specimen which was produced using 20% of kaolinite by dry gravel mass at a water content of 14.8% is shown in Figure 4.17. Its initial bulk density was 2.01 t/m^3. To facilitate the release of the specimen in an undisturbed state, the inner surfaces of both of the mould and its extension were coated with a thin layer of grease.

Two main observations can be made about the resulting fabric. First, the kaolin paste was well distributed and did not flow down toward the specimen base, indicating that the kaolin slurry bonded the gravel well rather than filling the macro voids between the gravel particles. Second, most of the contact points are between the gravel particles in which a clear gravel interlocking can be seen as shown in Figure 4.17. The specimen fabric shown in this figure seems denser than natural in-situ fabric shown in the soil profile in Figure 4.1. Thus, the collapsibility of these specimens expected to be very low. Results from 1-D loading of these specimens, formed by artificially bonding the natural Omdurman gravel, are given in Chapter 5.



Figure 4.17: Analogue specimen prepared with 20% kaolinite by dry mass at a water content of 14.8%

4.6.3 Preparing analogue specimens using Lytag

4.6.3.1 Analogue specimens in perforated base Perspex moulds for 1-D collapse testing

A total of twelve analogue specimens was prepared and tested under 1-D compression. The specimen characteristics, test procedure and results are covered in Chapter 5. In this section, only details concerning the preparation of the analogue specimen are discussed.

The main steps mentioned in Section 4.6.2 for preparing analogue collapsible gravelly specimens are summarised in Figure 4.18: mixing, pouring, levelling and drying. The only difference was that a new step was introduced as assigned by stage no. 4 in Figure 4.18. The function of this step was to check the specimen water content and its Lytag and kaolin content, just after levelling its upper surface by batching a significant proportion of the mix in a container. This batch was dried at 105°C instead of 60°C to calculate the initial water content. It was then washed to remove the kaolin and the clean Lytag placed in the oven at 105°C to dry so that the percentage of Lytag and kaolin could be calculated to check whether was any significant loss of the kaolin during the mixing process. The results from this check showed that the percentage of the kaolin content remained the same, indicating that the preparation process was carried out carefully. The density and water content of the analogue specimens are summarised in Section 5.4.2



Figure 4.18: Analogue collapsible specimens for 1-D collapse test

4.6.3.2 Preparing analogue collapsible specimens for triaxial testing

The aim of this procedure was to produce analogue collapsible specimens of dimensions of 100-mm diameter and 200-mm height for triaxial testing. Again, the procedure was similar to those described previously but with slight modifications such as introducing a tamping step which was necessary to minimise the specimen surface pores as is discussed later. As shown in Figure 4.19, this procedure can be summarised into six steps: (i) mixing the kaolin slurry with Lytag; (ii) tamping the mix in three layers; (iii) levelling the top surface of the specimen; (iv) drying in the oven at 60°C for 7 days; (v) weighing the specimen with the mould and the container before and after drying (also in this step, specimen properties were checked by measuring the water content and kaolin percentage of a small sub-specimen); (vi) extruding the specimen from its mould which was facilitated by coating all the inner surfaces of the mould and two facilitating acetate sheets with mould release silicon grease.

These triaxial specimens were prepared as sets of four identical specimens which were only from the fine Lytag group, with particle sizes ranging between 4-mm to 9-mm. Specimens were also prepared with coarse Lytag but in all cases, membrane rupture occurred when the cell pressure was applied in the triaxial apparatus (discussed in Chapter 5). The same problem was encountered if the voids on the surface of the specimens were too large (hence the need for

tamping). These membrane rupture issues are discussed in Chapter 6. During the course of preparing and testing these sets, some other slight modifications were introduced to limit specimen extrusion and membrane rupture issues. These modifications included: (i) increasing the number of tamping layers to four; (ii) using a long spatula to distribute the poured mixture into layers of equal thickness without causing additional compaction; (iii) using a light tamper to produce specimens with different lower densities by applying a specific number of tamping blows per layer.

Levelling off the top of these triaxial specimens properly was essential to avoid having one or more Lytag particles higher than the rest, thus initiating a gap between specimen and the loading platen. This was another cause of membrane rupture and also increased bedding strains. Therefore, a final circular horizontal movement on the top of the specimen was gently applied using the tamper without adding further compaction.

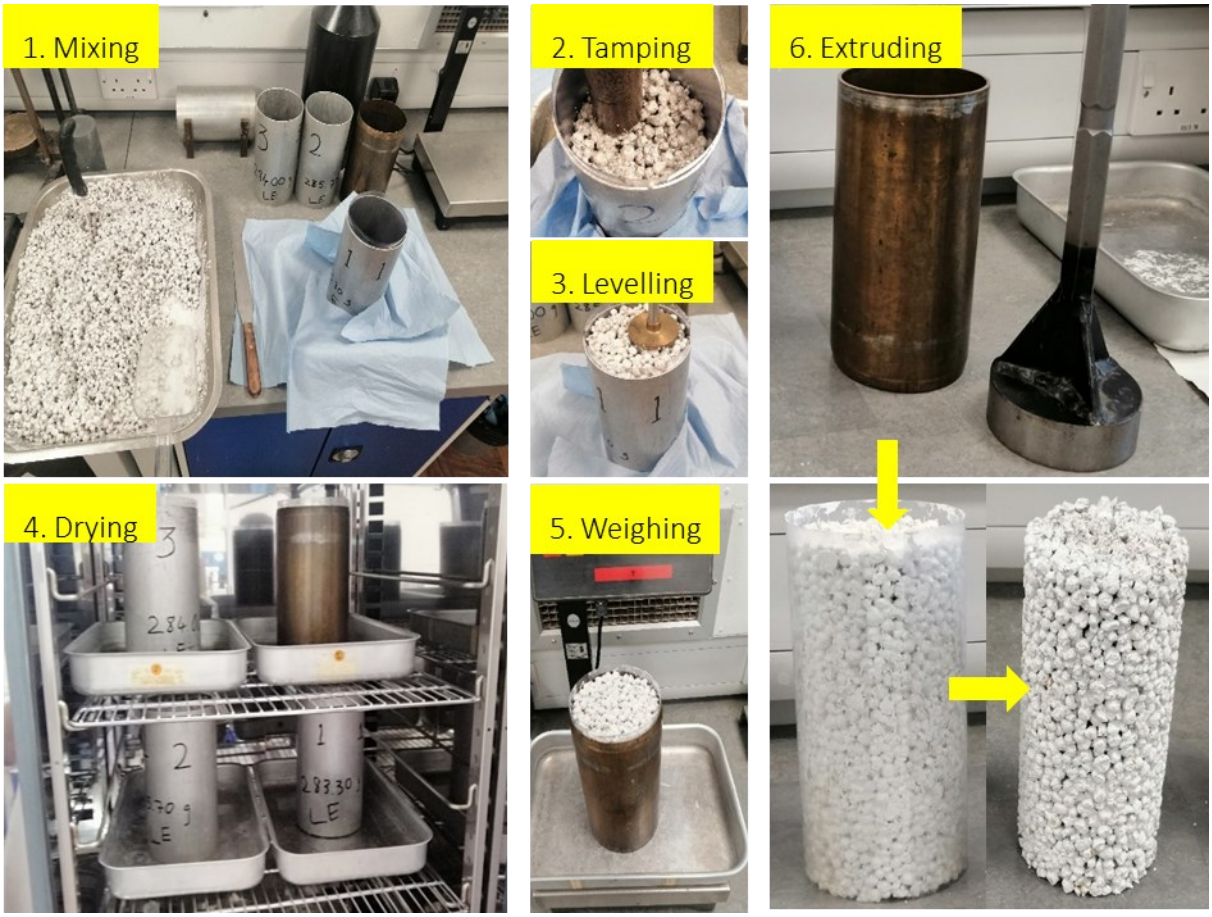


Figure 4.19: Analogue collapsible samples for triaxial collapse test

Preparing analogue collapsible specimens for triaxial testing was very challenging. Every specimen should have a minimum initial strength to be able to withstand the extrusion process, handling and setting up in the triaxial apparatus. To achieve this initial strength, denser specimens with reduced collapse potential were produced. Clearly this was not preferable because the main objective was to produce analogue collapsible specimens. There were three main concerns regarding the analogue specimens with a very loose fabric and high collapsibility: (i) specimen homogeneity; (ii) bond stability and (iii) membrane rupture due to large surface pores.

To avoid these concerns, trial specimens were prepared using different numbers of tamping blows, and kaolin percentages as shown in Figure 4.20. The data in each curve in Figure 4.20 were obtained by preparing four identical specimens from one mixture to avoid any specimen variability from the mixing process. It is evident from this figure, and not surprising, that the increase in both kaolin percentage and number of tamping blows led to an increase in the specimen dry density. It was noticed that specimens prepared with 15 tamps were more homogeneous, i.e., sets 1, 2,3 ,4 and 8 compared with sets 5, 6 and 7 which were prepared without tamping to increase their collapse potential.

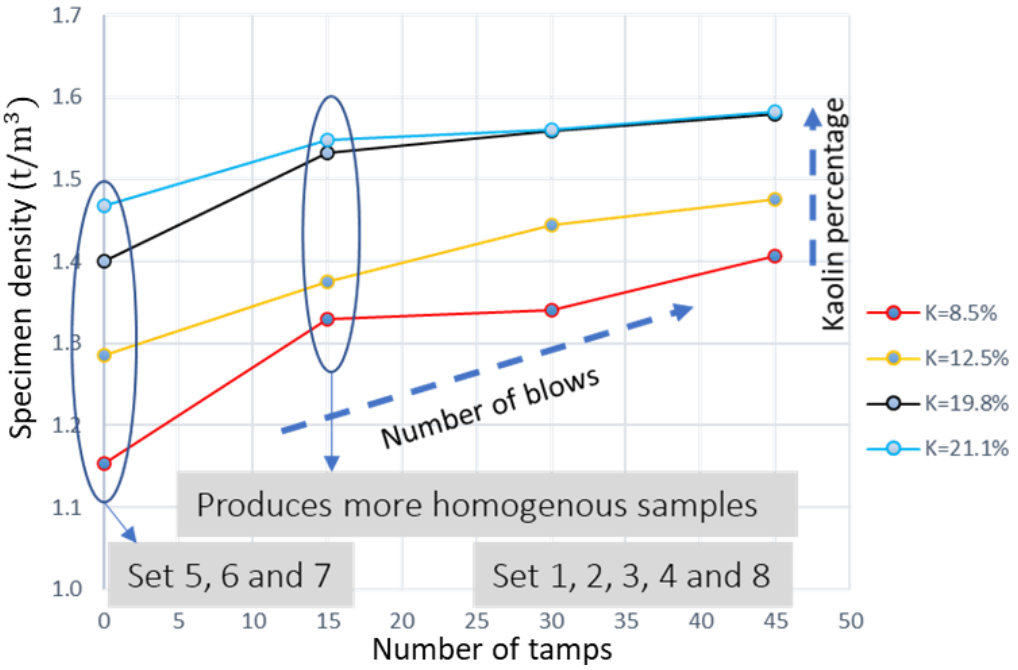


Figure 4.20: Effect of number of tamping blow and kaolin percentage on sample density

An example of a specimen collapse due to the extrusion process is shown in Figure 4.21. For this specimen, the kaolin percentage k was 8.5% and it was not subjected to any tamping (T=0 tamping blows). The reason for the collapse of this specimen is probably a combination of the low kaolin percentage and low density due to zero tamping.



Figure 4.21: Specimen collapse due to the extrusion process: k=8.5% and T=0

Chapter 5 : Collapse in compression tests with lateral confinement

5.1 Introduction

In this chapter, a description is given of two sets of collapse tests that were devised and conducted on (i) three artificially bonded natural gravel from Omdurman specimens and also (ii) 12 analogue specimens with particle sizes up to 14-mm. The term 'lateral confinement' is used here as although some of the tests were performed under 1-D conditions, others were similar to footing tests where parts of the soil mass could displace laterally. Collapse strains (vertical and volume strains) were measured for these specimens under a maximum target inundation collapse stress (the stress at which the specimens were to be inundated) of 280 kPa (chosen to be slightly higher than the maximum equivalent building stress of 262 kPa, estimated by Osman (2004) as discussed in Section 2.2.7.4). The Lytag particles in the analogue specimens were used repeatedly to minimize any Lytag size and shape variability. The effect of the Lytag size was assessed in this 1-D test set-up as Lytag was the main component in the specimen content. Also, the mould (or confining container) diameter was varied. All the specimens tested were prepared with 20% of kaolin as a binder to limit the effect of the binder percentage on collapse in this group of tests.

The focus of these sets of tests was to evaluate the effect of confinement on the 1-D collapse of the natural gravel and the analogue soil. To achieve this, tests were performed with two cylindrical container diameters with the same loading disc (platen). In the first tests the container diameter was equal to that of the loading disc diameter, allowing for a 2mm clearance, thus providing essentially 1-D conditions. A second set of tests was performed with a large diameter container but with the same loading disc, leaving an unloaded annulus of about 30 mm width. In the tests the target stress was applied, followed by an inundation stage. The basic hypothesis being investigated in these tests was that the larger container would result in a higher collapse strain because of the applied lateral freedom for movement resulting in heave in the annulus around the loading disc (upward soil movement) during collapse.

Although this test set-up was simple and any creep and the wall friction of the container were neglected, it provided a clear conclusion concerning the effect of the lateral confinement on the collapse strain as is discussed in Section 5.5.5.

5.2 Test considerations

From the field observations and the schematic diagram in Figure 3.13, the foundations (strip and square pad footings) were usually located directly on the top of the most fragile part of the collapsible gravelly layer. Fundamentally, because of different cross-sectional area, these foundations exert different stress distributions on the soil underneath and influence different volumes of the soil mass as shown in Figure 5.1. If there is a possibility of horizontal soil deformation during collapse, then the type of foundation affects the magnitude and extent of collapse. Mitchell and Soga (2005 p. 355) comment that horizontal stresses change during loading and unloading processes. This change in the horizontal stress level should lead to horizontal deformations. If a reduction of vertical stress occurs during collapse, this can be considered as an unloading process, and there is a possibility of lateral deformation. In this case, testing a soil element under these conditions cannot be fully represented by a one-dimensional oedometer test or any other zero lateral strain test set-up. Therefore, a partial degree of confinement was considered in some of the test set-ups.

To examine the lateral movement of particles during collapse, two confining containers with different diameters were used to provide two levels of soil confinement. For almost full confinement, a cylindrical container of 102-mm diameter with the same diameter as the loading disc was used. A larger 165-mm diameter container was then used with almost the same loading disc, providing less confinement, the diameter ratio between the container and the loading disc being increased from roughly 1:1 to 1.65:1. The heights of the two containers were 166 mm and 193 mm respectively (the exact dimensions are given in Table 5.1).

Table 5.1: Characteristics of the containers

Container No.	D (mm)	H (mm)	W (g)
1	101.6	166.0	1029.5
2	164.9	193.1	3847.5

The specimen height inside these containers was kept as constant as possible, even though comparisons were based on the vertical collapse strain. Sufficient vertical space was left above the upper surface of the specimens to facilitate the test set-up to allow for vertical adjustments and the expected heave in the second case.

The larger container, according to Figure 5.1, would allow for more than 85% of the disc stress to be distributed without interacting with the container walls. This test was more likely to give an indication of the collapse potential under loading from an isolated footing in the form of a small-scale model. Perspex, being a transparent material, was used in the manufacture of these containers to try to observe bond breakage and collapse mechanisms during collapse.

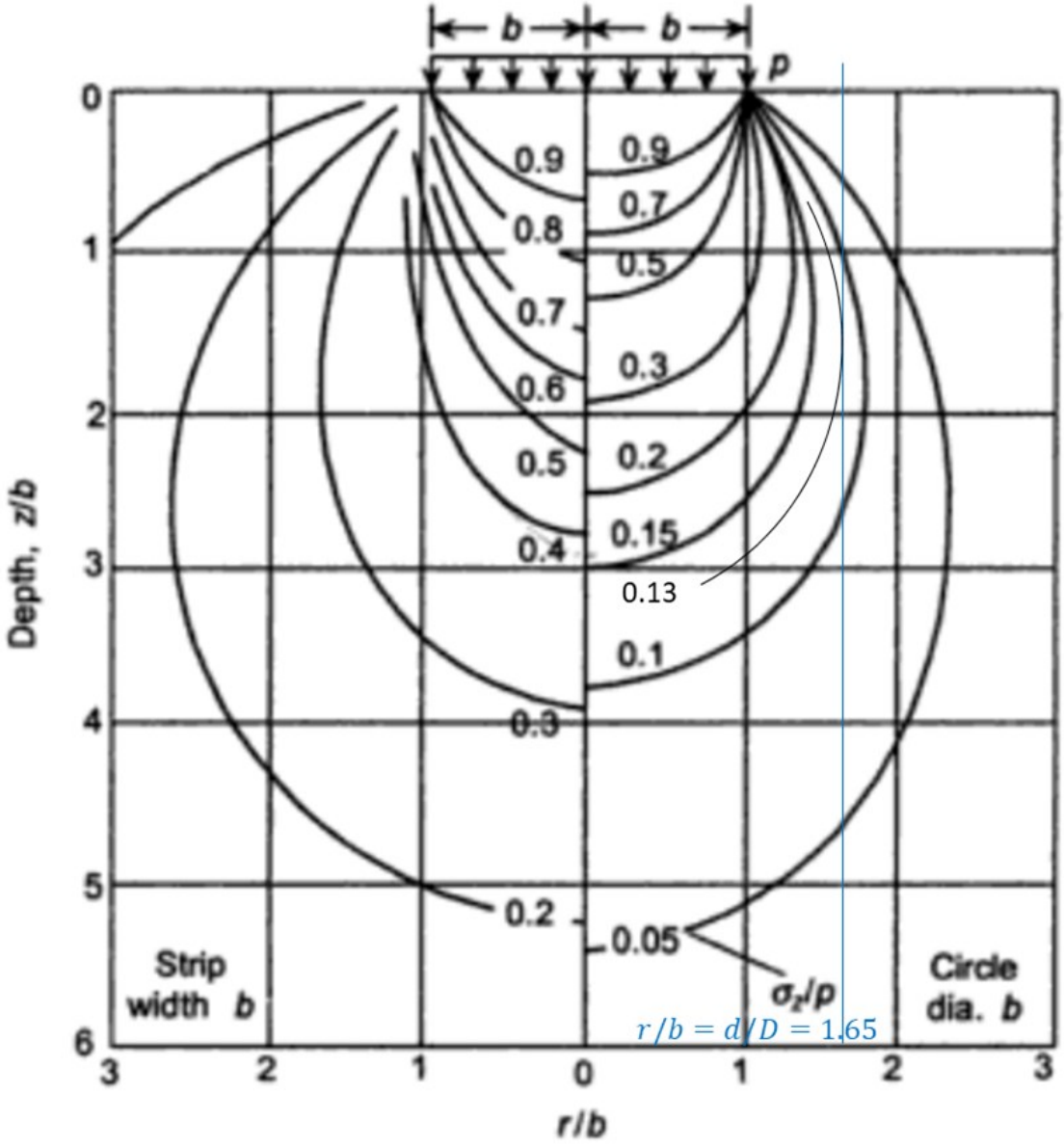


Figure 5.1: Stress distribution under strip circular footings (Som and Das, 2006)

Also, as the binder percentage was set to be constant, the effect of the Lytag particle size was assessed in terms of the degree of collapse and lateral soil movement. Two particle size ranges of Lytag were used in this set of tests, (i) 4 mm ≤ D < 9 mm and (ii) 9 mm ≤ D ≤ 14 mm, which are subsequently designated as ‘fine Lytag’ and ‘coarse Lytag’ respectively.

5.3 Analogue collapsible specimens

A total of twelve analogue specimens formed using the lightweight aggregate Lytag as a major component and kaolin as a binding material were prepared as described in Section 4.6.3.1. The prepared specimens were categorised into two groups according to the container sizes. Group one contained eight cylindrical specimens of 102-mm diameter and 150-mm height which were cast in two sets, set1 (S1, S2, S3, S4) and set2 (S5, S6, S7, S8), at the same time in four identical containers, acting as moulds. The other four specimens (S9, S10, S11, S12) were cast individually in the larger container, because there was only one available, but the preparation procedure was kept the same throughout. These specimens were of 164.9mm diameter and 150mm height. The Lytag range used in these specimens and the corresponding containers are summarised in Table 5.2.

Table 5.2: Lytag groups used in the specimens

Container No.	Fine Lytag	Coarse Lytag
1	S1, S2, S3, S4	S5, S6, S7, S8
2	S9, S10	S11, S12

All specimens were prepared using the same procedure to minimise the variability in specimen characteristics such as initial soil density and water content.

5.3.1 Protocol for preparing analogue collapsible specimens

All specimens used in this study were prepared as discussed in Section 4.6.3, this process was typically divided into two stages: casting and drying. In the casting stage, the primary component (Lytag) was carefully mixed with the slurry of secondary component (kaolin).

The preparation for the casting stage involved weighing out enough clean oven-dried Lytag (at 105^{o}C) for four specimens along with kaolin (20 % of the mass of the Lytag) and water (water > 30 % of the total solids weight).

The casting process started with adding the water to kaolin, mixing together thoroughly to form a homogenous slurry which was then mixed with the dry Lytag at room temperature to coat and create bonds between Lytag particles. The mixture of Lytag and the kaolin slurry was poured into each container in three layers using a scoop with each layer being levelled off using a spatula. During this layering process, care was taken to make sure there was no compaction

effect (n. b. there were the specimens prepared for the 1-D/footing tests). After placing the third layer, vertical clearances of about 15 mm in Container 1 and 43 mm in Container 2 were left to help to place the loading disc inside the container during the specimen set-up stage. The initial specimen height was measured accurately after applying a nominal stress as is discussed in Section 5.4.3.

After completing the casting process, the specimens were put in a temperature-controlled oven at 60°C for the drying stage. The loss of water was monitored for 7 days after which there was no further water loss. At this point the specimens were ready for the planned collapse tests. Changes during drying of the two sets of 102mm diameter specimens are compared in Figure 5.2. It is clear that there was excellent consistency and repeatability between the two sets of specimens.

5.3.2 Evaluation of changes during drying of analogue specimens

Water content and density were evaluated during the drying process at 60° C. Figures 5.2a and 5.2b show that the variation in water content in both fine (S1 to S4) and coarse (S5 to S8) Lytag has a very similar pattern with rapid drying in the first three days before levelling off. More than 80% of the drying process took place in the first three days which was long enough to produce a partially dry collapsible soil fabric, but the specimens were left for 7 days to ensure an equal bond strength throughout each specimen. It is evident from Figure 5.2b that the water content in coarse Lytag specimens does not reduce below about 5%, even though the water absorption of the fine Lytag is greater than the coarse Lytag (Section 4.5.4). The retained water is thought to be due to the larger macro pores in coarse Lytag trapping more kaolin slurry.

Density changes during this drying process, as shown in Figure 5.2c and 5.2d, are primarily caused by water loss as negligible specimen volume changes were observed. As would be expected, in line with water content changes, it decreased sharply from approximately 1.35 t/m^3 to less than 1.00 t/m^3 in three days and then decreased slightly to around 0.95 t/m^3 by the end of the week. The final values, especially for the fine Lytag, would be approaching the dry density. The fine Lytag specimens were slightly denser than the coarse ones before and after drying because of the higher content of fine Lytag per volume, as observed with the minimum density values in Section 4.5.5.

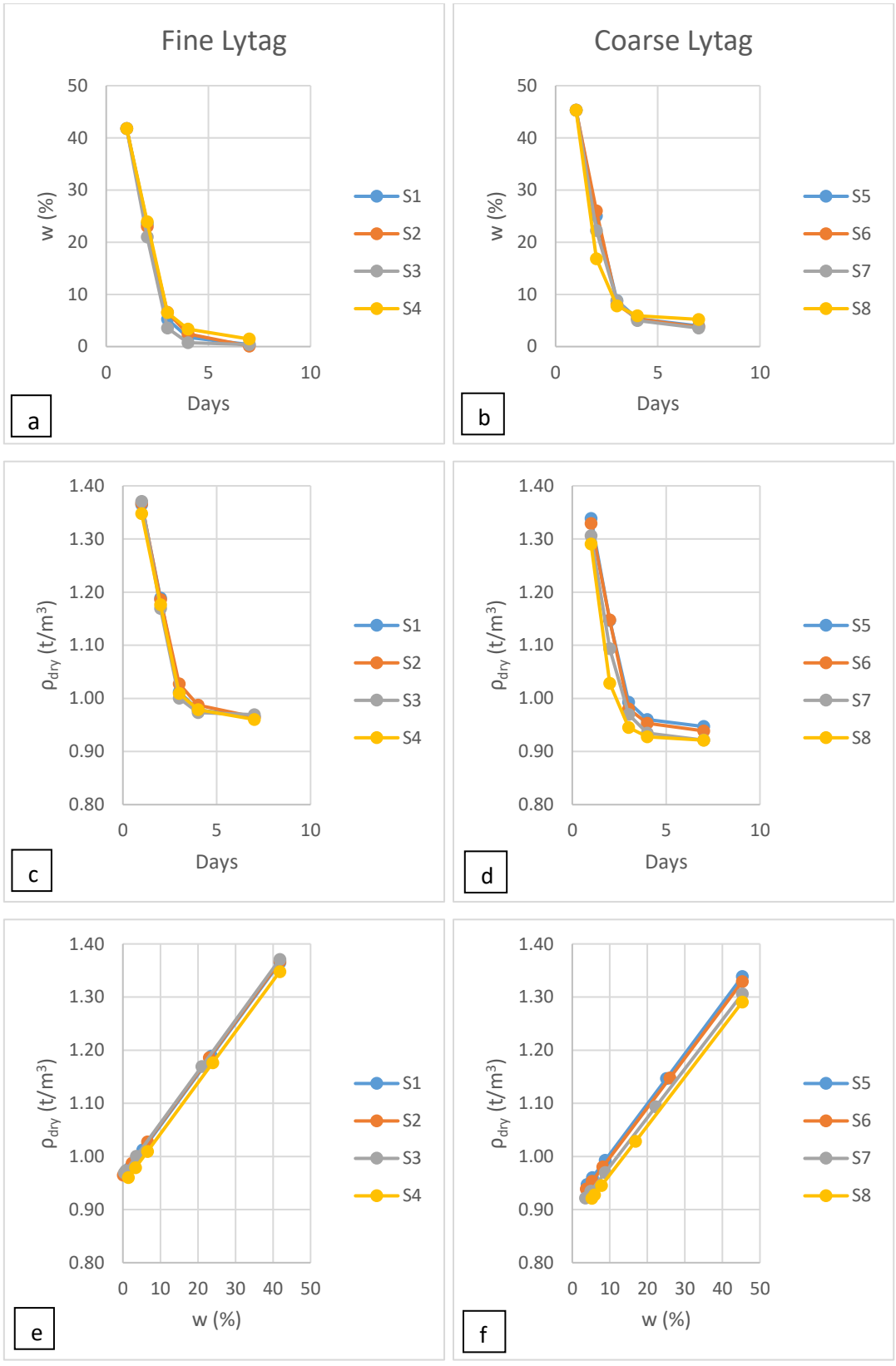


Figure 5.2: Analogue specimen properties during drying at 60°C: (a) and (b) water content w versus time; (c) and (d) dry density ρ_{dry} versus time and (e) and (f) w versus ρ_{dry} for specimens *S*1 to *S*4 (Fine Lytag) *S*5 to *S*8 (Coarse Lytag)

The rate of change in density with water loss is shown in Figures 5.2e and 5.2f. The change in water content is almost directly propositional to the change in density, conforming there is little effect from volume change. The rate of water loss was slightly higher in the coarse Lytag compared with the fine Lytag because of its higher permeability. It can also be seen that there is less variability in the fine Lytag than in the coarse Lytag, which could be due to the effect of the smaller ratio of the coarse Lytag particle diameter to the container diameter.

5.4 1-D Collapse test apparatus and procedure

5.4.1 Apparatus description

The configuration of the main parts of the 1-D collapse test apparatus are given and numbered in Figure 5.3. A 50-kN VJ Tech loading frame (1) was used which has a variable displacement rate, ranging from 20 mm/minute to 0.00001 mm/minute and 90-mm ram travel. A 15-kN capacity load cell of with a precision of ± 1 N was used which was connected to a 100-mm diameter loading plate (3). Ram travel and specimen compression were measured using a displacement transducer (4) of 0.0001 mm resolution. All of the above-mentioned components were controlled and/or logged automatically by a computer (5) using 'Triax' software (Toll and Ackerley, 1988; Toll, 2002). The specimen inside the container (6) was connected to a funnel (7) through a perforated base and plastic tube.



Figure 5.3: 1-D collapse test setup

5.4.2 Test set-up

The container was put on a rigid metal base fitted to the ram head. The tip of the displacement transducer was rested on this metal base to measure displacements. The perforated base of the container was connected to the funnel through a plastic pipe of 5 mm inner diameter. The funnel was held in place on a retort stand to provide a water head to allow water infiltration into the base of the specimen during inundation, as shown in Figure 5.3. The loading plate, connected to the load cell, was brought into contact with the top of the specimen. The cross bar/loading yoke of the loading frame provided reaction against the force initiated from the driving unit at the base of the loading frame and forces were measured through the load cell.

5.4.3 Test procedure

The test procedure was divided into four steps. (1) Position the container and specimen and zero the displacement transducer. (2) Gradually apply loading until reaching the 'collapse stress' (the stress at which the specimen was to be inundated). (3) Inundation of the specimen. (4) After the specimen settlement had ceased, the water was drained to check whether there was any further settlement, and it was then unloaded.

(1) The initial specimen height was determined by measuring for the vertical clearance above it, left to facilitate the process of adjusting the specimen beneath the loading plate. This provided an effective initial height because of the upper surface roughness resulting from the size of Lytag was relatively high which could lead to errors in measuring the specimen height. A nominal load of 100 N was used for measuring this initial height to guarantee a good contact between the specimen and the loading plate. This height is defined as that of the specimen under the initial 100 N applied by the loading ram.

(2) Using the 'Triax' software, the rate of loading was set to 0.09 mm/minute and to reach a target applied force of 2200 N, corresponding to the target stress of about 280 kPa. At this point it was left to equilibrate under this stress before water inundation. Equilibration was taken to be complete when there is no further settlement resulting from the applied stress (the creep rate criterion is discussed in Section 6.7.2).

(3) As soon as the inundation process began, collapse started to take place followed by a progressive settlement of the specimen structure. Once the specimen was fully inundated, the collapse settlement rate started to decrease until it diminished and reached a second equilibrium under the 280 kPa vertical stress (which was maintained by Triax during collapse). The time consumed from the start of the inundation process until the second equilibrium was less than 5 minutes because of the high permeability of the analogue specimens. At this point the measured collapse settlement was taken to represent the total collapse settlement of the specimen which was used to calculate the collapse potential. In some cases, collapse settlement led to a detachment between the specimen and the loading plate but after a few seconds the loading ram caught up to maintain the target load on the specimen. In this stage, some of the fine particles were observed to migrate down to the base of the container as the coarse particles rearranged themselves.

(4) To make sure there was no build-up of pore water pressure inside the specimen, water was drained from the specimen. In practice, because of the specimens' high permeability, no further settlement was observed in any of the specimens during this water drainage process. Finally, the specimen was unloaded to track any rebound response of the specimen.

5.5 Analogue specimen test results and discussion

The collapse potential CP (in essence vertical strain) is calculated based on the specimen vertical deformation due to inundation.

$$CP = (\Delta H/H_o) \quad (5.1)$$

where, H_o, represents the specimen height before inundation and Δh is the change in specimen height due to inundation.

5.5.1 Collapse from natural gravel analogue specimens

The first three analogue specimens were prepared according to the analogue procedure described in Section 5.3.1. The gravel content of these specimens was 80% by weight and bonded with 20% kaolin. The difference between these specimens was the gravel size in each specimen as described in the legend in Figure 5.4 because the plan was to study the effect of gravel size on the collapse potential.

These three specimens were tested within a one-dimensional compression in a standard compaction mould (112 mm height and 102 diameter) in a locally fabricated testing arrangement. This test set-up was not precise, and its main objective was to have an understanding of collapse in this gravelly soil in 1-D. Each specimen, to reach the maximum required stress that equivalent to a building stress on soil in the study area (262 kPa), was loaded incrementally by applying a series of loading dead weights. Specimen deformation was recorded manually from a reference point at each load increment. At the final load increment the specimen was inundated from the base to induce collapse. Figure 5.4 shows that, although the strain due to inundation is around 2 % for all tested specimens, collapse increases with the increase of uniformity of the gravel particles and particles size. If the effect of the gravel size is considered, this conclusion agrees with Rollins et al. (1994) results for sand shown in Figure 2.16.

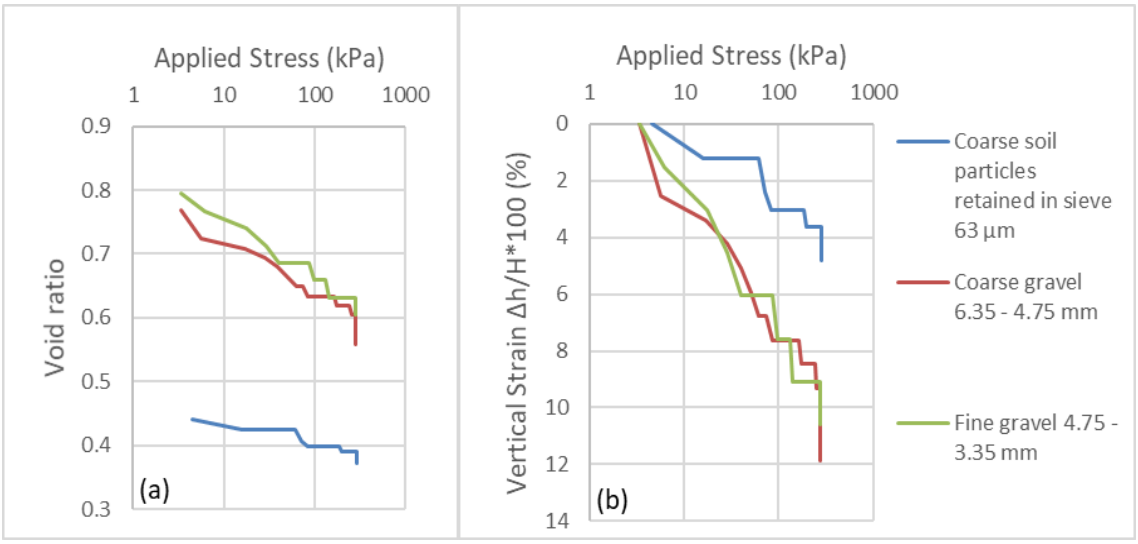


Figure 5.4: Variation of (a) void ratio and (b) vertical strain with stress level and gravel sizes

5.5.2 Collapse of the Lytag analogue specimens

For the specimens that were tested under a fully laterally restricted condition, the average collapse potential in the fine Lytag (S1, S2, S3, and S4) was 4.6% which is greater than that of the coarse Lytag (S5, S6, S7 and S8), which was 3.1% as shown in Figure 5.5. This is probably due to the effect of the smaller ratio of the coarse Lytag particle diameter to the container diameter. In contrast with Figure 5.2 the CP values of the coarse Lytag have a much lower standard deviation than the fine Lytag.

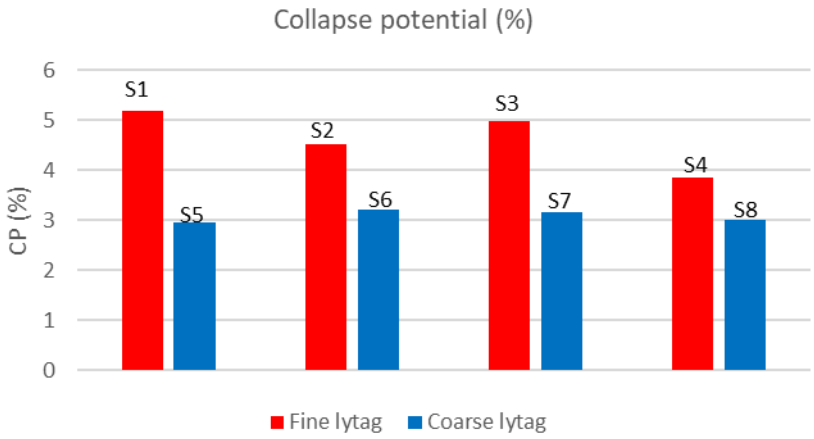


Figure 5.5: Collapse potential under full lateral confinement

Also, these values are slightly less than those provided by Ofosu (2019) under similar specimen preparation and testing conditions. He found that with 25% of the kaolin binder both fine and coarse Lytag had similar collapse strains of 6% as discussed in Section 5.5.4. n. b. Michael

Ofosu was an MSc student studying soil mechanics at ICL who completed the study described here as part of his research dissertation, working with the Author.

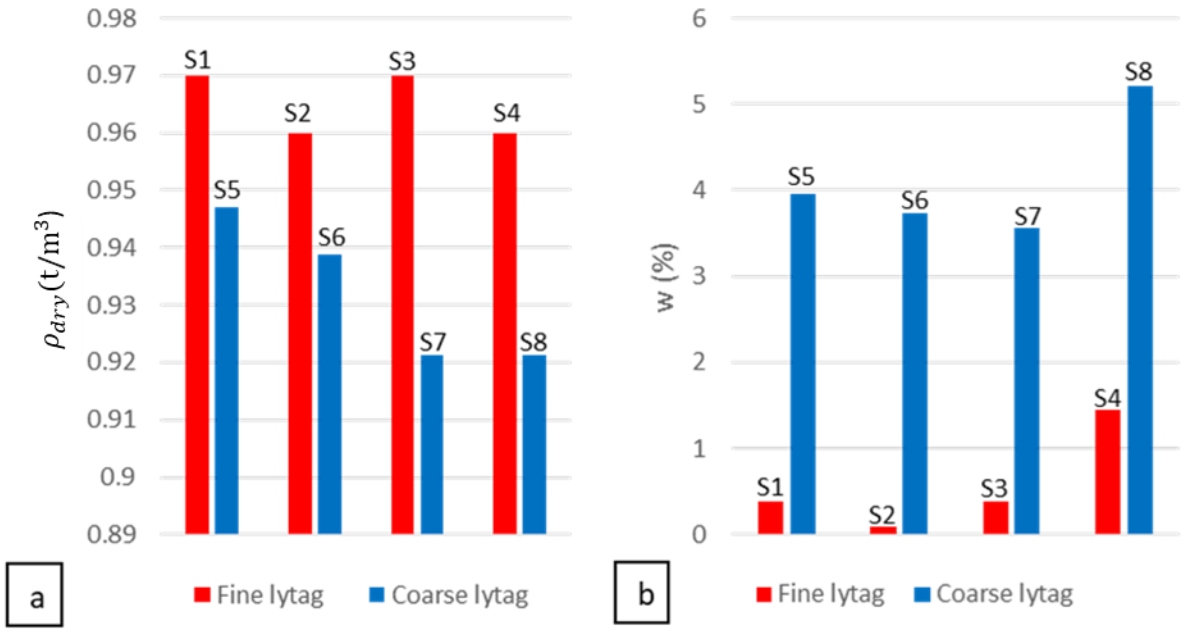


Figure 5.6: Specimen density (a) and water content (b) before testing

The dry density and initial water content of the tested specimens are shown in Figures 5.6a and 5.6b. These suggest that the collapse potential is not sensitive to density. The fine Lytag specimens were in a denser state and yet had the higher collapse potential. The influence of the initial water content is not that clear but possibly there was a more marked response to inundation with the drier fine Lytag specimens. Initial water content and dry density are plotted against collapse potential in Figure 5.7. The trends, particularly in terms of density, are not what might be expected.

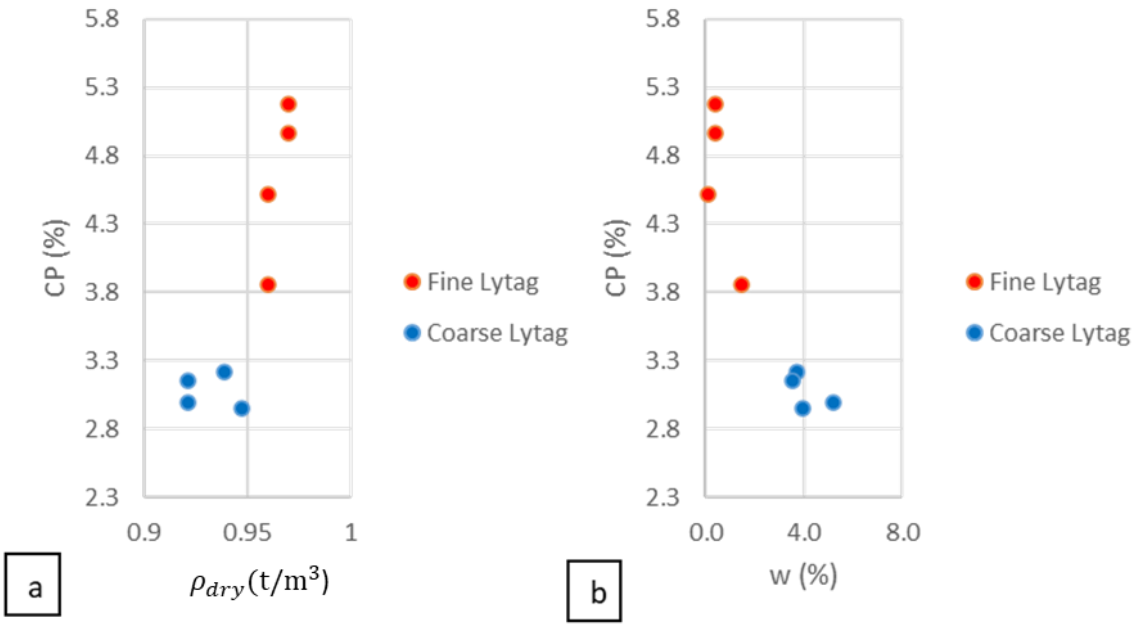


Figure 5.7: The effect of specimen density (a) and water content (b) on collapse potential

5.5.3 Collapse mechanism

The data given in Figures 5.8a and 5.8b show first how the vertical strain develops from the application of the collapse load and the subsequent additional strain from inundation. The collapse that starts taking place during inundation stages leads to the loading plate losing contact with the top of the specimen, hence in all cases there is an initial decrease in stress, sometimes quite rapid, followed by an increase back to the target value of 280 kPa. Strains continued to develop during this reloading and remained almost constant once it was reached.

In the unloading stage, both fine and coarse Lytag had a similar unloading response of less than 0.5% in all tests which indicates the specimens rebound is very limited in both Lytag particle sizes.

To investigate the effect of binder content and lateral confinement, further tests were performed using the larger container on specimens S9, S10, S11, and S12. These tests are now discussed in Sections 5.5.4 and 5.5.5.

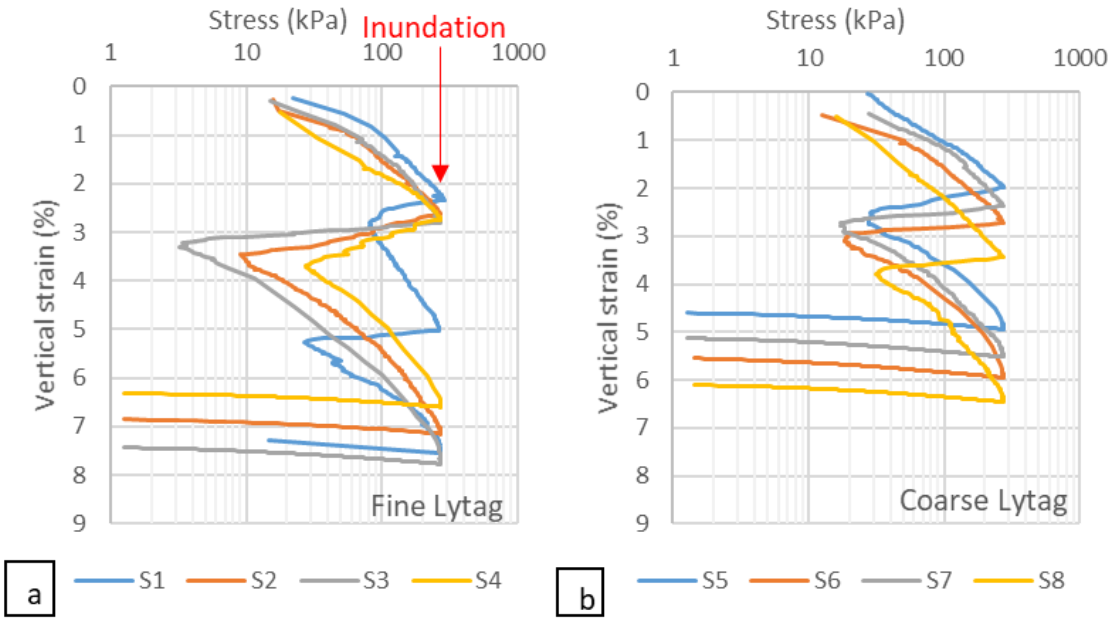


Figure 5.8: Vertical strains that developed during loading and inundation for the fully lateral confined specimens

5.5.4 Effect of kaolin percentage on collapse potential

In order to gain an initial understanding of the behaviour of collapse in gravelly soils using analogue specimens, Ofosu (2019) investigated the potential of gravelly soil fabric to collapse in 1-D compression using Lytag with different binder percentages. The Lytag size and groups and the mould dimensions were the same used in this study. The specimens were prepared using a similar procedure to that described in Section 4.6.3.1. He studied the effect of three percentages of kaolin as a binder (5%, 15%, and 25%) on collapse potential under a collapse stress of 220 kPa. Michael Ofosu's conclusions are summarised in Figure 5.9 which shows, that under this 1-D testing condition, the fine Lytag collapsed more than the coarse Lytag at the lower kaolin percentage. However, with 25% of kaolin, both the coarse and fine Lytag exhibited the same collapse potential.

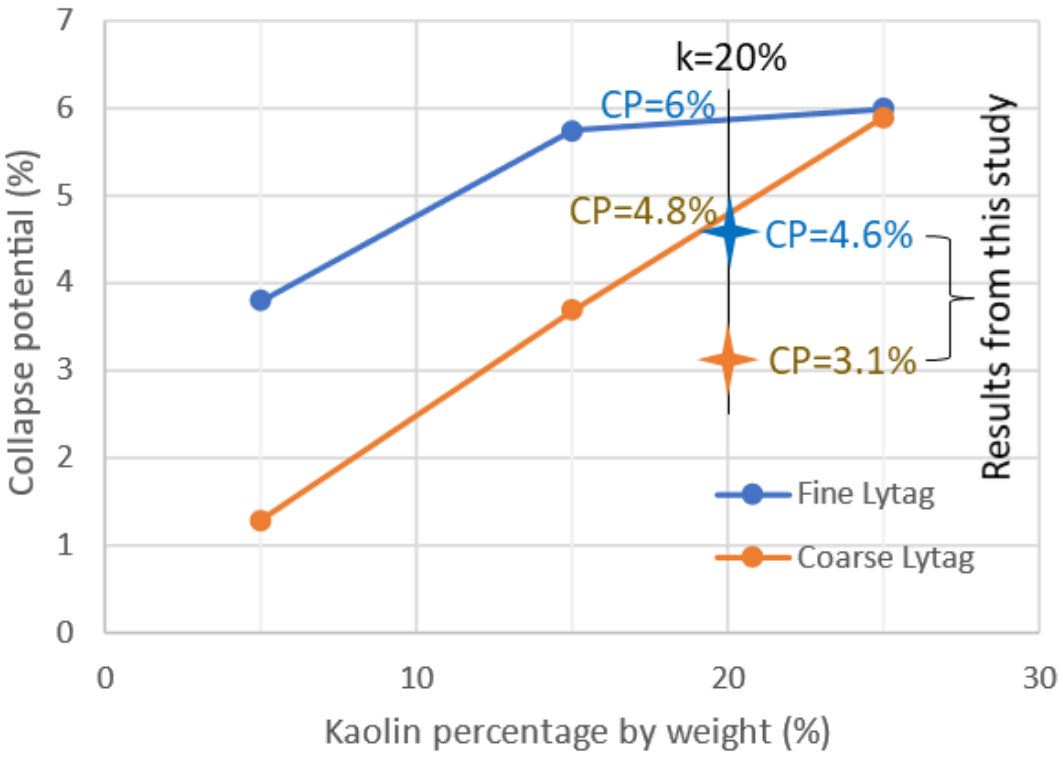


Figure 5.9: Effect of Lytag size and binder percentage on collapse potential (Ofosu, 2019)

At k = 20% the specimens in this study were prepared and tested at a slightly higher collapse stress of 280 kPa. The average collapse potential in the fine Lytag is 4.6 % and 3.1% in the coarse Lytag. These collapse values are slightly less than Ofosu's results at k=20% (6% and 4.8% as shown in the Figure 5.9), which were expected to increase with collapse stress rather than decrease. This suggests that collapse is sensitive to the kaolin percentage and potential differences in the specimen preparation procedure.

5.5.5 Collapse of partially confined specimens

The results from the tests with the reduced degree of confinement are shown in Figures 5.10a and 5.10b. As with the fully confined tests just described, the average collapse potential of the fine Lytag specimens is greater than that of the coarse specimens. However, the average collapse potential at this degree of confinement in the fine Lytag is 40.6% and 34.4% in the coarse Lytag. These collapse potential values are roughly an order of magnitude greater than the collapse values under the restrained conditions covered in Section 5.5.2.

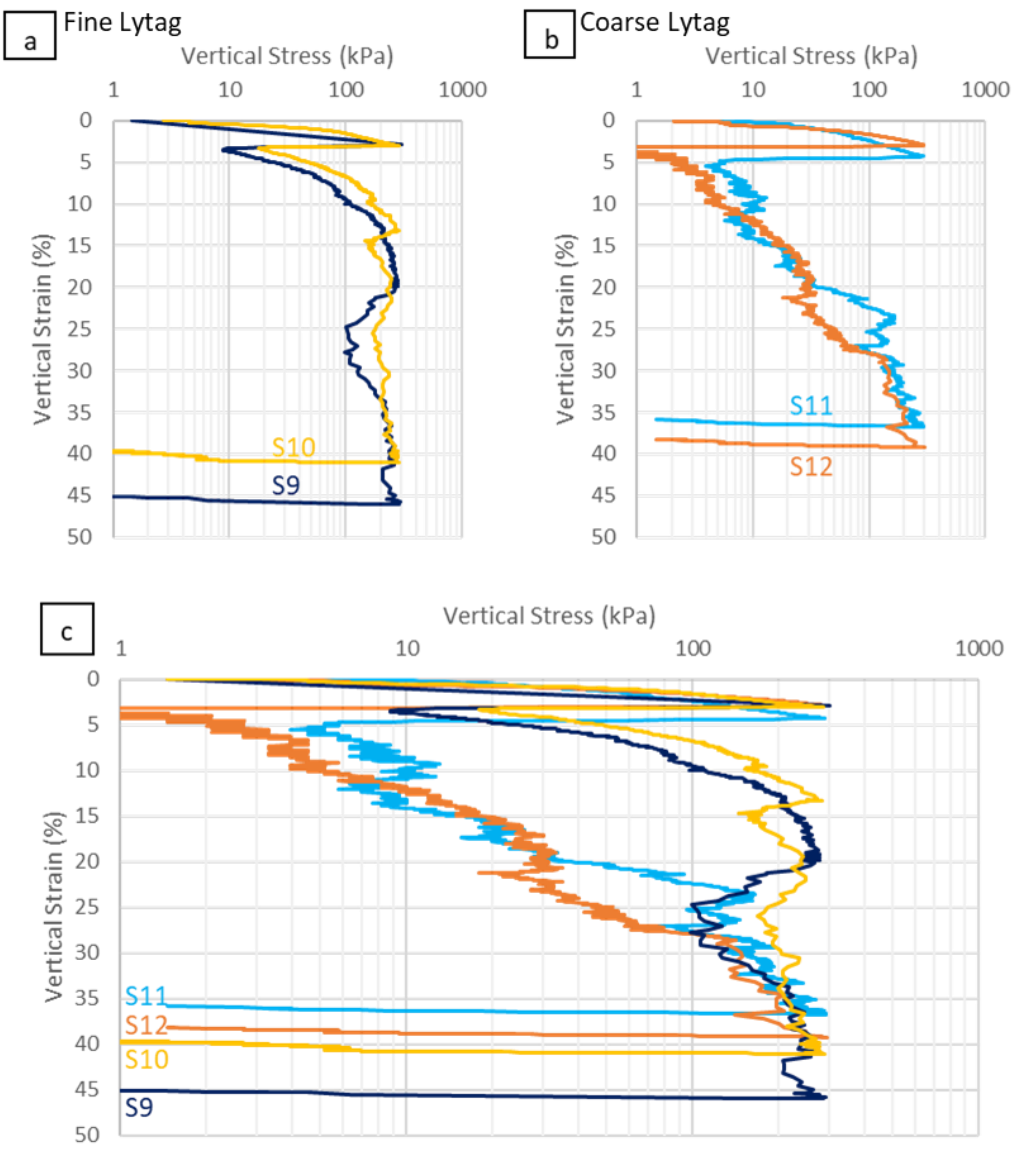


Figure 5.10: Vertical strains that developed during loading and inundation for the partially laterally confined specimens of (a) fine and (b) coarse Lytag and (c) combined results

Under this degree of partial confinement, when inundation started, the coarse Lytag specimens lost their contact with the loading plate more rapidly than the fine specimens and the stress dropped dramatically from 280 kPa to less than 10 kPa and then recovered gradually with strain increasing until reaching their equilibrium points as shown in Figure 5.10 band c. While the fine specimen stress levels dropped and recovered faster after about 10% strain and continued under the full collapse stress level (280 kPa) until collapse ceased. This is thought to be because the fine Lytag specimen has more contact points to transfer the stress during the inundation process compared with the coarse Lytag specimen.

5.5.6 General failure under partial confinement

An important observation is that the soil heaved around the loading plate after the inundation process indicating that as well as collapse there was also bearing capacity failure beneath the loading plate. If this is the case, the collapse strain values detailed in Section 5.5.5 are a combination of wetting-induced collapse and bearing capacity failure. The effect of specimen inundation at the vertical stress of 280 kPa under this partial degree of confinement resulted in these specimens reaching the limit of their bearing capacity. So, with this configuration, the test does not simulate the soil densification due to collapse alone, it overestimates it, but it has demonstrated the effect of lateral soil movement.

5.6 Chapter 5 conclusions

According to the summary in Section 5.5.5, the collapse potential increased by about 10 times under the condition of partial confinement compared with the fully confined specimens. This is a very significant increase in collapse potential which indicates that the degree of collapse is very sensitive to soil confinement. It can be concluded that assessing the collapse potential in the gravelly soils under the foundation at the study area using the conventional oedometer test under-estimates the values observed in the field. Therefore, developing a new procedure for assessing collapse more accurately in gravelly soils under such conditions is important. A 3-D controlled boundary condition procedure using triaxial apparatus would provide a better understanding concerning the effect of specimen confinement on collapse and the collapse mechanism under different stress configurations.

This conclusion was also confirmed from a parallel study to replicate the macro-response of these gravelly soils during collapse using the Distinct Element Modelling (DEM). Shen (2021) generated a 2-D DEM model to simulate collapse at the same particle-scale (Yue Shen was another MSc student studying at ICL who did her research dissertation under the supervision of Professor Catherine O'Sullivan with input from the Author). Nine collapse test DEM analyses were conducted using this model at different confining stresses of 50 kPa, 100 kPa, 150 kPa. At every confining stress, three levels of collapse stresses of 0.25, 0.5, 0.75 of the equivalent maximum shear stress were applied. The results from the DEM analyses of these tests indicated that the axial collapse strain decreases with increasing confining stress and increases with the inundation collapse stress. The volume deformation was found to increase with increasing confining stress and decrease with the increasing collapse stress.

Therefore, to measure and control more accurately collapse in a gravelly soil under the considered foundation types (strip and pad footings), a comprehensive study using a three-dimensional collapse testing procedure was developed, as discussed in Chapters 6 and 7. A triaxial apparatus was used for these 3-D collapse tests because it has greater flexibility in applying and controlling horizontal and vertical stresses.

Chapter 6 : Procedures for the 3-D triaxial collapse testing

6.1 Introduction

The necessity for conducting collapse tests in the triaxial apparatus was based on the observations and conclusions from the fully and partly laterally constrained tests, described and summarised in Chapter 5. Controlling the lateral stresses around the specimen was found to be important because they affect significantly the collapse potential values for the analogue gravelly specimens. Therefore, a new testing procedure for measuring collapse in gravelly soils in a three-dimensionally controlled test set-up was established using a triaxial system for testing 100-mm diameter specimens.

The modified triaxial collapse test procedure achieved the following: (1) A simplified, yet effective, testing procedure for measuring 3-D collapse in weakly bonded gravelly specimens was developed including specimen preparation and set-up. (2) Challenges relating to specimen set-up and membrane rupture were resolved and volume corrections for membrane penetration made. (3) Two different collapse mechanisms were observed. (4) Relationships between collapse potential and specimen density were developed.

In this chapter the following are presented and discussed: the characteristics of the analogue collapsible triaxial specimens; the specimen set-up; description of triaxial apparatus and collapse test procedure, the measurement of the membrane volume penetration and membrane rupture issues; a discussion about applying corrections to account for the deformed cross-sectional area and calculation of radial deformation; and the applied stress range. The results from the triaxial tests are presented, analysed and discussed in Chapter 7. The GDS testing software modules used in the collapse tests are provided in Appendix A.

The triaxial testing programme was implemented on eight sets of analogue collapsible specimens, each set containing four identical specimens, prepared according to the procedure described in Section 4.6.3.2. They were tested under a range of vertical stresses estimated to correspond to those imposed on the ground by the buildings in the study area, as assessed by Osman (2004) and under cell pressures ranging from 25kPa to 250kPa.

6.2 Studied parameters

A primary focus prior to the main triaxial testing programme was to establish an appropriate procedure for investigating collapse of the gravelly soil under triaxial conditions. The number of variables were minimised and so, in terms of stress, only the effects of cell pressure and deviator stress on collapse potential were studied. For the same reason the range of Lytag particle sizes used in the analogue specimens was kept constant to minimize the influence of particle size, shape and texture on collapse. Similarly, the percentage and plasticity of the binder material (kaolin) were kept constant as far as possible. The effect of specimen density on collapse was assessed both through inevitable small variations in density during the specimen preparation and also the specimen density was intentionally changed by varying the number of tamping blows to avoid membrane rupture issues as discussed in Section 6.6.1. Corrections were developed to account for density discrepancies in each set of specimens as discussed in Chapter 7.

6.3 Characteristics of the analogue specimens for triaxial testing

To facilitate tracking of the triaxial analogue specimens they were denominated, as explained by the example given in Table 6.1 (S406-0.09-0.86): a capital 'S' for 'specimen', followed three numbers separated by hyphens. The first number contained three digits (406) which stands for the specimen number with the first digit assigned to the mould number (4) and the second two digits the set number (06); the middle number stands for the kaolin mass as a ratio of dry weight of the Lytag; the final number relates to the specimen initial dry density before the test in t/m^3. It should be noted that the density value is very close to the dry density as the specimens were dried in an oven at $60^{\circ}C$ for seven days. Only a small amount of absorbed water is expected to be within the Lytag inner pores which is assumed to have no effect on the bond strength produced by kaolin. Therefore, these specimens were denominated as dry specimens in this testing programme.

Table 6.1: Example for explaining the triaxial specimens' denomination

Specimen: S406-0.09-0.86	**Description/Meaning**
S406	Specimen number S = Specimen 4 = Mould number 06 = Set number
0.09	Binder mass = 0.09 of the Lytag mass
0.86	Specimen dry density = 0.86 t/m^3

Table 6.2: Characteristics of the analogue specimens for triaxial testing

Count	**Set No.**	**Specimen symbol**	**Tamping process**
1	0	S200-0.09-0.90	3 layers - 5 blows(2.6kg)/layer
2		S400-0.20-1.00	
3	1	S101-0.09-0.92	3 layers - 5 blows(2.6kg)/layer
4		S201-0.10-0.94	
5		S301-0.09-0.92	
6		S401-0.09-0.92	
7	2	S102-0.10-0.92	3 layers - 5 blows(2.6kg)/layer
8		S202-0.09-0.91	
9		S302-0.10-0.91	
10		S402-0.10-0.93	
11	3	S103-0.13-0.94	3 layers - 5 blows(2.6kg)/layer
12		S203-0.13-0.98	
13		S303-0.13-0.97	
14		S403-0.14-1.01	
15	4	S104-0.11-0.98	3 layers - 5 blows(2.6kg)/layer
16		S204-0.11-0.97	
17		S304-0.11-0.96	
18		S404-0.11-0.95	
19	5	S105-0.09-0.90	4 layers - 0 blows/layer
20		S205-0.09-0.90	
21		S305-0.09-0.87	
22		S405-0.09-0.87	
23	6	S106-0.09-0.86	4 layers - 0 blows/layer
24		S206-0.09-0.87	
25		S306-0.09-0.88	
26		S406-0.09-0.86	
27	7	S107-0.10-0.88	4 layers - 0 blows/layer
28		S207-0.10-0.88	
29		S307-0.10-0.88	
30		S407-0.10-0.90	
31	8	S108-0.10-0.92	3 layers - 5 blows(0.2kg)/layer
32		S208-0.10-0.93	
33		S308-0.10-0.92	
34		S408-0.10-0.93	

As explained in Section 4.6.3.2, producing homogeneous triaxial collapsible specimens was challenging. In these specimen sets, two different tamping processes were used. Sets 1, 2, 3 and 4 were prepared using three layers compacted with a 2.6 kg tamper. Later in the programme, to maintain specimen homogeneity and produce specimens with lesser dry density, sets 5, 6 and 7 were prepared in four layers with no tamping, each layer being levelled off using a long spatula. However, two of the specimens from sets 6 and 7 collapsed during the extraction process due to their weak structure as described in Section 4.6.3.2 and shown in Figure 4.20. Set 8 was planned to be tested under a cell pressure of 200 kPa, therefore, a lighter tamper of 0.2 kg weight was used to tamp the three layers (5 tamping blows per layer). This was mainly to minimise the possibility of membrane rupture due to deep penetration of the membrane. This issue is discussed in Section 6.6.1.1. All the analogue specimens that were prepared for the triaxial testing programme and their characteristics are summarised in Table 6.2.

6.4 Description of triaxial apparatus

The testing apparatus used to conduct the 3-D triaxial collapse tests is a GDS permeameter that can operate under triaxial conditions. Although the apparatus is arranged such that it operates as a permeameter, it can operate as a conventional GDS triaxial system. The various elements of the apparatus are shown in Figure 6.1. It is an advanced multi-function system with flexibility in the operation processes which can be controlled manually and/or automatically using a computerized system through specifically designed software provided by the GDS company. The apparatus hardware contains eight main units: (1) a 50-kN capacity loading frame; (2) a cell chamber (2MPa pressure capacity); (3) a 50-mm range external displacement transducer; (4) a 16-kN capacity submersible load cell; (5) five volume/pressure controllers (each with a 200-cm^3 capacity and through which up to 4MPa water pressure can be applied); (6) an infinite volume control unit; (7) a 5-litre water storage tank; and (8) a computer connected to its display screen. Figure 6.1 shows the assembly and the annotation of these units including some other parts related to the cell chamber. A simplified schematic diagram showing the connection between the various apparatus components and their function in the testing programme is described later in this chapter (Section 6.7.2 and Figure 6.12). Checking and operation of the components of the GDS apparatus that were used are covered in Appendix A.

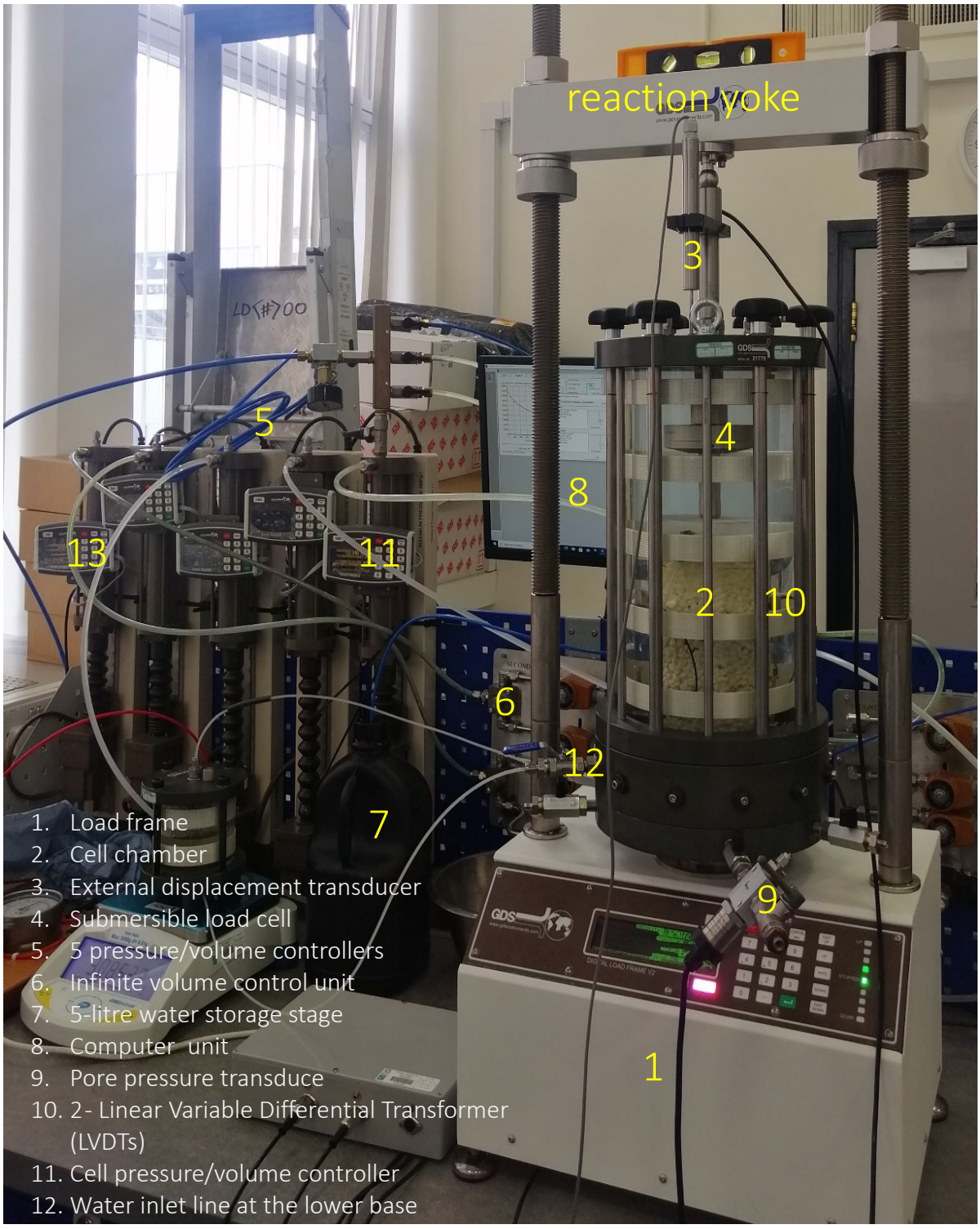


Figure 6.1: The GDS system used for the triaxial testing programme

6.5 Specimen set-up for triaxial testing

The specimen set-up is summarised in seven steps as shown in Figure 6.2, each step is labelled in the figure and referred to in the following descriptions. Having prepared the specimen as

described in Section 4.6.3.2, porous stones and filter papers, were placed in contact with its upper and lower surfaces, (1), to facilitate the inundation process. The porous stones were used to distribute the water evenly and the filter papers to minimise the amount of fines washed out of the specimen into the porous stones and the drainage tubes during inundation. Two fibre strips, each 3-cm wide, were wrapped around the top and base of the specimen to cover the gap between it and the porous stones (and platens), (2). These were to minimize the possibility of membrane penetration into the gap and consequent rupture as explained in Section 6.6.1.2. The effect of these strips on the magnitude of collapse is discussed in Section 7.5.3. After these precautions, a latex membrane, 0.3-mm thick, was positioned around the specimen using a membrane stretcher, (3). The membrane helped keep the bond between the Lytag particles stable by holding the specimen together during the process of transferring it to be set up within the cell chamber of the GDS permeameter.

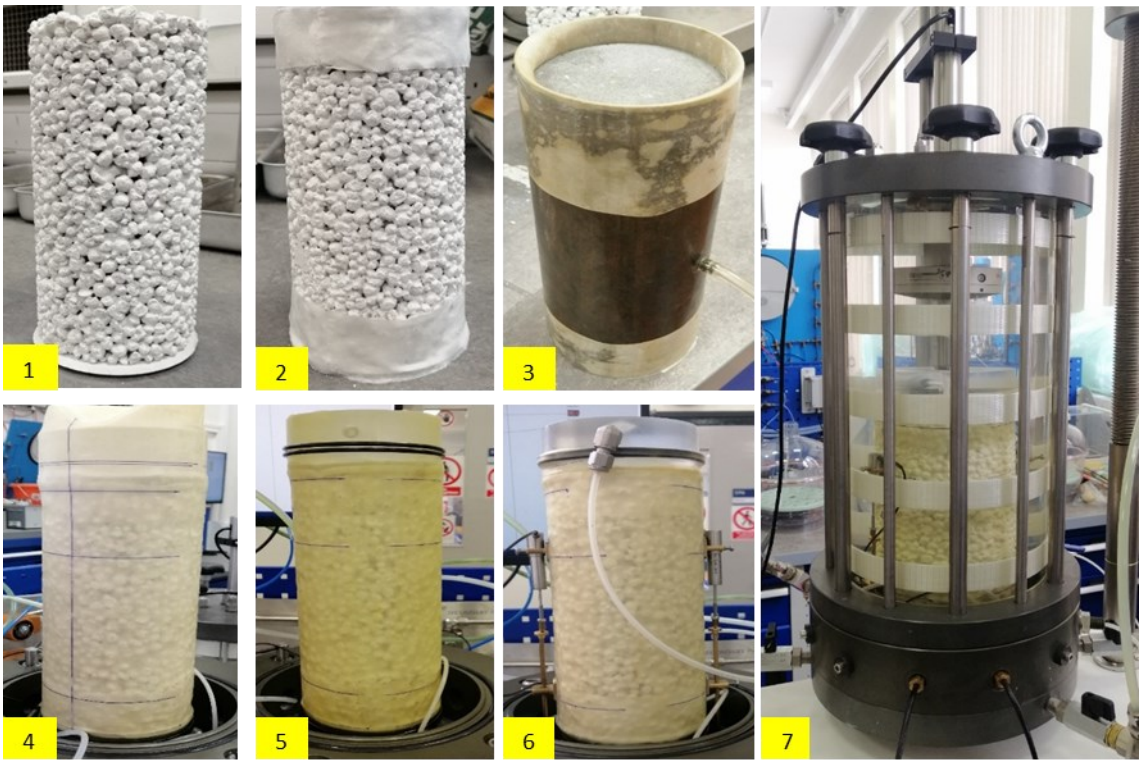


Figure 6.2: Specimen set-up for triaxial testing

Before placing the specimen on the base pedestal, the outer surface of the pedestal, where the membrane would be held tight, was coated with a thin layer of high vacuum silicon grease to eliminate any cell water leakage into the specimen during the test. Then the lower edge of the membrane was folded back outside, cleaned of any dust, the specimen placed concentrically on the pedestal and the folded membrane was rolled down gently around the greased pedestal,

avoiding trapping any air bubbles between the membrane and the pedestal, (4). Two O-rings were placed at the base to hold the membrane tight against the pedestal, (5). A similar procedure was followed for the top cap. Two local LVDTs for measuring axial strain were then attached (these LVDTs are discussed in Section 6.6.3). Finally, the top cap air drainage/venting tube was connected, (6).

The cell chamber was then placed around the specimen and the load cell extension was gently lowered so that the locating pin was just touching the top cap recess in the centre. This provided a good indication that the specimen was positioned straight without any tilting. The load cell was then raised slightly while screwing down the cell chamber bolts to connect the chamber tightly to its lower base, (7).

With the specimen and chamber securely in place, the loading frame reaction yoke (see Figure 6.1) was adjusted and connected to the submersible load cell and set in a zero position. The cell chamber and GDS cell controller were filled with water and air bubbles removed using the air-vent valve at the top of the chamber, by applying a nominal flow through cell pressure of about 5 kPa.

Finally, the external displacement transducer was set in the correct position with the transducer tip just touching the top of the cell chamber to capture the full range of vertical deformation (remembering that axial load is applied/maintained by raising the base unit of the loading frame). At this point the test set-up is complete and the system ready to perform a test.

6.6 Challenges related to testing gravelly specimens

6.6.1 Membrane rupture

The primary target was to investigate the 3-D collapse for the two Lytag groups that were used in the 1-D collapse tests described in Chapter 5, this range was categorised as fine Lytag (4 mm to 9 mm) and coarse Lytag (9 mm to 14 mm). However, the particle sizes of coarse Lytag was excluded from being tested under 3-D collapse conditions because of membrane rupture issues, an example of which is shown in Figure 6.3, and the limited time. This range of Lytag particle sizes resulted in considerable open voids at the surface of the analogue specimens which led to issues of membrane penetration into them and eventually rupture during the application of cell pressure and shearing stages, especially at higher values of cell pressure and collapse stress. This rough surface topography allowed the membrane to penetrate very deep locally at what initially seemed to be random locations on the specimen surface. After running

a number of tests, it was realized that the membrane rupture usually occurred at two main locations at either the middle or at the top/base of the specimen. Two improvement techniques to minimize the rupture possibility were evaluated to allow the triaxial testing programme to proceed successfully.

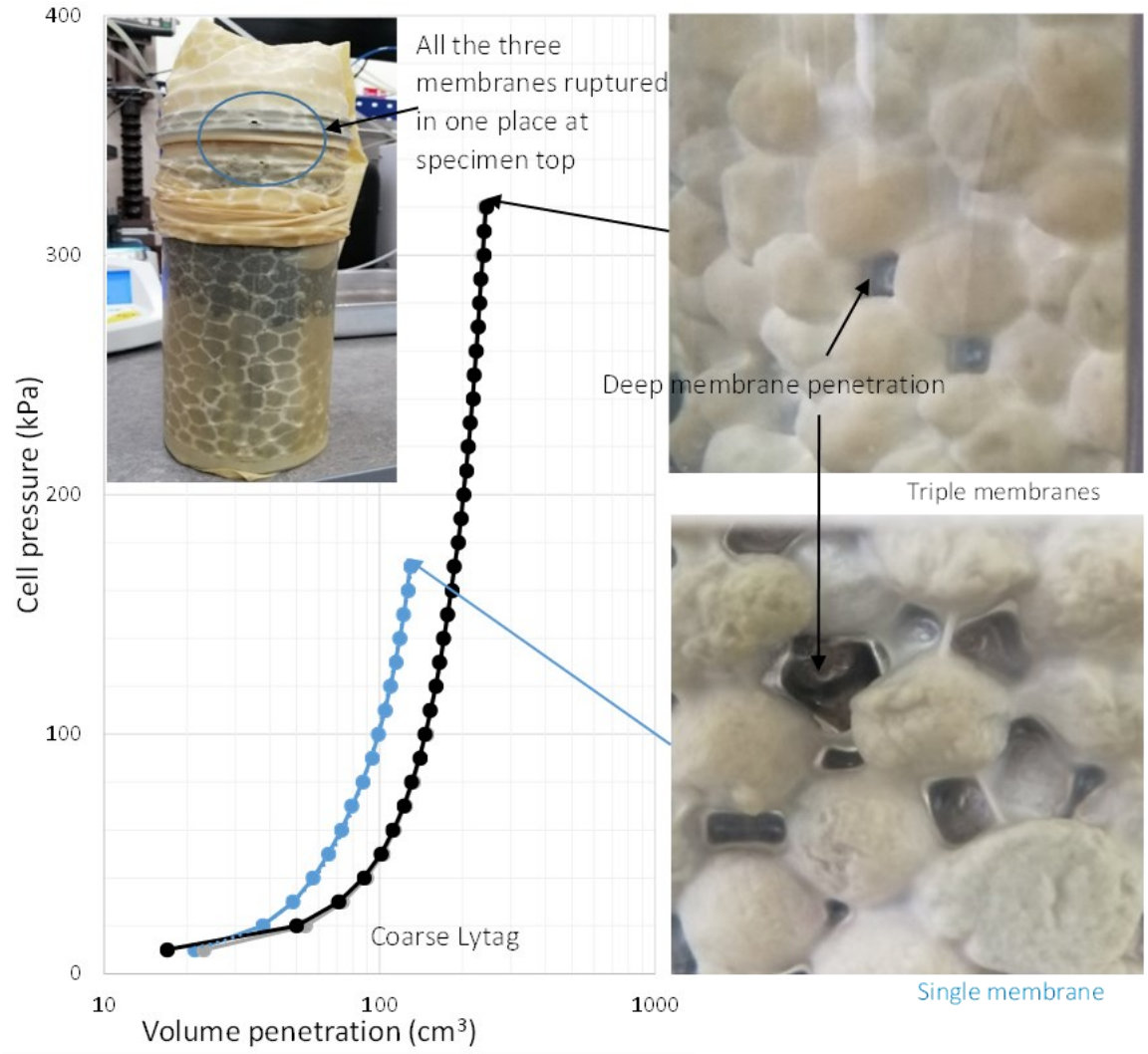


Figure 6.3: Improving the membrane rupture resistance by tripling the number of membranes

6.6.1.1 Increasing the numbers of membranes technique

Using various numbers and thicknesses of membranes or constructing a thin annular sand shell around the outside of a specimen have been attempted by other researchers to overcome the effect of membrane penetration and its influence on volume deformation in gravelly soils as shown in Figure 6.4 (Evans and Seed, 1987).

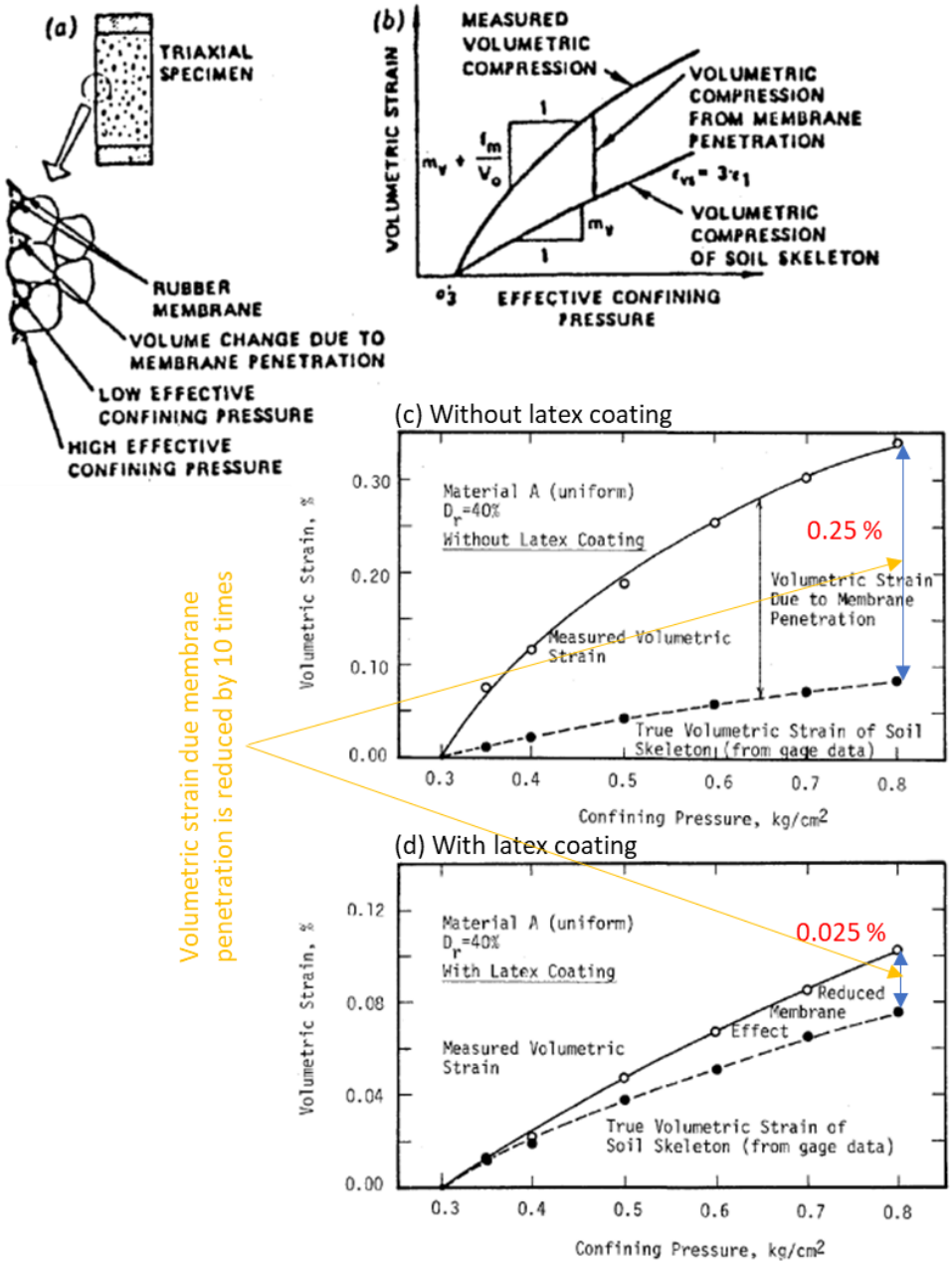


Figure 6.4: (a) membrane penetration in a triaxial specimen (b) determination of membrane flexibility from the results of isotropic compression tests (after Lade and Hernandez, 1977) & volumetric strain due to membrane penetration for tests (c) without and (d) with Latex Coated Membranes (after Torres, 1983) – cited by (Evans and Seed, 1987)

The effect of membrane thickness was not investigated in this testing programme but a trial using three membranes to reduce the possibility of membrane rupture was undertaken as shown in Figure 6.3, after observing that the effect of two membranes did not effectively reduce the membrane penetration. The three latex membranes (each 0.3-mm thick) were used to seal the specimen and were tested by applying 10 kPa increments of cell pressure, CP, to a target cell pressure of 200 kPa (the data points shown in grey in Figure 6.3). These three latex membranes

withstood rupture under this cell pressure (200 kPa). After that the cell was decreased incrementally (each 10 kPa) until it reached zero and then applied again with the same rate until they ruptured at *CP* = 320 kPa (the data points shown in black in Figure 6.3). The membrane penetration volume was compared with that of a similar specimen confined with one membrane. These three membrane layers successfully increased the resistance against rupture enabling a CP = 320 kPa to be applied before rupture occurred, almost twice that a single membrane could withstand with rupture occurring at CP = 170 kPa. Also, the volume and number of deep membrane penetrations decreased with the triple membranes, as evident from Figure 6.3.

However, tripling the number of membranes generated new uncertainties in the accuracy of measuring the specimen volume strain. This could increase the membrane compliance which might lead to underestimation of the specimen deformation and overestimations of its maximum shear stress. Both factors would need to be investigated and corrected for. An additional issue is that assembling these three membranes was very complicated and led to air bubbles being trapped between them. Consequently, the membrane volume penetration was erroneously measured as being greater with the three membranes set-up compared with one membrane set-up. In reality the membrane penetration volume should be less with three membranes, as can be seen in Figure 6.3.

Even at CP=320 kPa, the triple membranes ruptured at the top of the specimen which confirmed that the rupture issue is very localized as shown in Figure 6.3. Therefore, it was important to obtain a localized solution to solve this specific rupture problem and to overcome the tripling membrane drawbacks.

Another concern with using three membranes was that they might have adverse effects on the specimen when setting it up and during the test. Applying the membranes might induce an increase in the Lytag (inter-particle) stresses causing specimen compression. During the inundation stage of the test, they might inhibit radial dilation.

6.6.1.2 Using fibre cloth strips

After the triple membranes ruptured at the top of the specimen, it was concluded that the membrane was most likely to rupture at the top or base of the specimen. This is because the Lytag particles created a gap between the porous stones and the specimen ends (at its top and base). This gap was about 1-mm to 4-mm wide which, at its maximum value, is around half the maximum Lytag particle size. This gap could be associated with the main and secondary

bedding that is discussed in Section 7.5.3. Filling this gap with compressible material was considered but this could disturb the specimen and inevitably lead to overestimates of the specimen vertical strain. It was therefore decided to bridge and reinforce this gap from outside in the vicinity of where the membrane penetrates using fibre cloth strips.

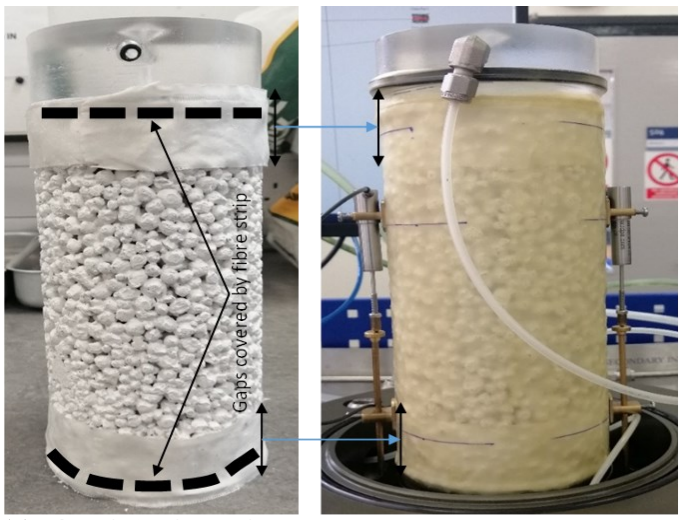


Figure 6.5: Reducing membrane rupture by using fibre cloth strips

Two fibre cloth strips, each of 3-cm width and 33-cm length, providing a 1.6-cm overlap and πD length, were wrapped around the specimen, before placing the membrane, to bridge the gaps at the top and base of the specimen as shown in Figure 6.5. The strips were sufficiently overlapped across the porous stones and the specimen in order not to slip inside the gap. Both ends of each strip were slightly greased, with mould release silicon grease, and overlapped to hold it in place during the process of placing the membrane.

These strips successfully solved the issue of membrane rupture at the top and base of the specimen and during the application of target cell pressure and shearing stage. The effect of these strips in the vertical strain was evaluated using local LVDTs as discussed in Section 7.5.3. It was concluded that the strips had no adverse effects on the specimen vertical strain.

After implementing these strips, rupture started occurring at a new location in the middle of the specimen, see Figure 6.6, leading to test termination. Fortunately, although this rupture happened many times, it was usually after the end of the inundation stage or sometimes as the wet specimen was approaching its maximum shear stress. So, the rupture occurred after the important stage of the test was complete. Rupture usually happened in places where the membrane penetrated between Lytag particles during the application of cell pressure and was then further squeezed during shearing by the relative movements of the particles between

themselves. This local rupture often occurred in the middle of the specimen from localised stress concentrations because, in this area, Lytag particles move and rotate to a greater degree than particles throughout the rest of the specimen height because specimen dilated more in its middle zone.



Figure 6.6: Membrane rupture at the middle of the specimen

6.6.2 Measurement of the volume of membrane penetration

To measure precisely overall changes in specimen volume, the membrane volume penetration and cell chamber expansion were quantified. Cell chamber expansion was assessed by filling the chamber with water only, without placing a specimen, and measuring volume changes with application of cell pressure incrementally. A mathematical expression was then developed with coefficient of correlation, R^2, of 0.999 as shown in Figure 6.7a. The quantification of the membrane volume penetration was complicated because of the dry nature of the tested specimens and their rough surface topography. The conventional procedure for measuring membrane volume penetration in saturated specimens is by subtracting the specimen volume change determined from measurements using local LVDTs from the specimen volume change as measured by the GDS back pressure volume gauge unit. This approach is not applicable for these dry specimens. Therefore, a different procedure for assessing the membrane volume penetration was developed based on a simple idea which involved measuring the membrane volume penetration for a series of dummy specimens with different surface pores and comparing them with representative analogue specimens. The membrane volume penetration

was measured by the GDS cell pressure controller which also provides an output of the volume of water pumped in/out of the cell and so constitutes a volume gauge unit as discussed in Section 6.8.1.

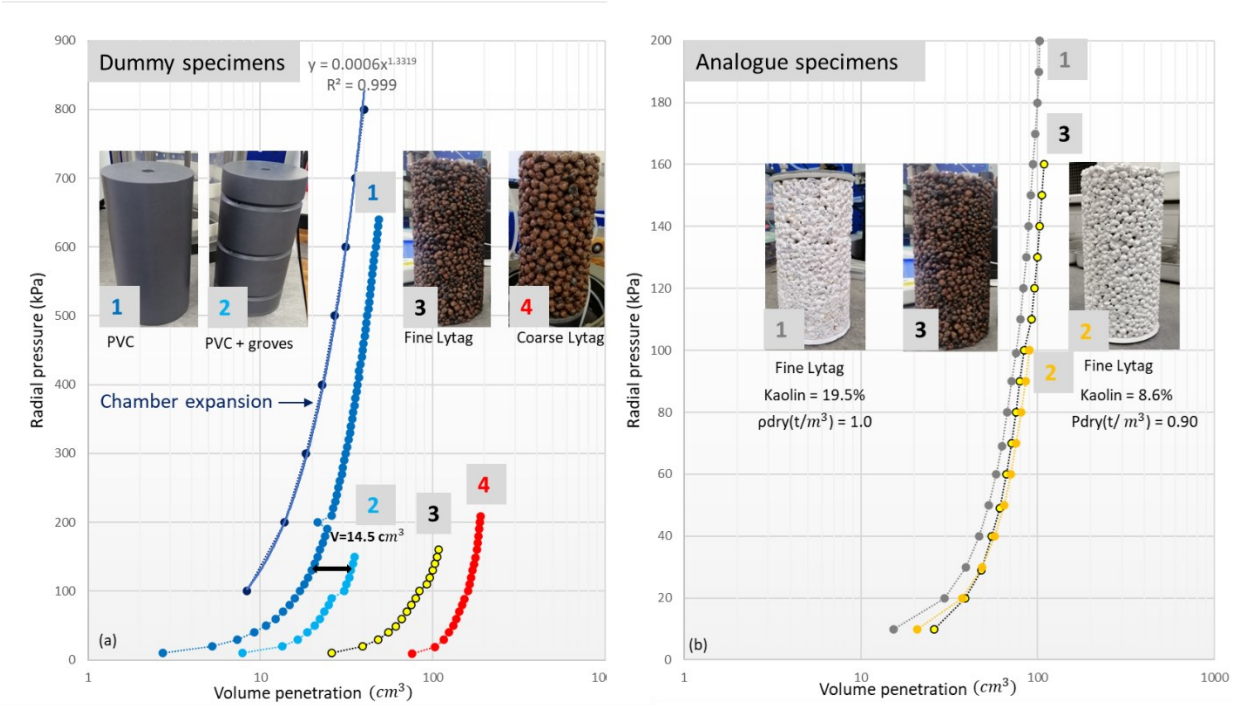


Figure 6.7: Membrane penetration and chamber expansion measurements

Four dummy specimens were made from different materials, as shown in the photographs in Figure 6.7a. Two dummy specimens were made from PVC (polyvinyl chloride), one was made without surface pores and the other with three circumferential V-shaped grooves with a known volume of 14.5 cm^3 to calibrate the membrane penetration volume measuring procedure. The groove width and depth are 8-mm and 4-mm respectively. The other two dummy specimens were made from mixing the two Lytag particle ranges with a strong epoxy resin. The first epoxy specimen was made from a similar range size of the Lytag (4 mm to 9 mm with D_{50} about 6.5 mm), that were used in preparing the analogue triaxial specimens, to provide a rigid specimen with relatively similar surface pores to the analogue specimens. The second resined specimen was made from coarser Lytag ranging from 9 mm to 14 mm (D_{50} = 11.5 mm). The purpose of these two resined dummy specimens was to allow comparisons to be made with the analogue collapsible specimens.

The membrane penetration volume of these dummy specimens is plotted against radial cell pressure in Figure 6.7a. It was found that there is good agreement between the membrane penetration volume curves of these dummy specimen with the volume of their surface pores.

First, the difference between the measured membrane penetration volume in the 'PVC' dummy specimens is exactly equal to 14.5 cm^3. This indicates that this membrane penetration measuring procedure, i.e. using the GDS cell pressure unit volume measurements, is appropriate. Also, the volume penetration in the coarse Lytag epoxy specimen is about 1.8 times the volume penetration in the fine Lytag epoxy specimen which is, from geometrical perspective, very close to the ratio between D_{50} for coarse and fine Lytag, 1.77.

The membrane penetration volume (MPV) of two analogue specimens prepared from fine Lytag with different kaolin percentages are compared with the resined fine Lytag dummy specimen as shown in Figure 6.7b. The density effect due to increasing the percentage of kaolin from 8.6 % to 19.5 % led to a minor reduction in the MPV. The MPV in the resined fine Lytag dummy specimen is slightly less but very close to that of the analogue specimen with 8.6% kaolin and is slightly higher than the analogue specimen with 19.5% kaolin. This means that the membrane penetration of these analogue specimens decreases with increasing amounts of kaolin which partially block the membrane penetration. By comparing the measured MPV with the epoxy resined dummy specimens (Figure 6.7), it can be seen that the effect of the size of the Lytag particles on the MPV is greater than the effect of the binder. It can also be seen in Figure 6.7b that, the membrane penetration into the analogue specimens does not increase significantly once the cell pressure increases above 100 kPa. In all these tests, the test terminated because of membrane rupture. As might be expected, the potential for the membrane to rupture early increases, in broad terms, with increasing MPV.

In summary, the MPV increases with cell pressure and surface pores. For the analogue specimens, more than the 90% of the MVP took place prior to the cell pressure reaching 100 kPa. In Figure 6.7b, the analogue specimen 1 exhibits less MPV than the rigid resined fine Lytag dummy specimen 3 which indicates that the volume deformation of the analogue specimens over this cell pressure range was very small. In view of this, it is assumed that volumetric strain of the analogue specimens during the application of the confining stress (cell pressure) is negligible and only starts to develop during application of deviator stress or inundation (these stages are discussed in Section 6.7). Consequently, all the volumetric strain measured by the cell pressure controller (also a volume gauge unit) is due solely to membrane penetration and chamber expansion. At any given cell pressure, the membrane penetration volume can be estimated by subtracting the relevant penetration curve from the chamber expansion curve. The analogue specimens' volumetric strain due to the subsequent stages at the specified cell pressure (25 kPa to 250 kPa) is determined by subtracting the cell pressure

volume gauge reading at the start of the application of deviator stress or inundation, which represents the total volume of the MPV and cell chamber expansion, from the current reading.

6.6.3 Development of local strain measuring system

A new local strain measuring system comprising two Linear Variable Differential Transformers (LVDTs) was devised to measure specimen vertical strains, especially during collapse. There were two main aims in using the two LVDT devices. The first was to evaluate the reliability of the collapse data captured using the external displacement transducer in its measurement of overall vertical deformation and from which the stiffness of these highly gravelly specimens can be determined. Second was to assess the effect of the local fibre cloth strips, used for minimizing the membrane penetration rupture at the top and base of the specimen as explained in Section 6.6.1.2, on the overall specimen collapse strain which is discussed in Section 7.4.3.1.

6.6.3.1 The LVDTs system description

This local measuring system was designed and fabricated by the technical staff in the Geotechnics Section at Imperial College London. Its main components are shown in Figure 6.8. The software for the GDS permeameter was designed to accommodate local strain measuring systems and the LVDTs were successfully connected and calibrated. The measuring range of the LVDTs is 10 mm and the maximum gauge length they can cover is 120 mm. The two LVDT sets were positioned diametrically opposite each other to compensate for any differences in the local axial deformation such as due to specimen tilting or bending.

Each set was designed to be attached to the specimen surface using two main supports at the ends and one secondary central support to adjust the verticality of the set. Each support has rectangular pad of 12 mm by 18 mm. The lower pad was positioned 20 mm from the specimen base to carry the transducer extension piece which is a brass bar of 3 mm diameter and 90 mm length. A small circular head of 8 mm diameter and 1.5 mm thickness was designed to be screwed into the top of the extension piece to support the core of the transducer. The top pad was positioned 140 mm from the specimen base to hold the transducer in place. The system was positioned down 20 mm from the middle of the specimen to capture accurately as much collapse as possible because the inundation process started from the base. Each pad was fitted with a flat-head screw to be able adjust and grip the transducer and the core in their initial positions to provide the maximum range of the transducer travel (10 mm).

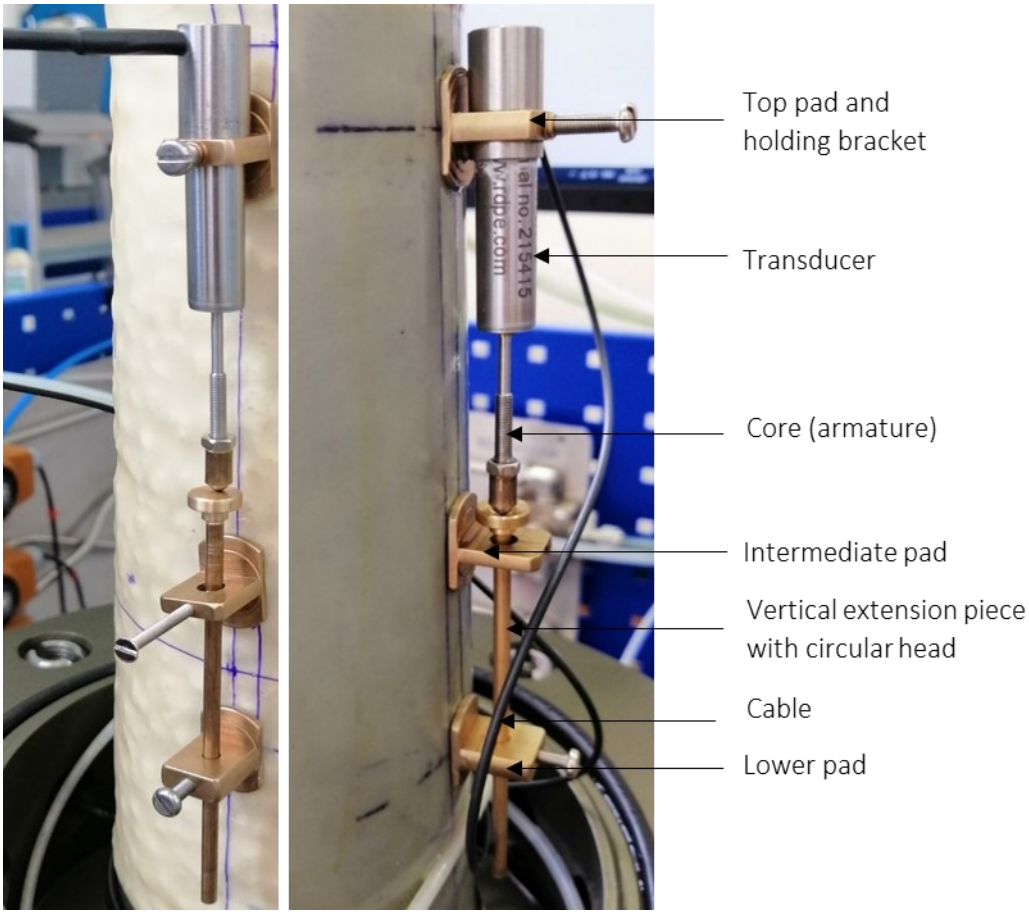


Figure 6.8: Description of the local LVDTs and their assembly

6.6.3.2 Calibration of the LVDTs

A micrometer was used for calibrating the LVDTs and their calibration plots are included in Appendix A. Their reading stability was successfully checked by testing them at 250 kPa cell pressure for 2 days. In this test the LVDTs were stuck to the PVC dummy specimen as shown in Figure 6.8.

6.6.3.3 Stability of the LVDTs at the specimen surface

When the LVDT system was first used with an analogue specimen, their output indicated instability during the application of cell pressure stage because of rough topography of the specimen surface. The membrane penetration tilted the system's pads causing the cores to slip from their circular supports and drop down. A simple solution was introduced to increase pad stability by increasing the pad contact area using a flexible circular acetate disc of about 30-mm diameter. This disc could easily be bent to be in full contact with the specimen and, at the same time, was rigid enough to resist any local movement under the pad due to any membrane penetration beneath it, as illustrated in Figure 6.9.

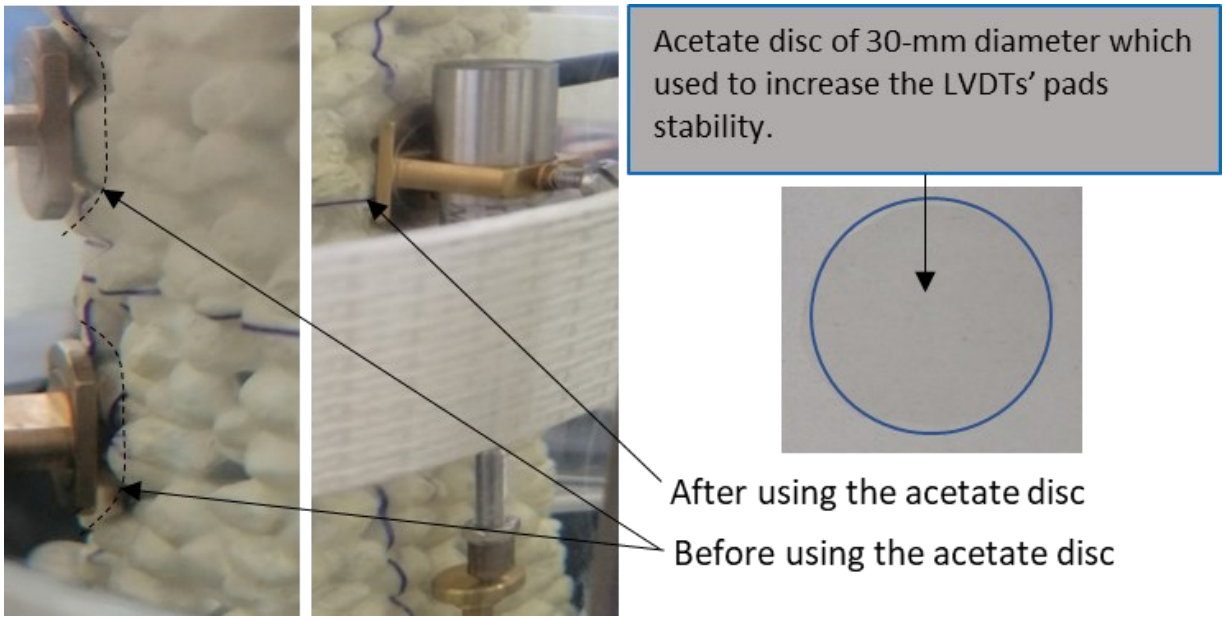


Figure 6.9: Improvement of the LVDTs stability by using 30 mm diameter acetate discs

6.7 Test stages and procedures

Two primary types of tests were conducted in the triaxial testing programme: dry shearing tests and collapse tests. Each of these contained various stages as described in the following sections. The triaxial GDS apparatus can be controlled using a number of modules. Those used in this testing programme are covered in Appendix A, where the input data and the sequence of mobilising these modules to accomplish a full test are illustrated using screenshots. The triaxial testing programme followed, where it is applicable, the standard triaxial procedures that was illustrated by Head (2014). A combination of consolidated undrained and drained tests was adopted as detailed in the following sections.

6.7.1 Dry shearing test description

This series of tests was conducted to develop the dry failure envelope of the analogue specimens. Each dry shearing test involved two stages: first the application of isotropic stress, setting a target cell pressure using the 'advance loading module', and then shearing using an appropriate 'standard triaxial test' GDS module, which is in fact for performing a consolidated undrained test type. These testing modules are described in Appendix A.

In the isotropic compression stage, the cell pressure was applied in increments of 10 kPa every 5 minutes. The volume of membrane penetration into the specimen surface pores was measured

after applying each increment during this stage using the cell volume/pressure controller. The confining/cell pressure values used in the study were 25, 50, 100, 150, 200 and 250 kPa.

The shearing stage was run by controlling the shearing strain rate. All specimens were sheared at a constant shearing rate of 0.0139 mm/min which is equivalent to about 10 % axial strain per day. This rate is twice the usual shearing rate adopted in the Geotechnics Section soil mechanics laboratories at ICL when testing clays, e.g., London Clay. This was deemed to be acceptable as the permeability of the analogue specimens is more than 10^5 higher than that of the London Clay, so this shearing rate for these gravelly specimens was appropriate while allowing sufficient readings to be made. The test termination condition was based on the axial strain, determined from the external displacement transducer output, such that it should not exceed 22%, as the capacity of the external transducer is 50 mm which allows a maximum axial strain of 25% to be reached (without resetting). However, most of the tests were terminated before reaching 22% because of membrane rupture.

6.7.2 Collapse test description

Four primary test stages were established, as shown in the schematic diagram in Figure 6.10a, to perform a full triaxial collapse test using the GDS apparatus. The first stage (1) is to subject the specimen to isotropic compression by applying a target all-around cell pressure using the cell pressure/volume controller unit. This controller pumps water into the cell chamber that surrounds the specimen to apply the target cell pressure. This was achieved, similar to the isotropic compression stage in the dry shearing test, using the 'advanced loading module' by controlling the stress rate to be incrementally applied of 10 kPa per 5 minutes.

The second stage (2 in Figure 6.10a) is the application of the deviator stress, q_c, at which inundation was to be affected (referred to in Chapter 5 as the 'inundation collapse stress'). The application of q_c was achieved using again the 'advanced loading module' by controlling the deviatoric stress rate to be applied continuously at a rate of 10 kPa per 5 minutes (as in the isotropic stage). The q_c values were calculated for each cell pressure as a percentage of the maximum shear stress that an analogue specimen could sustain at this cell pressure as explained in Section 6.9.1. This was the reason for running a series of tests with the specimens sheared dry to establish the failure envelope (as described in Section 6.7.1) before performing tests with an inundation stage. The maximum shear capacity for these low water content specimens tested is governed by the 'dry failure envelope' as annotated in the s' - t space plot in Figure 6.10b. The q_c values applied represented a percentage of the failure deviator stress, q_f, typically 10%,

25%, 50% and 75% were applied at each cell pressure level. The $\varepsilon_a - t$ plot shown in Figure 6.10c is used to describe a typical vertical stress-strain response for tested specimens during the application of q_c and the following steps of inundation and wet shearing.

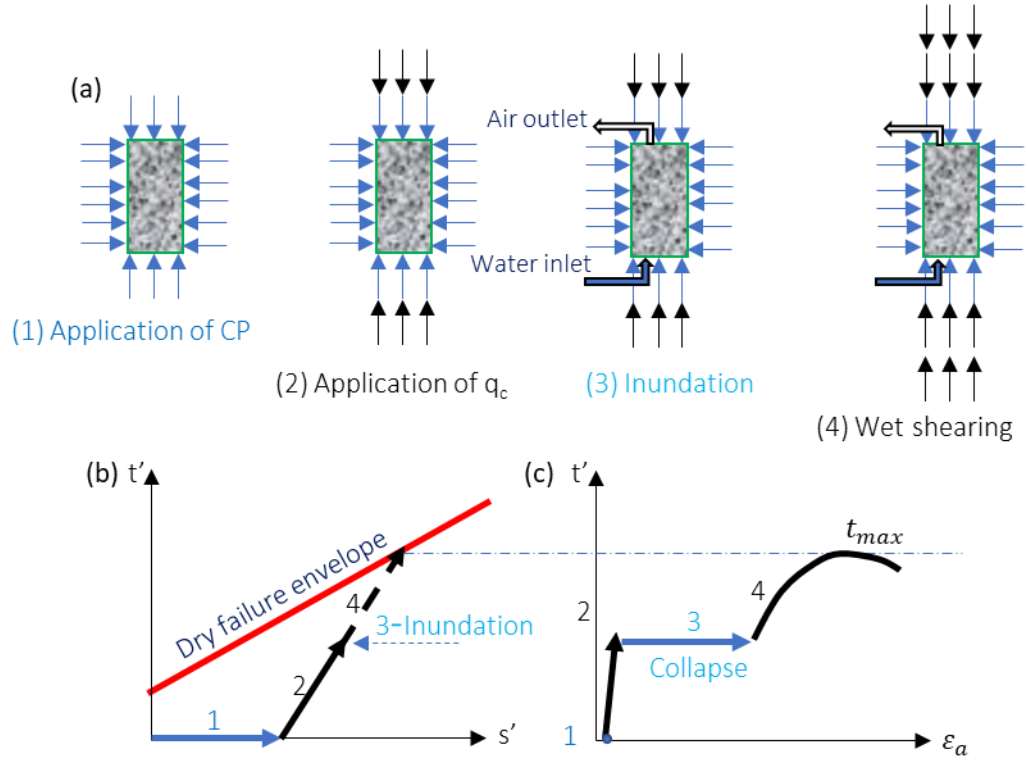


Figure 6.10: Schematic diagram describing (a) the triaxial collapse test stages; (b) the stress path followed; and (c) a schematic stress-strain plot.

The third stage (3) is inundation, by flooding at the specimen base, which was started once the specimen had equilibrated following the application of the inundation deviator stress, q_c. This equilibration was defined as when the change in the axial strain rate reached about 0.01%/minute (see Figure 6.11). The base pressure/volume controller unit was used to inundate the specimen through a base valve leading to its base (labelled 12 in Figure 6.1) while air was allowed to vent from the top of the specimen. The inundation rate was 40 cm^3/min and there was no build-up of pore pressure during the inundation process because of the air venting and the highly permeable nature of the specimens. To inundate the specimen fully, it was necessary to fill and empty the base volume controller unit three times consecutively which took five minutes each time using the 'fast fill' and 'fast empty' control options respectively, to achieve a maximum 'instant collapse' throughout the whole specimen height. During the emptying process, when water was pushed into the base of the specimen, there was a build-up in pressure unit indicated by the base pressure controller, reaching a maximum of about 50 kPa, but no

changes were registered by the pore pressure sensor at the base of the specimen. This build-up of water pressure is thought to be due to an increasing water velocity inside the tubes that link the controller with the specimen. During the inundation stage and the following specimen collapse, the q_c value (the axial stress) temporarily fluctuated/reduced by about 5kPa. This was different than in 1-D collapse that was discussed in Section 5.5.3 because the cell pressure controller kept equalising the subsequent volume changes due to collapse and maintaining the radial pressure constant.

The final stage (4 in Figure 6.10a) is wet shearing, which was applied after waiting for a second equilibration following inundation of 0.01%/minutes as illustrated in Figure 6.11. It is not defined as saturated drained shearing because the possibility of an entrapped air inside the Lytag micro pores is high. Wet shearing was performed at the same rate as that for dry shearing (10% axial strain/day). Reasons for continuing shearing after collapse were: (i) to observe whether there was any further collapse from increasing the deviator stress in addition to the expected axial compression from shearing; and (ii) to evaluate the effect of bonding loss on the peak shear strength by comparing the wet failure envelope with the corresponding dry failure envelope to gain insight into the soil behaviour after collapse. This topic is discussed in Section 7.5.

These four stages that were followed when conducting triaxial collapse tests and the relevant GDS triaxial system components used for implementing them are illustrated schematically in Figure 6.12.

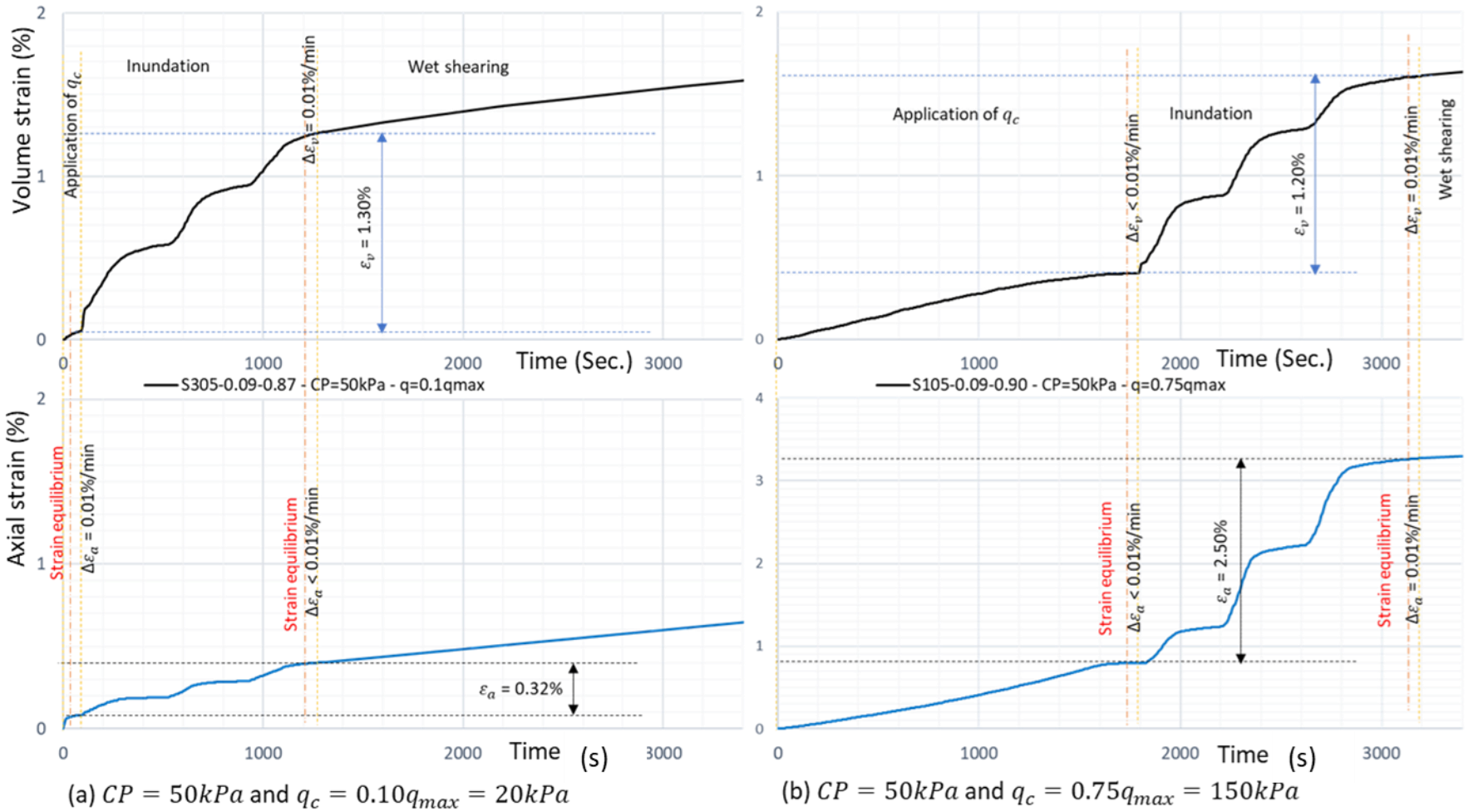


Figure 6.11: Typical examples of strain equilibrium before and after inundation

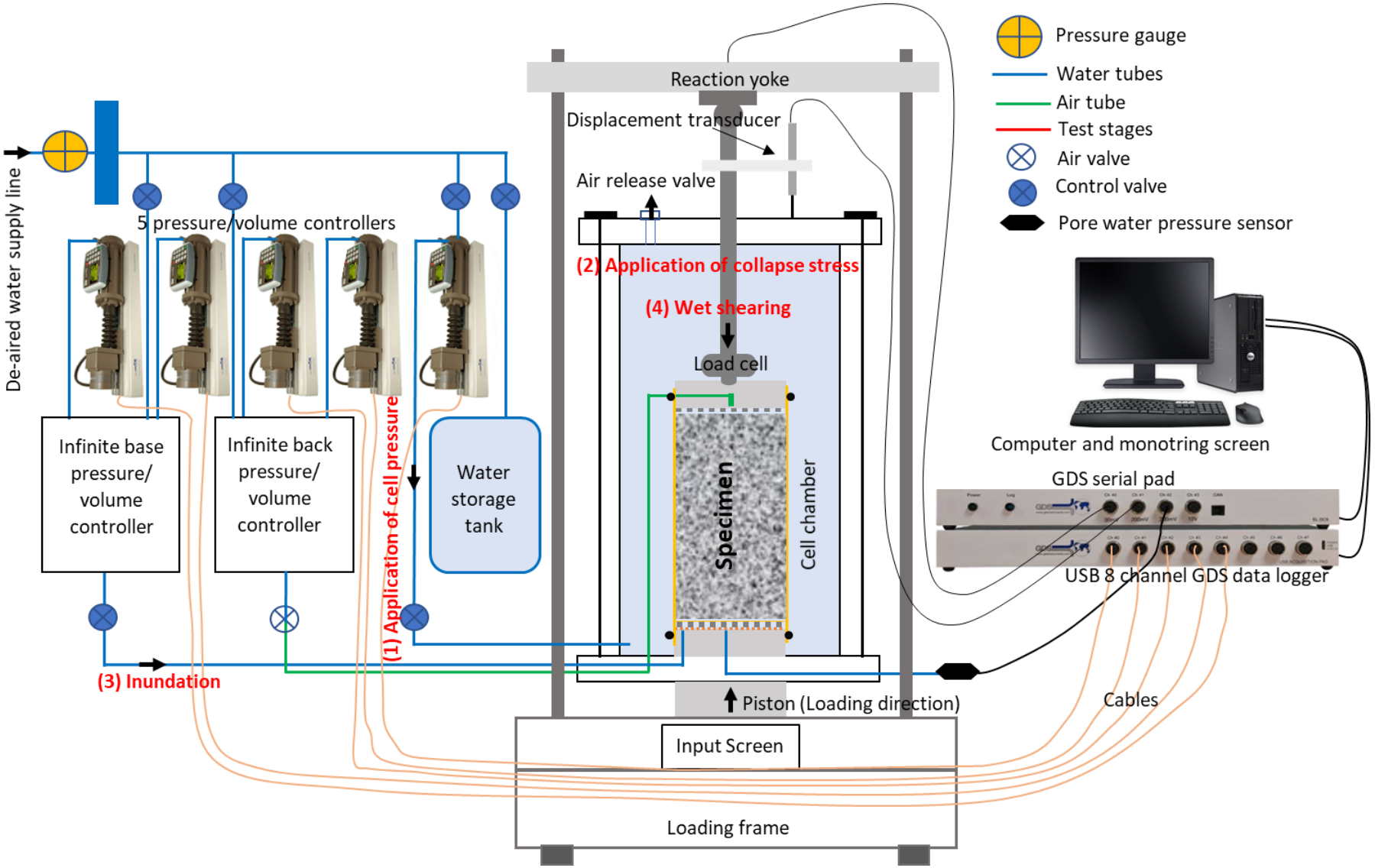


Figure 6.12: Schematic diagram illustrating the GDS triaxial system collapse test stages (labelled in red)

6.8 Recording and processing the triaxial testing data

6.8.1 Data collected from the GDS triaxial system

To obtain the required results from the 3-D triaxial collapse test, six primary sources of measured raw data were recorded and saved during each test by the GDS software, as described below.

1. Cell pressure (kPa) and volume change (cm^3); these two quantities are recorded independently of each other. The GDS standard pressure/volume controller (in essence a Bishop pump) has a 200 cm^3 volume capacity and can apply up to 4 MPa pressure and is used to apply the confining pressure and measure the overall specimen volume change. When the controller is programmed to target a higher pressure than its current one, the controller pumps water into the cell chamber to apply that pressure. When this targeted pressure is reached the controller stops pumping in water. Subsequently if any volume change occurs within the cell chamber due to membrane penetration or specimen deformation, the controller is automatically activated to maintain the target pressure which involves pumping more water in/out of the cell. For example, if the specimen inside the chamber contracts, the radial pressure decreases and immediately the controller starts pumping an equivalent volume of water to maintain the target pressure and vice versa. The water volume change in the controller is measured and so the overall specimen volume change can be determined, and whether the specimen is contracting or dilating during the test, see Figure 6.13. The term cell pressure volume gauge (CPVG) is assigned for the GDS standard pressure volume controller when volume change is considered to avoid confusion with the cell pressure (CP).

2. Pore pressure (kPa); there is a pore water pressure transducer connected to the base platen, on which the specimen rests, to measure the pore water pressure during the test. As the specimens were dry up to the inundation stage, initially a nominal zero measurement was registered up to that point. However, this transducer helped detect any membrane rupture during the test by registering a sudden increase in the pore water pressure. In all tests, this valve was kept closed to capture any build-up of pore water pressure. The data collected by this transducer revealed that there was a small increase during the shearing stage of 5kPa to 10 kPa, depending on the applied cell pressure, but generally this then remained constant. In some cases, the pressure decreased again when the specimen started to dilate in the late stages of shearing which is probably due to the considerable specimen volume change. Although, this

small pore water pressure was considered to have a low effect on the mean stress, it was corrected for.

3. Load cell output (kN); the GDS load cell is a submersible load cell type positioned inside the cell chamber and can measure applied loads up to 16 kN. As it is a submersible load cell, no corrections for ram up-thrust or ram friction need to be applied to the load cell readings. The loading rate of the 50-kN GDS load frame can be applied over a range from 0.00001 mm/min to 90 mm/min within which any required axial strain rate can be applied. For the specimens tested in this research 10%/day axial strain rate was set, equivalent to $0.0139\ \mathrm{mm/min}$.

4. Displacement transducer (mm); this GDS transducer is a linear displacement transducer (strain gauge type) with a range up to 50 mm, and a resolution of 0.0001 mm.

5. Time (S); in GDS, time is printed in two columns giving the total time of the test and that for each stage of the test separately. This time is very helpful to track the test development and to know exactly whenever there has been a manual pause. This was helpful because GDS software does not have the facility for comments to be written during the test.

6.8.2 Processing of the test data

6.8.2.1 Volumetric and axial strains

In this testing programme, the 'consolidated undrained standard triaxial' GDS module was used for shearing the specimen, even though it was dry, to avoid specifying a back pressure which is usually associated with the 'consolidated drained' test module. As the specimen was in a dry state during testing there is no build-up of pore water pressure as the specimen behaved as in a fully drained condition. Therefore, the corrected specimen cross-sectional area (A_c) during shearing is calculated as if the test were performed drained.

In stage (1) of applying cell pressure (Figure 6.10a), both this (the radial pressure, σ_r) and water volume change are recorded to calculate the membrane penetration and any specimen volumetric strain during this stage. The volumetric strain $\varepsilon_v = \frac{\Delta V}{V_0}$, where ΔV is the change in overall specimen volume which can be obtained from the CPVG after correcting for membrane penetration effects and cell expansion. V_o is the initial specimen volume, which is calculated from the initial specimen diameter, D_o, and height, H_o, values which are input into the GDS control software.

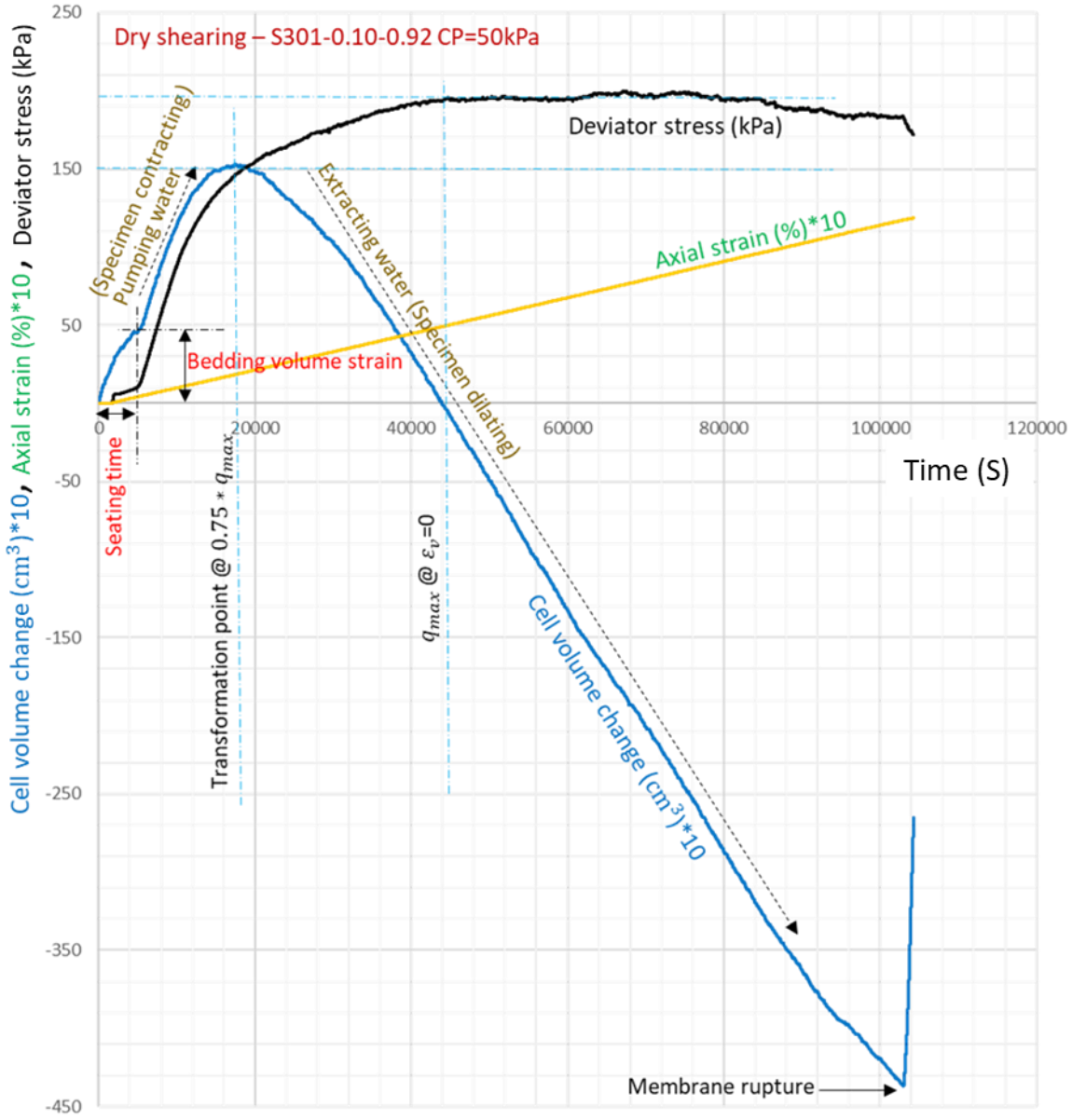


Figure 6.13: An example illustrating the capturing process of the specimen volume deformation (including the bedding strains), deviator stress and axial strain for one of the shearing tests

In the application of q_c (stage 2, Figure 6.10b), axial displacement, ΔH, and load cell readings, F, were recorded as raw data. Axial strain, ε_a, is calculated from the axial displacement measured by the external displacement transducer, $\varepsilon_a = \frac{\Delta H}{H_1}$. The deviator stress ($q$) is calculated from the load cell reading and the corrected area, $q = \frac{F}{A_c} = \sigma_a - \sigma_r$. Calculation of the corrected area, A_c, is explained in the following section.

From the uncorrected cell volume change plotted against time in Figure 6.13, the specimen contracted at the beginning of the shearing stage and then dilated. In this analysis, contraction is defined as $\varepsilon_v = +ve$ when water flows into the cell while dilation is defined as $-$ ve when the pressure volume controller starts extracting water.

The various specimen deformation modes (and the sign conventions associated with them) are given in Figure 6.14.

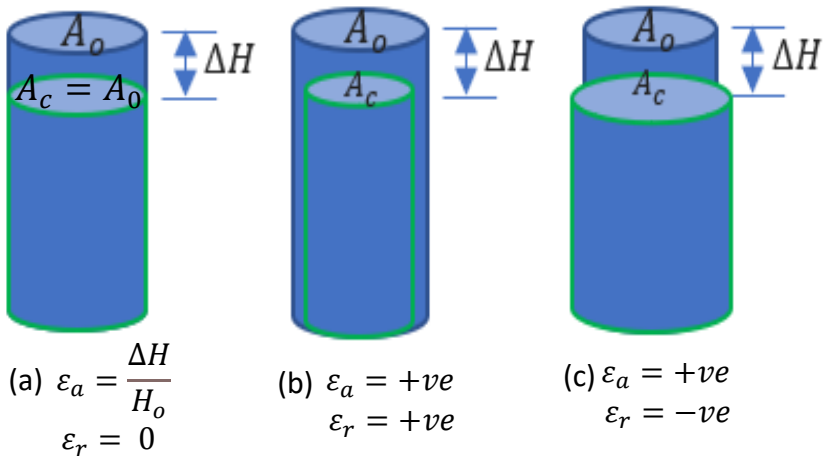


Figure 6.14: Schematic diagram explaining different specimens' deformation scenarios

Overall specimen volume change can be determined from the volume of water pumped out/in of the cell pressure GDS unit as illustrated in Figure 6.13. This volume change is expressed as ΔV_{CPVG}. Strictly speaking corrections need to be applied to account for membrane penetration and cell expansion/contraction. However, these were generally very small and during inundation there is no change in cell pressure and so in the following scenarios, these corrections are not considered.

(6) If $\Delta V_{CPVG} = \Delta H * A_o$ this means that the specimen contraction is axial in one sense and no correction is required but this is a very unlikely scenario.

(7) If $\Delta V_{CPVG} > \Delta H * A_o$ the specimen contracted in two senses axially and radially and so the corrected area is $A_c = \frac{\pi}{4} * D_c^2$ where D_c, the corrected diameter, is calculated from $\Delta V_{CPVG} = A_o \Delta H + \frac{\pi}{4}(D_o^2 - D_c^2)(H_O - \Delta H)$. According to the sign convention, these two terms are $+ve$ which means that the overall volume change is contraction. By rearranging the above expression, $D_c = \sqrt{\left[D_o^2 - \frac{4(\Delta V_{CPVG} - A_o \Delta H)}{\pi(H_o - \Delta H)}\right]}$.

(8) If $V_{CPVG} < \Delta H * A_o$ two scenarios of the specimen deformation are possible: contraction and dilation. In this case both the axial strain and volume strain are used to correct the specimen area, $A_c = A_o \left[\frac{1-\varepsilon_v}{1-\varepsilon_a}\right]$, where $\pm\varepsilon_v = \frac{\Delta V_{CPVG}}{V_o}$ (the sign of ε_v should be substituted) and $\varepsilon_a = \frac{\Delta H}{H_o}$.

6.8.2.2 Calculation of radial strain from axial and volume strains

It is important to calculate radial strain in order to understand the specimen's lateral deformation response. To determine its average value from the calculated axial and volume strains, it can be assumed that the deformed specimen form remains as a right cylinder as shown in Figure 6.15.

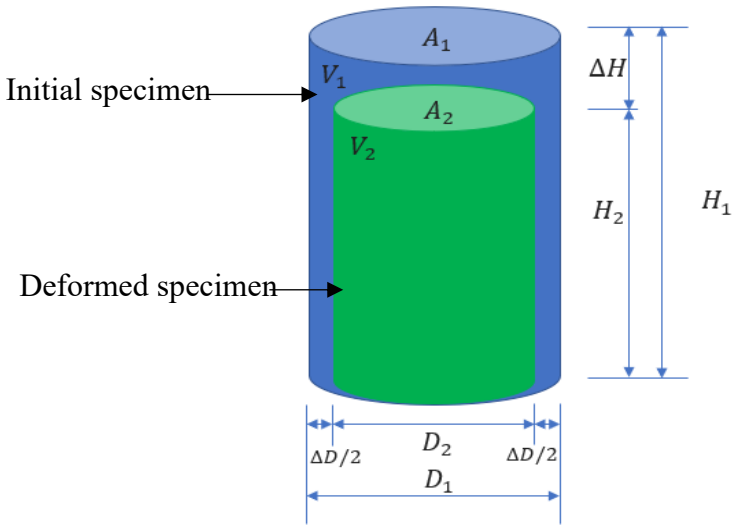


Figure 6.15: Schematic diagram illustrating the adopted specimen deformation for calculating radial strain

If the initial specimen height and diameter, at the beginning of a specific stage, are H_1 and D_1 respectively, the initial specimen cross-sectional area is $A_1 = \frac{\pi}{4}D_1^2$ and its initial volume is $V_1 = A_1 H_1$.

At any point during this stage, the specimen height and diameter are H_2 and D_2 respectively, the specimen cross-sectional area is $A_2 = \frac{\pi}{4}D_2^2$ and its initial volume is $V_2 = A_2 H_2$. Then the axial stain, ε_a, and volume strain, ε_v, at this point can be defined based on the change in the specimen height, $\Delta H = H_1 - H_2$, and the change in the specimen volume, $\Delta V = V_1 - V_2$, as

$\varepsilon_a = \frac{\Delta H}{H_1}$ and $\varepsilon_v = \frac{\Delta V}{V_1} = \frac{V_1 - V_2}{V_1} = 1 - \frac{V_2}{V_1}$ respectively. Thus, the ratio between these two volumes is $\frac{V_2}{V_1} = 1 - \varepsilon_v$.

This ratio can be used to find the corrected specimen cross-section area after deformation by substituting these volumes in terms of area and height as given below:

$$\frac{V_2}{V_1} = \frac{A_2 H_2}{A_1 H_1} = \frac{A_2(H_1 - \Delta H)}{A_1 H_1} = \frac{A_2}{A_1}\left[\frac{H_1}{H_1} - \frac{\Delta H}{H_1}\right] = \frac{A_2}{A_1}[1 - \varepsilon_a] = 1 - \varepsilon_v$$

$$\therefore \frac{A_2}{A_1} = \frac{1 - \varepsilon_v}{1 - \varepsilon_a} \tag{6.2}$$

The radial strain, ε_r, is defined as the change in the specimen diameter before and after deformation divided by the diameter at the start of the stage, $\varepsilon_r = \frac{\Delta D}{D_1} = \frac{D_1 - D_2}{D_1} = 1 - \frac{D_2}{D_1}$.

$$\therefore \frac{D_2}{D_1} = 1 - \varepsilon_r \tag{6.3}$$

Now, if the specimen cross-sectional areas before and after deformation, given by Equation 6.2, are substituted in terms of their diameters, $\frac{\frac{\pi}{4}D_2^2}{\frac{\pi}{4}D_1^2} = \left[\frac{1-\varepsilon_v}{1-\varepsilon_a}\right]$.

$$\rightarrow \left[\frac{D_2}{D_1}\right]^2 = \left[\frac{1 - \varepsilon_v}{1 - \varepsilon_a}\right]$$

By substituting $\frac{D_2}{D_1} = 1 - \varepsilon_r$ in this expression:

$$[1 - \varepsilon_r]^2 = \left[\frac{1 - \varepsilon_v}{1 - \varepsilon_a}\right]$$

$$\rightarrow [1 - \varepsilon_v] = [1 - \varepsilon_a] * [1 - \varepsilon_r]^2$$

$$\therefore \boldsymbol{\varepsilon_r = 1 - \sqrt[2]{\left[\frac{1 - \varepsilon_v}{1 - \varepsilon_a}\right]}} \tag{6.4}$$

Equation 6.4 gives the radial strain in terms of volume and axial strain. Also, it can be rearranged to find the volume strain if the radial strain is monitored as given in Equation 6.5.

$$[1-\varepsilon_v] = [1-\varepsilon_a] * [1-2\varepsilon_r + {\varepsilon_r}^2]$$

$$1-\varepsilon_v = 1-2\varepsilon_r + {\varepsilon_r}^2 - \varepsilon_a + 2\varepsilon_a\varepsilon_r - \varepsilon_a{\varepsilon_r}^2$$

$$\varepsilon_v = 2\varepsilon_r - {\varepsilon_r}^2 + \varepsilon_a - 2\varepsilon_a\varepsilon_r + \varepsilon_a{\varepsilon_r}^2$$

$$\varepsilon_v = \varepsilon_a + 2\varepsilon_r - {\varepsilon_r}^2 + \varepsilon_a{\varepsilon_r}^2 - 2\varepsilon_a\varepsilon_r$$

$$\therefore \varepsilon_v = \varepsilon_a + 2\varepsilon_r - {\varepsilon_r}^2\left(1 - \varepsilon_a + \frac{2\varepsilon_a}{\varepsilon_r}\right) \quad (6.5)$$

For small strains, if the higher order terms can be neglected, Equation 6.5 reduces to:

$$\varepsilon_v = \varepsilon_a + 2\varepsilon_r \quad (6.6)$$

Equation 6.6 is used when the difference between natural strain, ε_{nat}, and engineering strain, ε_{eng}, is negligible, $\varepsilon_{nat} = -\ln(1-\varepsilon_{eng})$. Natural strains relate to when changes in dimension are normalised by the current dimension rather than the initial dimension. Natural strain, also known as true strain, is defined as follows:

$$\varepsilon_{nat} = \int_{l_1}^{l_2} \frac{dl}{l} = ln\left(\frac{l_1}{l_2}\right) = -ln\left(\frac{l_2}{l_1}\right) = -ln(1-\varepsilon) \quad (6.7)$$

To check the suitability of Equation 6.6 for calculating the radial strain for the triaxial specimens, the radial strain for specimens tested under 150 kPa cell pressure was calculated using Equations 6.4 and 6.6 as explained in Section 7.5.4. The resulting stress-strain curves provided similar radial strain values for both the stages of q_c application and collapse deformation.

6.8.2.3 Calculation of maximum deviator stress

To plot the dry failure envelope for these analogue specimens using Mohr circles, the maximum deviator stress, q_{max}, was calculated using Equation 6.8.

$$q_{max} = (F/A_c)_{max} = (\sigma_1 - \sigma_3)_{max} \quad (6.8)$$

Where F is the load cell reading at τ_{max}. A_c is the corrected area at τ_{max} which is calculated using Equation 6.2. σ_1 and σ_3 are the principal major and minor stresses respectively.

6.9 Stress paths

6.9.1 Range of the applied inundation collapse stress

In this testing programme, the maximum deviator stress, $q_{\max}$, for a given cell pressure, CP, is used as a reference for each collapse test. Each collapse test stage was run under a collapse stress, q_c, of $(k * q_{\max})$ and a specific cell pressure value, CP, where $0 < \mathrm{k} < 1.0$. To evaluate the effect of the inundation collapse stress on the collapse strain, ε_c, values of $k = 0.10, 0.25, 0.50$ and 0.75 were chosen for each of the target cell pressures. These ratios were intended to provide safe and viable inundation collapse stresses, q_c, before inundation as the percentage of their maximum deviator stresses was always below their failure shear stress. The studied cell pressures were $25, 50, 100, 150, 200,$ and 250 kPa. However, at 250 kPa cell pressure, there was a considerable risk of membrane rupture during the collapse test for the reasons discussed in Section 6.6.1.1.

6.9.2 Dry failure envelope

The dry failure envelope was established as the tangent of five Mohr circles in the $\tau - \sigma'$ plot space which their principal stresses (σ_1) were calculated from Equation 6.8, where $\sigma_3 = CP$. The dry shearing tests were conducted to produce data for plotting these Mohr circles according to the procedure described in Section 6.7.1.

To illustrate the inundation collapse stress range that is described in Section 6.9.1 with their maximum shear stress in the stress path plot space to facilitate the comparison process, the dry failure envelope is replotted in the stress path $t - s$ plot space. To draw the failure line in this $t - s$ plot space, mean effective stress values, s', and their corresponding shear stress values, t', were calculated from the dry shearing test data using Equation 6.9 and 6.10 respectively. As during testing of these specimens there was no build up in the pore-water pressure because of the dry nature of these specimens and they were open to the atmosphere during testing, the effective stresses are assumed to be equal to the total stresses.

$$s' = s = \frac{1}{2}(\sigma_1 + \sigma_3) \tag{6.9}$$

$$t' = t = \frac{1}{2}(\sigma_1 - \sigma_3) \tag{6.10}$$

6.10 Chapter 6 Summary

In this chapter a detailed description is given of how the triaxial testing programme was delivered. This included: properties of the analogue triaxial collapsible specimens; apparatus description; specimen set-up and test procedure; the test challenges that were confronted; and the recording and processing of the acquired data from this triaxial testing programme.

The GDS triaxial system was slightly modified to test the analogue collapsible dry specimens. An air-vent valve was connected to the specimen top to release air during testing and the base pressure/volume controller was used to inundate the specimen from its base.

Challenges associated with membrane deep penetration and membrane rupture were overcome by introducing a thin fibre cloth strip at the outside surface of the connection areas between specimen and the top and base loading plates.

A relatively stable LVDT local axial strain measuring system was devised and used on the highly irregular specimen surface. The stability of this system was achieved by placing a circular acetate disc of 30-mm diameter under each pad of the LDVT system.

The membrane penetration volume (MPV) and cell chamber expansion were measured separately by the CPVG. The MPV was measured on dummy specimens and then compared with analogue specimens while the chamber expansion was measured separately without a specimen.

The analogue specimen volume change was measured in a similar procedure using the cell pressure/volume controller and then corrections for the MPV and chamber expansion were applied.

The triaxial testing programme described in this chapter includes dry shearing tests and collapse tests. The details of these tests and the GDS modules used for conducting them are discussed and the range of the applied stresses are stated. The purpose of conducting dry shearing tests was to establish the dry failure envelope for the analogue specimen to allow a range of collapse stress to be applied.

The data processing procedure is defined based on the measured parameters from these tests such as the applied force and the subsequent axial and volume changes. The relation used for calculating the deformed specimen cross-sectional area is formulated and the resulting radial strain as well. The calculation procedures for the dry failure envelope and stress path parameters are explained.

Chapter 7 : Analysis and discussion of the 3-D triaxial tests results

In this chapter the detailed results from the triaxial tests are presented, discussed and advanced to develop a new framework accounting for interaction between collapse strains, stress levels and dry density. First the scope of results is explained. Dry shearing tests were performed to stablish the dry failure envelope – the results from these are presented and detailed before covering those from the collapse tests, the main emphasis of the thesis. New mechanisms of collapse are described and discussed. Finally, the overall results are discussed within the context of the assessment of collapse and its effect on buildings and their structural damage.

7.1 Triaxial tests results

Information relating to the triaxial tests conducted, including specimen properties, test descriptions, shearing rates and key variables and parameters ($c, \varphi, q_{\max}$) are tabulated in Table 7.1. Specimens were tested to establish the dry failure envelope, which include specimens 1 to 8 and specimen 14. The other specimens were loaded and inundated to measure their collapsibility under different levels of collapse stress, q_c, and cell pressure, $CP = \sigma_r$. Specimens 1 and 2 (Table 7.1) were the first analogue trials for triaxial specimens prepared with kaolin percentages of 9% and 20% respectively. After this, four moulds were used to increase the number of specimens per set, following which the specimen denomination system was devised, as described in Section 6.3. Therefore, the set containing these two specimens is labelled '0'.

Five of the nine dry shearing tests were used to provide the best fitting dry failure envelope to the Mohr circles as shown in Figure 7.1d which were performed under cell pressures of 25, 50, 100, 150, and 250 kPa (S401, S301, S200, S101 and S202 respectively). A total of 20 successful collapse tests were conducted on specimens from sets 2 to 8, tested under the applied deviator stress range given in Section 6.9.1 and included in column three of Table 7.2. Five specimens were not successfully tested for reasons such as being destroyed during the extraction process or membrane rupture, these are marked in Table 7.1.

A summary of the detailed results, including axial, volumetric, and radial strains and density and void ratio changes resulting from the triaxial collapse tests (due to the application of q_c and inundation stages), is given in Table 7.3 in which the specimens are grouped based on the cell pressure values. The first column shows the denomination of the tested specimens, as

described in Section 6.3, in which the percentage of the kaolin in the analogue specimens and their initial densities before testing are given. The second and third columns give the values of the cell pressure, CP, and collapse stress, q_c, respectively. The resulting axial, volumetric and radial strains before and after collapse are grouped in the followed six columns. The specimens' initial density and their values before and after collapse and their corresponding void ratios values are tabulated in the last six columns in Table 7.3.

Local axial strains were also successfully determined from the LVDTs installed on three specimens tested under CP = 150 kPa in set 7. For these specimens, the local axial strains calculated avoided any spurious bedding errors as discussed in Section 7.5.3. From these tests it was established and confirmed that bedding errors were negligible. This was primarily understood by comparing the axial strain calculated from external displacement transducer with those from the locally installed LVDTs.

Table 7.1: Summary of the triaxial testing programme

Count	Set No.	Symbol	Target Test	CP (kPa)	CP rate (kPa/min)	Dry shearing rate (mm/min)	Dry shearing rate (kPa/min)	Inundation rate (cc/min)	Wet shearing Rate (mm/min)	c' (kPa)	$\varphi'(^0)$	q_{max} (kPa)
1	0	S200-0.09-0.90	Dry Failure Envelope (DFE)	100	2	0.014	-	-	-	15	35.5	335
2		S400-0.20-1.00		200	2	0.014	-	-	-			750
3	1	S101-0.09-0.92	Dry Failure Envelope	150	2	0.014	-	-	-			480
4		S201-0.10-0.94	(DEF)	200	2	0.014	-	-	-			700
5		S301-0.09-0.92		50	2	0.014	-	-	-			200
6		S401-0.09-0.92		25	2	0.014	-	-	-			125
7	2	S102-0.10-0.92		25	2	0.014	-	-	-			120
8		S202-0.09-0.91		250	2	0.014	-	-	-			775
9		S302-0.10-0.91	Collapse	25	2	-	2	38	0.014	9	42.3	138
10		S402-0.10-0.93		50	2	-	2	38	0.014			220
11	3	S103-0.13-0.94	Collapse	100	2	-	2	38	0.014			360
12		S203-0.13-0.98		150	2	-	2	38	0.014			590
13		S303-0.13-0.97		200	2	-	2	38	0.014			800
14		S403-0.14-1.01	DFE	200	2	0.014	2	-	-			720
15	4	S104-0.11-0.98	**Destroyed during extraction**									
16		S204-0.11-0.97	Collapse	100	2	-	2	38	0.014	-	-	425
17		S304-0.11-0.96		100	2	-	2	38	0.014			465
18		S404-0.11-0.95		100	2	-	2	38	0.014			410
19	5	S105-0.09-0.90	Collapse	50	2	-	2	38	0.014	-	-	204
20		S205-0.09-0.90		50	2	-	2	38	0.014			192
21		S305-0.09-0.87		50	2	-	2	38	0.014			-
22		S405-0.09-0.87	**Membrane ruptured just after the start of the test-manufacturing fault**									
23	6	S106-0.09-0.86	Collapse	25	2	-	2	38	0.014	-	-	90
24		S206-0.09-0.87		25	2	-	2	38	0.014	-	-	100
25		S306-0.09-0.88		25	2	-	2	38	0.014	-	-	95
26		S406-0.09-0.86	**Fell apart just after the extraction process**									
27	7	S107-0.10-0.88	**Fell apart just after the extraction process**									
28		S207-0.10-0.88	Collapse	150	2	-	2	38	0.014	-	-	-
29		S307-0.10-0.88		150	2	-	2	38	0.014	-	-	-
30		S407-0.10-0.90		150	2	-	2	38	0.014	-	-	-
31	8	S108-0.10-0.92	Collapse	200	2	-	2	38	0.014	-	-	-
32		S208-0.10-0.93		200	2	-	2	38	0.014	-	-	-
33		S308-0.10-0.92		200	2	-	2	38	0.014	-	-	-
34		S408-0.10-0.93	**Fell apart during the extraction process**									

7.2 Dry shearing response

The dry shearing response of the analogue specimens that were tested, in their initial dry states, until reaching shearing failure is summarised in Figure 7.1. The relation between deviator stress and axial strain, q vs ε_a, is plotted in Figure 7.1a and the secant stiffness versus axial strain, E_s vs ε_a, of these specimens in Figure 7.1b. The volume strain versus axial strain, ε_v vs ε_a, is plotted in Figure 7.1c. The Mohr circles, τ_n vs σ_n plot space, and the resulting dry failure envelope are given in Figure 7.1d.

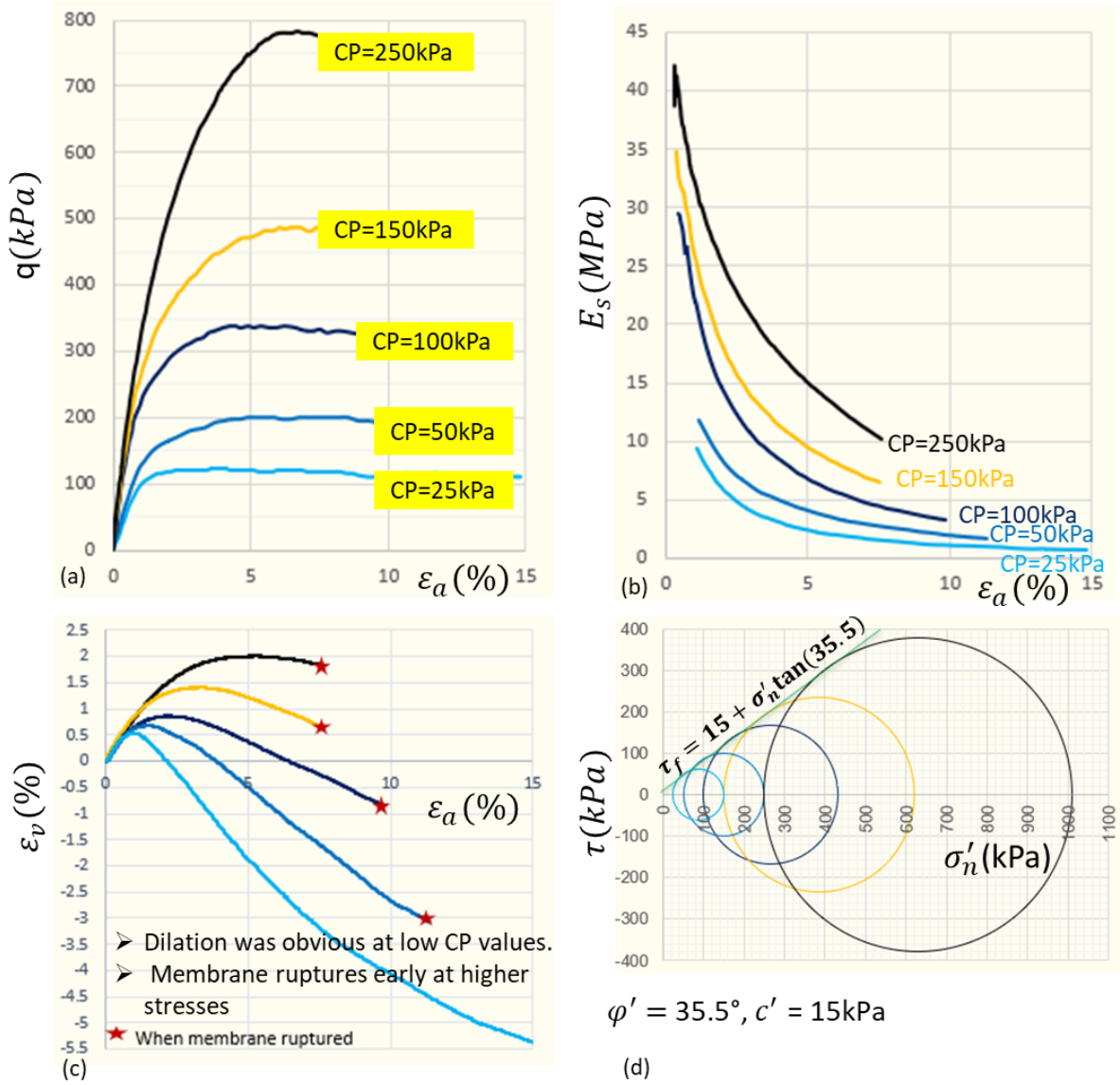


Figure 7.1: The dry shearing response of analogue triaxial collapsible specimens

The above-mentioned variables, plotted in Figure 7.1, show a consistent response to shearing at these given cell pressure values and indicate the homogeneity and quality of the tested specimens. It is clear that the maximum deviator stress increased with cell pressure as shown in Figure 7.1a. The rate of this increase slightly decreases with increasing of cell pressure. In other words, if it is assumed that $q_{\max} = A * CP$, then it can be found that for the tests with *CP* = 25, 50, 100, 150, and 250 kPa and their corresponding values of $q_{\max}$ = 120, 200, 335, 480, and 775 kPa (marked in red in the last column in Table 7.1), $A = 5, 4, 3.35, 3.2$ and 3.1 with values decreasing with increasing cell pressure. This decrease is probably because the interlocking between the Lytag particles, especially after an initial contraction, tends to lead to dilation (Figure 7.1c) but this is inhibited as the cell pressure increases.

The secant stiffness, Figure 7.1b, increases with increasing cell pressures, when $CP = 25, 50, 100, 150, 250$kPa, the corresponding stiffness values are $E_s = 9, 12, 29, 34,$ and 43 MPa respectively. The secant stiffness is chosen as an example to be presented in Figure 7.1 because it had a steadier relationship with axial strain than the tangential stiffness which it is covered in Section 7.2. It appears that the specimens' maximum secant stiffness increased with cell pressure but then dropped dramatically with increasing axial strain and shearing.

The change in volume strain and axial strain of these specimens during the increase of the deviator stress is shown Figure 7.1c. Initially, all the specimens contracted and then reached a phase transformation point followed by dilation. The contraction phase increased with increasing cell pressure leading to an increase in both volumetric strain and axial strain until reaching the phase transformation point, after which the specimens started dilating. In this case if the specimens tested at the higher cell pressure of $150\ kPa$ and $250\ kPa$ the membrane ruptured just after the phase transformation point, and there is no clear record of a dilation phase. However, from inspection of the data from all five tests it is clear that the dilation phase decreased with increasing cell pressure. At higher all-round cell pressures dilation is suppressed. These two deformation phases are investigated within the context of the collapse strain results from the collapse tests, which have led to more than one collapse mechanism, as discussed in Section 7.7.

In these dry shearing tests, as shown in Figure 7.2, the dilation phase started at deviator stress levels with $q \geq 0.75\ q_{\max}$. If the collapse stress at inundation, q_c, reached this range of stress at which a specimen started to dilate, the collapse mechanism might not have a strong tendency

to collapse and then might develop a different collapse mechanism. The collapse response of such specimens inundated at $q_c = 0.75\, q_{max}$ is discussed in Section 7.5.2.

Inundation was always applied at values of $q_c \leq 0.75\, q_{max}$ to assess the degree of collapse over a range of deviator stresses (for a range of confining stresses), trying q_c to avoid reaching the transformation point (see Figures 7.2a and b) which occurred after the 'yield point' at which the bonds between bonded/cemented particles start to break (Coop and Atkinson, 1993) and before reaching the maximum deviator stress. The yield points of these specimens in this test set-up were not identified. In hindsight it might have been interesting to inundate some specimens under lower stress levels (e.g., *CP*= 50 and 25 kPa) after they have undergone significant dilation as the volumetric strains indicate volume increases of about 3% to 5% for these two lower *CP* values respectively. However, it is important to consider the mechanism that is causing these volumetric strains. This is discussed in Section 7.5.4.

To understand the effect of clay fines on the strength of these specimens, the stress-strain and volumetric strain curves of the specimen sheared at *CP* = 100 kPa were compared with four Ottawa sand specimens, which were prepared with different fines content (FC) of kaolin clay of *FC* = 0%, 2%, 5%, and 10% to evaluate their effects on the shear strength and stiffness of sand. They were all sheared similarly under confining pressure of 100 kPa (Carraro et al., 2009). The similarity and differences between these specimens are summarised in Figure 7.2, including: the coarse fraction's particle shape, size and content; kaolin content; depositional method for preparing the clayey sand specimens; relative density of the specimens; and the type of conducted test and the stress level.

In spite of the huge difference between the particle size of the coarse fraction of these two sets of specimens (Lytag average particle size is about 15 time the average particle size of Ottawa sand), the response of the specimen having 10% kaolin clay is similar to the Lytag specimen sheared under *CP* = 100 kPa. The Lytag specimen showed higher strength of about 1.5 times the clayey sand specimen (around 200 kPa, see Figures 7.2a and b respectively). However, both typically contracted and then dilated (maximum ε_v is about 1% and -1% as shown in Figures 7.2c and d respectively) in a similar way, although the clayey sand specimen was dense (D_R = 82%, see Figure 7.2b). This indicates that the effect of the clay on the stress-strain response of these two soils with round shaped particles is similar, despite the fact that they were in extreme states (dry and saturated) when they were sheared drained.

The effect of this clay content range in the strength and the volumetric strain of these clayey specimens, as shown in Figures 7.2b and d, is remarkable. The shear strength reduced from 300 kPa in the clean sand specimen to 200 kPa in the 10% clayey sand specimen (see Figure 7.2b) although they both had D_R = 82%. This 10% of kaolin clay reduced the maximum volume strain from about 6% to 1%. Thus, it can be concluded that the effect of increasing the clay content changes the soil response to loading dramatically, even if it is saturated (soil suction is negligible). In the case of inundating such specimens under specific stress level in their dry state (soil suction is its maximum limit) they would probably collapse providing they are transitional soils. Transitional soils relate to coarse-grained soils having different stress – strain responses due to their fines content being less than the threshold fines content (FC_{th}), i.e. with its fabric referred to as 'non-floating', in which there is still contact between its coarse particles. If the fines content reaches the threshold fines content, its coarse particles are not necessarily in contact with each other, and they are referred to as having 'floating' fabric. A typical range of the threshold fines content is usually between 25 and 35% (Salgado et al., 2000; Carraro et at. 2009).

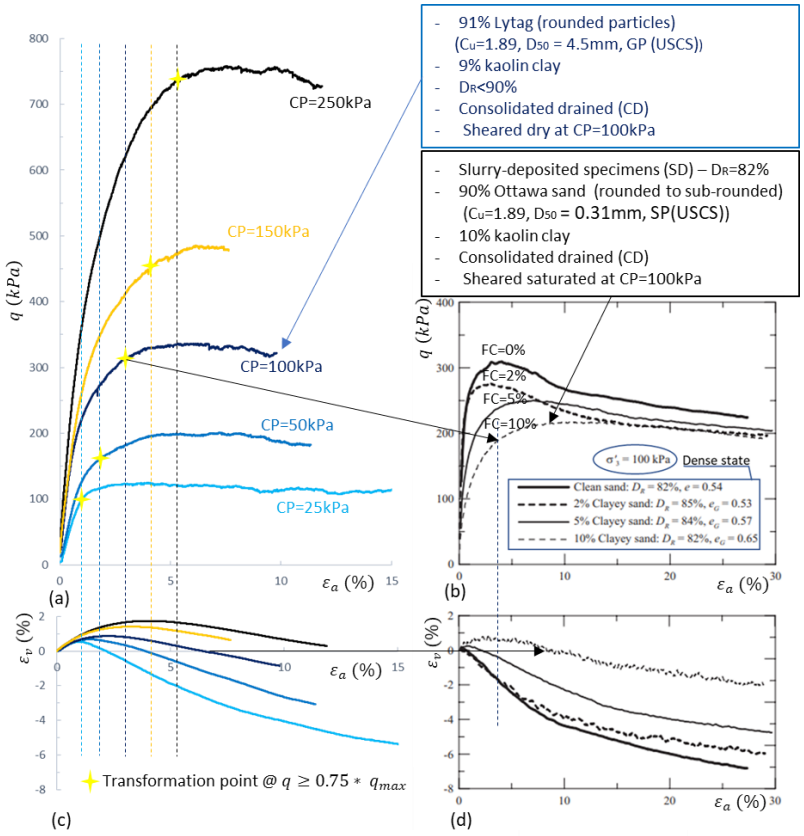


Figure 7.2: Stress-strain response of (a) Lytag (gravel scale) (b) Ottawa sand, after Carraro et al. (2009), and their corresponding volumetric strain (c) and (d) respectively

The shear strength parameters (c and φ) for the analogue specimens are calculated based on the Mohr circles drawn in Figure 7.1d. Five Mohr circles fitted well with each other and allowed one distinct tangent to be developed that touches all circles to define the Mohr-Coulomb failure envelope. The angle of internal shearing resistance, φ, and cohesion, c, of these analogue specimens from this failure envelope are found to be 35.5° and 15 kPa respectively.

$$\tau_{\mathrm{f}}(kPa) = 15(kPa) + \sigma_n(kPa)\tan(35.5) \qquad (7.1)$$

The failure envelope is defined by Equation 7.1. For any applied values of the principal stresses (σ_3 and σ_1) on these specimens, the normal stress, σ_n, on the failure plane and the corresponding failure shear stress, τ_{f}, can be determined from the geometry of the Mohr circle and failure envelope, assuming that the position of the pole of planes corresponds to that of the minor principal stress, σ_3.

7.2.1 Stiffness of the analogue specimens

The stiffness was calculated from the $q - \varepsilon_{\mathrm{a}}$ plot shown in Figure 7.1a. Tangent and secant stiffnesses were calculated from the tangent and secant slopes of the $q - \varepsilon_{\mathrm{a}}$ curves. The results are plotted in Figures 7.3a and 7.3c respectively. Both tangent and secant stiffnesses have also been normalized by dividing each one by its corresponding confining pressure as shown in Figure 7.3b and 7.3d. As the specimens were sheared after just isotropic compression, the cell pressure values also represent the initial mean effective stress, $p_{\circ}$, at the start of the shearing. Specimen stiffness values, both tangent and secant, increased with cell pressure while the opposite trend is observed for the case of the normalized stiffness. The initial stiffness values range between 40 MPa and 10 MPa for cell pressure of 250 kPa and 25 kPa, respectively, and the initial normalized stiffness values vary between 150 to 375 for the same range of cell pressures.

Over this range of cell pressure, these specimens had relatively high initial stiffness values, when they showed negligible volume deformation due to the application of the isotropic compression, as was clearly shown when comparing the membrane volume penetration between analogue specimens and the dummy specimens as explained in Section 6.6.2. This initial stiffness was followed by an immediate drop in its value as the axial strain increased by more than 0.5%. Specimen stiffness at axial strain less than 0.5% was not well defined. Within this zone, stiffness fluctuated, and stiffness curves were not smooth. This probably due to the resolution of the external displacement transducer not being sufficiently high and also perhaps

bedding errors. Another potential factor is bond breakage and changes in the particle contact areas as the bonded particles start rearranging themselves.

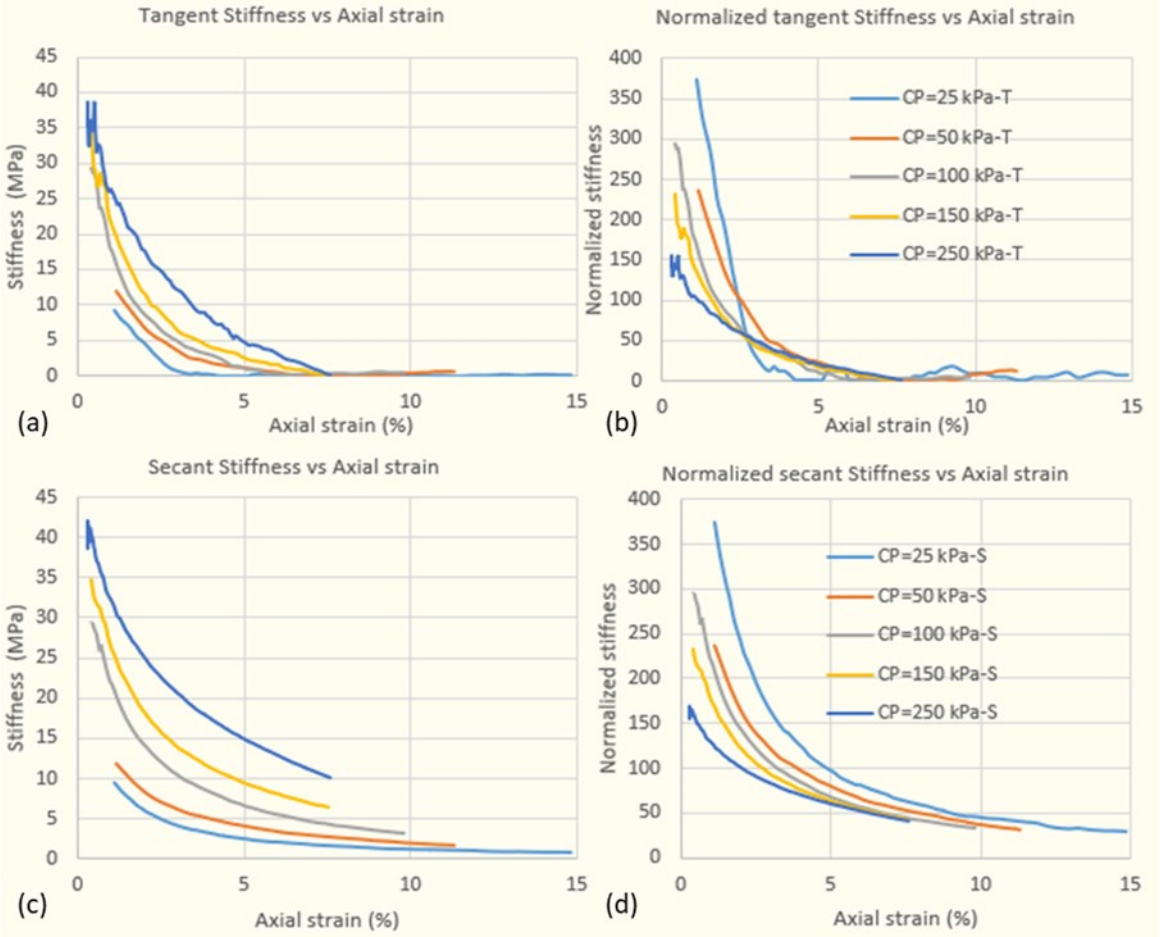


Figure 7.3: Tangent and secant stiffnesses and their normalized values from the dry shearing tests

7.3 Wet failure envelope

Prior to presenting and discussing the response of the specimens to inundation, the results from a final stage of these tests are given here. In order to maximize the output from the collapse tests, once the collapse stage was complete, the specimens were sheared under inundated (saturated) but fully drained conditions, as described in Section 6.7.2 and Figure 6.10. The wet shearing stage was started and continued until the specimen reached failure. The wet shearing stage applied on the first three specimens tested for collapse, under cell pressures of 25, 50, and 100 kPa and at deviator collapse stresses of $q_c = 60, 90, \text{and } 167.5$ kPa respectively, developed higher q_{max} values, of $q_{max} = 138, 220, \text{and } 360$ kPa respectively, i.e. higher than their corresponding values from dry shearing (Table 7.1).

When these wet failure points were plotted in Mohr circle plot space, they led to another well-defined envelope to be drawn as shown in blue alongside the dry failure envelope in Figure 7.4. Although these specimens were wet sheared at different density states due to different q_c values, they were sheared to their maximum stress, resulting in a well-defined new failure envelope slightly higher than dry failure envelope. In this wet failure envelope, the angle of internal shearing resistance increased from 35.5° to 36.9° and the cohesion increased as well from 15kPa to 16kPa.

The denser fabric due to the application of q_c and subsequent collapse due to the inundation, which referred to as fabric densification, is expected to be the reason for the increased q_{max} values. This denser fabric would increase particle interlocking justifying the reason for the increase in cohesion. This would also contribute to the increase in the angle of internal shearing resistance.

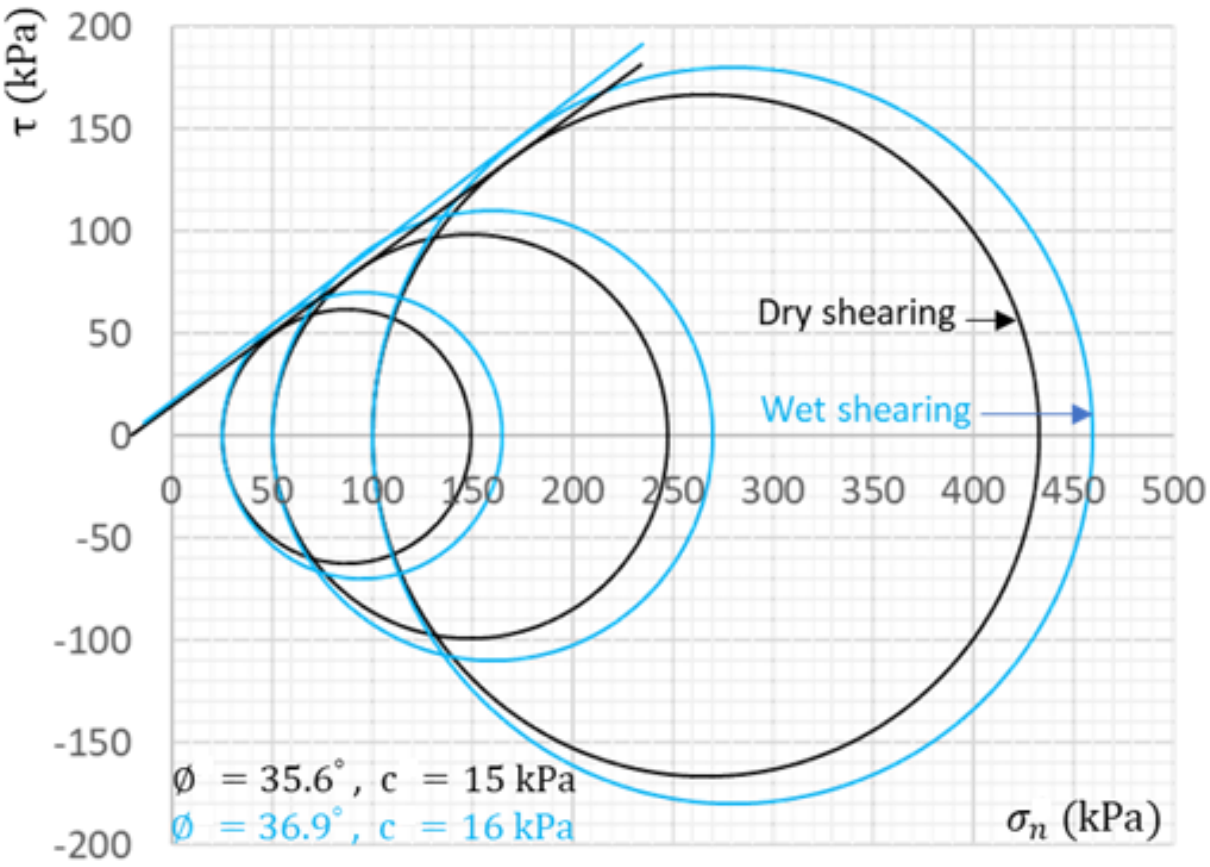


Figure 7.4: Comparison between dry and wet shearing failure envelopes

7.4 Stress paths for the tested specimens

7.4.1 Dry failure envelope in (t' vs s') plot space

To draw the stress path for the specimens tested for collapse, the dry failure envelope is first plotted in the stress space defined by the stress the stress invariants s' and t as annotated in Figure 7.5. The mean principal stresses, $s = s'$ (assumption), and the corresponding shear stress values, $t = t'$, were calculated from the dry shearing test results using Equations 6.9 and 6.10 respectively. The slope of failure envelope is given by, $\alpha = 28°$, and its intersection with t axis at $t = a = 11$ kPa. All the collapse stress values, at which the specimens were inundated, were chosen to be below the failure line as discussed in Section 6.9.1. This failure envelope is plotted in Figure 7.5 to facilitate the understanding of the stress paths followed for the subsequent specimens that were tested for collapse.

7.4.2 Stress paths of specimens tested for collapse

After plotting the dry failure envelope for the specimens sheared at dry state, the stress path parameters, $t = t'$ and $s = s'$ were calculated for the other specimens that were to be tested for collapse as given in Table 7.2. These t and s values were plotted in the (t vs s) plot space in Figure 7.5 to have a clear idea of how far these stress points were from the failure envelope. Specimens grouped in Table 7.2 were to be loaded first isotropically, by the application of cell pressure, and then deviatorically by increasing the axial stress. The resulting paths are a set of five parallel inclined lines inclined at 45° as shown in dotted lines in Figure 7.5. Each line, includes the stress path and final stress point at which inundation was to take place for each of a group of four specimens which were tested for collapse under a specific confining cell pressure, starting at $t = 0$ kPa and $s = CP$ (cell pressure value). The hierarchy of these points on each line represents the difference in specimen stress state at which the inundation process to induce collapse was applied. The blue and red arrows are plotted to explain the two stages, application of CP and q_c respectively, that were applied to reach the required stress state. Note that the symbol q_c is used throughout this thesis to denote the inundation collapse stress: $q_c = 2t$.

These inclined lines and the stress points marked on them, can be considered as a grid of inundation collapse stress states of the tested specimens. This grid then can be used to project axial strain values before (due to application of q_c) and after the inundation process and the resulting densification as discussed in Section 7.6. This stress grid provides another view

concerning the effect of stress level on collapse strain in this stress path plot space. Currently, collapse potential is defined simply in terms of the magnitude of collapse related to the thickness of the layer (or height of the specimen) with no reference to the effect of changing the inundation collapse stress.

Table 7.2: Stress path parameters

Specimen symbol	CP (kPa)	q_c (kPa)	t (kPa)	s (kPa)
S204-0.11-0.97	100	33	16.5	116.5
S304-0.11-0.96	100	83	41.5	141.5
S103-0.13-0.94	100	167.5	83.75	183.75
S404-0.11-0.95	100	251	125.5	225.5
S305-0.09-0.87	50	20	10	60
S205-0.09-0.90	50	50	25	75
S402-0.10-0.93	50	90	45	95
S105-0.09-0.90	50	150	75	125
S106-0.09-0.86	25	12	6	31
S206-0.09-0.87	25	30	15	40
S302-0.10-0.91	25	60	30	55
S306-0.09-0.88	25	90	45	70
S207-0.10-0.88	150	62	31	181
S407-0.10-0.90	150	250	125	275
S203-0.13-0.98	150	310	155	305
S307-0.10-0.88	150	420	210	360
S308-0.10-0.92	200	70	35	235
S208-0.10-0.93	200	175	87.5	287.5
S303-0.13-0.97	200	370	185	385
S108-0.10-0.92	200	515	257.5	457.5

7.5 Stress-strain relations from triaxial collapse tests

7.5.1 Effect of cell pressure on collapse strains

7.5.1.1 Deviator stress and axial strain relationship

To evaluate the effect of cell pressure (*CP*), five specimens from sets 2 and 3 (Table 7.1) were tested for collapse at different cell pressure of 25, 50, 100, 150, and 200 kPa and under constant collapse stress levels of about $q_c = 0.5q_{max}$ of their corresponding maximum deviator stress determined from the dry shearing tests. Deviator stresses plotted in Figure 7.6a. These stress versus strain plots included all the three test stages as described in Section 6.7.2 (application of $q_c = 0.5q_{max}$, inundation and, wet shearing respectively).

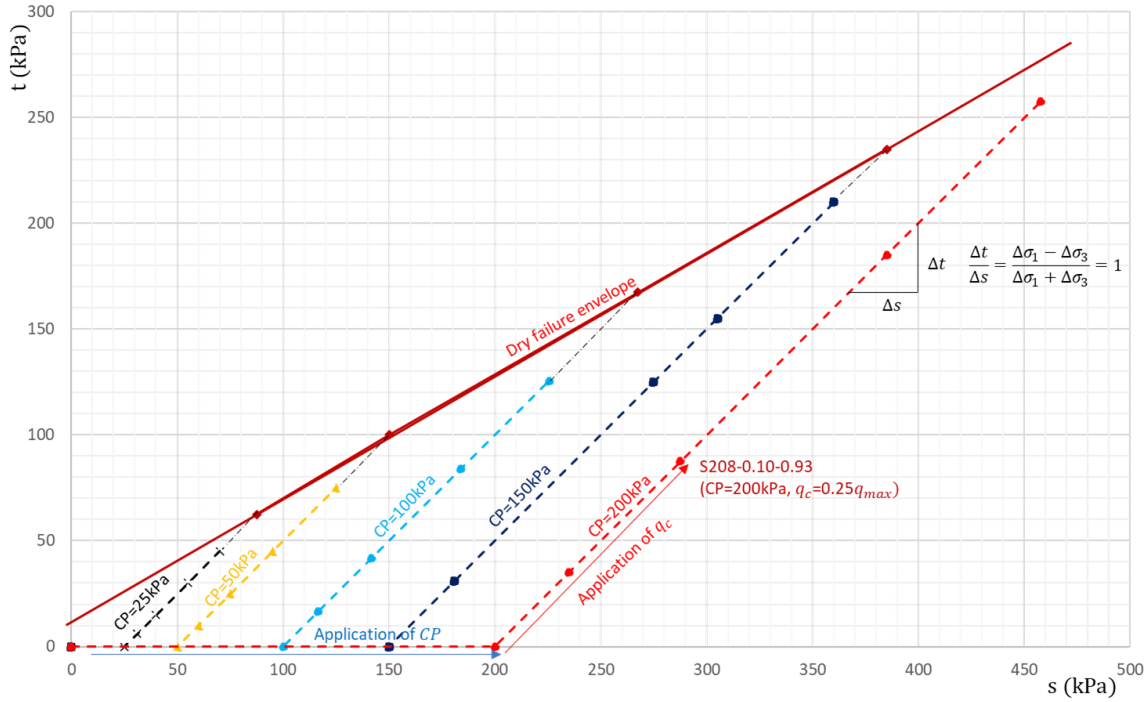


Figure 7.5: Stress paths for the tested specimens

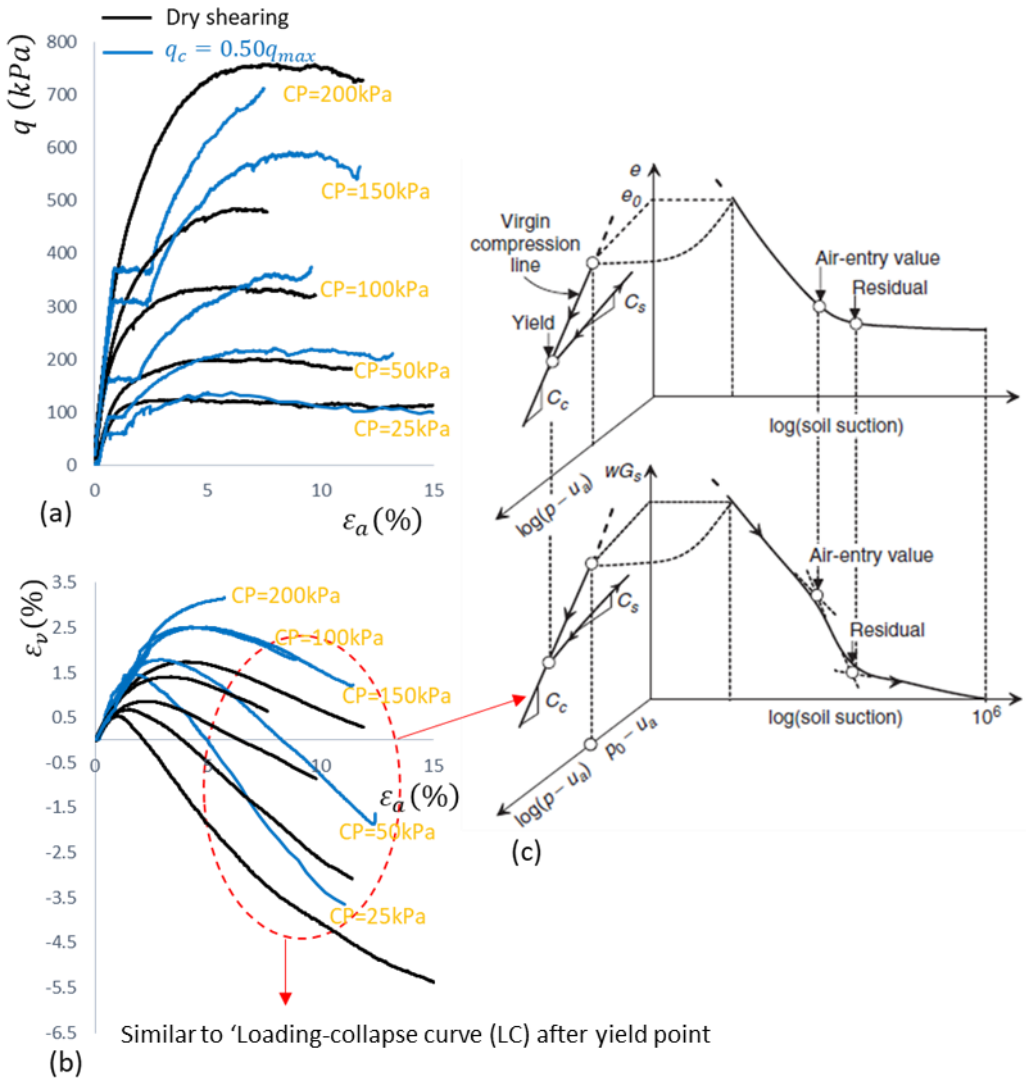


Figure 7.6: Effect of cell pressure on collapse deformation at $q_c = 0.5q_{max}$: (a) $q - \varepsilon_a$ (b) $\varepsilon_v - \varepsilon_a$ (c) bounding relationships for typical clayey silt soil (Fredlund, 2006) - cited by Fredlund et al. (2014)

These stages are plotted together (blue curves) alongside the curves from Figures 7.1a and c, for the specimens that sheared in a dry state under the same confining pressures (black curves). In Figure 7.6a, the axial collapse strain (the horizontal part in the middle of each blue curve), which results from the inundation process, increased with collapse stress, q_c, and cell pressure, CP. Only the specimen that was tested at $CP = 50$ kPa showed slightly less axial collapse strain and this is because it was tested at $q_c = 0.45q_{max}$ instead of $0.5q_{max}$. The values of the applied stresses, q_c, and the resulting axial strains before and after inundation for these specimens are summarised in Table 7.3.

In the wet shearing stage, after collapse, all these specimens showed an increasing resistance to shearing and reached failure at a higher q_{max} than the dry sheared specimens as shown in

Figure 7.6a. This difference between $q_{\max}$ in wet shearing and dry shearing increased with cell pressure. Some proposed reasons for this increase of q_{max} are discussed in Section 7.3.

7.5.1.2 Volumetric strain versus axial strain relationship

Volumetric strain was calculated from cell pressure volume controller data after subtracting the membrane volume penetration and chamber expansion following the assumptions discussed in Section 6.6.2. The volumetric strain increased with axial strain until it reached a peak, the phase transformation point, and then decreased while axial strain was increasing as shown in Figure 7.6b. This peak in volume strain increased with cell pressure. Due to this reverse in volumetric strain, it can be concluded that these specimens were deforming in two stages, contraction followed by dilation which later helped to define two different collapse mechanisms as is discussed in Section 7.7. Therefore, it was necessary to calculate the corresponding radial strains from these axial and volumetric strains as discussed in Section 6.8.2.2.

Furthermore, as expected, the specimens tested for collapse (plotted in blue in Figure 7.6b) experienced greater volumetric strains than the specimens tested in a dry state but still both contracted before dilating. The vertical distance between each two curves tested under equal cell pressure (between blue and black curves) represents the total collapse between each pair of tests including the wet shearing. However, it is difficult to quantify the increase in collapse strain because of the increasing q in the wet shearing stage. Therefore, the increase in q_c is considered separately as percentages of $q_{\max}$ of 0.1, 0.25, 0.5 and 0.75 for each cell pressure level applied, as discussed in the following section.

In both dry shearing and wet shearing, the volumetric strain of these specimens involved contraction followed by dilation. After they dilated back to their initial volume, dilation continued in straight parallel lines for every given cell pressure (see Figure 7.6b). Beyond these points ($\varepsilon_v = 0\%$), these specimens join a unique boundary limit similar to the 'Loading-Collapse' (LC) yield curve. To illustrate this, a typical LC curve for unsaturated clayey silt soil is given in Figure 7.6c (Fredlund, 2006). After these specimens return to $\varepsilon_v = 0\%$, collapse ceases, and they join their normal collapse curve. This observation is similar to what was found from 1-D tests on unsaturated silty sand specimens with different degrees of saturation, as shown in Figure 2.14 (Jennings and Burland, 1962). In this figure, after inundating these specimens at different applied stresses they joined the virgin compression curve (tested at saturation $S_r = 100\%$).

7.5.2 Effect of inundation collapse stress on collapse strains

The deviator stress and the resulting axial and volumetric strains for the 20 specimens tested at collapse stresses of $q_c = 0.10, 0.25, 0.5$ and $0.75\ q_{max}$ and at cell pressures of *CP*= 25, 50, 100, 150 and 200 kPa, are plotted together in Figure 7.7 for the three stages of the test with their corresponding dry shearing tests. Plots in Figure 7.7 were zoomed in as shown in Figure 7.8 to identify carefully changes in axial and volumetric strains due to these stress ranges within 5% axial strain. Also, to compare the effect of changing the cell pressure values for all collapse stress levels (0.10, 0.25, 0.5 and $0.75q_{max}$), these sub-figures are regrouped and plotted again in Figure 7.9. The resulting axial and volumetric strain values before and after collapse due to these range of stresses are summarised in Table 7.3 and analysed and discussed including their density changes in Sections 7.6, 7.7 and 7.8.

In Figures 7.7 and 7.9, axial collapse strain increased with q_c and CP while the inundation volumetric collapse strain decreased slightly with increasing CP and q_c. The maximum shear stress values due to the wet shearing increased with increasing q_c level (because of increasing densification of the specimen with q_c) and CP and reached higher values than the dry sheared specimens (the black curves). Potential reasons for this were put forward and discussed in Section 7.5. Specimens tested at values of $q_c = 0.75q_{max}$ responded slightly differently than the rest. This is thought to be because they were close to the shear failure point before inundation. After they were inundated, they deformed differently because their axial collapse was noticeably higher than other specimens loaded to lower q_c values, but their volumetric strain fluctuated between the volumetric strain of the other specimens. Also, the maximum shear stress from wet shearing these specimens (tested for collapse) at $q_c = 0.75q_{max}$ was slightly less. This is probably because their higher deformation prior to inundation reduced the Lytag particle interlocking before the start of wet shearing.

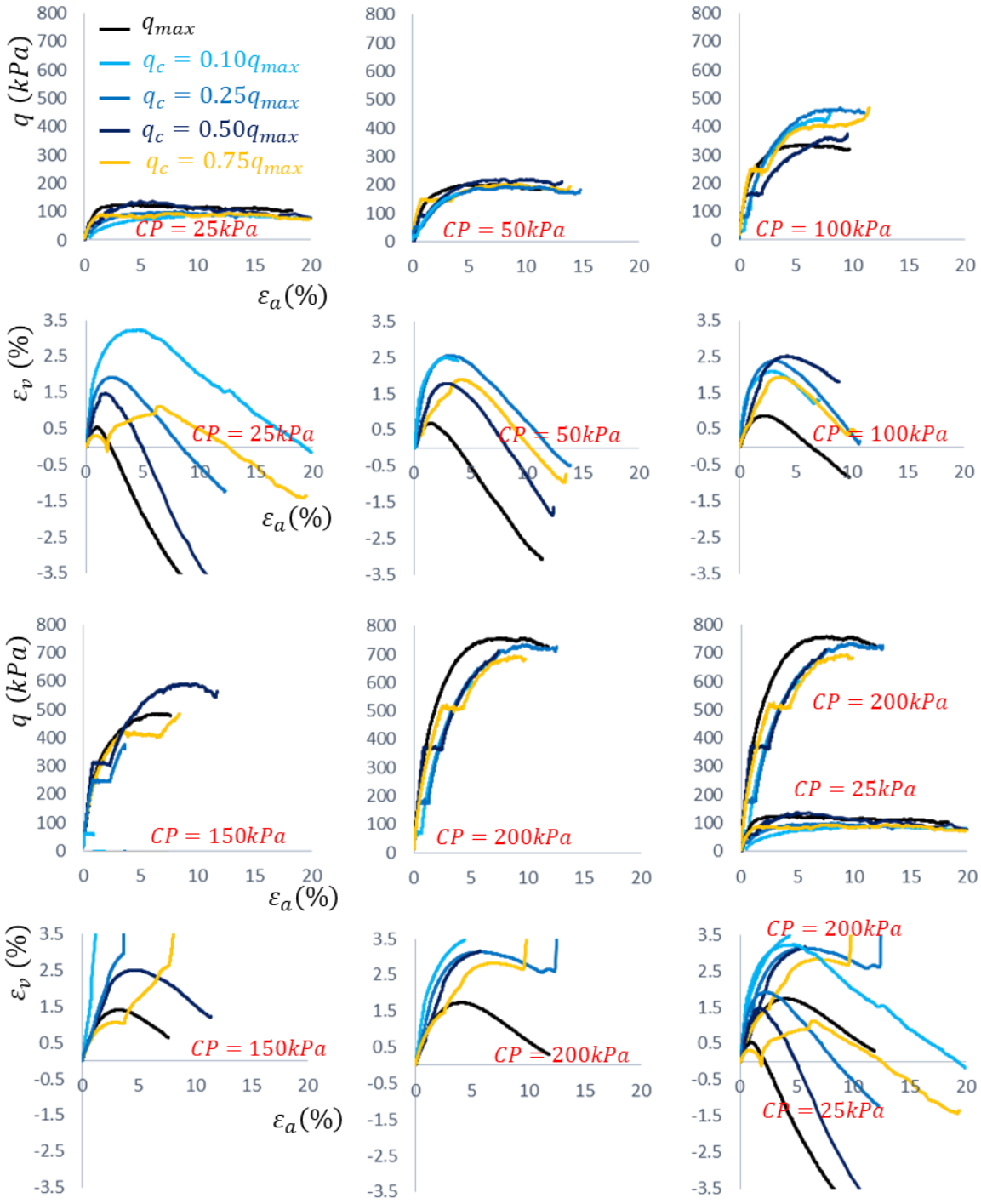


Figure 7.7: Stress-strain response due to collapse stresses of $0.10, 0.25, 0.5\ and\ 0.75q_{\max}$ and at $CP = 25, 50, 100, 150, and\ 200$kPa (final two plots set compares the two extreme CP levels of 25kPa and 200kPa)

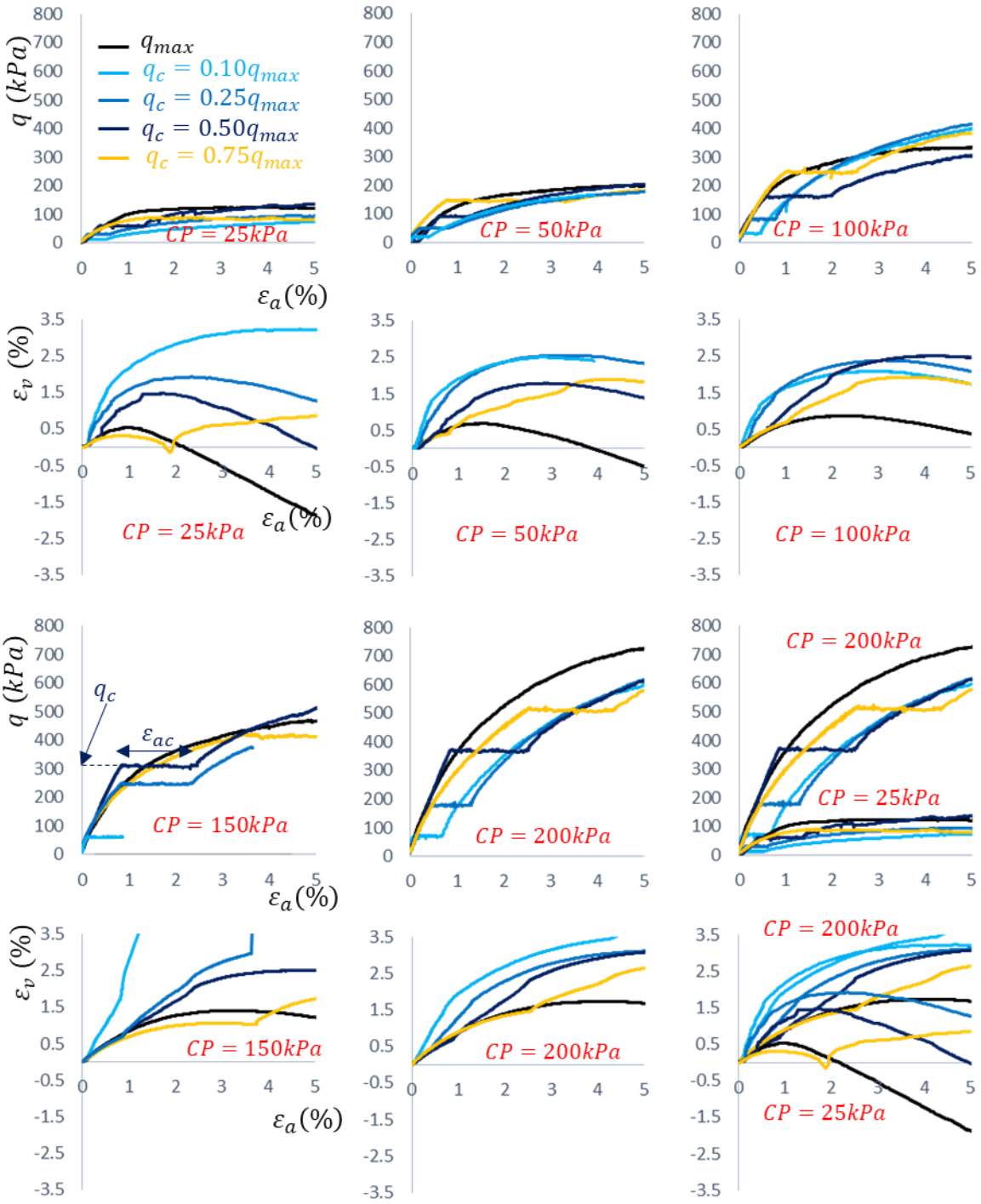


Figure 7.8: Stress-strain response for all tested specimens for axial strain range between 0% to 5% (zoomed-in image from Figure 7.7)

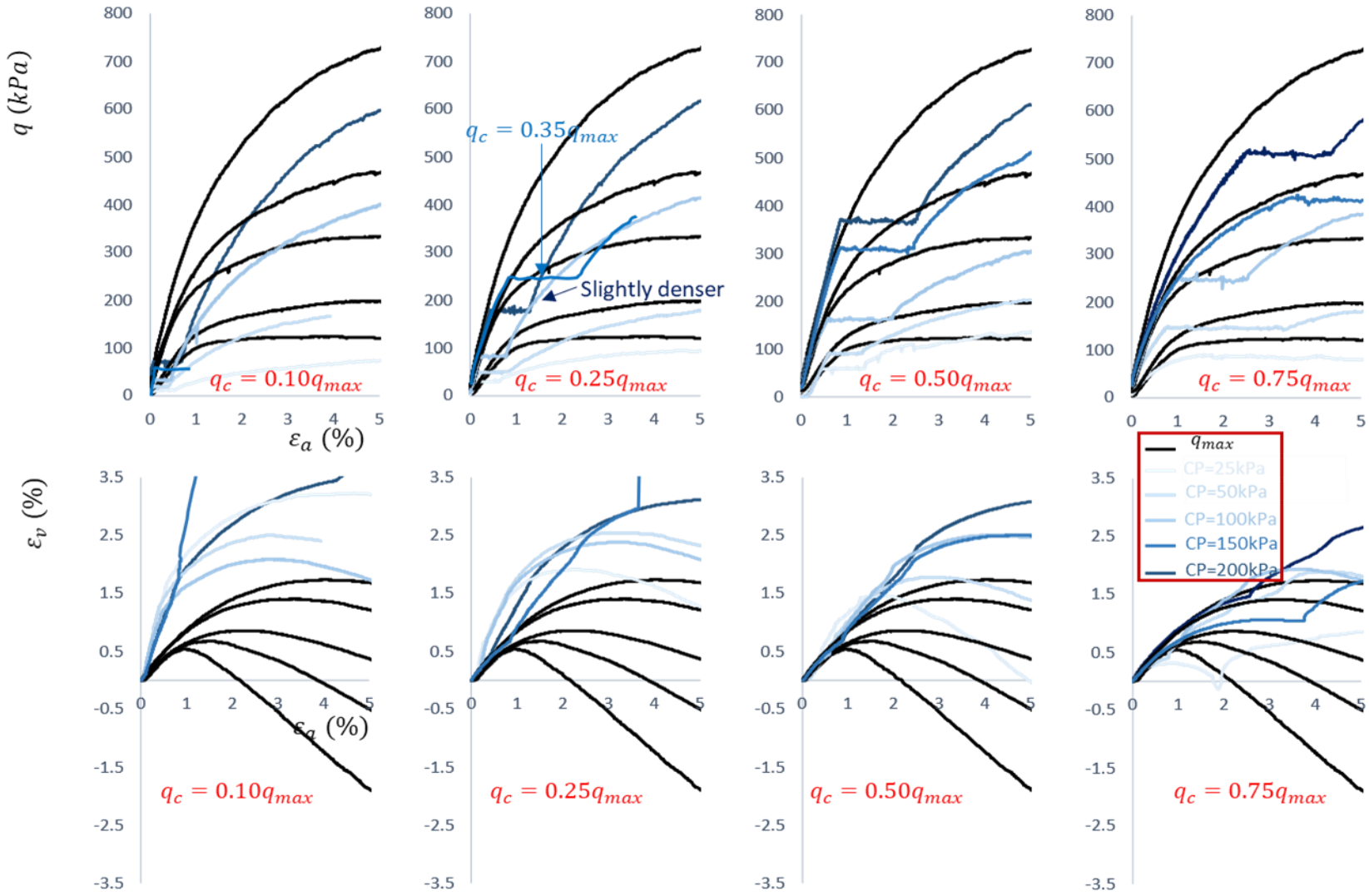


Figure 7.9: Effect of cell pressure on the stress-strain response (zoomed in images covering ε_a < 5%)

Table 7.3: Strain results from triaxial collapse tests

Specimen symbol	*CP* (kPa)	q_c (kPa)	Due to loading only			Due to loading and inundation			ρ_0	$\rho_{at\ inun}$	$\rho_{after\ inun}$	e_0	$e_{at\ inun}$	$e_{after\ inun}$
			$\varepsilon_a(\%)$	$\varepsilon_v(\%)$	$\varepsilon_r(\%)$	$\varepsilon_{ac}(\%)$	$\varepsilon_{vc}(\%)$	$\varepsilon_{rc}(\%)$						
S204-0.11-0.97	100	33	0.06	0.10	0.02	0.40	1.10	0.35	0.970	0.971	0.982	1.062	1.060	1.037
S304-0.11-0.96	100	83	0.22	0.22	0.00	0.58	1.28	0.35	0.960	0.962	0.975	1.083	1.079	1.052
S103-0.13-0.94	100	167.5	0.60	0.50	-0.05	1.40	1.47	0.04	0.940	0.945	0.959	1.128	1.117	1.086
S404-0.11-0.95	100	251	1.10	0.80	-0.15	1.40	0.90	-0.25	0.950	0.958	0.966	1.105	1.088	1.069
S305-0.09-0.87	50	20	0.07	0.20	0.07	0.33	1.00	0.34	0.870	0.872	0.881	1.299	1.294	1.271
S205-0.09-0.90	50	50	0.20	0.20	0.00	0.60	1.34	0.37	0.900	0.902	0.914	1.222	1.218	1.188
S402-0.10-0.93	50	90	0.62	0.50	-0.06	0.72	0.84	0.06	0.930	0.935	0.943	1.151	1.140	1.122
S105-0.09-0.90	50	150	0.80	0.50	-0.15	2.50	1.13	-0.69	0.900	0.905	0.915	1.222	1.211	1.186
S106-0.09-0.86	25	12	0.12	0.10	-0.01	0.43	1.50	0.54	0.860	0.861	0.874	1.326	1.323	1.288
S206-0.09-0.87	25	30	0.15	0.10	-0.03	0.48	1.15	0.34	0.870	0.871	0.881	1.299	1.297	1.270
S302-0.10-0.91	25	60	0.40	0.30	-0.05	1.00	1.10	0.05	0.910	0.913	0.923	1.198	1.191	1.167
S306-0.09-0.88	25	90	1.70	0.10	-0.80	4.40	0.80	-1.80	0.880	0.881	0.888	1.273	1.270	1.252
S207-0.10-0.88	150	62	0.13	0.15	0.01	0.70	1.65	0.48	0.880	0.881	0.896	1.273	1.269	1.232
S407-0.10-0.90	150	250	0.86	0.70	-0.08	1.51	1.60	0.05	0.900	0.906	0.921	1.222	1.207	1.171
S203-0.13-0.98	150	310	0.87	0.70	-0.09	1.60	1.40	-0.10	0.980	0.987	1.001	1.041	1.027	0.998
S307-0.10-0.88	150	420	3.76	1.05	-1.36	3.14	1.40	-0.87	0.880	0.889	0.902	1.273	1.249	1.217
S308-0.10-0.92	200	70	0.08	0.10	0.01	0.60	1.30	0.35	0.920	0.921	0.933	1.174	1.172	1.143
S208-0.10-0.93	200	175	0.45	0.50	0.03	0.83	1.20	0.19	0.930	0.935	0.946	1.151	1.140	1.114
S303-0.13-0.97	200	370	0.90	0.70	-0.10	1.64	1.60	-0.02	0.970	0.977	0.993	1.062	1.047	1.014
S108-0.10-0.92	200	515	2.56	1.45	-0.56	1.84	1.00	-0.42	0.920	0.934	0.943	1.174	1.142	1.121

7.5.3 Strain captured using LVDTs

7.5.3.1 Axial strain from LVDTs

The local LVDTs were set up in the specimens of set 7 which were tested under a cell pressure of 150 kPa and at different q_c values of 60, 250, 420 kPa as shown in Figure 7.10. The results of this set were used to evaluate the effectiveness of the external displacement transducer (EDT) in capturing the axial displacement of the tested specimens. This was felt necessary because the external transducer is relatively far from the specimen and indirectly connected to it which can lead to significant bedding and other errors which have been well documented in the past (e.g., Burland et al., 1979; Jardine et al., 1984). It is held by a clamping plate connected to the load cell with its tip being in contact with the top surface of the cell chamber, as shown in Figure 7.10 (EDT), to measure the load cell shaft movement with respect to the cell chamber.

The locations of the external transducer and LVDTs and their captured data are shown in Figure 7.10. Although the local LVDTs stability on this rough gravelly specimen surface was improved as discussed in Section 6.6.3, achieving good data from both LVDTs simultaneously did not happen in the tests performed. The initial intention of placing them diametrically opposite each other was so that an average reading for both could be calculated. However, in each test only one LVDT successfully captured the axial displacement and its calculated axial strain data are presented in blue and orange in Figure 7.10b (LVDT2 and LVDT1 respectively). In the first test, at $q_c = 60$kPa, the axial strain due to inundation calculated from LVDT1 was 0.65% which is slightly less than that captured by the external displacement transducer which was 0.72%. While in the second and third tests, at $q_c = 250kPa$ and $420kPa$, the axial collapse strain calculated from the axial displacement captured by LVDT2 and the external displacement transducer were equal, having values of 1.55% and 3.30% respectively. It is likely that axial compliance (and hence bedding) was not fully overcome at lower q_c values. However, the observed difference at $q_c = 60\ kPa$ is still considered small bearing in mind that the primary purpose of these tests was to measure collapse strains of moderate magnitude rather than determining small-strain stiffness.

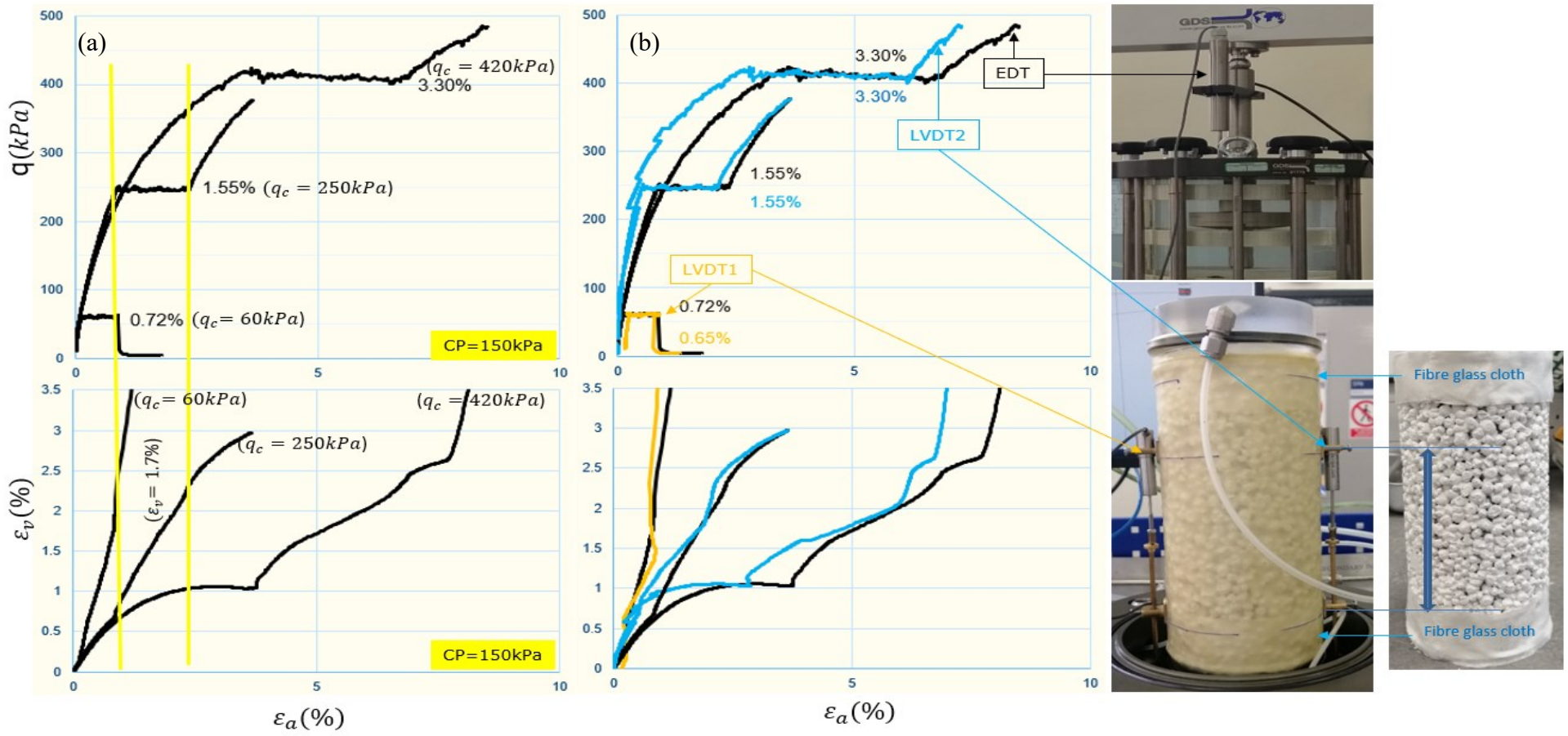


Figure 7.10: Locations of the axial strain measuring units and their captured axial strain data

(External displacement transducer (a) and local LVDTs (b))

Also, as shown in Figure 7.10b, the local LVDTs captured stiffer specimen responses during the application of the collapse stress, q_c, and gave very similar collapse results to the external displacement transducer in both the $q - \varepsilon_a$ plot space and $\varepsilon_v - \varepsilon_a$ plots. This indicates that the fibre cloth strips, used to minimize the membrane penetration (see Section 6.6.1), did not have any considerable effect on the magnitude of specimen axial collapse.

Specimen bedding/seating deformation at the beginning of the test formed part of the measurement from the external displacement transducer which is evident from its higher deformation rate than the local specimen deformation rate. This error always gives a flatter slope than the actual specimen strain slope. However, during the test, minor bedding described as 'secondary bedding', could occur at the contact areas between the specimen and the platens because of particle re-arrangement or particle breakage due to stress concentration. However, it is thought that this rarely happened. The local LVDTs system confirmed that the effect of this redundant secondary specimen bedding, due to the Lytag particle sizes, on collapse strain was negligible.

The local LVDTs successfully captured a stiffer specimen response as plotted in Figure 7.10b. This is because they were positioned within the specimen height, and so were not affected by any 'secondary bedding', because it associated with the Lytag particles' rearrangement near or in contact the top and base platens, which was included in the external displacement transducer reading as shown in Figure 7.11. The horizontal difference between these two pair of slopes, captured by the external displacement transducer and the LVDTs, in all three tests represent the 'secondary bedding' strain. Fortunately, at the point of inundation, after applying q_c, these bedding effects had a negligible effect on the axial collapse strain values, tending to cancel themselves out when subtracting the axial strain before inundation from the axial strain after inundation to determine the axial collapse strain.

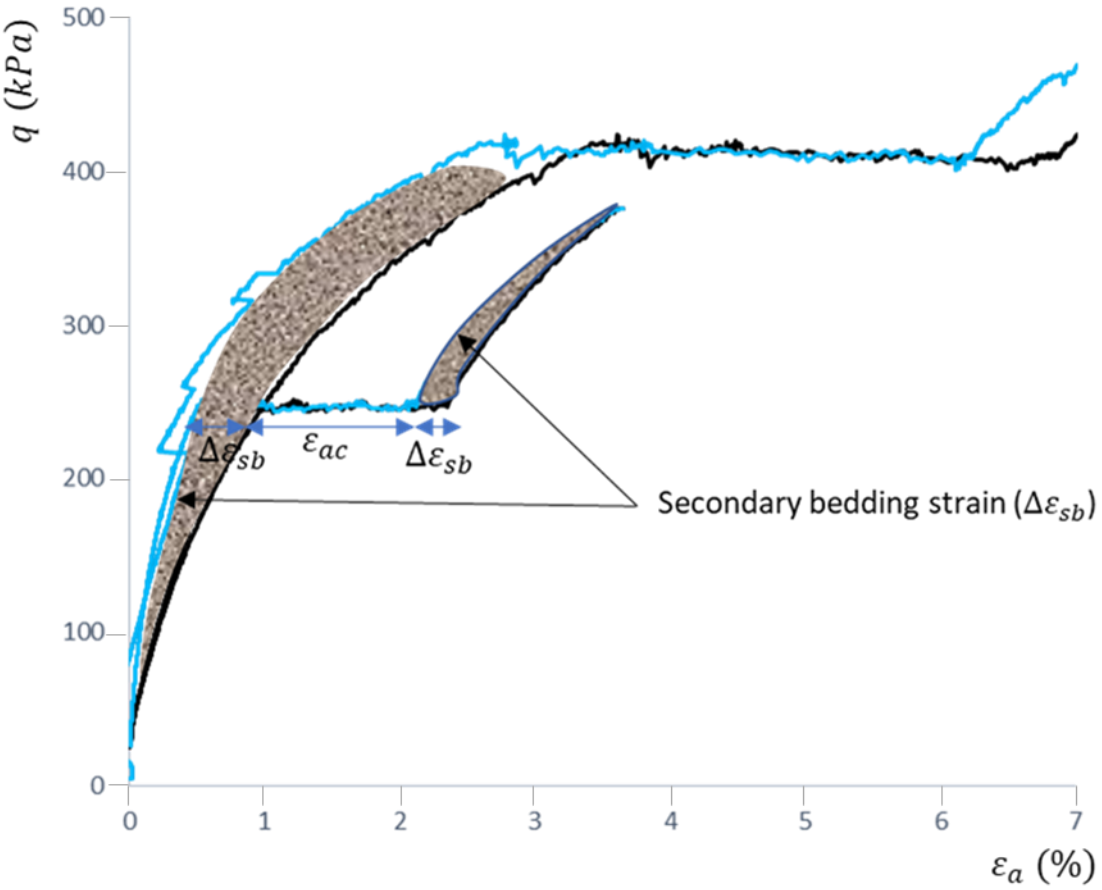


Figure 7.11: Secondary bedding strain area in $q - \varepsilon_a$ plot

7.5.4 Radial strain assessment

It was necessary to calculate the corresponding radial strain because it is an essential variable for understanding the lateral collapse in these specimens which is one of the aims of this research. To evaluate the effectiveness of Equation 6.6, used for calculating radial strain as detailed in Section 6.8.2.2, data from three tests conducted on specimens tested at $CP = 150$ kPa were used for recalculating the axial strain using the natural-linear strain equation, $\varepsilon_{nat} = -\ln(1 - \varepsilon_{eng})$. The results are plotted in Figure 7.12. In this figure, the natural strain (calculated from the measured axial strain) matches almost perfectly with the more commonly used engineering axial strain, ε_{eng}, in the application of q_c stages for these three tests. There is only a minor difference in these strains during the inundation stage of the specimen tested at $q_c = 0.60q_{max}$ which experienced the greatest axial strain. Therefore, the short form of Equation 6.4 (Equation 6.6,$\varepsilon_v = \varepsilon_a + 2\varepsilon_r$) was adopted for calculating radial strains for these specimens. As further confirmation, radial strains for these specimens were calculated using both Equations 6.4 and 6.6 to compare them as illustrated in Figure 7.13.

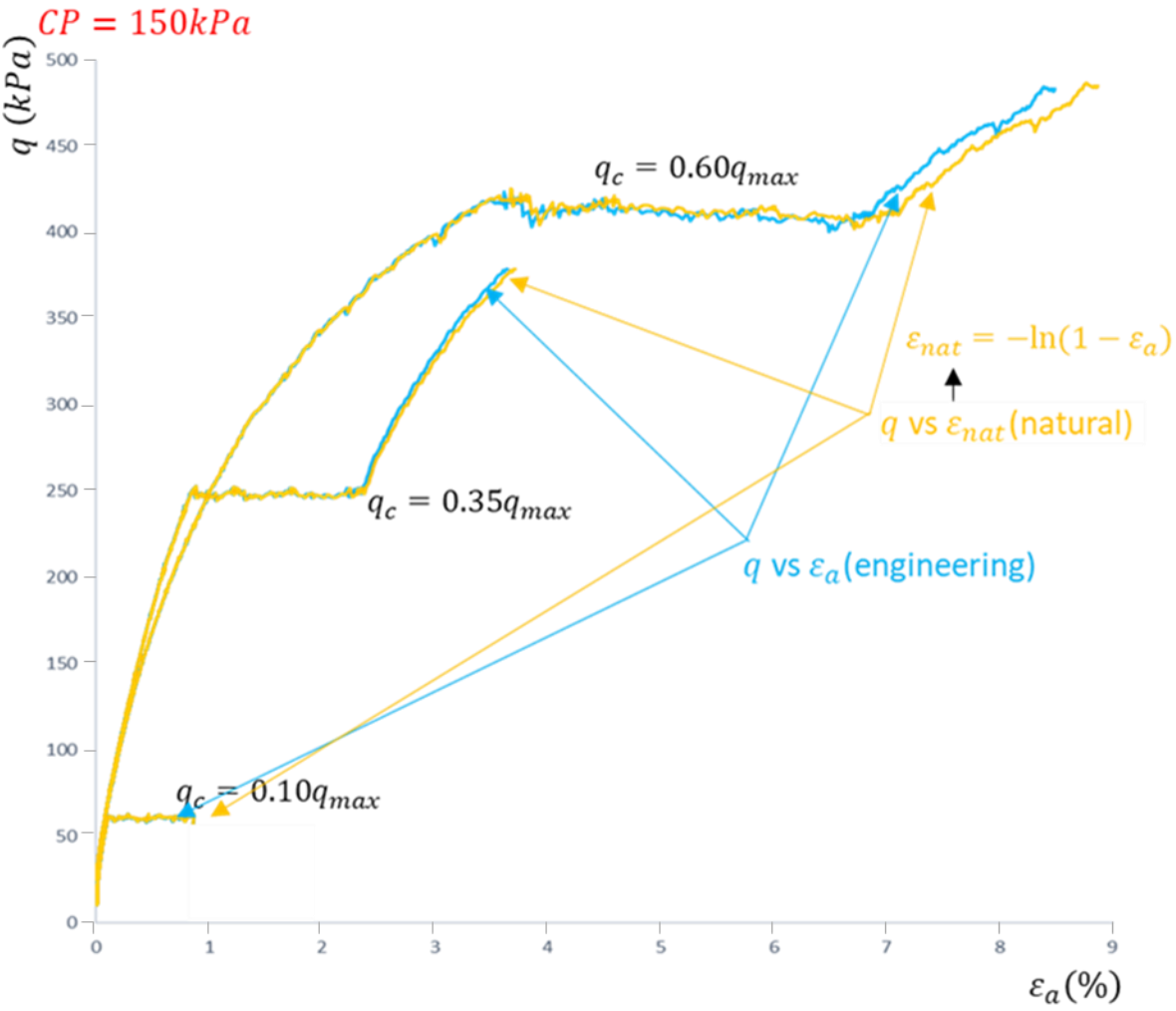


Figure 7.12: Comparison of radial strain calculated from the linear expression of the measured axial strain

The implications of calculating the radial strain using Equation 6.6 (short equation), $\varepsilon_v = \varepsilon_a + 2\varepsilon_r$, and its original version (long equation - Equation 6.4) are evident from Figure 7.13. At $q_c = 0.10q_{max}$ and $0.35q_{max}$, there is no major difference in the radial strain calculated from the long and short expressions, including the strains from the inundation stage. The lower part of Figure 7.13 shows the differences in radial strain calculated from the long and short expressions, $\Delta\varepsilon_r = \varepsilon_{rl} - \varepsilon_{rs}$, expressed as percentages. As the differences are very small, values of $\Delta\varepsilon_r$ have been multiplied by 100. The difference in the radial strain at $q_c = 0.60q_{max}$ using the two expressions was about 0.03% at the start of the inundation and about 0.14% at the end of it, while at $q_c = 0.10$ and $0.35q_{max}$, the $\Delta\varepsilon_r$ values before and after inundation are 0%. In summary, the radial strain assessment using Equation 6.6 is acceptable for inundation stages but not for the wet shearing stage (but this is not the main focus of the investigation).

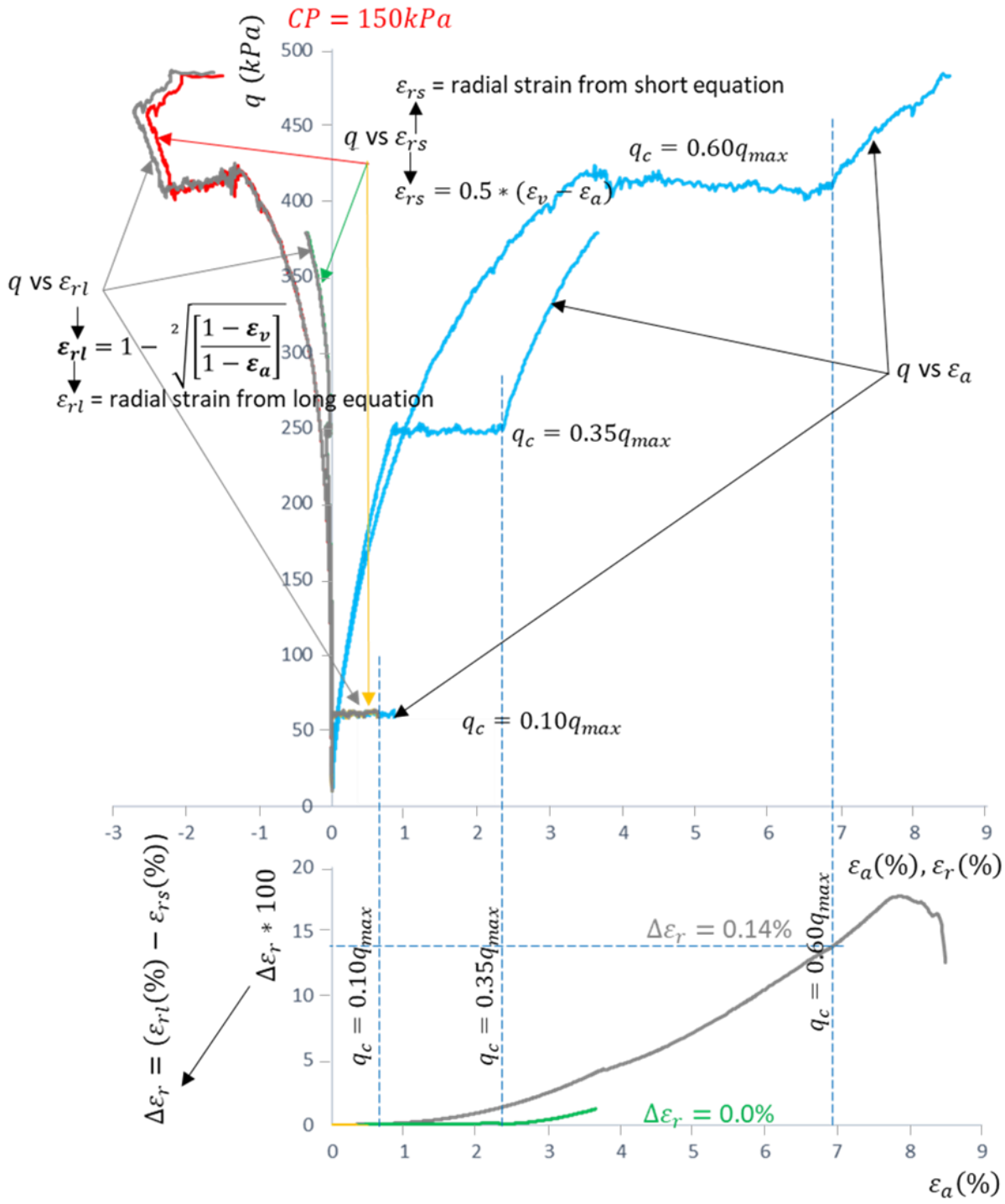


Figure 7.13: Radial strain assessment using the long (shown in grey) and short (shown in red) radial strain equations

The calculated radial strain using Equation 6.6 is plotted against volumetric strain as shown in Figure 7.14. It is evident that the radial strain is affected by the collapse stress, q_c, value. At low collapse stresses, the radial strain was positive, indicating contraction as shown in the orange curve for $q_c = 0.10q_{max}$, in Figure 7.14. At $q_c = 0.60q_{max}$, the specimen radial strain was negative indicating dilation, while at $q_c = 0.35q_{max}$ the radial strain is roughly zero. The

calculated radial strains for other tested specimens are summarised Table 7.3. How they were used in the identification of collapse mechanisms is discussed in Section 7.7.

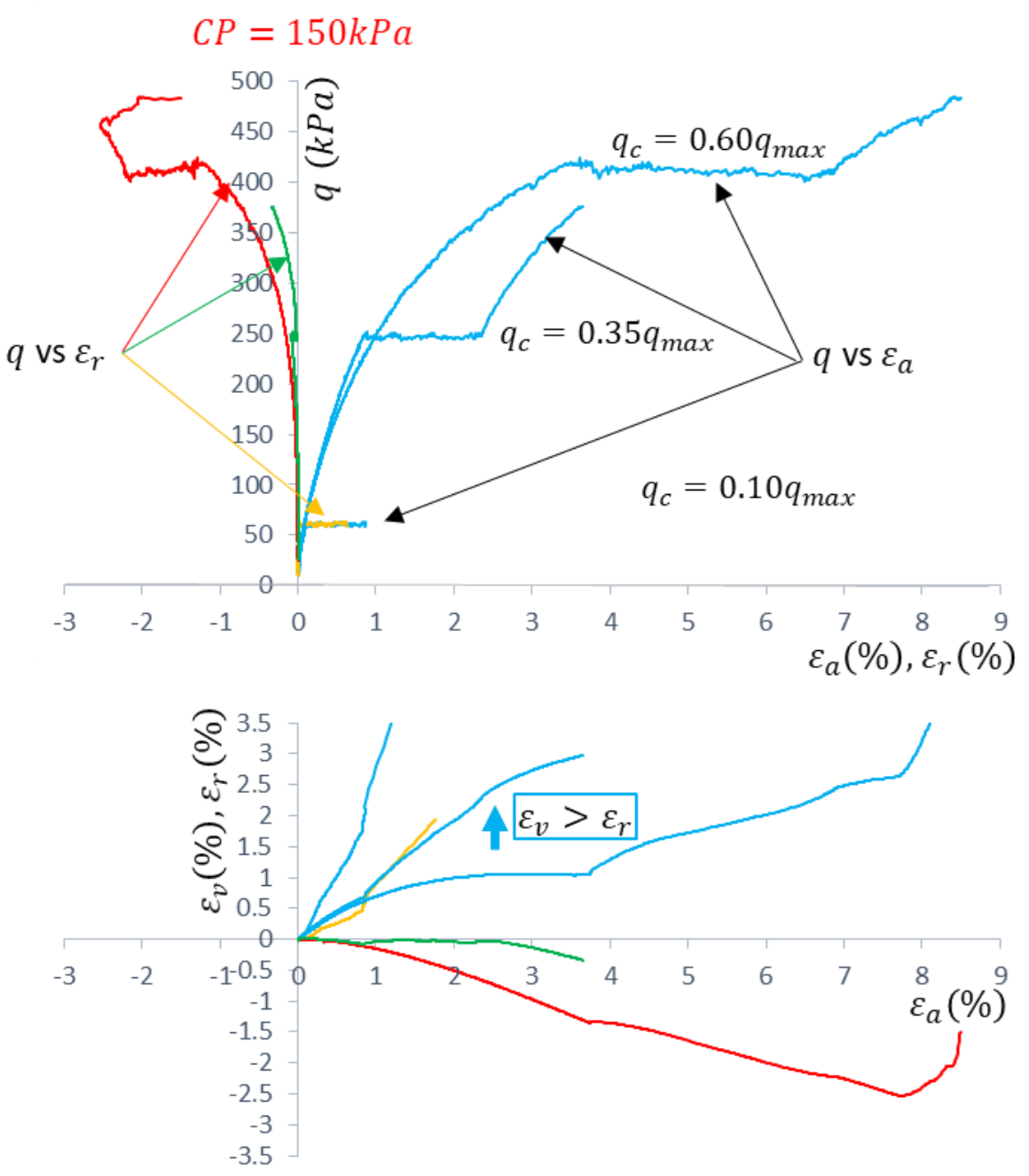


Figure 7.14: Effect of collapse stress (q_c) on axial strain (ε_a), volume strain (ε_v), and radial strain (ε_r)

7.6 Axial strains before and after collapse

As a trial of plotting the axial collapse strain values (see Table 7.3) from the application of q_c and the subsequent inundation onto the stress paths plot shown in Figure 7.5, a new variable which is referred to as the axial strain factor, $A_f = 0.5 * \varepsilon_a\ (\%) * t(\text{kPa})$, was calculated, to normalize/scale the strain values to be plotted against the mean stress (s) as shown in Figures 7.15a and b. This axial strain factor increases with mean stress (s) and cell pressure (CP) in both stages, before and after inundation. This increase starts gradually up to a certain point and then rises sharply with the mean stress, s. These figures also show that axial strain resulting from inundation is greater than that from the application of the collapse stress (q_c). This indicates that these gravelly specimens had the potential to collapse due to inundation under the applied stresses. Mathematical exponential expressions to describe these experimental trends are given in Figure 7.16 which is presented with an enlarged scale to show the full A_f values for the tests with CP = 150 kPa and 200 kPa. The exponential functions fit the test data better at these higher A_f values. The fits are not so good for the lower A_f values for the higher confining stresses (they fit the lower *CP* values very well) but despite this, the coefficient of determination values $R^2 > 0.9$.

7.6.1 Density before and after collapse

A similar exercise has been done to assess the values of density before and after inundation for the tested specimens, given in Table 7.3. These are multiplied by the t values and denominated as density factor, $D_f = \rho_{dry}(\text{t/m}^3) * t\ (\text{kPa})$ and are incorporated into the t vs s plot as shown in Figures 7.15c and d. The D_f value has a relatively linear increase with the mean stress (s), and it has no significant increase with the increase of t values before and after the inundation. Mathematical linear expressions to describe these experimental trends are given in Figure 7.17. These linear functions fit the experimental data very well with $R^2 > 0.98$.

The dry density values were calculated by subtracting the change in volume before (due to application of q_c) and after inundation from the initial volume, assuming the specimen mass remained constant. There were differences between specimens' initial densities even when using a similar binder percentage. Therefore, it was important to understand the effect of specimen density changes before and after collapse on the axial strain values to develop the density-strain relationship which is covered in Section 7.8.

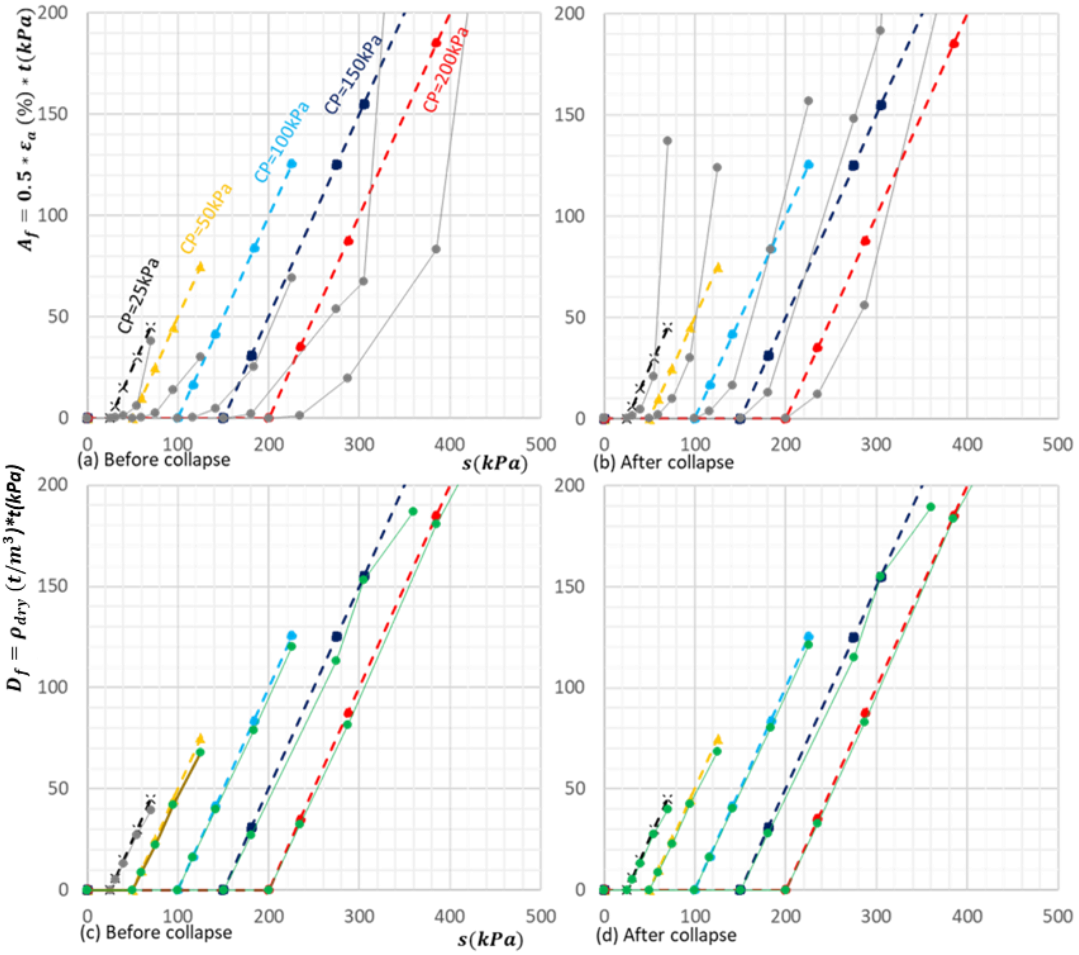


Figure 7.15: Change in axial strain and density due to application of qc and inundation

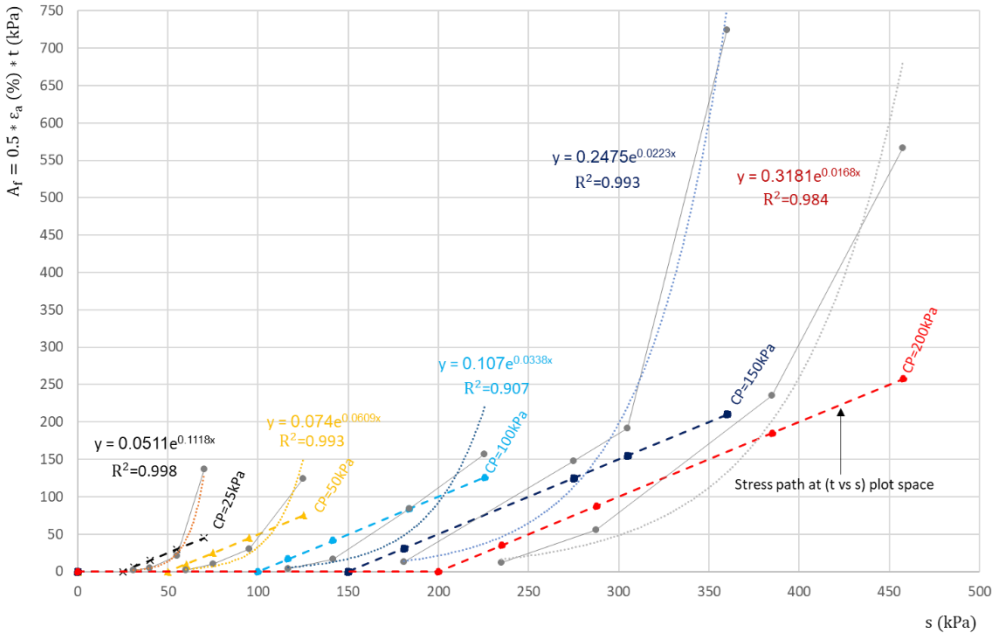


Figure 7.16: Mathematical exponential expressions for describing the A_f factor

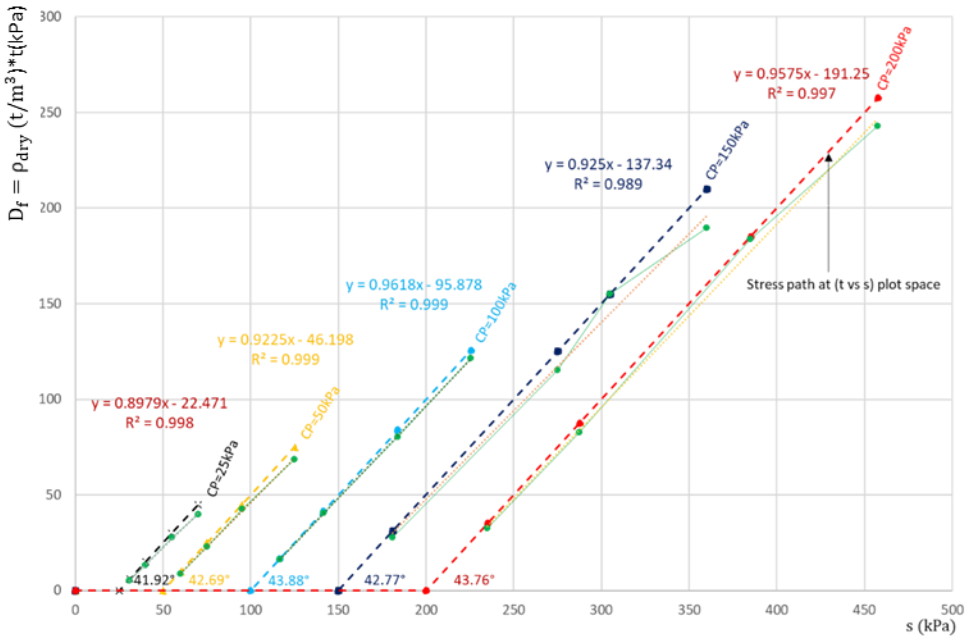


Figure 7.17: Mathematical linear expressions for describing the D_f factor

7.7 Collapse mechanisms

From this triaxial testing programme, two collapse mechanisms have been identified which are controlled by the levels of the cell pressure and collapse stress q_c and are associated with the radial contraction or dilation. Collapse stress, q_c, was plotted against the axial and radial strains resulting from inundation of the specimens as shown in Figure 7.18. In this figure, it is clear that the axial strain increased with both collapse stress and cell pressure while radial strain started with small positive (contractive) values at low collapse stress levels and then increased toward higher negative (dilative) values with increasing collapse stress and cell pressure.

The collapse mechanism developed is defined based on the collapse radial strain sign. The defined sign convention for the radial strain to classify the collapse mechanism is identical to volume strain sign that was defined and discussed in Section 6.8.2.1. For positive radial strain, the collapse mechanism is defined as contractive and for negative radial strain it is defined as dilative. Accordingly, as shown in Figure 7.18, thirteen specimens (indicated by symbols on each of the CP lines) were tested for collapse at q_c values less than or equal $0.50q_{max}$. These contracted radially and their resultant overall collapse mechanism is contraction. The five specimens tested at $q_c = 0.75q_{max}$ and one at $q_c = 0.60q_{max}$ (*CP*=150kPa) dilated radially and their resultant overall collapse mechanism is dilation. One specimen tested at $q_c =$

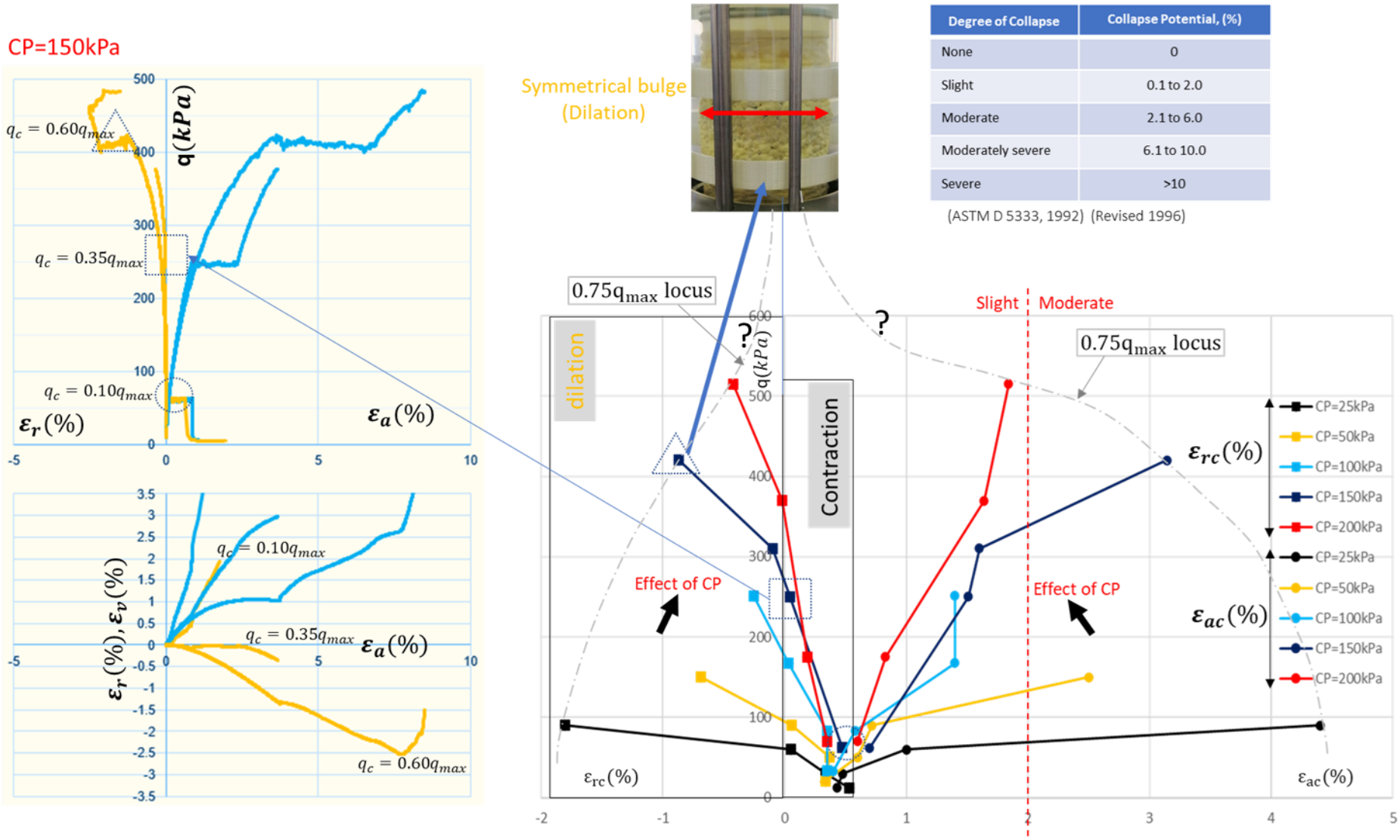
$0.50q_{max}$ (*CP* = 200kPa) dilated radially by a small negative ε_{rc} value close to zero ($\varepsilon_{rc} = -0.02\%$). This indicates that, for *CP* > 200 kPa, a dilative mechanism will start to take place at $q_c = 0.50q_{max}$ values as well.

Axial collapse strain for all specimens ranged from 0.4% to 4.4% within this cell pressure range (*CP* = 25 kPa to 200 kPa). If collapse in these specimens was classified according to the ASTM D5333 (for 1-D collapse) as given in Figure 7.18, the axial collapse strain for three specimens collapsed fill within the specified range of 2% to 6%, their collapse potential would be classified as moderate collapse. The collapse potential for the other specimens were within the slight collapse zone. The data points relating to the $q_c = 0.75q_{max}$ collapse stresses have been connected with a broken line which forms a quite well defined '$0.75q_{max}$ locus' which extends from the zone of negative radial strains towards zero with increasing cell pressure and inundation collapse stress and similarly the axial strain also tends to zero with increasing cell pressure and inundation collapse stress. It can be seen that the locus for lower percentage of q_{max} shrink (although they are not as well defined) so that the locus for low values are within positive zones of both axial and radial strain.

To compare the developed collapse mechanism with the classification based on the ASTM D5333, all the specimens that were classified as moderate collapse potential dilated radially and the ones that contracted radially showed slight collapse potential. Thus, it can be concluded that when the collapse due to outwards radial dilation (negative), the collapse potential in the field would be assessed as moderate or greater. This can be considered as experimental evidence for lateral soil collapse under the foundations in the study area. However, these moderate collapse potential values are still small in comparison with the magnitude of field collapse that caused the observed damage seen in Figure 3.2. This is probably due to the significant void ratio difference between the fabric of the natural gravelly soils (see Figure 7.22) and the fabric of these analogue specimens.

7.8 Effect of specimen dry density on collapse potential

In this section, the effect of the difference in the dry density of the analogue specimens on their collapse potential is assessed. Relationships between specimen collapse strain and the corresponding density changes due to inundation were developed by utilizing the effect of cell pressure and inundation collapse stress on the axial collapse strain.



Degree of Collapse	Collapse Potential, (%)
None	0
Slight	0.1 to 2.0
Moderate	2.1 to 6.0
Moderately severe	6.1 to 10.0
Severe	>10

(ASTM D 5333, 1992) (Revised 1996)

Figure 7.18: Collapse mechanisms in the tested specimens

First, it was noticed that axial strains due to inundation and the resulting densification of the tested specimens had random different slopes, instead of a clear trend, when plotted against corresponding collapse stress q_c values as shown in Figures 7.19 and 7.20 respectively. This is mainly due to the difference in the initial density of these specimens. Thus, it was decided to normalise their effects by dividing the change in density caused by collapse, $\Delta\rho_c$, by the axial collapse strain, ε_{ac}, and then plotting the result against the collapse stress, q_c, values. This process simply moderates high density changes with high axial collapse strains and the vice versa.

After plotting the ratio between density change due to collapse to its corresponding axial collapse strain, $(\Delta\rho_c/\varepsilon_{ac})$, against collapse stress, q_c, it was noticed that there is a unique trend between them. This unique trend is similar to the form of the moon at the start of its cycle; therefore, these trends are referred to here as 'moon curves' for simplification. For the different values of cell pressure, these moon curves were fitted by: (a) power, (b) polynomial, (c) logarithmic, and (d) linear functions as shown in Figure 7.21. All of these mathematical functions give a good representation of the experimental curves, but the polynomial function (Figure 7.21b) gives the best fit (R^2 between 0.971 and 0.996). The cell pressure controlled the hierarchy of these curves. The increase in cell pressure rotated these curves anticlockwise around their upper ends causing them to sweep outwards. The angle of rotation for each curve increased with cell pressure as illustrated in Figure 7.23.

To correct for the effect of specimen density differences in axial strain, if each of these mathematical polynomial curves shown in Figure 7.21b is assumed to represent the corrected curve then it can be considered that the vertical difference between the curve and its corresponding experimental data at any point, represents the error in the slope $(\Delta\rho_c/\varepsilon_{ac})$ at a particular collapse stress q_c point. However, it is necessary to relate the change in collapse strain to the change in density. To develop a correction approach, a relationship between $\Delta\rho_c$ and ε_{ac} needs to be established. Initially an approach might be to consider that the change in density increases linearly with collapse strain, but this depends on both the collapse stress and cell pressure as shown in Figure 7.15c. Therefore, to relate the collapse strain (ε_{ac}) with change in density $(\Delta\rho_c)$, it is necessary to conduct a further series of tests at different densities and constant cell pressure and constant collapse stress. It was not possible to pursue this

approach in the current research because of time limitations but it is proposed as a topic for future study in Chapter 8.

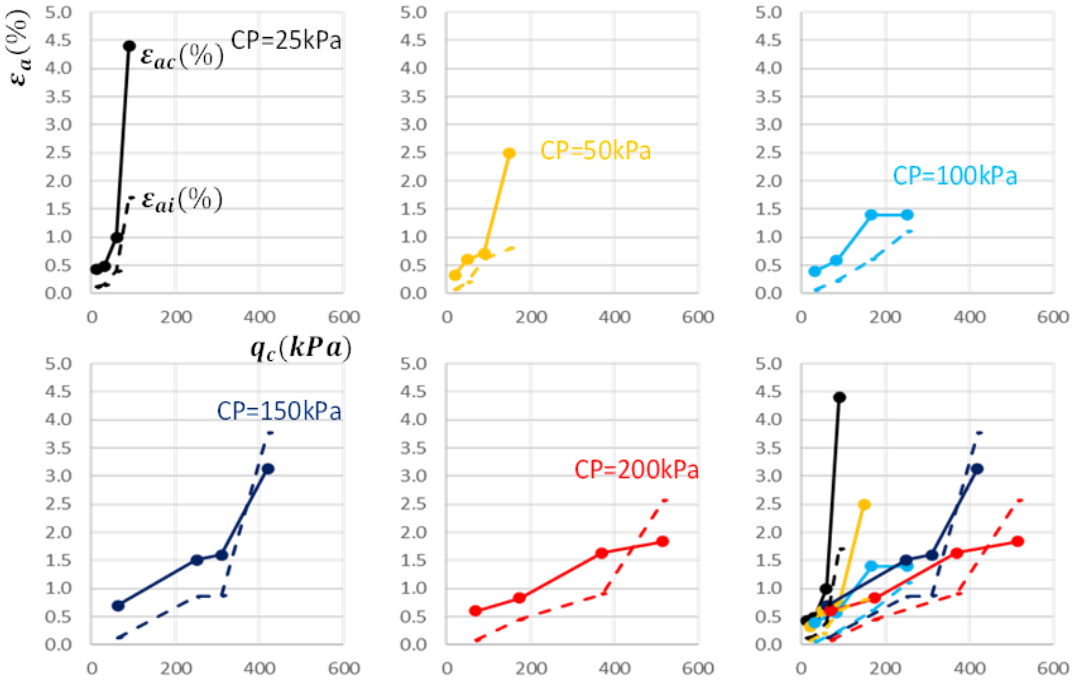


Figure 7.19: Change in axial stress due to collapse versus collapse stress

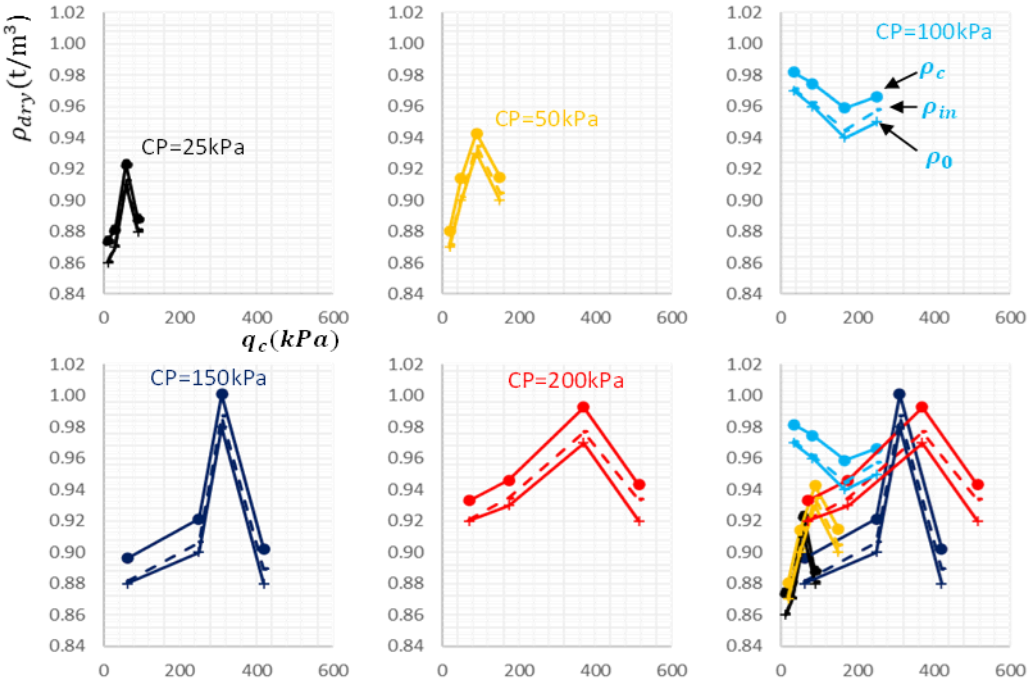


Figure 7.20: Density changes against collapse stress

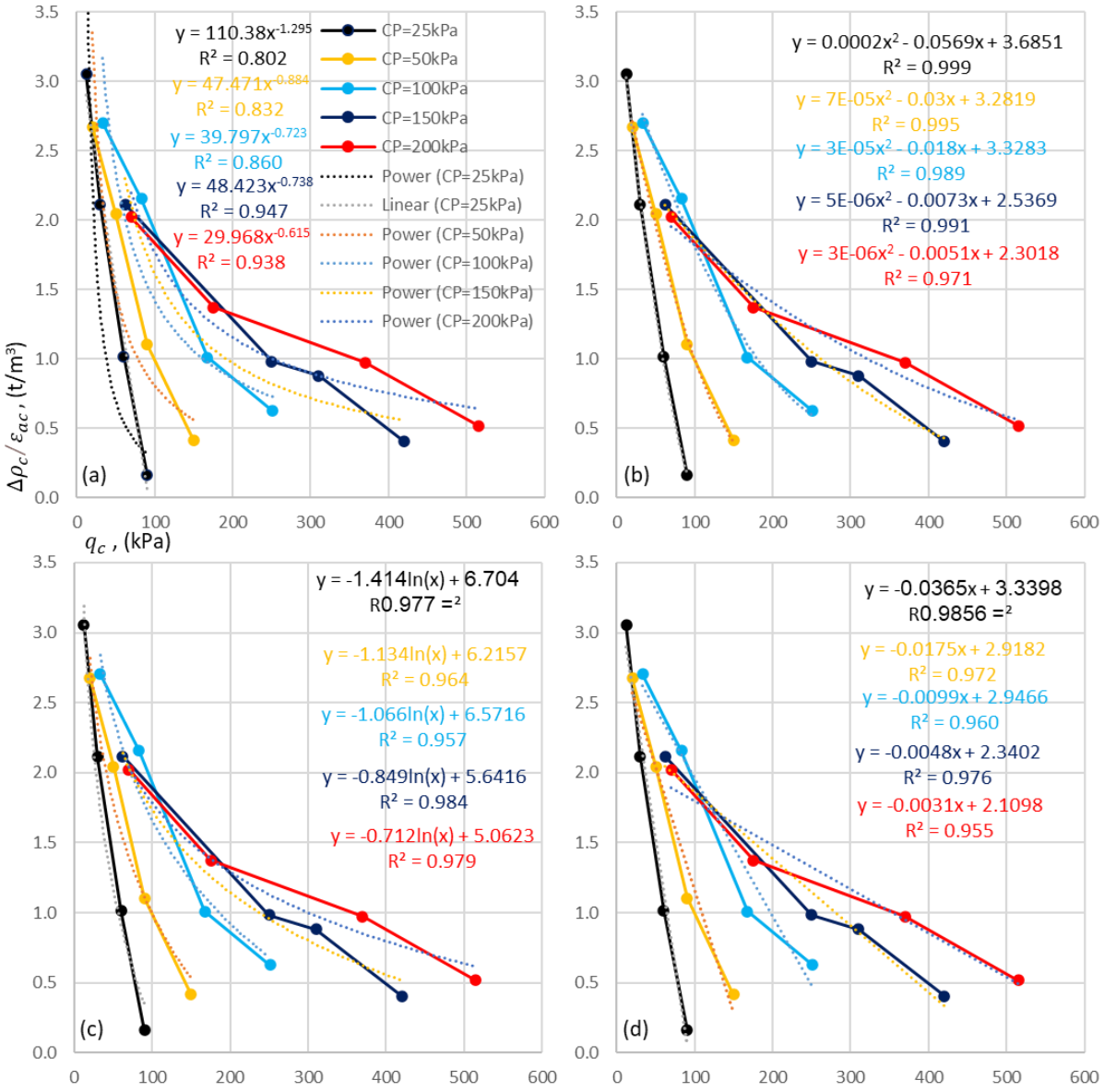


Figure 7.21: Relation between density-axial strain ratio to collapse stress experimental data and mathematical fits using (a) power trend, (b) polynomial, (c) logarithmic, and (d) linear functions

7.8.1 Application of density charts

To estimate collapse in the field, curves similar to these in Figure 7.21b which correlate the normalised change in the specimen density with axial strain changes due to collapse ($\Delta\rho_c/\varepsilon_{ac}$) produced from the analogue specimens, would have to be developed for the actual in-situ soils. Then if the change in density is assumed to be equal to the difference between the maximum and the in-situ densities and the cell pressure considered as the lateral stress, axial collapse strain can be estimated from the reproduced curves by assigning the existing building stress as the collapse stress q_c.

Accordingly, the moon curves provided in Figure 7.21b would be a good starting point to develop a standard chart for estimating collapse strain from basic measurable soil properties such as soil density under different stress levels. The primary limitation of this idea is that the natural soil fabric is more complex than this simple arrangement of spherical Lytag particles bonded with kaolin paste.

However, this triaxial collapse testing procedure developed could be implemented using more complicated analogue collapsible specimens by including more accurate soil properties such as the shape of the coarse particles and the content and percentage of the fine particles.

To do so, an enhancement in the procedure developed for forming analogue specimens is needed to produce specimens with more open fabric, similar to the soils encountered in the study area as shown in Figure 7.22. If this is successfully achieved, it is expected that for any different collapsible soil, these reproduced moon curves will cluster or scatter from each other depending on the properties of the soil under investigation.



Figure 7.22: Examples for the actual gravelly soil fabric in the study area

7.8.2 Defining the collapse mechanism using density charts

In Section 7.8, it is discussed that the collapse mechanism can involve one of two forms: with radial contraction or dilation depending on the combined effect of the collapse stress q_c and cell pressure. Based on the collapse data presented in Table 7.3 and plotted in Figure 7.18. The collapse mechanism can be also defined from the slope of the normalised density to collapse

strain ($\Delta\rho_c/\varepsilon_{ac}$) and collapse stress ($q_c$) plot space shown in Figure 7.21 (moon curves). Figure 7.23 was further generated by adding additional dotted lines to separate between these two collapse mechanisms for each cell pressure curve (example shown for *CP* = 25 kPa). Each line was plotted from the origin to intersect with the point of collapse stress at q_c at $\varepsilon_{rc} = \text{zero}$ which was picked from the equivalent curve (at the appropriate cell pressure) in Figure 7.18. The angle of rotation of these lines from the vertical axis increased with cell pressure leading to an increase in the zone of contraction and a decrease in the zone of dilation. However, for every cell pressure, the collapse stress range that induced dilation still increased significantly with cell pressure. This means that for a given cell pressure, a range of collapse stresses can be defined that would induce contraction and another higher range to induce dilation.

The curvature of these curves, at which they are intersected by the dotted lines, can be defined as 'critical collapse stress'. Any collapse stress higher than this stress produces a dilation mechanism at which the degree of collapse transfers from slight collapse to more considerable collapse states.

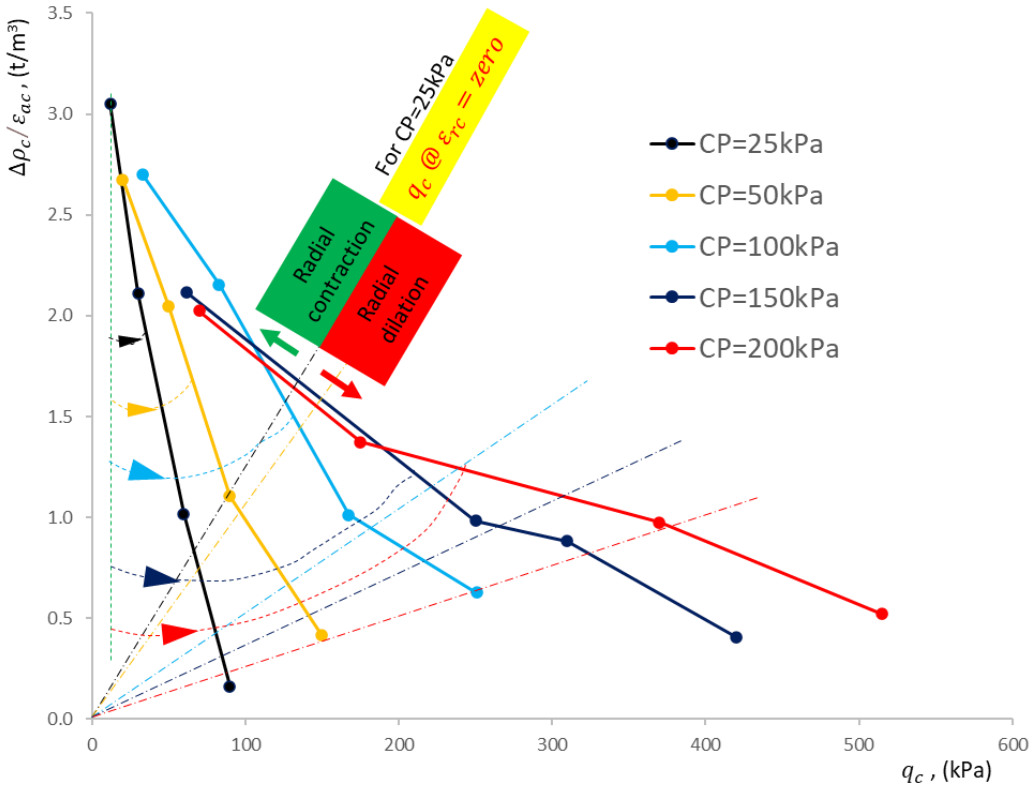


Figure 7.23: Effect of cell pressure (CP) on the change of density to the axial collapse strain against innudation collapse stress (q_c)and the collapse mechanism

7.9 Summary of Chapter 7

In Chapter 7, the results of the triaxial testing programme have been presented, analysed and discussed. The dry failure envelope based on the dry shearing tests on the analogue specimens was established. The stress paths for the specimens tested for collapse then were drawn alongside with their axial strain and density values. Stress-strain relations for both dry and wet shearing tests are plotted and discussed. Two collapse mechanisms from the 3-D collapse tests were identified and defined. A procedure for connecting collapse strain with density variation is established to consider the differences in the initial specimen density for each set of specimens and their influence on collapse. A proposal for producing similar relations between stress-strain and density changes, due to collapse, for the natural soil to estimate the collapse potential under field conditions is put forward.

Chapter 8 : Main conclusions and recommendations for future research.

Assessing collapse behaviour in the gravelly soils encountered in Omdurman city, Sudan, had not hitherto been achieved through a meaningful quantifiable experimental approach. This new area of research, relating to soils containing more than 50% rounded gravel particles bonded with clay fines, is tackled in this study by developing a unique experimental triaxial testing procedure to quantify and assess collapse behaviour in such soils using analogue specimens prepared from Lytag bonded with kaolin.

8.1 Collapsibility of the soils at the study area

Previous research on the collapse problem in the study area was conducted by Osman (2004) and Hamid (2012). In 2018, the Author visited the area and made comprehensive observations of existing and new structural damage and collected representative soil samples for characterisation and testing purposes. Soil collapse has been established as the reason for the structural damage. The collapsible soils are located at shallow depth of about 3 m and are dominated by poorly graded clayey gravels (GC) bonded by clay and silt fines with less than 10% water content. This gravel has particles ranging between 2 mm and 15 mm and has a weakly bonded fabric. This shallow collapsible layer rests on the thick stable Nubian Sandstone formation.

The main reasons for the collapsible nature of the soil are relatively low in-situ density and water contents, the high gravel content and permeability, and the dispersive nature of the fines that coat the coarser particles. These features make the soil fabric highly susceptible to any water flow and collapse whenever there is a free water source, and this is exacerbated when there are stress increases from new building loads.

The earlier studies established that the thickness of the collapsible layer is variable. This in conjunction with localised ground loading by strip and/or pad footings of the new buildings and indiscriminate inundation has led to differential settlements and consequent structural cracking. The photographs of the damage shown in Figures 2.25, 2.26 and 3.2 provide evidence of settlements at building corners producing wide open diagonal cracks while more centrally

there are more vertical cracks, wide open at the top and narrow at the base, indicating a hogging mode of deformation.

The brittle nature of this weakly bonded gravelly fabric meant that taking block samples was not feasible with the resources available. The processes of cutting soil blocks or taking tube samples and trimming them to a specific geometry are not applicable because of the high gravel content and the very weak bonds between the gravel particles compared with the gravel strength. The soil fabric is usually destroyed during the field sampling processes.

8.2 Theoretical evaluation of collapse

Prior to embarking on experimental studies to assess collapse potential, the Author developed a theoretical procedure for quantifying the maximum limit of collapse potential of this soil by utilising data compiled by Hamid (2012).

The average natural density of the collapsible soil (from TP1) is about 1.80 t/m^3 and its maximum compacted density about 2.20 t/m^3 (from modified compaction testing). Therefore, the difference in density is used to evaluate the hypothetical collapsibility of these natural gravelly soils.

With this approach, density data from two different soil profiles (trial pits) were used to calculate the hypothetical collapse potential at 0.5 m intervals. The maximum possible collapse potential for one of the trail pits was about twice the other, confirming the spatial variability of collapse. Both maximum collapse potential values, 22% from TP1 and 12% from TP2, can be classified as a severe collapse potential according to ASTM (D5333, 1992) because they are greater than 6%. The total maximum expected settlement from this method is 45 cm for TP1 and 26 cm for TP2 both of which could lead to serious structural damage.

8.3 Analogue specimens

A procedure for forming appropriate analogue collapsible specimens was developed to overcome the issue of not being able to sample the natural in-situ soil. Initially the natural gravel was used with a clay binder but there were difficulties producing a fabric of sufficient low density to lead to collapse. After various trials, artificial materials were adopted with a lightweight aggregate, Lytag, as the coarse material and kaolin as the binder to produce low density collapsible specimens.

Lytag was selected because it has high crushing strength and spherical particles similar to the natural gravel. It has an overall particle density of 2.0 t/m^3 which makes it lighter in weight than the natural gravel which helped produce looser specimens.

A procedure for preparing analogue specimens was developed that successfully produced consistent collapsible specimens. A very specific procedure was adopted to control and minimise any subjectivity. This developed procedure is not standard and needed progressive improvement but finally it enabled collapsible analogue specimens to be successfully produced.

8.4 1-D and partially confined 3-D footing collapse tests

Initially the conventional approach of inundating the specimens under 1-D conditions was implemented. However, the collapse potential observed did not correlate with the ground subsidence that must have occurred in field to cause the observed severe damage.

Testing first the natural gravelly specimens and later the analogue specimens in 1-D compression, produced collapse potential magnitudes of less than 2%, significantly under-estimating actual collapse. This was attributed to two reasons: the analogue specimens produced were denser than the natural fabric and the test boundary conditions were not representative of those in situ. In a similar fashion, results from a field plate load test conducted by Osman (2004) in the study area resulted in a collapse of only 7.25 mm under 262 kPa collapse stress.

In both cases the primary reason for the under-estimation of collapse was considered to be non-representative boundary conditions. A larger diameter 1-D chamber was appropriated to check on sample size effects for these gravelly analogue specimens. Again, collapse was significantly under-estimated, even though its magnitude increased. The ratio between the confining chamber diameter and the loading platen was increased from 1.0, as used in the 1-D test to 1.65 to decrease the degree of confinement around the specimen. This in essence became a footing test. Even though no correction was applied to account for wall friction, the collapse increased dramatically from moderate, as observed under 1-D conditions, to severe collapse in the footing test, i.e. resulting in about 10 times more collapse.

It was concluded that gravelly soil deformations due to inundation collapse are highly dependent on the degree of confinement or lateral stress state. However, it was also realised

that the collapse in the footing test resulted from both upward soil movement beyond the platen, i.e. bearing capacity failure, due to lack of controlling the test boundary conditions, as well as inundation collapse. It was therefore decided to test these analogue collapsible specimens using triaxial apparatus, so that the lateral stresses, as well as deviatoric stresses, could be controlled.

8.5 Triaxial collapse test

The triaxial testing programme was successfully run using four repeatable main stages: preparing analogue collapsible specimens; setting-up the triaxial specimens and the apparatus; running the collapse tests including resolving issues such as the nature of the rough surface texture of the specimens; utilising the test results to develop correlations between specimen density and applied stress with the resulting collapse strains.

Analogue triaxial collapsible specimens

The procedure for preparing analogue triaxial collapsible specimens had to be slightly modified because of issues that arose because of membrane rupture and specimen extrusion. As a result, the specimens were denser than the originally intended and so with a less collapsible structure. Despite this it was still possible to assess the effect of stress level on collapse potential and two collapse mechanisms were identified. The procedure successfully produced cylindrical triaxial analogue collapsible specimens with known dimensions, density and moisture content.

Specimen and test set-up

The specimen set-up procedure inside the triaxial chamber evolved during preliminary tests. specimens were transferred from the preparation bench to the apparatus relying on global confinement from placing the membrane and porous stones at the top and base of the specimen. Fibre cloth strips were used to minimize membrane penetration and rupture at the top and base of the specimen. Local axial strains were measured using a conventional approach using LVDTs (as described by Cuccovillo and Coop, 1997) but with modifications to deal with the rough surface texture. These were only developed in the later stages of testing. The local measurements confirmed that the external displacement transducer had sufficient accuracy for determining axial collapse strains reliably.

Prior to starting the testing programme on the analogue specimens, a number of tests were performed on dummy specimens to assess and formulate corrections for cell chamber expansion and membrane penetration. This was important as the overall specimen volume

change was measured using the cell pressure control unit which could resolve to 1 mm^3. Comparison of the membrane volume penetration between the dummy specimens and analogue specimens showed that the analogue specimen contraction due to application of all-round cell pressure was negligible and the specimen volumetric strain in this stage was assumed to be zero. This assumption did not affect the calculation of specimen volume change because any specimen deformation before the start of applying deviator stress was deducted including the chamber expansion, membrane volume penetration and bedding strain.

Findings from the triaxial collapse test programme

Prior to commencing the triaxial collapse tests it was necessary to establish the dry failure envelope so that the viable stress range to which specimens could be subjected before inundation was established. The dry failure envelope was defined by an internal angle of shearing resistance of 35.5° and cohesion of 15 kPa, calculated from the best fitting Mohr circles from tests on five analogue specimens that were dry sheared under cell pressures of 25, 50, 100, 150, and 250 kPa. The maximum secant stiffness determined increased with cell pressure reaching 9, 12, 28, 34, and 40 MPa respectively. This range of stress levels was chosen to be close to the estimated in-situ foundation stresses in the Omdurman study area.

Inundation collapse stress

Inundation collapse stress $q_c$values were chosen as a percentage of the maximum deviator stress that analogue specimens could sustain based on the failure envelope. Four levels of collapse stress of 0.10, 0.25, 0.50, 0.75 of their corresponding maximum deviator stresses at given cell pressures were applied to investigate the effect of collapse stress. The collapse stress of $q_c = 0.10\, q_{max}$ was selected to be close to the isotropic condition to make sure that the external displacement transducer was in contact to record vertical displacements.

Collapse strains

Collapse strains were defined by the additional specimen axial, radial and volumetric strains resulting from inundation under constant collapse stress. Volumetric and axial collapse strains were calculated from apparatus transducer measurements while radial collapse strain was calculated based on the volumetric and axial strains. Strain formulations were developed to check the effect of the magnitude of strain in applying commonly used approximations for triaxial conditions ($\varepsilon_v = \varepsilon_a + 2\varepsilon_r$). For the range of collapse strains measured, differences between the approximate and exact formulation were negligible. From the analysis of the

triaxial results, it was found that axial collapse strain increases with inundation collapse stress, q_c. Contracting radial collapse strains occurred at lower levels of collapse stress while there were dilating radial strains at higher collapse stress values. The volumetric collapse strain remained relatively constant, indicating that collapse within this gravelly soil is basically due to a countering combination of vertical and lateral particle movements than fabric collapse and consequent volume reduction as usually associated with other types of collapsible soils (with much smaller particle sizes).

Accordingly, from the radial strains determined, two collapse mechanisms were defined involving radial contraction or dilation. Both radial contraction and dilation were observed at all studied cell pressure values, but the difference was in q_c values. At $q_c < 0.50q_{max}$ collapse occurred under radial contraction while for $q_c \geq 0.50q_{max}$ collapse occurred under radial dilation.

Density correlations

It was found that collapse strains are affected by specimen density before collapse. Denser specimens generated lower strains. It is not straightforward to link collapse strain with density in either a theoretical or empirical relationship. However, a reasonable approach has been developed which links the change of specimen density to the change of axial collapse strain and collapse stress at constant cell pressure. This empirical relationship has been plotted in the form of curves ($\frac{\Delta\rho_c}{\varepsilon_{ac}} vs\ q_c$) which have two main slopes from which the two collapse mechanisms can be described. The bilinear nature of the curves becomes more prominent at higher cell pressure values. These curves were plotted in Figure 7.23 which is repeated here as Figure 8.1. The first slope is very steep which represents collapse due to specimen radial contraction while the flatter section relates to radial dilation.

In order to gain a full understanding of the effect of density on collapse, more tests are required using specimens with different densities that should be tested under similar stress conditions of cell pressure and inundation collapse stress.

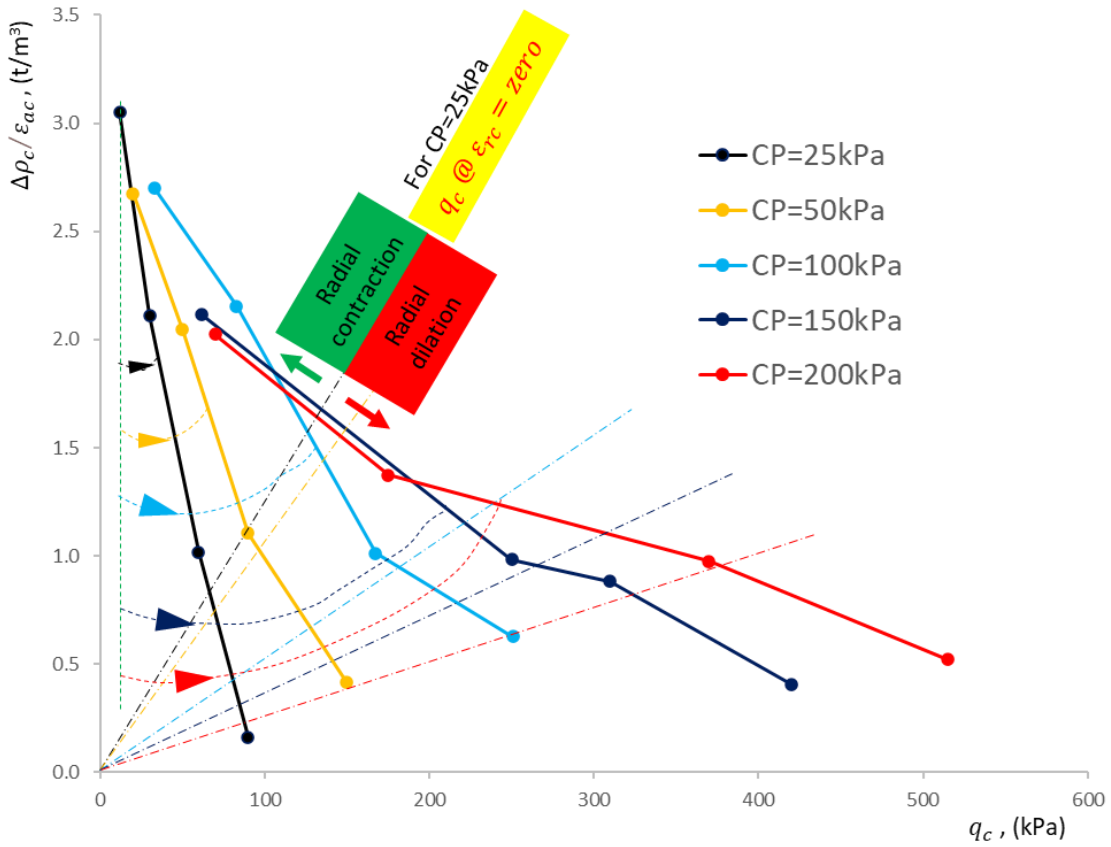


Figure 8: Effect of cell pressure (CP) on the change of density to the axial collapse strain against innudation collapse stress (q_c)and the collapse mechanism

8.6 Recommendations for future research

Factors affecting collapse in gravelly soils

There is scope for improving the analogue collapsible specimen preparation procedure that has been developed. Additionally, a new procedure for preparing analogue collapsible specimens from the natural gravel could be developed. The effect of several variables such as water content and fines content and plasticity on collapse potential could then be studied. Also, gravels with different particle shapes and surface textures could be introduced to study their effect on collapse potential. There are numerous permutations that could be explored.

Collapse test

The fundamental idea of measuring collapse using an oedometer with zero lateral strain during the test is questionable when assessing collapse in gravelly soils under shallow foundations. However, a small-scale instrumented model with suitable boundary conditions to replicate

collapse under two types of footing (isolated pad and strip footing) would allow comparisons and correlations to be made with results from triaxial tests.

Specimen size

Testing specimens with diameters greater than 100 mm are recommended to investigate the effect of specimen diameter and maximum particle size on collapse deformation. This is particularly relevant given the small particle to specimen diameter ratio.

Sand and silt effect

The effect of the silt/sand on the bond between gravel particles, which is the main trigger of collapse, is considerable and there is great scope for further investigation. Silt and sand might initiate a greater gap between coarse particles if they form bridges between the gravel particle contacts. However, adding or mixing silt/sand soil with gravel might lead to more stable soil fabric against collapse if they fill the gaps between gravel particles.

Collapse mechanism

A micro-scale study of the nature of the bonds within this gravelly soil is required before and during collapse to understand their effects on the collapse mechanism at the micro-scale.

Cracks due to collapse

Studying collapse using a prototype building model in the field could provide great insight into how cracking develops and propagates and the resulting crack patterns and how they can be linked to collapse potential values.

Equally, installing survey monitoring points on newly-built and existing building would allow the magnitude of settlements and the structural deformation modes to be established more clearly. The monitoring points could be for performing levelling, providing information on vertical displacements, or for 3-D measurements using theodolites or total stations.

List of references

Al Haj, K. (2014). *Mechanical response of two plastic clay soils from Sudan*. PhD thesis, Imperial College London, UK.

Al Haj, K. M. A. and Standing, J. R. (2015). Mechanical properties of two expansive clay soils from Sudan. *Géotechnique* 65, No. 4, pp. 258–273.

Al Haj, K. M. A. and Standing, J. R. (2016). Soil water retention curves representing two tropical clay soils from Sudan. *Géotechnique* 66, No. 1, pp. 71-84.

Alrakoba news. (2018). Babanusa collapse. [online] Available at: https://www.alrakoba.net/index.php [Accessed 15 Jun. 2018].

Alzubair, M. A. (2020). Geographical and hydrological effects of Nubian sandstone formations on ground water in Khartoum State – Sudan. *International Journal of Hydrology*, No. 4, pp. 270–279. DOI: 10.15406/ijh.2020.04.00254.

ASTM (1996). *Standard Test Method for measurement of collapse potential of soils, D5333-92*. Annual Book of Standards, ASTM International, West Conshohocken, PA.

ASTM (1998). *Standard Test Method for One-Dimensional Consolidation Properties of Soils Using Controlled-Strain Loading, D4186-89*. Annual Book of Standards, ASTM International, West Conshohocken, PA.

ASTM (2000). *Standard Test Methods for Laboratory Compaction Characteristics of Soil Using Modified Effort, D1557-98*. Annual Book of Standards, ASTM International, West Conshohocken, PA.

ASTM (2003a). *Standard Test Method for One-Dimensional Consolidation Properties of Soils, D2435–02*. Annual Book of Standards, ASTM International, West Conshohocken, PA.

ASTM (2003b). *Standard Test Method for One-Dimensional Consolidation Properties of Soils Using Controlled-Strain Loading, D4186-89* (1998). Annual Book of Standards, ASTM International, West Conshohocken, PA.

ASTM (2006). *Standard Practice for Classification of soils for Engineering Purposes (Unified Soil Classification System), D2487*-06. Annual Book of Standards, ASTM International, West Conshohocken, PA.

ASTM (2016). *Standard Test Methods for Minimum Index Density and Unit Weight of Soils and Calculation of Relative Density, D4254-16*. Annual Book of Standards, ASTM International, West Conshohocken, PA.

Barden, L., McGown, A., and Collins, K. (1973). The collapse mechanism in partly saturated soil. *Engineering Geology*, No. 7, pp. 49-60.

Bishop, A. W., and Blight, G. E. (1963). Some aspects of effective stress in saturated and partly saturated soils. *Géotechnique* 13, No. 3, pp. 177-197.

Bishop, A.W. and Wesley, L.D. (1975). A hydraulic triaxial apparatus for controlled stress path testing. *Géotechnique* 25, No. 4, pp. 657-670.

Brink, A. B. A., and Kantey, B. A. (1961). Collapsible grain structure in residual granite soils in southern Africa. *In Proceedings of the 5th International Conference on Soil Mechanics and Foundation Engineering*, pp. 611-614.

British Standard (1990). *Testing aggregates - Methods for determination of physical properties, BS 812-2:1975*. London.

British Standard (1990). *Methods of test for soils for civil engineering purposes, Part 2: classification tests BS 1377-2: 1990*. London.

British Standard (1990). *Methods of test for Soils for civil engineering purposes, Part 4: Compaction-related tests BS 1377-4: 1990*. London.

British Standard (1990a). *Methods of Test for Soils for Civil Engineering Purposes. Compressibility, Permeability and Durability Tests*, BS 1377-5:1990, 1990a. London.

British Standard (1990b). *Methods of Test for Soils for Civil Engineering Purposes. Consolidation and Permeability Tests in Hydraulic Cells and with Pore Pressure Measurement, BS 1377-6:1990, 1990b*. London.

British Standard (1990). *Methods of Test for Soils for Civil Engineering Purposes. In-Situ Tests, BS 1377-9:1990*. London.

British Standards Institution (2020). *Code of practice for ground investigations. BS 5930:2015+A1:2020*. London.

British Standards Institution (2016) BS EN ISO 18847:2016 Solid biofuels. *Determination of particle density of pellets and briquettes*. London.

Building and road research institute (BRRI), University of Khartoum. (2020) Soil profile of borehole (1), project: Block No. (5-10), Alhettana, North Omdurman.

Building and road research institute (BRRI), University of Khartoum. (2017a) Soil profile of borehole (2), project: Block No. (24), Hai Aljamaa, South Omdurman.

Building and road research institute (BRRI), University of Khartoum. (2017b) Soil profile of borehole (1), project: Block No. (4 -5), Hai Althawra (7), South Omdurman.

Burland, J.B. (1961). *The concept of effective stress in partly saturated soils*. M.Sc. Dissertation, University of Witwatersrand, South Africa.

Burland, J.B., Simpson, B and St John, H.D. (1979). Movements around excavations in London Clay. *Proceeding VIIth ECSMFE*, 7(1) pp. 13-29, Brighton.

Buscarnera, G., and Nova, R. (2009). "An elastoplastic strainhardening model for soil allowing for hydraulic bonding–debonding effects." Int. J. Numer. Anal. Methods Geomech., 33(8), 1055–1086.

Casagrande, A. (1936). The Determination of Preconsolidation Load and its Practical Significance. *In proceeding, 1st International Conference on Soil Mechanics Foundation Engineering, Cambridge*, No. 3, pp. 60–64.

Carraro, J.A.H., Prezzi, M. and Salgado, R. (2009). Shear strength and stiffness of sands containing plastic or nonplastic fines. Journal of geotechnical and geoenvironmental engineering 135, No. 9, pp. 1167-1178.

Chwała, M. (2020). Soil sounding location optimisation for spatially variable soil. *Géotechnique* Letters 10, No. 3, pp. 409-418.

Clemence, S.P. and Finbarr, A.O. (1981). Design considerations for collapsible soils. *Journal of Geotechnical and Geoenvironmental Engineering 107, ASCE (16106)*, pp. 305-317.

Coop, M. R., and Atkinson, J. H. (1993). The mechanics of cemented carbonate sands. *Géotechnique*, 43(1), pp. 53-67.

Cuccovillo, T. and Coop, M. R. (1997). The measurement of local axial strains in triaxial tests using LVDTs. *Géotechnique* 47, No. 1, pp. 167-172.

Derbyshire, E. (1995). *Genesis and properties of collapsible soils*. Dordrecht / Boston / London, Kluwer academic Publishers.

Edmonds, J.M. (1942). The distribution of the Kordofan sand (Anglo-Egyptian Sudan). *Geological Magazine* 79, No. 1, pp. 18-30.

Elsharief, A.M., Mohamedzein, Y.E. and Hussien, Y (1999). Geotechnical properties of Qoz soil. *Proceedings of the Twelfth Regional Conference for Africa on Soil Mechanics and Geotechnical Engineering*, pp. 317-320.

Evans, M.D. and Seed, H.B. (1987). *Undrained cyclic triaxial testing of gravels: the effect of membrane compliance*. College of Engineering, University of California - Berkeley, California. Source: National Science Foundation, Washington, DC., July 1987, 437 p. Identifying Number (report no.) UCB/EERC-87/08.

Fredlund, D.G., Rahardjo, H. and Fredlund, M.D (2014). *Unsaturated soil mechanics in engineering practice*. John Wiley and Sons, Hoboken, New Jersey, USA.

Fredlund, D. G. 2006. Unsaturated soil mechanics in engineering practice, The 2005 Terzaghi Lecture*: Journal of Geotechnical and Geo-environmental Engineering*, ASCE 132, No. 3, pp. 286–321.

Fredlund, M. D. (2000). *The role of unsaturated soil property functions in the practice of unsaturated soil mechanics*. PhD Thesis, University of Saskatchewan, Saskatoon, SK.

Freeman, T.J., Driscoll, R.M, and Littlejohn, G.S. (2002). *Has your house got cracks?* A homeowner's guide to subsidence and heave damage. BRE and Thomas Telford limited, 1994, 2002. Second edition 2002. ISBN 0727730894.

Hamid, W.O. (2012). *An experimental study on collapsible soils in Omdurman*. MSc thesis, BRRI, Univ. Of Khartoum.

Head, K. H. (2014). *Manual of soil laboratory testing*, No. 3: Effective stress tests (Third edition) Whittles Publishing, Scotland, UK.

Ho, C.L., Steadman, L.L. and Fragaszy, R.J. (1988). Influence of fines on the collapse potential of compacted sandy soil. *In Proceedings of the 24th symposium on engineering geology and soils engineering*. pp. 57-72.

Holtz, W.G. and Hilf, J.W. (1961). Settlement of soil foundations due to saturation. *Proceedings of the 5th International Conference on Soil Mechanics and Foundation Engineering*, Paris, 1: 673-679.

Houston, S.L., Mahmoud, H.H. and Houston, W.N. (1995). Down-hole collapse test system. *Journal of geotechnical engineering* 121, No. 4, pp.341-349.

Jardine, R.J., Symes, M.J. and Burland, J.B. (1984). The measurement of soil stiffness in the triaxial apparatus. *Géotechnique* 34, No. 3, pp. 323-340.

Jennings, J. E. B., and Burland, J. B. (1962). Limitations to the use of effective stresses in partly saturated soils. *Géotechnique* 12, No. 2, pp.125-144.

Jennings, J.E. and Knight, K. (1956). Recent experiences with the consolidation test as a means of identifying conditions of heaving or collapse of foundations on partially saturated soils. Transport Section. *The South African Institution of Civil Engineers*, No. 8, pp. 255-256.

Jennings, J.E. (1957). The additional settlement of foundations due to a collapse of structure of sandy subsoils on wetting. *In proceeding 4th in the international conference on soil mechanism and foundation engineering*, No. 1, pp. 316 -319.

Jennings, J. E. and Knight, K. (1975). A guide to construction on or with materials exhibiting additional settlement due to 'collapse' of grain structure. *Proc. 6th Regional Conf. for Africa on Soil Mech. Foundation Engineering*, Durban, No. 1, pp. 99-105.

Knight, K. (1960). *The collapse of structure of sandy sub-soils on wetting*. Ph.D. thesis, University of Witwatersrand, South Africa.

Lade, P.V., and Hernandez, S.B. (1977). Membrane penetration effects in undrained tests. JGED, *ASCE*, No. 103, GT2, February 1977.

Levy, M. C., Neely, W. R., Borsa, A. A., and Burney, J. A. (2020). Fine-scale spatiotemporal variation in subsidence across California's San Joaquin Valley explained by groundwater demand. *Environmental Research Letters* 15, No. 104083.

Lommler, J.C. and Bandini, P. (2015). Characterization of collapsible soils. *In Proceedings of the International Foundations Congress and Equipment Expo* (IFCEE 2015), pp. 1834-1841.

Lunne, T., Powell, J.J.M. and Robertson, P.K. (1997). Cone penetration testing in geotechnical practice. CRC Press, London.

Lytag - Specialist Aggregates Ltd (2006). From: Safety data sheet according to Lytag Ltd - Lytag health and safety (December 2006) and how it's made by LYTAG® data sheets.

Mahmoud, H.H.H., (1991). *The development of an in-situ collapse testing system for collapsible soils*. Doctoral dissertation, Arizona State University, USA.

Mahmoud, M. (1989). *Aspects of the measurement of soil strength using rotating shear devices, with particular reference to the vane test*. PhD thesis, Imperial College, University of London.

Maswoswe, J. (1985). *Stress paths for compacted soil during collapse due to wetting*. PhD thesis, Imperial College, University of London.

Maswoswe, J., Burland, J. B., Vaughan, P. R. (1992). Stress path method of predicting compacted soil collapse. *In proceeding of the 7th international conference on expansive soil* – Dallas, Texas (USA), pp. 61-66.

Mihalache, C. and Buscarnera, G. (2015). Is wetting collapse an unstable compaction process? *Journal of Geotechnical and Geoenvironmental Engineering* 141, No. 2 (2015): 04014098.

Mitchell, J.K. and Soga, K., (2005). *Fundamentals of soil behaviour* (3rd Edition). Hoboken, NJ: John Wiley and Sons.

Moussa, N.S.H. (2019). *Geophysical and hydrogeological investigation of ground water aquifers at the area west of Omdurman - Sudan.* MSc dissertation. International University of Africa.

Ng, A.M., Yeung, A.T., Lee, P.K. and Tham, L.G. (2006). Design, fabrication, and assembly of a large oedometer. *Geotechnical Testing Journal* 29, No. 4, pp. 298-305.

Ofosu, M., (2019). *Investigating the fabric of collapsible gravel*. MSc dissertation. Department of Civil and Environmental Engineering. Imperial College London.

Omer, O.M. (1973). *Collapse in a partly saturated soil from Sudan*. PhD Thesis, University of Birmingham.

Osman, M.A. and Ahmed, E.M. (2015). An experimental study on the identification and classification of collapse potential of some soils in Sudan. *Innovative Geotechnics for Africa - Bouassida, Khemakhem and Haffoudhi* (Eds.) ISBN: 978-9938-12-936-6.

Osman, Y.I. (2004). *Failure investigation of a two-storey load bearing building in Omdurman*. MSc thesis, Building and Road Research Intitute (BRRI), University of Khartoum.

Rogers, C. D. F. (1995). Types and distribution of collapsible soils. *Proceeding, NATO Advanced Research Workshop*. Genesis and proporties of collapsible soil, Loughborough, U.K. (Eds. E. Derbyshire, T. Dijkstra and I. J. Smalley). Kluwer academic Publishers, Dordrecht / Boston / London. p.p. 1 – 17.

Rollins, K.M., Rollins, R.L., Smith, T.D. and Beckwith, G.H. (1994). Identification and characterization of collapsible gravels. *Journal of geotechnical engineering* 120, No. 3, pp. 528-542. ASCE, ISSN 0733-9410/94/0003-0528.

Salgado, R., Bandini, P., and Karim, A (2000). Shear strength and stiff-ness of silty sand. *J. Geotech. Geoenviron. Eng*. 1265, pp. 451–462

Seedahmed, G. (2021). An overview of modern application of surveying engineering. Professional expertise sharing webinars (First webinar - 26 June 2021). Source: https://youtu.be/alNZgUyayrs. [Accessed on 07/12/2021].

Selley, R. C. (2000). *Applied sedimentology*. Second Edition. Harcourt/Academic Press/San Diego/USA, pp. 118 - 119.

Shakoor, A., and Cook, B. D. (1990). The effect of stone content, size, and shape on the engineering properties of a compacted silty clay. *Bulletin of Association of Engrg. Geologists*, XXVII (2), pp. 245-253.

Shen, Y. (2021). *Modelling collapsible soil using DEM. MSc dissertation*. Department of Civil and Environmental Engineering. Imperial College London.

Singhal, S., Sharma, R.S. and Phanikumar, B.R. (2016). A laboratory study of collapse behaviour of remoulded loess under controlled wetting and flooding. *Geomechanics and Geoengineering* 11, No. 2, pp.159-163.

Smith, P.G.C. (2003). *Numerical analysis of infiltration into partially saturated soil slopes*. PhD thesis, Imperial College, University of London.

Som, N. N., Das, S.C. (2006). *Theory and Practice of Foundation Design* (3rd printing). New Delhi-110001 ISBN-81-203-2190-1. pp. 92.

Toll, D.G. (2002). *TRIAX user manual*. Geotechnical System Group, Durham University, Durham. Version 4.

Toll, D.G. and Ackerley, S.K. (1988). The development of two data acquisition systems for a geotechnical laboratory. In: Rio de Janeiro (ed.). *Proceeding of the International Symposium on New Concepts in Laboratory and Field Tests in Geotechnical Engineering*, pp. 453-456.

Torres, L.P. (1983). *Membrane Penetration in Cyclic Triaxial Test*. Unpublished report, CE299, College of Engineering, University of California - Berkeley, December 1983.

Vaughan, P.R. (2006). *Embankment fill material materials*: Lecture 2 notes and figures. Notes from Imperial College short course on Earthworks and Embankments.

Whiteman, A. J., (1971). *The geology of the Sudan Republic*. Oxford: Clarendon Press.

Wu, C. L., Li, J. H., & Liu, J. C. (2020). Experimental study of a shallow foundation on spatially variable soils. *Georisk*: Assessment and Management of Risk for Engineered Systems and Geohazards, pp. 1-10.

Appendix A: The GDS permeameter – triaxial apparatus

A.1 the GDS permeameter description, operation, and calibrations

A.1.1 Description

The GDS permeameter is devised to measure the soil permeability under controlled stress or strain conditions and it has capability of applying infinite water flow. This represents the main feature of this apparatus in which two pairs of volume controllers are connected to the specimen and a water tank through a volume distributing panel as shown in Figure 6.12. The pair connected to the specimen base known as base controllers and at the top known as back controllers. The other features of this apparatus are conducting the triaxial standard tests, stress path tests and it has capability of applying different load types and rates through the 'advance loading module'. In this part, the focus is on the relevant modules that used in this research.

Since the tested specimens are tested in a dry condition and opened to the atmosphere from top, these essential test modules were suitably used to conduct the triaxial shear and collapse tests that described in Section 6.7. Consolidated undrained (CU) triaxial module was used for both dry and wet shearing because the specimen top was opened to the atmosphere which means explicitly back pressure control was disconnected. Also, in this test setup, as long as there was not any built up pore water pressure, the total stresses were defined to be equal to the effective stresses. For collapse test the 'advance loading module' was used to control the rate of the application of collapse stress and maintaining its target value constant under constant cell pressure.

A.1.2 Operation for conducting the considered tests

After the completion of specimen set-up stage as described in Section 6.0, the first window that appears after opening the GDS operation software and naming and saving the test data file is presented in Figure A.1. It is known as 'test plan' which is used for entering the specimen dimensions and then adding a test to the test list, the windows that used for entering this test plan are shown in Figures A.2 to A.5. After setting the test plan, the button at the bottom right of this window is used to open a window associated with running and tracing the test, known as 'test display', while it is running through a set of plotting spaces relating the main test parameters (see Figure A.6).

The 'advanced loading module' was used for applying the cell pressure and collapse stress (axial stress) as shown in Figure A.2. Pressing the 'next' button, in the bottom right of this window, opens the 'optional test termination conditions' window shown in Figure A.3.



Figure A.1: Test plan window

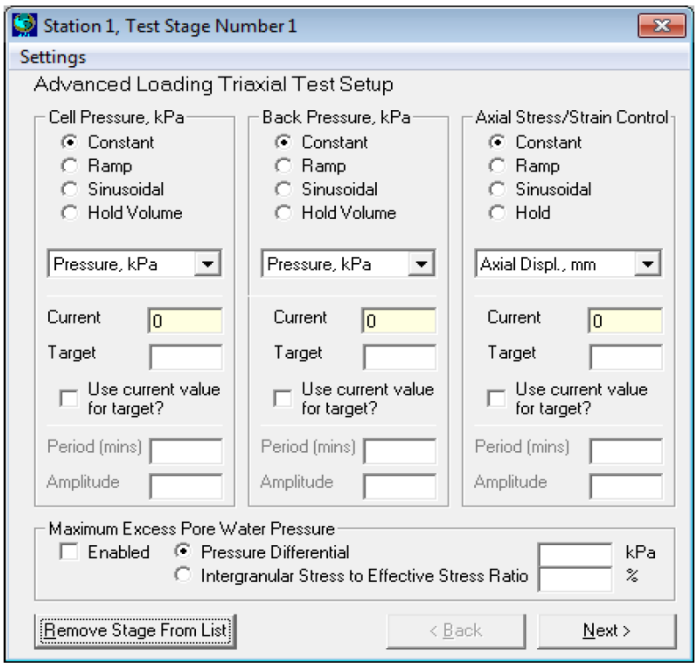


Figure A.2: Advanced loading module window

The test termnation conditon was ticked in the list below, see Figure A.3, to terminate the test in this stesting programme the is maximum axial strain = 22%. Howerever, most of the tests terminated because the cell presure volume controller was run out of water due to membrane rupture (see Figure A.5). This test termination conditions window leads to one of two options: (I) pressing 'advance' button leads to more temination conditions 'advance end of stage options' (see Figure A.4), (II) or pressing 'add to test list' to return to the 'test plan' window shown in Figure A.1.

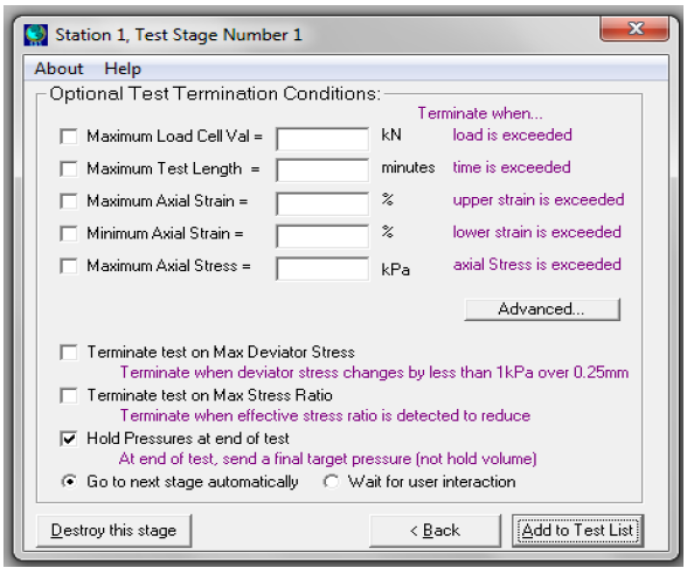


Figure A.3: Test termination conditions window

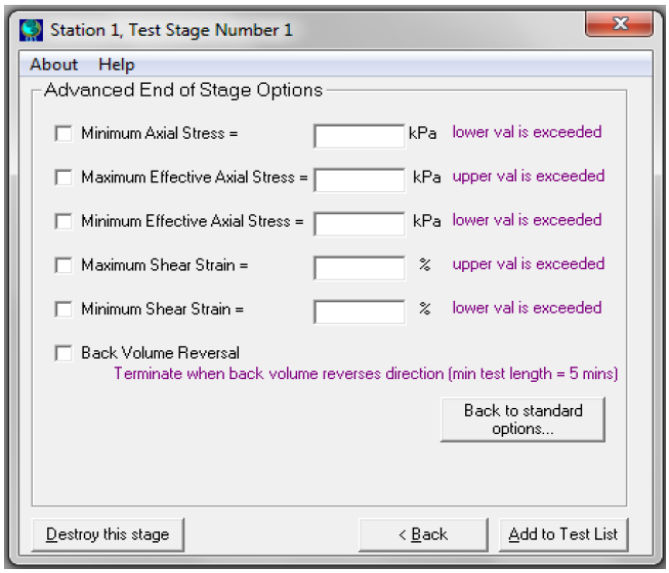


Figure A.4: Advanced setting of test termination window

The dry and wet shearing tests were set up by entering the target cell pressure value and loading velocity (0.0139 mm/min.) in the test type 'consolidated undrained' window shown in Figure A.5. This window is opened by choosing the standard triaxial test type from a list of tests that can be run through this GDS software.

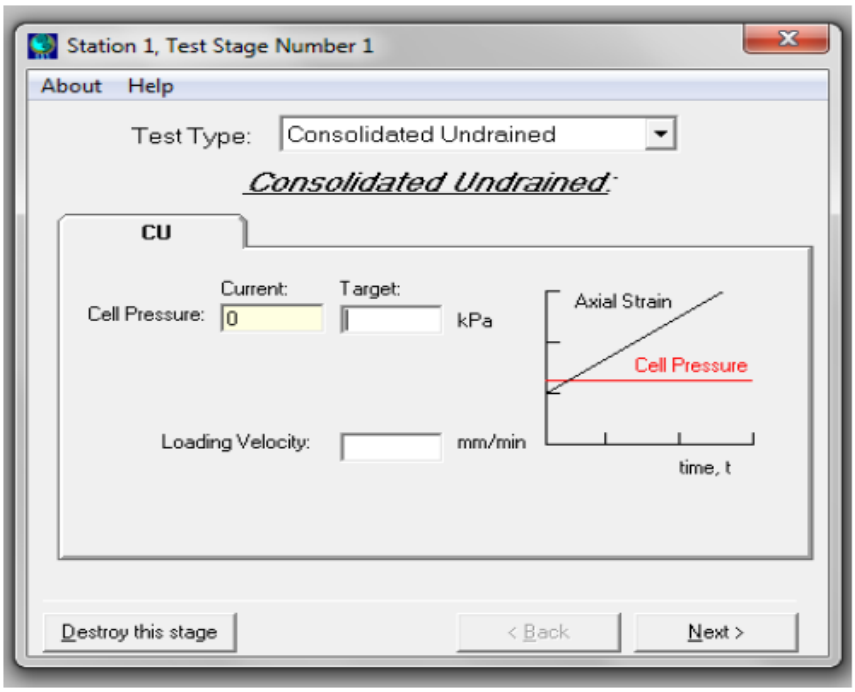


Figure A.5: Consolidated undrained (CU) test type window

Finally, the test display unit shown in Figure A.6 controls the start of the test, makes manual test pause or manually moving to the next stage of test. Also, live test data such as stage number and time and test parameters are displyed. In the display screen, three graphs can be displayed alternatively (one at a time) and Excel data can be shown as well.

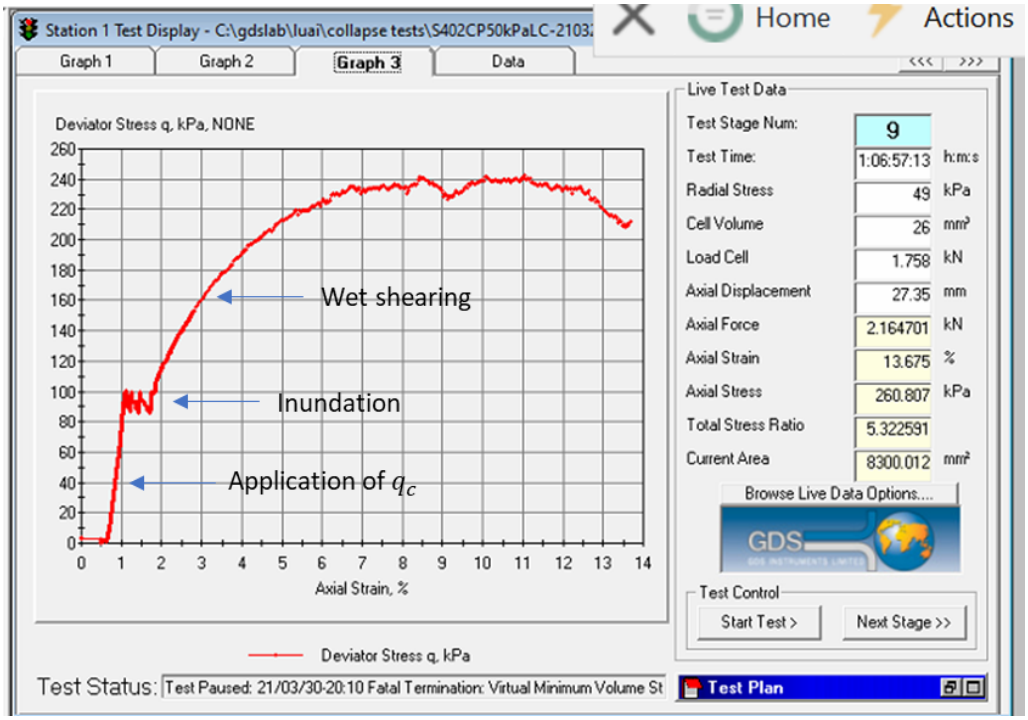


Figure A.6: Test display window

A.1.3 Calibrations

A.1.3.1 Calibration of the cell pressure/volume controller

Table A.1 Calibration of the cell pressure/volume controller

Calibration results – Cell pressure/volume controller	
Date	2nd July 2018
Transducer type	Pi620C-4MPag-B2AV-2.5-GDS01
Serial No.	520886
Pressure range	0 to 4MPa gauge
Zero output	0.000mV
Span	99.890mV
Full scale output	99.890mV
Non-Linearity	±0.048% FS
Hysteresis	0.040% FS
Supply voltage	10.0000Vdc
Thermal zero shift	<±0.01%/FSO/°C
Thermal span shift	<-0.015%/°C
Insulation resistance	> 1000 megaohms at 100Vdc

A.1.3.2 Calibration of the load cell

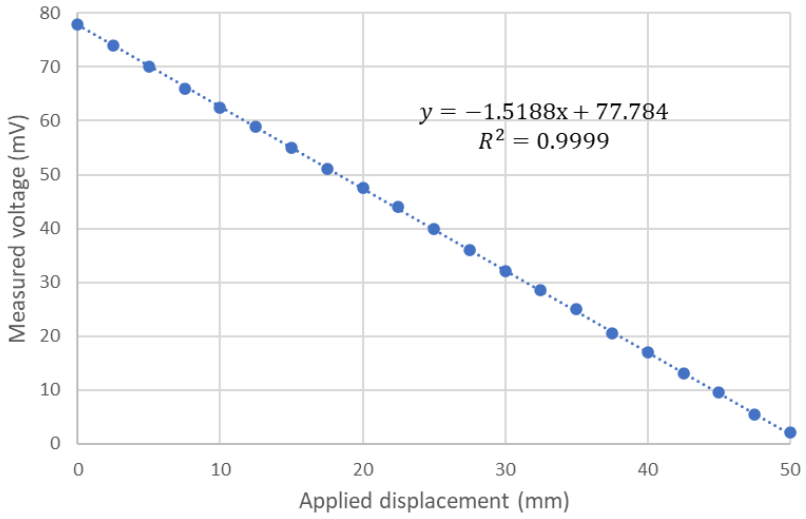
Table A.2 Calibration of the load cell

Calibration results – Load cell	
Date	10th October
Transducer type	STALC9-16kN-003-000
Serial No.	54244
Load rating	16kN
Proof rating	24kN
Calibration mode	Compression
Zero output	0.000mV @ 10Vdc
Sensitivity	2.2057mV/V
Non-Linearity	<±0.022% FS
Hysteresis	<-0.032% FS
Supply voltage	10.0000Vdc
Input resistance	750 Ohms
Insulation resistance	> 20 GOhms at 100Vdc

A.1.3.3 Calibration of the external displacement transducer

Table A.3 Calibration of the external displacement transducer

Calibration results – Linear displacement transducer (Strain gauge)	
Serial number	G10327
Range	50mm
Calibration supply	10 Volts DC
Quoted linearity	<±0.07 %
Temp range	-10 °C to +70 °C
Sensitivity @ 10V DC	0.65756019 mm/mV



A.1.3.4 Calibration of the internal LVDTs

The micrometre in Figure A.7 was used for calibrating the LVDT1 and LVDT2 in an interval of 0.5mm. The result of this calibration is given in Tables A.4 and A.5 respectively.

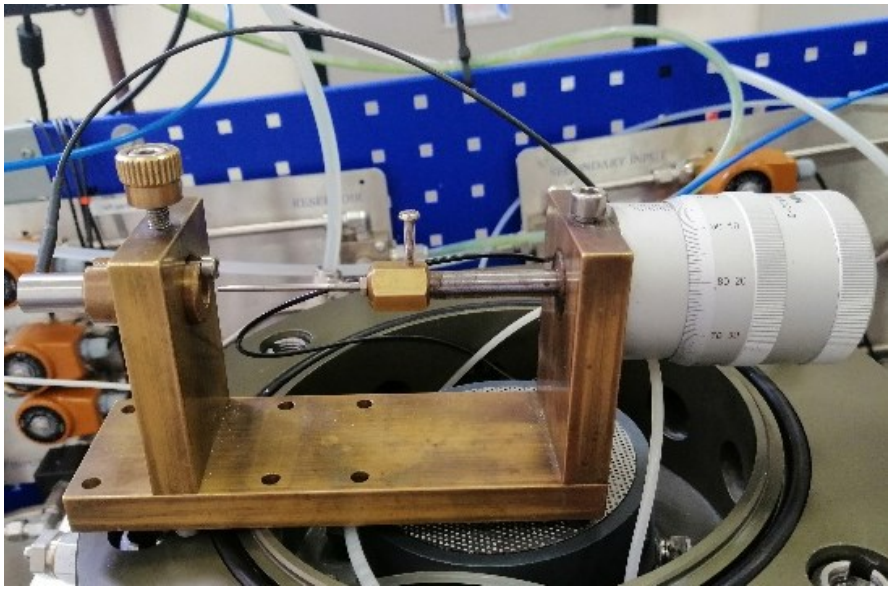
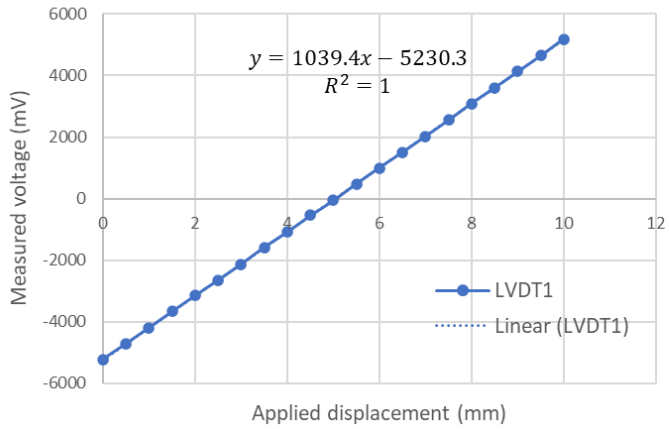


Figure A.7 the micrometre used for calibrating the LVDTs

Calibration of the LVDT1

Table A.4 Calibration of the LVDT1

Calibration results – LVDT1	
Date	21st May 2021
Serial number	1
Range	10mm
Full range output	10000mV
Sensitivity	0.000962mm/mV

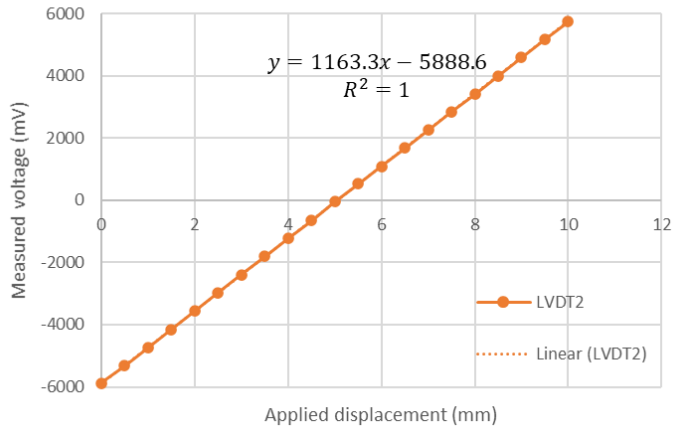


Applied displacement (mm)	Measured voltage (mV)
0	- 5222.938
0.5	- 4698.935
1	- 4187.750
1.5	- 3665.883
2	- 3142.796
2.5	- 2642.598
3	- 2123.173
3.5	- 1583.300
4	- 1079.440
4.5	- 542.314
5	- 44.252
5.5	474.563
6	998.566
6.5	1513.718
7	2033.143
7.5	2552.873
8	3083.895
8.5	3606.067
9	4135.868
9.5	4658.650
10	5181.738

Calibration of the LVDT2

Table A.5 Calibration of the LVDT2

Calibration results – LVDT2	
Date	24th May 2021
Serial number	2
Range	10mm
Full range output	10000mV
Sensitivity	0.00086mm/mV



Applied displacement (mm)	Measured voltage (mV)
0	- 5871.761
0.5	- 5317.545
1	- 4741.355
1.5	- 4152.349
2	- 3569.140
2.5	- 2979.522
3	- 2398.755
3.5	- 1811.579
4	- 1237.526
4.5	- 649.434
5	- 46.999
5.5	526.139
6	1086.764
6.5	1673.635
7	2253.487
7.5	2837.001
8	3409.833
8.5	3997.009
9	4579.607
9.5	5162.206
10	5738.396

Appendix B:

Soil profile B1

North Omdurman (Project: Block No. (5-10), Alhettana – Building and road research institute, University of Khartoum) (B.H(1)) December 2020

Depth (m)	Description	Group Symbol	Atterberg Limits			%pass sieve #200	SPT-Results		Remarks
			L.L %	P.L %	P.I %		Blows Each 6,3,3,3,3 in	N-Value	
1.0									
	Medium dense, light brown, Gravelly Clayey SAND		36	18	18	29	20,8,8,5,6	27	
2.0									
									Penetration
3.0	Becomes very dense, yellowish light brown, Clayey SAND		31	18	13	30	24,14,14,16,7	>50	1.25”
	(highly weathered sandstone)								
4.0									Penetration
	Becomes Gravelly Clayey SAND with few calcareous		31	17	14	23	29,17,16,16,2	>50	0.25”
5.0	material								
		SC							Penetration
6.0			35	19	16	21	28,21,27,3	>50	0.25”
7.0									Penetration
	Becomes pinkish		31	17	14	11	51,51	>50	1.5”
8.0									
									Penetration
9.0			23	15	8	28	51,51	>50	0.25”

Soil profile 2

South Omdurman (Project: Plot 521, Block 24, Hai Aljamaa – Building and road research institute, University of Khartoum) (B.H(2)) September 2017

Depth (m)	Description	Group Symbol	Atterberg Limits			N.M.C %	%pass sieve #200	SPT-Results		Remarks
			L.L %	P.L %	P.I %			Blows Each 6,3,3,3,3in	N-Value	
1.0	Medium dense, light brown, dry, Clayey GRAVEL with calcareous materials.	GC	37	20	17	5.88	21	7,6,7,7,8	28	
2.0	Becomes Dense.		35	17	18	6.53	19	13,8,8,9,11	36	
3.0	Dense, light brown, wet, Gravely Clayey SAND with calcareous materials.	SC	47	22	25	6.40	27	9,12,11,11,10	44	
4.0	Hard, light brown, wet, Gravelly Silty CLAY of high Plasticity (Completely weathered Mudstone Sandstone).	CH	63	24	39	18.58	54	10,6,8,11,11	36	
5.0	Becomes without gravel.		58	24	34	20.41	48	12,8,10,11,12	41	
6.0	Hard, light brown, wet, Silty CLAY of low plasticity (Completely weathered Sandstone).	CL	46	20	26	17.92	61	18,14,18,19	>50	Penetration 2.5”
7.0			46	21	25		66	27,30,21	>50	Penetration 1.5”
8.0										Penetration
9.0	Hard, light brown, Silty CLAY of high Plasticity (Completely weathered Mudstone and Sandstone).	CH	59	20	39		57	42,51	>50	1”
10.0	Becomes (Completely weathered Sandstone).		61	22	39		71			
11.0										

Soil profile 3

North Omdurman (Project: Plot No. (9/4), Block No. (4/5), Building and road research institute, University of Khartoum) (B.H(1)- Coordinates: E:443240 N:1729498), February 2017

Depth (m)	Description	Group Symbol	Atterberg Limits L.L %	P.L %	P.I %	%Pass sieve #200	SPT-Results Blows Each 6,3,3,3,3in	N-Value	Remarks
1.0									Penetration
	Very dense , light brown, Clayey GRAVEL	GC	33	20	13	11	34,28,15,8	>50	2.5”
2.0	with calcareous material								
3.0	Stiff , dark brown, Silty CLAY of low		48	25	23	57	7,5,5,6,7	23	
	plasticity with calcareous material.	CL							
4.0									
	Hard , light brown, Silty CLAY of high		54	27	27	66	14,6,7,9,10	32	
5.0	plasticity	CH							
6.0	Dense , light brown, Clayey SAND		50	23	27	46	10,10,10,12,13	45	
		SC							
7.0									Penetration
	Hard , light brown, Silty CLAY of high		55	24	31	60	15,10,15,20,6	>50	0.5”
8.0	plasticity								
									Penetration
9.0			56	24	32	55	25,20,23,8	>50	0.5”
		CH							
10.0									
			53	25	28	52	34,24,27	>50	
11.0									